Practical and efficient solid-state sources of single and indistinguishable photons for quantum applications

Marie Billard

université
PARIS-SACLAY

Practical and efficient solid-state sources of single and indistinguishable photons for quantum applications

Vers des sources semi-conductrices de photons uniques et indiscernables, efficaces et faciles à utiliser, pour des applications quantiques

Thèse de doctorat de l'Université Paris-Saclay

École doctorale n° 572, Onde et Matière (EDOM)
Spécialité de doctorat: Physique
Unité de recherche: Université Paris-Saclay, CNRS, Centre de Nanosciences et de Nanotechnologies, 91120, Palaiseau, France
Référent: Faculté des sciences d'Orsay

Thèse présentée et soutenue à Paris-Saclay, le 4 mars 2021, par

Marie BILLARD

Composition du Jury

Jean-François ROCH Professeur des universités, ENS Paris-Saclay	Président
Thierry AMAND Directeur de recherche, INSA Toulouse	Rapporteur et Examinateur
Valia VOLIOTIS Professeur des universités, Sciences Sorbonne Université	Rapporteure et Examinatrice
Julien CLAUDON Directeur de recherche, CEA-IRIG-PHELIQS Grenoble	Examinateur
Delphine MARRIS-MORINI Professeur des universités, C2N Palaiseau	Examinatrice
Jean-François ROCH Professeur des universités, ENS Paris-Saclay	Examinateur

Direction de la thèse

Olivier KREBS Directeur de recherche, C2N Palaiseau	Directeur de thèse
Valérian GIESZ CEO, Quandela	Invité

Thèse de doctorat
NNT: 2021UPASP015

"Quelque soit votre rêve vivez-le, car l'audace est empreinte de génie, de puissance et de magie"

Goethe

Contents

Résumé

Depuis la seconde moitié du XXe siècle, une succession d'avancées technologiques majeures ainsi que l'étude des concepts de la mécanique quantique comme la superposition ou l'intrication quantique ont marqué le début de la "deuxième révolution quantique" dans quatre domaines principaux : la simulation [1], la détection [2], la communication [3, 4], et l'informatique [5, 6] quantique.

Parmi les applications émergeantes, certaines se basent sur la photonique quantique [7] et nécessitent des sources de photons fiables et efficaces. L'amélioration constante des performances des sources semi-conductrices de photons uniques en ont ainsi fait des composants essentiels pour les applications quantiques nécessitant un flux élevé de photons uniques et indiscernables [8]. Dans ce travail, nous utilisons des boîtes quantiques couplées à des micropiliers optiques développées par l'équipe du Prof. P. Senellart [9]. Dans ce contexte, et au sein de la start-up Quandela, nous développons différentes techniques pour obtenir une source efficace, tout en améliorant la facilité d'utilisation pour les utilisateurs non experts.

Dans ce travail, nous détaillons tout d'abord le développement et l'optimisation d'un microscope confocal stable et compact pour collecter efficacement les photons uniques dans une fibre monomode pendant plusieurs jours. Ce dernier s'adapte à la fois à différents types de collection (espace libre ou fibré) ainsi qu'à différentes techniques d'excitation de la boîte quantique : excitation sous fluorescence résonante, ou assistée par l'interaction et l'émission de phonons acoustiques longitudinaux. Grâce à des études précises de l'efficacité de couplage dans une fibre monomode et du filtrage du laser d'excitation, les transmissions totales de ces systèmes sont de l'ordre de $65\% \pm 5\%$. Dans un second temps et afin d'augmenter la brillance de nos sources dans la fibre de collection, nous avons étudié un régime d'excitation se basant sur les interactions entre les transitions de la boîte quantique et les phonons acoustiques longitudinaux (AL-phonons) [10, 11]. Pour cela le laser d'excitation est légèrement désaccordé en énergie. Il est donc possible de le filtrer spectralement, ce qui permet de collecter tous les photons uniques émis. Nous démontrons alors une brillance avant la première lentille multipliée par un facteur trois, ainsi qu'une émission, linéairement polarisée ($D > 98\%$), de photons uniques et indiscernables. Enfin, afin de fournir une source de photons uniques "plug-and-play", nous détaillons le développement d'un système complétement fibré afin de s'affranchir de positionneurs et d'un cryostat à faibles vibrations, volumineux et onéreux. Ainsi, nous proposons une méthode pour placer et fixer une fibre monomode au-dessus d'un pilier. Ce projet constitue un défi technique et est toujours en cours. Néanmoins, les premiers résultats sont très encourageants et démontrent déjà le potentiel de ce développement qui permettra de placer la source dans un cryostat standard. Il serait ainsi possible de mettre tous les composants, du laser d'excitation à la source en passant par le système optique dans le même produit à hauteur d'homme.

Ainsi, nous avons développé et optimisé un produit compact, stable et facile d'utilisation pouvant être mis dans des modules de rack, et dont la brillance fibrée, sous excitation as-

sistée par AL-phonons, est au moins aussi élevée que celle mesurée avec le plus optimisé des systèmes d'excitation/collection en espace libre.

Les prochains projets portent sur l'augmentation de la brillance intrinsèque des sources par l'étude des pertes et du taux d'extractions de la structure semi-conductrice, mais aussi sur la conversion ou l'émission des photons dans les bandes de longueurs d'ondes télécoms.

Remerciements

Je souhaiterais tout d'abord remercier l'équipe de Quandela dans son ensemble, équipe qui a bien grandi depuis mon arrivée en 2018. Merci à eux d'avoir fait en sorte que ma thèse se passe dans les meilleures conditions possibles. Ce fut un réel plaisir et un honneur de travailler à leur côté et l'aventure continue, encore merci à eux.

Je remercie aussi toute l'équipe GOSS pour m'avoir accompagnée pendant ces trois années. A leur côté j'ai découvert la physique et l'optique quantique. En observant et en applicant leur façon d'utiliser les sources de photons uniques, j'ai pu comprendre et mettre en place des sytèmes efficaces et plus faciles d'utilisation.

Merci aussi aux équipes de la salle blanche (épitaxie, gravure, lithographie, ...) de nous permettre de travailler avec des sources de photons uniques efficaces. Enfin merci à toutes les équipes du C2N (l'atelier mécanique, les équipes techniques, informatiques et administratives) pour m'avoir permis de travailler dans les meilleures conditions possibles malgré le déménagement et la crise sanitaire.

Merci à Valérian et Niccolo pour m'avoir fait confiance dès le début de l'aventure Quandela et de m'avoir offert la possibilité d'en faire partie. Le chemin n'a pas toujours été facile mais il m'a fait grandir scientifiquement et personnellement.

Merci à Pascale pour sa confiance et son soutien, tant scientifique que personnel, qui m'a permis de m'affirmer dans mon travail.

Merci à Olivier d'avoir accepté d'être mon directeur de thèse. Bien que mon sujet soit assez éloigné de ses travaux de recherche, il a toujours pris le temps de répondre à mes questions et m'a beaucoup apporté notamment pour la compréhension de la théorie de l'excitation assitée par des phonons acoustiques longitudinaux.

Je souhaiterais aussi remercier ma famille qui m'a soutenue et accompagnée jusque là. Merci plus particulièrement à mes parents, car je n'y serais jamais arrivée sans eux. Merci aussi à mes frères, mes tantes, mon grand-père.

Merci à Thomas pour nos discussions historiques toujours captivantes qui m'ont changer les idées tout en élargissant mes connaisances dans ce domaine qui me passionne.

Merci à mes tantes Agnès et Cécile pour leur écoute attentive et toujours bienveillante.

Merci à Thibaut pour son soutien en début de thèse et le jour de ma soutenance. Sans lui je n'aurai jamais osé commencer cette aventure, il m'a donné confiance et je lui en serai toujours reconnaissante.

Merci à Katia, pour nos coups de folie, nos sorties mémorables et pour son soutien indefectible.

Merci à Clément pour nos balades dans Paris, les expos, les visites, les week-ends, les dégustations de thés. Son soutien et nos escapades nous ont permis de nous évader du quotidien très très scientifique.

Merci à Martin pour son temps, sa gentillesse, ses connaissances, sa patience, sa table optique et son cryostat. Ma thèse n'aurait pas aussi bien avancée sans lui. Il a toujours été là quand j'avais besoin d'aide, un grand merci à lui.

Je souhaiterais aussi remercier Florian. Un grand merci à lui pour son optimisme, son soutien, sa bonne humeur contagieuse et ses sources fibrées.

Merci à Ilse pour sa gentillesse et son soutien. Nos escapades culinaires (viticoles) et touristiques resteront toujours gravées.

Je souhaiterais aussi remercier Petr. Arrivé durant les derniers mois de ma thèse, il a néanmoins été un réel soutien.

Merci aussi à Alexandre, malgré quelques différences de points de vues, son expertise scientique m'a souvent aidée et permis d'avancer plus efficacement.

Merci à Loïc pour sa gentillesse et le temps qu'il a pris pour répondre à mes questions. Merci pour nos longues discussions scientifiques (et pas que).

Merci à Mohammed pour son soutien psychologique. Merci pour nos discussions et nos parties de Plato (sans oublier la flûte bien sûr).

Merci à Sarah, Stephen, Nathan et Hélène pour leur aide et leur soutien. En particulier concernant la compréhension de la théorie et des résultats de l'excitation assistée par des phonons acoustiques longitudinaux.

Merci à Nicolas. Cher ancien co-bureau merci pour nos discussions tant scientifiques que sur d'autres sujets. Partir de notre bureau fut vraiment difficile.

Merci à Matthias qui en mettant en place les améliorations du système nous apprend à gérer nos stocks.

Merci à Pierre pour nos choco-chauds et son soutien.

Enfin merci à tous ceux qui, par une paroles, une présence, un acte, m'ont permis d'avancer, un grand merci à vous.

Je dédie cette thèse à mamie et papa, partis trop tôt ils m'ont mis sur les rails. Je suis fière d'être arrivée jusque là, merci à eux du fond du cœur.

Abbreviations glossary

The abbreviations are listed in the order of appearance.

HBT	Hambury and Brown and Twiss
HOM	Hong-Ou and Mandel
BS	Beam Splitter
PBS	Polarising Beam Splitter
$\mathcal{P}$	Single photon purity, $\mathcal{P} = 1 - g^2(0)$
$\mathcal{M}_{\text{Th}}$	Theoretical mean wave-packet overlap
QD	Quantum dot
PDC	Parametric Down Conversion
SPDC	Spontaneous Parametric Down Conversion
η	Extraction efficiency from either the bulk or the pillar
$\text{F}_{\text{P,cav}}$	Purcell factor of the optical cavity
Q_0	Cavity quality factor
V_{eff}	Effective volume of the optical cavity mode
ZPL	Zero Phonon Line
PSB	Phonon Side Band
β	Fraction of photons emitted in the fundamental optical mode of the cavity
$\mathcal{B}_{\text{FL}}$	First lens brightness, $\mathcal{B}_{\text{FL}} = \beta \times \eta \times \text{p}_\text{e}$
p_e	Occupation probability of the excited state
V_{HOM}	HOM Visibility
$\mathcal{M}_{\text{exp}}$	Experimental mean wave-packet overlap
$\mathcal{M}_{\text{corr}}$	Corrected mean wave-packet overlap
$\mathcal{B}_{\text{PFL}}$	Polarised First lens brightness, $\mathcal{B}_{\text{PFL}} = \mathcal{B}_{\text{FL}} \times \text{r}_{\text{pol}}$
r_{pol}	Fraction of emitted photons in the collection polarisation
$\mathcal{B}_{\text{F}}$	Fibred lens brightness, $\mathcal{B}_{\text{F}} = \mathcal{B}_{\text{FL}}(\times \text{r}_{\text{pol}}) \times \eta_{\text{syst}} \times \eta_{\text{coupl}}$

Chapter 1

Introduction

In the 20th century, we witnessed two quantum revolutions. Each of them has led to a better understanding of both atomic and solid-state physics and has enabled a succession of technological breakthroughs. During the first quantum revolution, progresses were achieved owing to an improved knowledge of microscopic laws and resulting phenomena such as the electron motion in solids and light-matter interactions. These allowed the development of practical devices such as the GPS, transistors, and lasers. Furthermore, in the last twenty years, theoreticians, researchers, and engineers continued to innovate by exploring more advanced concepts of quantum mechanics including quantum superposition and entanglement. This started the "second quantum revolution", with the development of four main fields of applications: quantum simulation [1], quantum sensing, [2], quantum communication [3, 4], and quantum computing [5, 6]

Starting from theoretical concepts, practical implementations of quantum technologies have come a long way. In 2019, Google already claimed to have reached a quantum computational advantage by manipulating superconducting qubits [12]. However, to suppress noise and decoherence such technology requires an ultra-high vacuum environment and operating temperatures close to absolute zero. In contrast, quantum photonics does not suffer from these requirements and photons stand as a promising alternative to matter qubits. Indeed, since photons do not interact much with their environment, they hardly suffer from decoherence, and are then low-noise carriers of quantum information [13, 14].

Optical quantum technologies have then shown impressive progresses in the last decade, as illustrated in the following examples: [7]:

- Regarding quantum computing [13,15], single-photons have already proved their ability to be used for Boson sampling experiments [16, 17]. In 2019, the group of Prof J.W. Pan proposed a reliable protocol with 20 photons [18] and has very recently reported a real quantum computational advantage using a continuous variable protocol [19].

- Optical quantum simulations has also been used in the chemistry field to predict chemical transformations and perform simulations of molecules [20, 21].

- In the sensing field, one can use absorption of two entangled photons to improve spectroscopy measurements, in particular on ultrafast timescales [22]. Single-photons can

also be used in phototherapy, diagnostic and fluorescence microscopy [23]. Indeed, photon entanglement can lead to a significant reduction of the power needed for imaging. It is then possible to achieve a better resolution without deteriorating the tissues [24]. For imaging in general, photon counting can improve image precision [25] and with high efficiency single-photon detectors, it is also possible to make sub-shot noise measurements [26–28].

- The non-cloning property of single photons and the near-unity sources brightness are also the basis of secure [14] and long distance [29] communications, and are used for quantum key distribution (QKD) [30, 31]. With entangled photons, Alice and Bob can exchange secured keys. Indeed, if a single-photon is intercepted, its absence can be detected. If it is measured, and if another photon is send at its place, the replacement can also be identified. Beyond quantum key distributions, reliable building blocks for quantum networks are developed [32, 33].

- Finally, multi-photon entangled states such as cluster states [34–36] are highly sought for developing measurement based quantum computing [37, 38] or quantum networks [36, 39, 40].

To push photonic quantum technologies furthers, large efforts have been made on the technological side from the quantum-light sources to the detectors and all the components necessary for photon manipulation and interactions. However, it is still an outstanding goal to develop an ideal generator of optical qubits, that is an "on-demand" source of single and indistinguishable photons. The source must be triggered and emits only one photon at the time with a unity probability. In addition, all emitted photons must be indistinguishable. This property is essential for application such as quantum computing or quantum relays which are based on photon quantum interference [8].

For the last twenty years, many groups have then worked on different technologies to implement such single-photons sources. The most widely used are based on frequency conversion in non-linear crystals [30, 31]. However, such sources suffer from intrinsic limitations in terms of efficiency. This is why single-photon sources based on single quantum emitters are explored. These emitters can be either trapped ions [32, 41], trapped atoms [42, 43], NV or SiC-defects in diamond [39, 44], or quantum dots (QDs) [45–47]. Most implementations have then demonstrated great progress in fulfilling the requirements of single-photon purity and indistinguishably. However, combining high single-photon purity and indistinguishability with high efficiency has long remained a great challenge for many systems [9, 48–53]. One major issue is that of extracting and collecting all the emitted photons in a well-defined optical mode. Most emitters are then embedded in waveguides or cavities. The latter have the added benefit of enhancing the spontaneous emission by reducing the decay time of the emitter. The interaction between the emitter and its environment are then reduced, leading to an improvement of the photon indistinguishability.

This thesis has been carried out in the start-up Quandela in collaboration with the group of Prof. P. Senellart (at the Centre de Nanosciences et de Nanotechnologies, CNRS-C2N), and under the supervision of Prof. O. Krebs. The main objective of this work was to implement practical and efficient sources of single and indistinguishable photons for quantum

applications. The source, developed by the CRNS-C2N group over the past fifteen years, is based on a InGaAs/GaAs QDs embedded in micro-pillars, and has already proven its ability to deliver single and indistinguishable photons with a brightness of up to 80% [49]. However, this is only the brightness before the first lens of the optical system. The source is then intrinsically bright but when I started my PhD, the transmission of the subsequent optical system was a strong limitation to the effective source brightness. In order to perform continuous experiments lasting days, the optical system also needed to be more stable and easier to use.

My first work was to develop and optimise a confocal microscope able to efficiently collect the single photons. This has led to a bright fibred-source stable during days under resonant fluorescence. To go further, we have also developed, and are still working on a technique to fix a single-mode fibre directly above a source. This is a crucial step towards a "plug-and-play" system where experimenters only need to plug the output fibre into their quantum applications and work directly with the emitted single photons. To push the brightness of our single photon sources even further, we then studied an excitation scheme based on longitudinal acoustic phonons (LA-phonons). This enabled us to overcome the brightness limitation imposed by the cross-polarisation configuration under a resonant excitation, under which at least half of the emitted photons are not collected. In contrast to this regime, the LA-phonons assisted excitation allows the collection of all photons without deteriorating the purity and the indistinguishability of the emission. Finally, we reported that this excitation regime is a good way to obtain a high-purity linear-polarisation emission, which is highly required for quantum applications [54].

This manuscript is organised as follows:

- In **Chapter 2**, we introduce the single-photon sources. We describe and compare different technologies following three benchmarks: source brightness, single-photon purity and indistinguishability. In this chapter, we mostly report the technical choices and the fabrication process of the sources developed by the group of Prof. P. Senellart. We present their conception, from the molecular beam epitaxy to the "in-situ" lithography and the source characterisation. In the final parts of this chapter, we describe and identify the two main transitions of the QD, the exciton and the trion, and we describe the source operation under resonant fluorescent excitation.

- In **Chapter 3**, we present the development and optimisation of a confocal microscope for resonant excitation of our single photon emitters. In this chapter the source is excited and emits in free-space. In the first part of the chapter, we report on the optimisation of the coupling efficiency between the emitted single photons and a single-mode fibre, using lenses and collimators. Under this excitation regime both the excitation laser and the emitted photons have the same energy and the same mode. To obtain an efficient laser suppression, we also discuss the polarisation selection and the cross-polarisation configuration. Finally, we detail the characterisation of sources, with a focus on the measured brightness into the collection fibre.

- In **Chapter 4**, we introduce the longitudinal acoustic (LA) phonon-assisted excitation regime. The first part of this chapter is about theoretical considerations: the excitation process and the expected emission characteristics. In the second part, we detail the

experimental results obtained with our sources. We report that this excitation regime has allowed us to demonstrate a factor of two increase in the brightness for sources of single and indistinguishable photons. We also demonstrate a single-photons emission with a high linear-polarisation purity, collecting in a parallel-polarisation configuration. The fibred brightness can be then improved by a factor of at least two in comparison with the resonant excitation scheme.

- In **Chapter 5**, we describe the study carried out to set a fibre directly on top of the source. We present the theoretical and the experimental coupling efficiencies between different fibre types and sources with various diameters. Standard and "lensed" fibres are considered. In the second part, we discuss the process of connecting a fibre to a source. Then, we present the experimental results, and we compare them with the results measured in the free-space configuration. With the possibility of moving the sample at 4K, we demonstrate a coupling efficiency close to the theory. Concerning the process of setting a fixed fibre above the source at room temperature and then cooled them down, the work is still in progress to reach the theoretical coupling efficiency. The first results are very promising and close to the state-of-the-art so far only reached with complex optics and user non-friendly environments.

Chapter 2

Single-photon sources

"Quand on veut on peut, et quand on peut on doit"

attribuée à Napoléon Bonaparte

2.1 Introduction

Many quantum applications based on light require ideal sources of "on-demand" single and indistinguishable photons. Emitting one and only one photon with a near-unity probability is the key for applications such as secure and reliable quantum communications [4] or robust quantum simulations and calculations [1, 6, 29]. Being based on quantum interferences between single photons, these applications also require indistinguishable photons. This quantum property demands that all emitted photons have the same physical properties (same energy, same polarisation, same spatial and temporal profiles).

In the 80', sources based on non-linear crystal have been proposed and, since then, have been the most widely used for quantum applications [55–57]. Then, over the past twenty years, other technologies have been developed to meet the theoretical expectations. These sources are based on emitters such as trapped ions [32, 58], atoms [59], diamond NV, SiC and SiV-centres [60] or quantum dot (QD) [9, 45, 61–63]. Depending on the applications, each type of source presents either strength or weaknesses.

In this chapter, we give a rapid overview of single photon sources. We discuss the various parameters that we use to benchmark the various technologies, yet, our main focus is on QD-based sources. As we go along, we will detail the fabrication of the single photon sources developed in the group of Prof. P. Senellart. The technical choices will be presented and the emission characteristics will be detailed.

Hence, the first part will be about the three requirements that a single photon source must fulfill: high brightness, high purity and indistinguishability. These will be general parameters to which sources will be compared to.

In a second part, we will describe the QD as trap for carriers with optical transitions that can be incoherently or coherently driven to emit single and indistinguishable photons.

The third part will be about the QD control of spontaneous emission using either a 2D- and a

3D-confinement of the optical field. After detailing the quantum electro-dynamics theory, we will give short descriptions of light confinement solutions explored by many groups.

In the fourth part, we will detail the choices of the Prof. P. Senellart group about the optical field confinement and their influences on the QD states emission. We will then report their deterministic fabrication from the molecular beam epitaxy to the in-situ lithography.

Finally, the last part will detail the emission characteristics of our single photon sources based on self-assembled QD embedded in a pillar. We will more precisely discuss the emission processes from different QD transitions under resonant excitation.

2.2 Single-photon source benchmarks

A single-photon source can be characterised by three main parameters: the source brightness, the single-photon purity and indistinguishability. They define the potential of the source to be used for quantum applications.

Even if it is possible to excite a single photon source with a continuous-wave laser, certain characteristics such as the purity are not well defined under this excitation regime. Moreover, most applications rely on clocked emission processes. In the following, we thus focus on sources operated under pulsed excitation regime.

2.2.1 Brightness

The brightness is defined as the probability of having one emitted photon per laser pulse. It is the ratio between the number of photons emitted from the source and the laser repetition rate.

In the ideal case, a deterministic single photon source emits one and only photon per laser pulse (figure 2.1a). The only possible Fock state is $|1\rangle$ and so $\mathcal{B} = 1$, in a given mode.

However, real single photon sources are more likely to be approximations of single photons sources (figure 2.1b) or lossy single photon sources (figure 2.1c). In the first case, we consider sources emitting vacuum component $|0\rangle$ as well as Fock states with one or more than one photon. Such approximated single-photon sources are for instance attenuated lasers, or based on either parametric down conversion (PDC) or spontaneous parametric down conversion (SPDC) processes. On the other hand, sources based on SiV, SiC defects, trapped atoms, trapped ions, NV-centers or QDs can be considered as "lossy" single-photon sources. Based on quantum emitters, these sources can reach a near-unity purity with a very low probability of multi-photon emission. Still, for various reasons (such as an imperfect population of the emitter excited state), these sources can still deliver vacuum components with a certain probability.

To consider the approximated purity of real single photon sources, the brightness is corrected by a factor $\sqrt{1 - g^{(2)}(0)}$, assuming a poissonian noise [64].

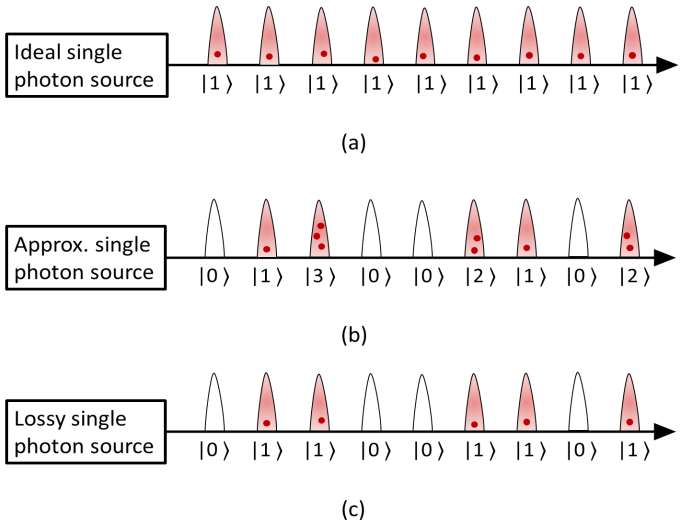

Figure 2.1: Drawings of (a) an ideal single photon source and (b), (c) of a real single photon source. In the ideal case, one photon is emitted and collected at each pulse laser. But, with real single photon sources, the photon is not always emitted and some pulses contain more than one photon.

Finally, independently of the emitter, once emitted the single photons must be collected. We define as "first lens brightness" ($\mathcal{B}_{\mathrm{FL}}$), the fraction of extracted and collected photon by a lens. This requires technological developments to ensure an emission of the single photons in a well-defined mode in order to obtain a first lens brightness as close as possible to the intrinsic source brightness.

2.2.2 Single-photon purity

The single-photon purity is defined as the probability of having no more than one photon per pulse. This is the central characteristic of a single photon source. To measure it, we use the interferometer proposed in 1994 by Hanbury-Brown and Twiss (HBT) for the study of the correlation between two photons from the coherent light of two stars [65]. Its application for the detection of wave-packets containing exactly one photon at the input of a beam-splitter (BS) has been shown in 1977 [66] and 1986 [67]. Eventually, the characterisation of a single-photon source based on QD emitters has been demonstrated in 2000 by the group of Prof. Imamoğlu [45].

In the ideal case (figure 2.2a), input state on the BS can be described as $|\psi\rangle_{12} = |1\rangle_1 |0\rangle_2$: a one-photon wave-packet $|1\rangle$ at the input (1), and the vacuum at the input (2). The beam is split and then sent to two detectors. We measure the second order auto-correlation of the signal at zero delay ($g^{(2)}(0)$) [68]. In other words, we measure the delay between two detections. When a detector registers an event, a time interval analyser measures the delay between the latter and the next detection.

Figure 2.2b presents the plot of the second order correlation measurement [45]. The delay between subsequent peaks is linked to the laser repetition rate. The side peaks correspond

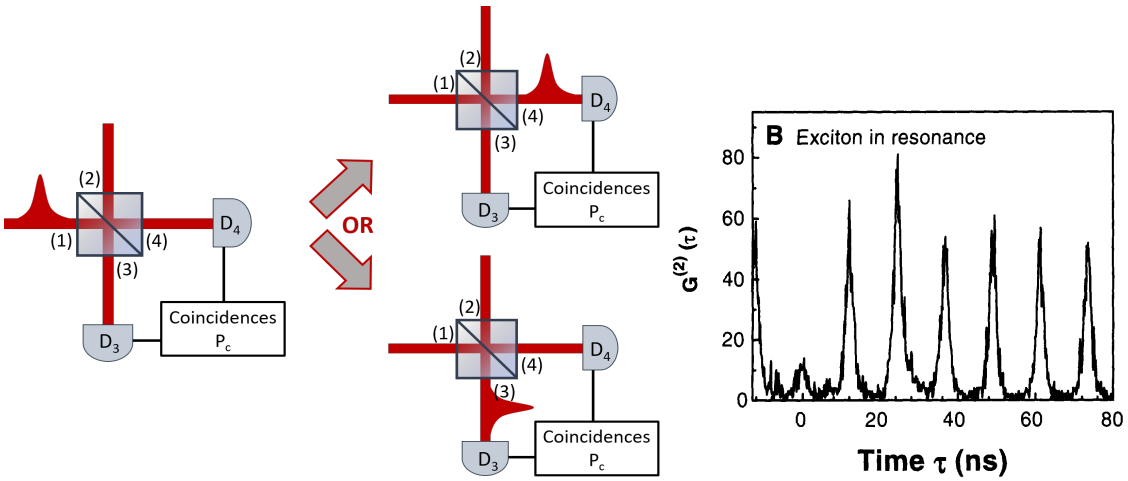

(a) (b)

Figure 2.2: (a) Schematic of the Hanbury-Brown and Twiss experiment applied for a single photon source. A photon arrives at the input (1) of a beam splitter (BS) and goes out from either (3) or (4). (b) Second order auto-correlation measurement at zero-delay plot (from ref [45]). The peak at zero-delay corresponds is written as $\mathcal{A}_0$ while the lateral ones are labeled $\mathcal{A}_i$ with $i = \pm 1, \pm 2, \pm 3, ...$ The laser repetition rate is 82MHz.

to the second photon detected after a certain delay proportional to $\pm 12.2ns$, for a repetition rate of 82MHz. Considering a perfect single photon source, a perfect collection system, and ideal detectors, we should have only the two first lateral peaks. In practice, photons could either not be emitted or be lost between the source and the detectors. So, the time delay between to detection can be higher than $12.2ns$. The second order correlation plot has then several lateral peaks, whose the intensities decrease as the delay becomes large. Hence, for a near perfect system, the lateral peak intensities quickly vanish.

Around the zero delay, we are counting correlation events for which both detectors simultaneously detect a photon. The probability of a double-detection is written P_C. For an ideal single photon source, we expect a vanishing height at zero delay, $P_C = 0$. Nevertheless, this peak could rise because of multi-photons emission during the pulse duration or due to scattered light from the excitation light source.

To calculate the purity of the emission, we consider peak areas instead of their intensities. The purity of the source is determined in the following manner:

$$\boxed{\mathcal{P} = 1 - g^{(2)}(0) = 1 - \frac{\mathcal{A}_0}{\mathcal{A}_i}} \tag{2.1}$$

with $\mathcal{A}_i$ with $i = \pm 1, \pm 2, \pm 3, ...$, the average area of the side peaks (usually three or four on each side) and $\mathcal{A}_0$, the area of the peak into a window of $\pm 1ns$.

2.2.3 Photon indistinguishability

The photons indistinguishability is the last figure of merit. It is a measurement of how identical are consecutively emitted photons: same temporal and spatial profiles, same energy, same polarisation, ... To do so, we use the method proposed in 1987 by Hong, Ou and Mandel (HOM) [69], which allows to measure the mean wave-packet overlap, M. The principle is based on the interference between two photons sent on a beam splitter (BS). On the latter, the input state can be written as $|\Psi_{\text{in}}\rangle_{12} = |1\rangle_1 |1\rangle_2$. At its outputs, three cases can be considered:

- $|1,1\rangle$, each photon leaves trough an output of the BS and the two detectors register an event,
- $|2,0\rangle$ or $|0,2\rangle$, the photons interfere and leave together through one of the BS outputs and are detected by the associated detector

The state at the output of the BS is [70]:

$$|\Psi_{\text{HOM}}\rangle = (R-T)\,|1,1\rangle + i\sqrt{2RT}\,|2,0\rangle + i\sqrt{2RT}\,|0,2\rangle \tag{2.2}$$

with R (resp. T) the reflection (resp. transmission) coefficients of the BS.

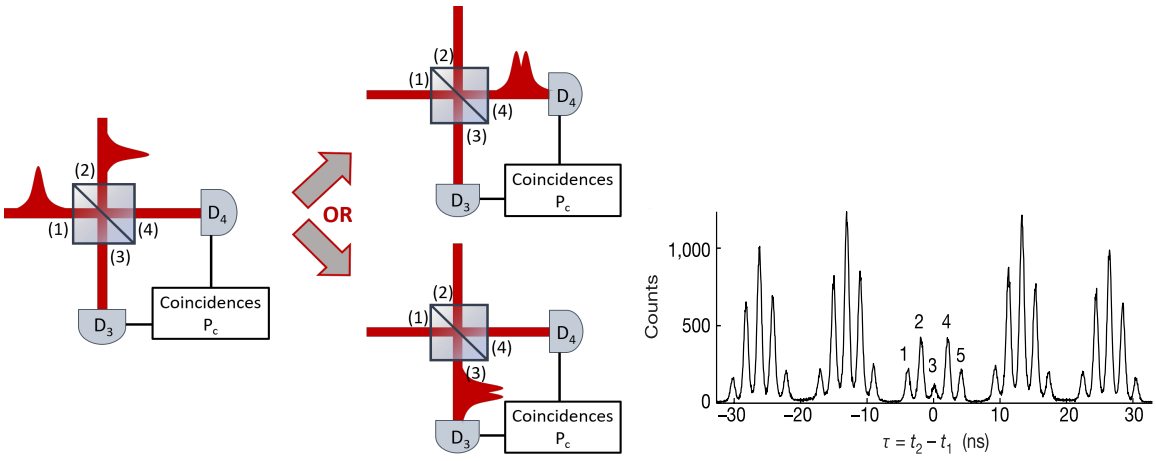

(a) (b)

Figure 2.3: (a) Schematic of the Houng-Ou-Mandel effect on the beam splitter. If two indistinguishable photons arrive in (1) and (2), they interfere and go out of the beam splitter from the same output. (b) (from [71]) Time trace plot of the mean wave-packet overlap measurement. Only the central peaks of each peak groups are considered in the calculation.

Following a pure quantum mechanical effect, when two indistinguishable photons each enter into one of the two inputs of a perfect BS (R=T), their amplitudes interfere destructively and the output state $|1,1\rangle$ vanishes (figure 2.3a). So, in the ideal case, it is not possible to have a double-detection since the source emission linewidth is Fourier transform limited. However, in general it is not the case with real sources. Figure 2.3b presents the result of the

mean photon wave-packet overlap measurement. We can notice a non-null peak at zero-delay. Considering only the single photon source, the mean photon wave-packet overlap is given by:

$$\boxed{M_{\text{th}} = \frac{{T_2}^*}{{T_2}^* + 2T_1} = \frac{T_2}{2T_1}} \tag{2.3}$$

with, T_1 is the decay time and ${T_2}^*$ is the pure dephasing time, and T_2, the coherent time of the photons, defined as $T_2 = (\frac{1}{2T_1} + \frac{1}{{T_2}^*})^{-1}$.

A distinguishable emission is due to either interactions of the emitted photons with their environment [72–76], spectral fluctuations [77–79] or dephasing. To decrease the environment effect and so improve the photon indistinguishability, we can firstly increase the pure dephasing time ${T_2}^*$ by minimizing sources of decoherence such as the charge noise or the phonon coupling. We can also decrease the radiative decay time T_1 by accelerating the spontaneous emission from the QD. The latter is then less prone to feel the environment effects if the spontaneous emission is faster than the sources of pure dephasing.

Experimentally, the Hong-Ou-Mandel effect is measured by optical systems based on either Michelson interferometer [71] or Mach-Zender interferometer. The former was used by Santori et al. [71] in 2002 to demonstrate the first interference measurement between two photons emitted successively by a QD (figure 2.3b). They reported a mean overlap of single photons between 0.72 and 0.81 with a QD excited under a quasi-resonant excitation. Due to the experimental system, peaks 1, 2, 4, and 5 are not considered in the calculation.

2.2.4 Approximated versus deterministic sources

In practice, several technologies of single-photon sources have been developed over the past twenty years. In this part, there main emission characteristics will be detailed.

Attenuated lasers, and sources based on either parametric down conversion (PDC) or spontaneous parametric down conversion (SPDC) processes are considered as approximated single-photon sources. Considering attenuated lasers, which can be modelled by sources of Glauber states, the average of photon number is written n, and the probability that one pulse contains exactly k photons is given by the Poisson law, $P_{\text{n}}(k) = \frac{n^k}{k!}\, e^{-n}$. We then have:

$$\begin{cases} P_{\text{n}}(1) = n\, e^{-n} \\ P_{\text{n}}(2) = \frac{n^2}{2}\, e^{-n} \\ P_{\text{n}}(k>1) = 1 - P_{\text{n}}(0) - P_{\text{n}}(1), \text{ with} \quad \sum_{k>1} P_{\text{n}}(k>1) < 0.05 \end{cases} \tag{2.4}$$

With an attenuated laser, the probability to get one photon per pulse is then limited at $1/e = 0.37$. Nevertheless, with $n = 1$, the probability to get more than one photon is then close to 0.3. To use such a source as an approximation of a single photon source, the mean number of photons must be set to $n \ll 1$ so as to minimise the probability of having more than one photon. Therefore, attenuated lasers are used in quantum key distribution protocols but not in quantum computation or simulation. Indeed, the $g^{(2)}$ is given by $\frac{2P(2)}{[P(1)+2P(2)]^2}$ (for $n \ll 1$), and always amount to 1 for a Poissonian distribution.

PDC or SPDC sources are based on the frequency conversion of a laser in a non linear-crystal which leads to the generation of photon pairs. At low excitation power ($\eta << 1$), the output state can be described as:

$$|\psi\rangle \approx |0_s, 0_i\rangle + \eta\,|1_s, 1_i\rangle + \eta^2\,|2_s, 2_i\rangle$$

where the subscripts "i" and "s" stand for "signal" and idler". Such state can be reduced to a state close to a single photon state by detecting the idler photon of the pair. This removes the vacuum component of the state so that the heralded signal state then reads as:

$$|\psi\rangle_h \approx \frac{\eta}{|\eta|}(|1_s\rangle + \eta\,|2_s\rangle)$$

These sources are then considered as "non-lossy" sources as the heralded state contains almost exactly one photon with no vacuum component. However, the overall brightness, i.e. the probability to get a photon on demand scales as η^2. In this simple picture, when increasing the power to increase η, hence the source brightness, the emission purity deteriorates as $\mathcal{P} = 1 - 2|\eta|^2$. Even though for such "single photon sources" the theoretical limit of brightness is 25% [80], it is also not possible to simultaneously reach a high brightness and a near-unity purity. To overcome the probabilistic nature of photon-pair generation, time-multiplexing techniques were first proposed and demonstrated by Pittman et al. [81] in 2002. In 2019, Kaneda et al. [82] provided a first demonstration with SPDC sources. They then measured a purity about 91.2%$\pm$0.7% for a single-photon probability of 41.2$\pm$1.3% in periodic output time windows. They also reported a maximum single-photon probability of 66.7$\pm$2.4% but at degraded purity and indistinguishability with a $g^{(2)}(0)$ of 26.9%$\pm$0.7%. If this technique improves the "on-demand" property of the SPDC sources, it does not increase the number of emitted single-photons in a time window and hence reduces the available photon rate. On the contrary, by spatially multiplexing the sources, Collins et al. [50] demonstrated an increase of 62.4% and 63.1% in the heralded single-photon output without an increase in unwanted multipair generation ($g^{(2)}(0) = 0.19\pm0.02$). The former was measured using two separately pumped sources while the latter considered two sources pumped through a common input.

For sources based on quantum emitters such as NV-centers, SiC^--center in diamond [60, 83–85], or QDs [45], the emission purity is independent from the brightness. These sources can in principle lead to a deterministic generation of a single photon. Their brightnesses depend on the excitation scheme and the engineering developed around the emitter to collect the photons using photonic structure confining light either in 2D or 3D. Indeed, in order to emit the single photons in a well-defined mode, most of single-photon emitters are embedded in waveguides or cavities. The light is then extracted preferentially from a precise spot and in well define mode, whose the numerical aperture is compatible with a lens.

In the following, we discuss the techniques and the different processes used to extract and collect efficiently the single-photons emitted by such deterministic emitters.

2.3 InAs QDs: a promising single-photon emitter

2.3.1 A trap for carriers

In this work, we study InGaAs QDs made of an InAs cluster embedded in a GaAs bulk (figure 2.4).

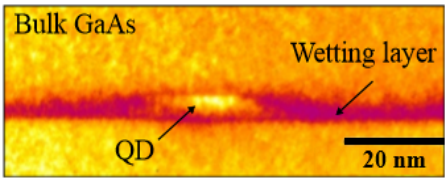

Figure 2.4: Cross-section view of a TEM image of a QD in a GaAs bulk.

Due to a lower energy of the InAs bandgap compared to the GaAs, the level structure of a self-assembled QD can be described as charges confined in a potential well both for holes and electrons [86, 87]. Here, we give a very rough description of the effect of confinement by considering the trapping of an electron or a hole with a simple model of the rectangular potential well, with a volume of $V=L_xL_yL_z$.

To do so, we consider an electron in the conduction band of a semiconductor and describe it by the function $\psi(x,y,z)$. Using the effective mass approximation [88], the latter is defined as a solution of the Schrödinger equation:

$$\left(-\frac{\hbar^2}{2m^*}\nabla^2 + V(x,y,z)\right)\psi(x,y,z) = E\psi(x,y,z), \tag{2.5}$$

with m^*, the electron effective mass in the quantum dot and V(x,y,z) = V(x)+V(y)+V(z).

Further simplifying and considering boundary conditions are infinite potential walls for each space coordinates, we can write:

$$V(j) = \begin{cases} 0, & 0 \leqslant \mathrm{j} \leqslant \mathrm{L_j},\ \forall\ \mathrm{j} = (\mathrm{x,y,z}) \\ \infty, & \text{otherwise} \end{cases} \tag{2.6}$$

Under this condition, the state can be considered as separable:

$$\begin{cases} E = E_\mathrm{x} + E_\mathrm{y} + E_\mathrm{z} \\ \psi(x,y,z) = \psi_\mathrm{x}(x)\psi_\mathrm{y}(y)\psi_\mathrm{z}(z) \end{cases} \tag{2.7}$$

So, the function ψ, for each coordinates, must verify

$$\psi''(j) + {k_\mathrm{j}}^2\psi(j) = 0 \tag{2.8}$$

with ${k_\mathrm{j}}^2 = \frac{2m^*E_\mathrm{j}}{\hbar^2}$, $\forall$ j = (x,y,z).

Since $\psi(0) = \psi(L_\mathrm{j}) = 0$, the solution is [70]:

$$\begin{cases} \psi(j) \propto sin(k_j j) \\ E_j = \frac{\hbar^2 {n_j}^2 \pi^2}{2m^* {L_j}^2} \qquad n_j \geqslant 1 \end{cases} \tag{2.9}$$

with n_j, the number of the confined state in the well and defined as $n_j = \frac{k_j L_j}{\pi}$.

So,

$$E = \frac{\hbar^2}{2m^*}\left(\frac{{n_x}^2\pi^2}{{L_x}^2} + \frac{{n_y}^2\pi^2}{{L_y}^2} + \frac{{n_z}^2\pi^2}{{L_z}^2}\right) + E_{gap}, \text{ with } L_x, L_y \gg L_z \tag{2.10}$$

Considering the x-direction (with $L_x = 10nm$), this model gives the correct order of magnitude for the energy gap between the lowest energy level "s" reachable by an excited electron ($n_x = n_y = n_z = 1$) and the level just above, often referred to as "p-shell" because of the symmetry of the envelop part of the wavefunction:

$$\Delta E_{s,p} = \frac{3\hbar^2\pi^2}{2m^* {L_x}^2} \approx 150meV$$

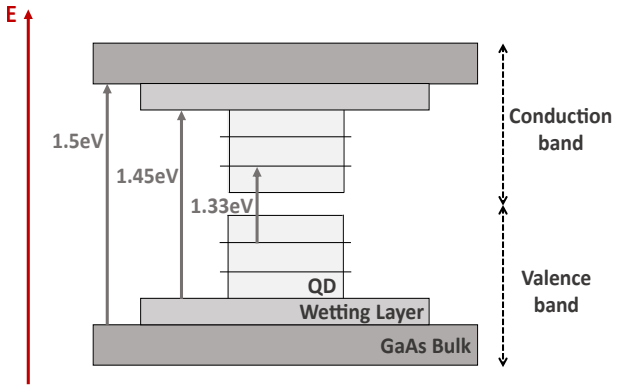

Figure 2.5: Schematic of a QD energy levels

In the case of an electron, we have $k \approx 10^9 m^{-1}$. So, only one electronic state is confined in the growth direction z ($L_z \approx 4nm$) and there are at least two confined electronic states in the x- and y-directions (L_x and L_y around 10-20nm). The uncertainty about the dimensions, due to a random shape and size, leads to an uncertainty about the energy confined in the well. Considering the height fluctuations in the growth direction, the energy fluctuations in this direction are:

$$\frac{\Delta E_z}{E_z} = 2\frac{\Delta L_z}{L_z}$$

With $n_z = 1$ and $L_z = 4nm$, the energy gap is $E_z \approx 350meV$. So, if the height fluctuation is around one atom size (10%), $\Delta E_z \approx 70meV$. Despite a highly optimized growth process, this energy uncertainty must be taken into account for the rest of the source manufacturing.

2.3.2 Electronic state occupations in a QD

InAs QDs are traps both for electrons and holes. By exciting it with an energy around the one of the bulk GaAs or wetting layer (830 - 850nm) and due to electronic and phononic relaxations, the QD emission can arise from different electronic state occupations. Depending on its size and the its electronic environment before the radiative electron-hole pair recombination, the emitted photons can come from four main relaxation phenomena [89–91] (figure 2.6a).

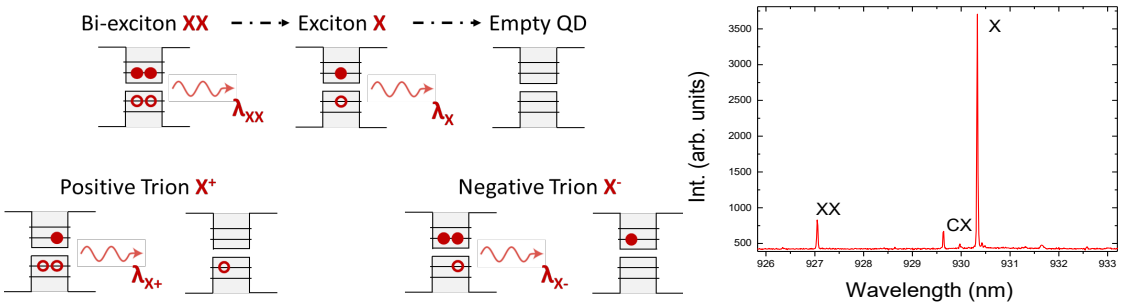

(a) (b)

Figure 2.6: (a) Schematic of the four different QD transitions. (b) Photoluminescent spectrum from a QD in a planar cavity, under continuous-wave non resonant excitation.

Since the effect of Coulomb interactions depends on the number of trapped charges, these four states correspond to different emission energies [92,93]. These are clearly visible in the photoluminescence spectrum in figure 2.6b. The first state, called "exciton" or "excitonic state" (X), corresponds to an electron-hole pair. By recombination the photon is then emitted at the wavelength λ_X. The second relaxation process is from a state called "biexciton" (XX). In this case, two electron-hole pairs are present at the same time. When the first one recombines, the photon is emitted at the wavelength λ_{XX}, which differs from the exciton wavelength. This difference of energy is explained by the difference in the Coulomb interactions when two electrons and two holes are trapped at the same time. Depending on the QD indium concentration, shape and strain, both configurations $E_{XX} - E_X > E_X$ and $E_{XX} - E_X < E_X$ can be observed [94], with E_X and E_{XX} the total energy of the exciton and the biexciton respectively. Once the first photon is emitted, the recombination of the excitonic state emits a photon at λ_X. The two last possible charge states are from a charged exciton (CX), also called trion [95]. In the first case, an electron can be already present in the conduction band before the excitation. When the QD is excited, the state is called "negative trion" and the emission wavelength is at λ_{X^-}. On the contrary, a hole can be already present in the valence band before the excitation. The excited state is called "positive trion" and it emits at the wavelength λ_{X^+}. These two states depend on the presence of extra-charge before the excitation/emission process. Nevertheless, it may happen that these charges do not stay trapped. The trion state is then not stable and the resonant excitation is not efficient. This case is discussed in part 2.6.2.4.

Figure 2.6b shows a typical photoluminescence (PL) spectrum of a QD in a planar cavity. To name the states linked to each line, different physical properties are used. Exciton (X) and biexciton (XX) emission lines are identified by their behavior during a saturation

measurement. By increasing the non-resonant laser power, the emission intensity from a biexciton follows a quadratic dependence [96, 97] while from an exciton it raises linearly. With a continuous-wave laser, and at saturation, the biexciton is preferentially re-excited reducing the emission from the excitonic state. Hence, an exciton saturation curve drops after reaching the saturation. To distinguish a charged state from a neutral one, a magnetic field [98] or the excitation polarisation [99] can be used (more detailed in parts 2.6.2.3 and 2.6.2.4).

In the following parts, we will see that a source is designed to enhance preferentially one of these QD states.

2.3.3 Quantum dot fine structure splitting

Once excited, at least one electron and one hole are simultaneously trapped in the QD. Coulomb direct and exchange interactions must be then considered to account for the energy levels [100]. They have been theoretically studied in many works [101, 102] and experimentally probed. Here we only consider heavy holes and electrons to build the exciton and bi-exciton states [103]. Considering the hole, its spin is written as either $|\Uparrow\rangle$ or $|\Downarrow\rangle$ and its angular momentum component along the growth direction is $J_{\mathrm{h,z}} = \pm 3/2$. The electron spin is then written as either $|\uparrow\rangle$ or $|\downarrow\rangle$ and its angular momentum component along the growth direction is $S_{\mathrm{e,z}} = \pm 1/2$ [104]. So, we obtain four possible spin states along the z-component:

$$\begin{cases} |+1\rangle \equiv |\Uparrow,\downarrow\rangle = |+\frac{3}{2},-\frac{1}{2}\rangle \\ |-1\rangle \equiv |\Downarrow,\uparrow\rangle = |-\frac{3}{2},+\frac{1}{2}\rangle \\ |+2\rangle \equiv |\Uparrow,\uparrow\rangle = |+\frac{3}{2},+\frac{1}{2}\rangle \\ |-2\rangle \equiv |\Downarrow,\downarrow\rangle = |-\frac{3}{2},-\frac{1}{2}\rangle \end{cases} \tag{2.11}$$

The $|\pm 1\rangle$ states represent bright exciton states while the $|\pm 2\rangle$ states denote dark excitons. The difference between the two lies in the spin momentum conservation. Photons carry a "pseudo-spin" equal to one. So according to spin conservation, only states $|\pm 1\rangle$ can be created by photons absorption and can emit photons by a electron-hole pairs recombination. However, due to a flip of one of the two spins, the spin conservation makes the $|\pm 2\rangle$ transition optically inactive. Since no photons emitted from a dark exciton state are detected, we only consider states $|\pm 1\rangle$.

In this exciton spin basis, the exchange interaction Hamiltonian can be written as:

$$\hat{H}_{\mathrm{exc}} = \tfrac{1}{2} \begin{pmatrix} \delta_0 & \delta_2 & 0 & 0 \\ \delta_2 & \delta_0 & 0 & 0 \\ 0 & 0 & -\delta_0 & \delta_1 \\ 0 & 0 & \delta_1 & -\delta_0 \end{pmatrix}$$

$$\text{with} \begin{cases} \delta_0 = \frac{3}{2}(a_{\mathrm{z}} + \frac{9}{4} b_{\mathrm{z}}) \\ \delta_1 = -\frac{3}{4}(b_{\mathrm{x}} + b_{\mathrm{y}}) \\ \delta_2 = -\frac{3}{4}(b_{\mathrm{x}} - b_{\mathrm{y}}) \end{cases}$$

The a_i and b_i terms are spin coupling constants along each axis. The z-axis corresponds to the growth axis while x- and y-axis build the QD plane. The diagonal term δ_0 traduces the splitting between the bright and the dark states while the off-diagonal terms traduce a state mixing and a splitting. δ_1 and δ_2 represent respectively the mixing and the splitting of the dark and of the bright states. Considering the latter, the splitting occurs if there is an asymmetry in the (x,y) plane.

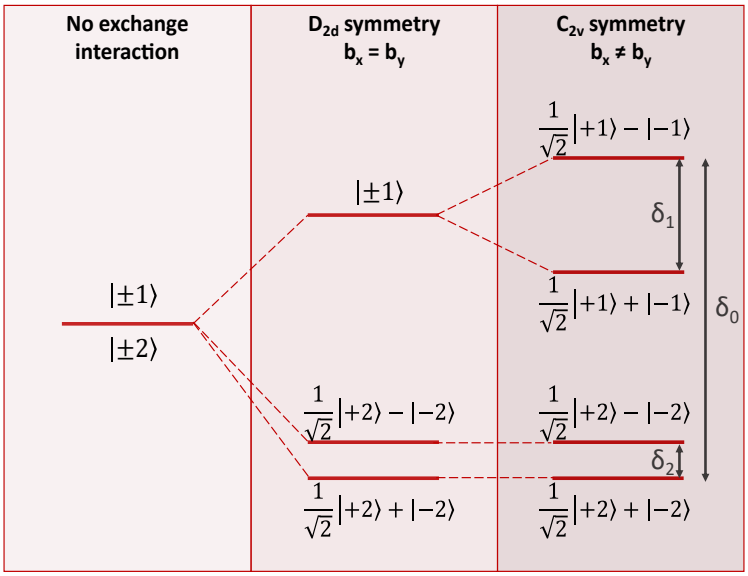

Figure 2.7: Schematics of the QD energy levels considering various symmetries [105].

As shown in figure 2.7, if the QD is not symmetric in this plane ($b_x \neq b_y$), there is an energy splitting between the two states $|\pm 1\rangle$. It is the so-called exciton fine structure splitting (FSS) and it is typically several tens of μeV [106]. Different techniques have been developed to control it. Thermal annealing method, used in the fabrication process to tune the QD energy, has been shown to increase the number of QDs with a small FSS [107, 108]. The application of an external strain with a piezo actuator [109] as well as the addition of an external electric field [110, 111] or an in-plane magnetic field (B perpendicular to the growth axis) [112] are other efficient techniques.

Controlling the FSS can have different impacts. The main one is to emit entangled photons from a biexcitonic state [113]. Indeed, if the FSS is negligible, we can use the radiative cascade to emit two photons, generally entangled in polarisation.

As shown in figure 2.8a, the FSS must be suppressed to remove the distinction between the two relaxation paths. If the first photon is emitted with a circular left polarisation, hence the second one will have a circular right polarisation (and vice versa). But to ensure the entanglement, the two paths must be indistinguishable.

On the contrary, to increase the brightness of an exciton, during resonant fluorescent experiments, the FSS must be enlarged. This will be more detailed in the part 2.6.3.3, but in brief, due to a cross-polarisation selection, all the photons emitted in the excitation laser V-polarisation are not collected. So, the ratio of photons emitted in the H-polarisation must be as high as possible. Since a large FSS leads to a faster flip between the eigenstate $|X\rangle$ to $|Y\rangle$,

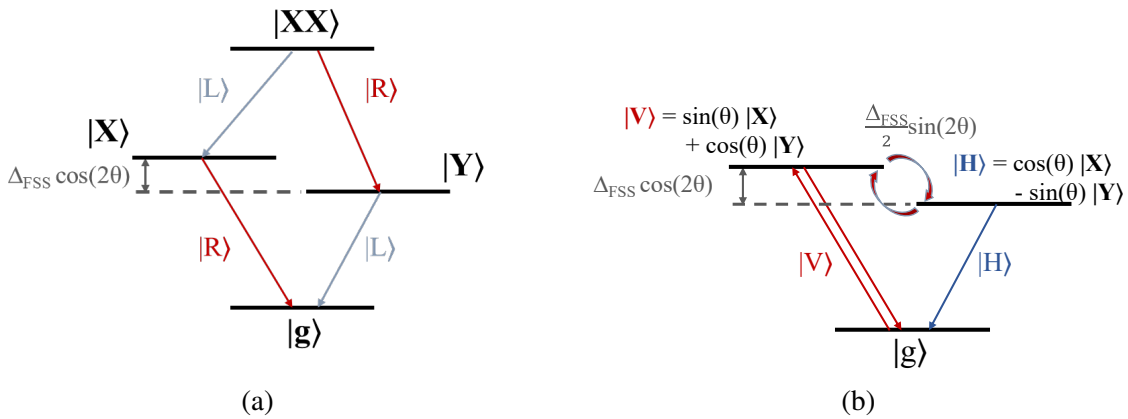

Figure 2.8: (a) Energy level of a radiative cascade, or bi-exciton sate. The polarisation of the first emission (λ_{XX}) set the polarisation of the second emission (λ_X) (b) Energy level of an exciton. In both cases, the two eingenstates $|X\rangle$ and $|Y\rangle$ are split by an energy proportional to the FSS.

the probability of emitting a photon in the H-polarisation raises and the source has a higher polarised first lens brightness.

2.4 Enhancement of the collection by coupling the QD to a photonic structure

QDs can be considered as deterministic single-photons emitters as long as they are properly excited, i.e. when the excitation bring the QD in its excited state with unity probability. However in the bulk, due their wide ranges of the emission angles, and total internal reflexions, a low photons rate is extracted from the top and then collected by a microscope objective with a finite numerical aperture (NA). In these conditions, the maximal fraction of extracted photons from the bulk is typically:

$$\eta \approx \frac{1}{4n^2} \approx 2\%$$

with $n \approx 3.5$ for GaAs.

Having an efficient single photon source and an effective photon collection require to create a photonic structure around the QD.

2.4.1 Cavity Quantum Electro-Dynamics theory (CQED)

Since a QD behaves in many ways as an artificial atom, we can use the tools of cavity quantum electrodynamics to extract the single photon. We thus consider QDs embedded in a cavity and describe the QD-cavity interactions.

2.4.1.1 Jaynes-Cummings model

The Jaynes-Cummings model describes the interactions between a two level-system atom coupled to a single quantized electric-field mode of a cavity (figure 2.9).

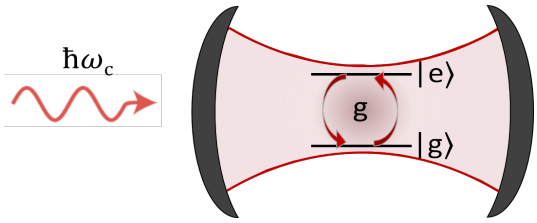

Figure 2.9: Schematic of a two level system in a cavity, excited by a laser ($\hbar\omega_c$). "g" is the light-matter coupling constant of the system.

In other words, it is a simplified model of the light-matter interaction in a cavity without losses [114]. With this model, the system is determined by the Hamiltonian:

$$\hat{H}_{JC} = \hat{H}_{QD} + \hat{H}_C + \hat{H}_I \tag{2.12}$$

$\hat{H}_{QD} = \hbar\omega_{QD} |e\rangle \langle e|$ and $\hat{H}_C = \hbar\omega_c \hat{a}^\dagger \hat{a}$ represent respectively the Hamiltonian of the QD and of the photons in the cavity mode. This model considers part of the light-matter interaction with the term $\hat{H}_I$ defined as:

$$\hat{H}_I = \hbar g \left(|g\rangle \langle e| \hat{a}^\dagger + |e\rangle \langle g| \hat{a} \right)$$

with g, the light-matter coupling constant between the QD transition and the cavity mode.

The total Hamiltonian $\hat{H}_{JC}$ can be diagonalised with the eigenenergies written as follows:

$$E_\pm = \hbar \left(\omega_c - \frac{\Delta}{2} \pm \frac{1}{2}\sqrt{\Delta^2 + 4g^2} \right) \tag{2.13}$$

with $\Delta = \omega_c - \omega_{QD}$, the energy detuning between the cavity energy and the energy of the two level-system atom. The associated eigenvectors are:

$$\begin{cases} |\Psi_+\rangle = cos(\theta) |g,1\rangle + sin(\theta) |e,0\rangle \\ |\Psi_-\rangle = -sin(\theta) |g,1\rangle + cos(\theta) |e,0\rangle \end{cases} \tag{2.14}$$

with θ such as $tan(2\theta) = \frac{2g}{\Delta}$.

These equations have a simpler form at resonance, when $\Delta = 0$ and $\omega_c = \omega_{QD} \equiv \omega_0$. The states are dressed and we obtain:

$$\begin{cases} E_\pm = \hbar(\omega_0 \pm g) \\ |\Psi_\pm\rangle = \frac{1}{\sqrt{2}}(|e,1\rangle \pm |g,0\rangle) \end{cases} \tag{2.15}$$

2.4.1.2 Spontaneous emission and Purcell factor

Let us consider a QD, described as an artificial atom, coupled to a cavity and in resonance with the cavity mode. At $t = 0$, the QD is in an excited state and there is no photon in the cavity. We write it as $|\Psi(0)\rangle = |e,0\rangle$, or as:

$$|\Psi(0)\rangle = \frac{1}{\sqrt{2}}\left(|\Psi_{+}\rangle + |\Psi_{-}\rangle\right) \tag{2.16}$$

The evolution from this initial state is described according to:

$$|\Psi(t)\rangle = \tfrac{1}{\sqrt{2}}\left(|\Psi_{+}\rangle\, e^{\frac{-iE_{+}t}{\hbar}} + |\Psi_{-}\rangle\, e^{\frac{-iE_{-}t}{\hbar}}\right)$$

$$\iff |\Psi(t)\rangle = e^{-i\omega_c t}\left(-i\,sin\left(\frac{gt}{4}\right)|g,1\rangle + cos\left(\frac{gt}{4}\right)|e,0\rangle\right) \tag{2.17}$$

So, the probability that it makes a transition to the excited state is

$$p_e(t) = |\,\langle e,0|\Psi(t)\rangle\,|^2 = cos^2\left(\frac{gt}{4}\right) \tag{2.18}$$

The system oscillates from the fundamental state to the excited state by coherently exchanging energy among the QD and the cavity. This phenomenon, known as "vacuum Rabi oscillation", takes place when the cavity losses are negligible. In pratice, the photon inside the cavity presents a finite decay rate κ so that this coherent exchange of energy is experimentally achieved under the **strong coupling regime** ($4g > \kappa$). In this case, the losses and the state radiative decay, κ are small enough to allow a re-absorption of the emitted photon. This regime is not the proper one to obtain a bight single photon source.

Instead, to obtain a single-photon source, the system is operated in the **weak coupling regime condition** ($4g < \kappa$), where the QD-cavity mode coupling is enhanced but, once the QD emits a photon, the latter rapidly escapes outside the cavity. The state $|g,1\rangle$ decays towards the state $|g,0\rangle$ following the decay rate, κ. The cavity is lossy and the relaxation of the electromagnetic field is efficient. The cavity is then empty most of the time. Since κ is directly linked to the cavity quality factor, $Q_0 = \omega_m/\kappa$, embedding QDs reduces the emission lifetime and enhances their spontaneous emission into the cavity mode. To evaluate the maximum amount of spontaneous emission acceleration provided by a cavity, we introduce the Purcell factor, F_P [115]. It is defined as the ratio between the decay rate of the emitter in the cavity and in the bulk, respectively noted Γ_{CM} and Γ:

$$\boxed{F_{P,\,cav} = \frac{\Gamma_{CM}}{\Gamma} = \frac{3}{4\pi^2}\frac{Q_0}{V_{eff}}\left(\frac{\lambda}{n}\right)^3} \tag{2.19}$$

with, $\Gamma_{CM} \propto \frac{1}{\kappa}$, Q_0, the cavity quality factor, V_{eff}, the effective cavity volume, n, the refractive index of the QD matrix, and λ, the emission wavelength.

2.4.1.3 Reducing phonon-induced spectral broadening and decoherence

Once resonantly excited, the QD emits single-photon via an electron-hole pair recombination. As seen in part 2.3.2, the photons energy depends on the transmission which is enhanced by the cavity at the excited state frequency. Under fluorescent resonance, this emission is called the "zero phonon line" (ZPL). Nevertheless, the electron-hole pair can interact with the QD environment. The photons can also be emitted via phonon-assisted processes. Due to either the absorption or the emission of a phonon, these photons are emitted on either side of the ZPL in the "phonon-sidebands" (PSB). Since the PSB emission arises from incoherent phonon processes, its indistinguishability is deteriorated [116]. Cooling the source at 4K is a first solution to reduce the crystal vibrations and phonon populations. To further reduce the effect of phonon-sidebands, the Purcell effect in a high quality factor cavity can be used. Indeed, the cavity can play a role of a filter whose bandwidth is defined by the DBRs reflectivity (equ. (2.22)), and so its quality factor (equ. (2.23)) (more details in part 2.5.1).

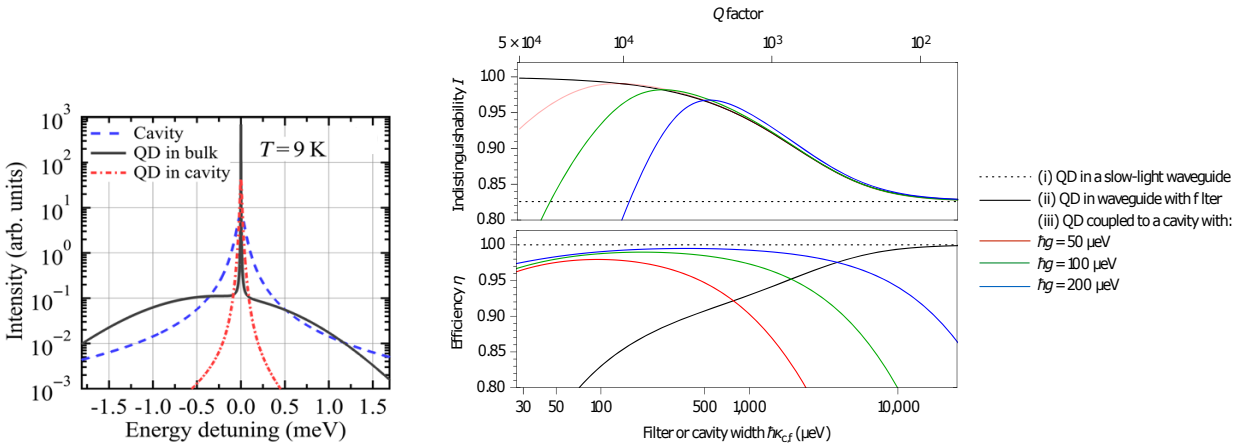

(a) (b)

Figure 2.10: (a) From reference [116]. Theoretical comparison of the emission spectra of a QD in a bulk (black solid line) and coupled resonantly to a cavity (red dashed-dotted line) at 9 K. The blue dashed line corresponds to the cavity spectrum. (b) From reference [117]. Theoretical plots of the indistinguishability and the efficiency of a single photon source as a function of the Q-factor (upper x-axis) and the cavity linewidth (lower x-axis). The QDs are cooled down at 4K, and embedded either (i) in slow-light waveguide, (ii) in waveguide with a filter or (iii) in a cavity with various QD-cavity coupling efficiency

Figure 2.10a, from the work of Grange et al. [116], presents the influence of the Purcell effect in a high-Q cavity on the QD emission spectrum. The solid black line corresponds to the broad spectral emission of a QD in the bulk with clear phonon sideband emissions. The ZPL is the peak at zero detuning to which the cavity is resonant (presented by the blue dashed line). The emission spectrum of the QD coupled to the cavity mode is shown by the red dot-dashed line. We can clearly notice that due to the QD embedding in the pillar cavity, the ZPL experience a stronger acceleration of spontaneous emission in the cavity mode. As a result, most of the emission takes place in the ZPL, with a strong suppression of the PSB. Nevertheless, the linewidth of the cavity mode is about 100μeV. This remains ten times

broader than the linewidth of the QD ZPL emission about of few μeV. Hence, the PSB not are fully filtered.

Figure 2.10b is from the work of Iles-Smith et al. [117]. It plots the photon indistinguishability and the source efficiency, η, as a function of the Q-factor (upper x-axis) and the cavity linewidth (lower x-axis). The evolution of the indistinguishability is a clear indicator of the PSB filtering efficiency. The theoretical results are calculated with QDs cooled down at 4K, and embedded either (i) in slow-light waveguide, (ii) in waveguide with a filter or (iii) in a cavity with various QD-cavity coupling constants g. Considering a QD in a (i) waveguide, the extraction efficiency is unitary but due to a long radiative decay, the indistinguishability is limited below 85%. On the contrary, under the weak coupling regime and embedded in a (iii) cavity, the QD emission indistinguishability can reach values above 95%. To filter perfectly the PSB, the cavity linewidth must be close to the ZPL linewidth, which is about 15μeV. However, to get a narrow cavity linewidth and so a large Q-factor, the distributed Bragg mirrors (DBR) reflectivity must be high, reducing the ratio of extracted photons. Following this work, a cavity-based source cannot simultaneously reach near-unity efficiency and indistinguishability by simply increasing the cavity Q factor or QD-cavity coupling strength. Nevertheless, the theory predicts that with the achievable experimental values of $\hbar g = 30$ μeV and $\hbar\kappa = 120$ μeV, we can expect $\mathcal{M} = 99\%$ and $\eta = 96\%$ at T = 4 K.

Thus, the cavity enables to both accelerate the QD spontaneous emission, increasing the coherence time of the photons T_2 (relatively to the decay time T_1 decrease), and filter the emission from the interactions with the charges environment or with the phonon bath [118]. To achieve the PSB filtering, a Fabry-Pérot etalon can also be added in the collection path. Nevertheless, since both the etalon and the QD emission have Lorentzian spectral shapes, to efficiently suppress the PSB, the ZPL is also filtered. As a consequence, the brightness can be then reduced up to 30%.

2.4.2 Benchmarks of the various structures

2.4.2.1 Waveguides

To extract the QDs emissions in a well-defined mode and from the top, groups such as the one of P. Lodahl, K. Jöns, or J.-M. Gérard and J. Claudon, decided to work on the QDs embedded in waveguides [48, 119]. In their sources, almost five or six QDs are located in **Photonics Crystal Waveguide** [119] or at the base of **Nano-trumpet waveguides** [51] or **Nano-wires** [48, 120]. Thus, the emissions is guided to the side of the photonic crystal waveguide or to the top of the nano-trumpet and nano-wire by the periodic holes lattice or by both the lateral confinement ($n_{\mathrm{GaAs}} >> n_{\mathrm{air}}$) and a bottom gold coated wafer respectively.

Considering the nano-trumpet solution, figure 2.11a presents a SEM picture of the source from the group of Prof. J.-M. Gérard and Prof. J. Claudon. The conical shape of the GaAs top layer guides the emitted photons until their extraction. The emission is monomode thanks to a base diameter of around 150nm and 200nm [123]. Since there is no cavity mode, but rather an inhibition of the spontaneous emission, the state lifetime is the same as a

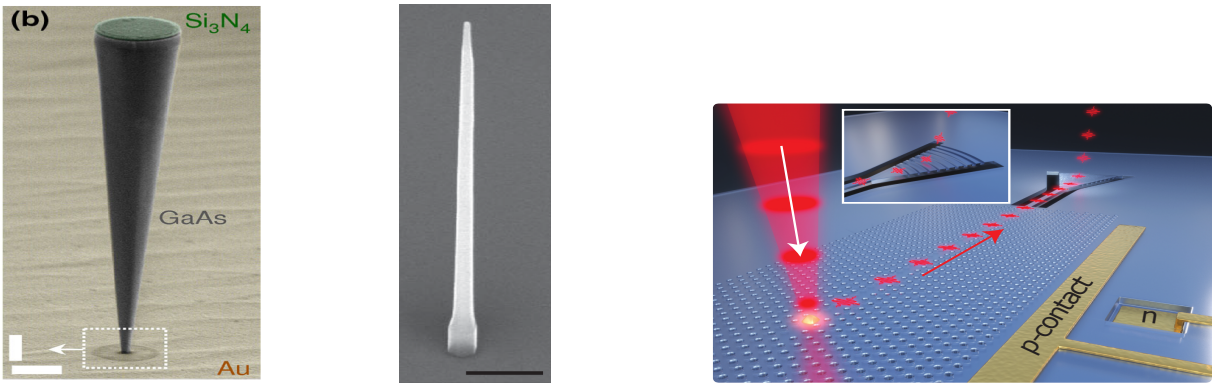

(a) (b) (c)

Figure 2.11: (a) Nano-trumpet waveguide picture [51]. (b) Nano-wire SEM picture [121]. (c) Schematic of the source proposed by Uppu et al. [122]. The laser excite directly the QD and the photons are extracted from the side of the photonic crystal via a shallow-etch grating.

QD in a bulk, around 1ns or even longer. But the extraction efficiency is very high. Hence, the first lens brightness is over 75%. The main issues with this technology is the waveguides fragility and the vicinity of the QD to etched surfaces. Moreover, since there is more than one QD embedded in the waveguide and the latter is sensible to the trumpet mechanical vibrations, the purity and the indistinguishability of the emission are highly limited. Nevertheless, this sensitivity can be an advantage in application such as a tip coupling to a single-mode fibre for atomic force microscopy [124].

Regarding the nano-wire, the functioning principle is the same. Figure 2.11b is a SEM picture of the design proposed in 2010 by the group of Prof. J.-M. Gérard and Prof. J. Claudon [48] and which is also developed in the V. Zwiller group [121, 125]. The shape of the waveguide enables a mono-mode emission and a high extraction from the top. The source brightness can then reach about 0.72 ± 0.09 and has been successfully coupled to a single mode fibre with a coupling efficiency of 97% [121]. Moreover, with the creation of a larger waveguide around the nano-wire, this source has been implemented on chip [125]. Finally, the group of Prof. N. Akopian has very recently demonstrated the first biexciton–exciton cascade emission via resonant two-photon excitation and resonance fluorescence [126].

Embedding the QD in a waveguide also enables to spatially separate the excitation spot to the collection's. For instance, in the work of Monniello et al. [127], the QD was excited from the side of the structure and the single-photon were extracted from the top. They then reported a photon indistinguishability greater than 0.7 without any post-selection and a single-photon purity about 93%. In the same principle, the group of P. Lodahl has recently shown theoretically the ability of a on-chip waveguide with bottom DBR and a shallow-etch grating to extract more efficiently the emitted photon in a near-Gaussian mode [122] (figure 2.11c). If the theoretical out-coupling is not reached yet, they show a chip-fiber coupling efficiency of 28%±1%. The fibred brightness is then $\mathcal{B}_F = 4\% \pm 1\%$ for a first lens brightness of 20%±1%. In the same work, they also reported an emission purity of 98.5%±0.5% and a non-corrected photons indistinguishability of 93%±2%. We need to notice that this indistinguishability value has been measured with a Fabry-Pérot etalon, reducing the fibred brightness to 3.5%±1%. The same group also published a work in which the design of the chip enables

to reach the same benchmarks but only collecting Y-polarised photons from an exciton [128].

	Source Brightness	Single-photon purity	Indistinguishability
Nano-trumpet waveguide [51]	0.75 ± 0.1	between 0.69 (T_1=0.82ns) and 0.98 (T_1=1.26ns)	–
Tapered nanowire [48]	0.72 ± 0.09	> 0.992	–
Photonic crystals waveguide [122]	0.2 ± 0.01 or 0.04 ± 0.01 (fibred)	0.985 ± 0.005	0.93 ± 0.02

Table 2.1: Figure of merit of the other collection solutions. The reported brightnesses are the first lens brightnesses, except for the photonic crystal waveguide for which there is also the fibred brightness.

Table 2.1 summarises the figure of merit of these sources based on QDs embedded in waveguides. Except for the photonic crystal waveguide, the measurements have been performed under non-resonant excitation. As a result, these technologies enable high extraction efficiency and purity, but the emitted photons are not always indistinguishable. This is mostly due to the long lifetime of the state (around 1ns). Indeed, due to an increase of the state's dephasing time (equ. (2.3)), the control of the emitted photon properties is degraded [71]. An alternative is to decrease the lifetime by coupling the QDs to optical cavities.

2.4.2.2 Cavities structures to obtain a 3D optical confinement and a mono-mode emission

In this PhD work, we study single photon sources based on QDs in micropillar cavities. These sources have long led the race for the most efficient photon source of indistinguishable single photons. The technology at the core of Quandela is based on the development conducted at the CNRS-C2N over the last decade. We will present this technology in great details in the remaining of this chapter. Here we wish to present technologies that are being developed worldwide, and represent the current state of the art of alternative (competing) approaches.

- **Photonic crystals cavity** [122, 129–131].

  The single QD is coupled to the optical mode of a 2D-photonic crystal. This is usually a suspended membrane composed of a periodic holes lattice whose shape, distribution and size are designed at will (figure 2.12). The optical confinement is obtained by setting the holes parameters and varying locally their positions [129, 132, 133]. Due to their high quality factors and small mode volumes, they are well suited for enhancing the light-matter interaction and collecting non-classical light. However, the collection is

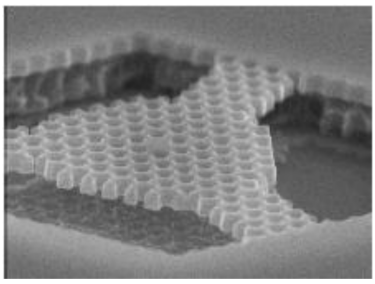

(a)

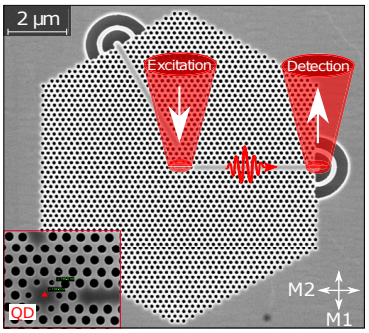

(b)

Figure 2.12: (a) SEM image of a suspended photonic crystal cavity obtained with a missing hole in the center of the image, reproduced from [130]. (b) SEM image of the device from reference [131]. The QD is excited via the cavity and the single-photon emission is collected from the out-coupler. **Inset**: A close-up of the cavity.

usually in the plane of the membrane. The photon collection is then deteriorated due to mismatching issues with external optics. Nevertheless, Madsen et al. [134] measured a collection efficiency of 0.443±0.021 from a L3 cavity [135]. The single-photon purity was then 96% ± 5% at 2.1 times the saturation power. Moreover, the planar geometry of photonic crystals makes them ideally suited for coupling to waveguides and on-chip photonic circuits [136–138]. Thus, Liu et al. [131] demonstrated recently the generation of single photons in a cavity coupled to a waveguide with a very high Purcell enhancement (F_P= 43±2) and a non-corrected indistinguishability of 89.4%±3.5% for a purity of 97.3±0.7%.

- **Open microcavity** [52, 53, 139, 140].

  Proposed by the group of Prof. G. Khitrova [141], this solution is based on a miniaturised Fabry-Pérot cavity composed of a bottom planar DBR on which QDs are grown and a movable concave top DBR (figure 2.13a). This technique allows to precisely position the QD in the cavity center and match the resonance energy of the cavity with the QD's by tuning the distance to the top mirror. This type of cavity was recently used to obtain a very bright source of single photons in the group of Prof. R. Warburton. By controlling its reflectivity, the cavity proposed in the work of Tomm et al. [53] has a Q-factor of 12600. To obtain a perfect positioning of the top mirror relative to the QD position, the chip is moved in-situ with piezo actuators. Due to a large energy splitting between the two cavity polarised-modes, the exciting laser can be a little blue-detuned. Figure 2.13b presents the energies spectra of the two polarised cavity modes (blue and green dashed lines), of the excitation laser in orange and of the QD emission in grey. Being V-polarised, the laser excites one of the modes while the QD state, in resonance with the second mode H-polarised, emits in the orthogonal polarisation with a probability of 86%. Moreover, due to a near-Gaussian output mode, and since the laser is both filtered in polarisation and spectrally, the fibred brightness reaches 55%±3%. With this technique, the emission purity is about 97.9% and the non-corrected photons indistinguishability is about 92.5%. Finally, the emission and the optical setup enable to get an

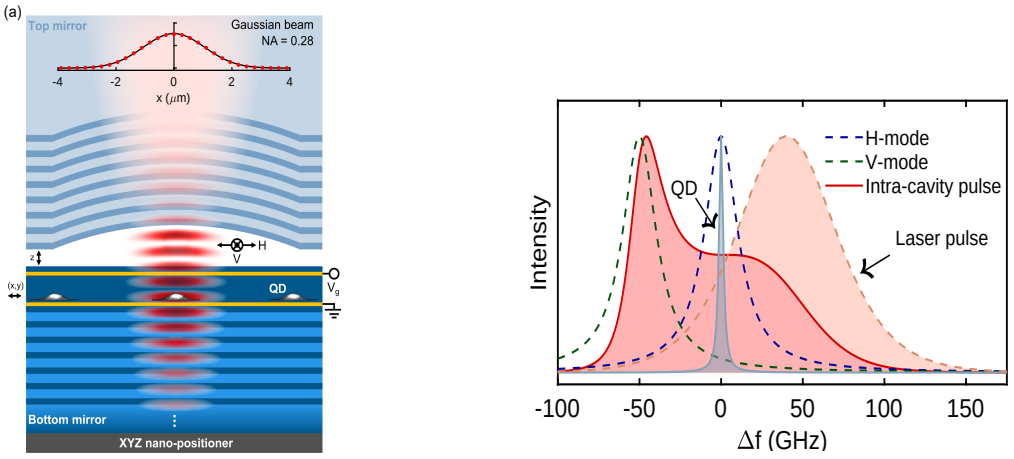

(a) (b)

Figure 2.13: (a) Schematic of an open cavity (from the ref [53]) (b) Spectra plot of the excitation scheme (from the ref [53]). The cavity polarised-modes are split by about 50GHz (blue and green dashed lines). The QD is in resonance with the H-mode, while the blue-detuned laser is V-polarised. This enables an increase the laser extinction while guaranteeing a high single photons collection efficiency.

operational single photon source over hours. This recent work has set a new record for bright single photon sources.

- **Bulls-eye cavity** [62, 142–144].

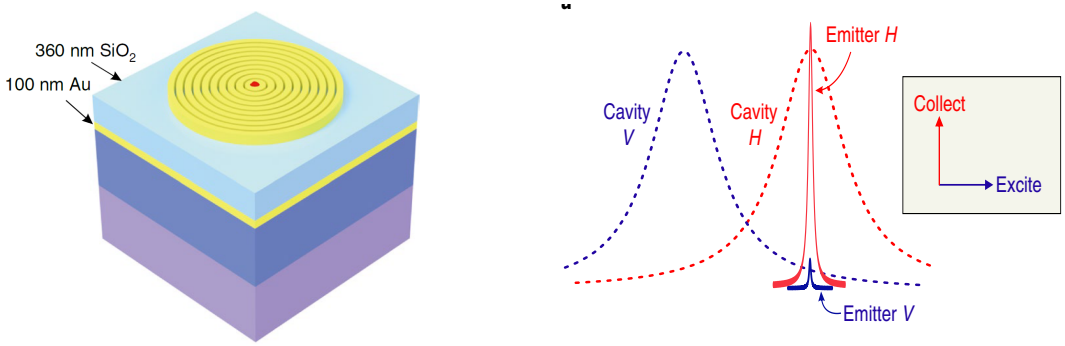

(a) (b)

Figure 2.14: From reference [62] (a) Schematic of a bulls-eye cavity. The QD is placed at the bull-eye center (red dot). (b) Spectra plot of the excitation scheme. The cavity polarised-modes are split by about 2.8THz (blue and red dashed lines). The QD state is in resonance with the H-polarised cavity mode and the excitation is aligned with the energy of the V-polarised cavity mode. Due to a cross-polarisation selection, most of the emitted photons are collected while the laser filtering is increased.

Figure 2.14a presents the design proposed by the group of Prof. J.-W. Pan [62]. As

sketched, the QD is placed in the center of a transverse Bragg grating which ensures the in-plane confinement of the optical field. The structure is composed of sub-λ thickness concentric rings [143]. The central disk radius and the grating period ensure the matching between the QD state energy and the one of the structure. Its ellipticity is used to set the splitting between the two cavity polarised modes. All of these parameters must be precisely chosen and realised to enhance the QD state emission. For instance, 1nm change in the central disk radius causes a 1.14nm shift in the cavity mode [145]. In this type of design, the Purcell factor can be higher than 20. The collection efficiency has also been improved by adding a thin low-refractive-index layer of SiO_2 and a gold mirror at the bottom of the bulls-eye (figure 2.14a). Due to the splitting of the two cavity polarised-modes (figure 2.14b), the laser is blue detuned and horizontally polarised while the single photons are emitted along the V-polarisation with a efficiency of 56%. In this condition, they proved an emission purity of 99.1%$\pm$0.3% and a photons indistinguishability of 95.1%$\pm$0.5%. Such sources were also used by the group of X. Wang [146] to produce entangled photon pairs via a biexciton radiative cascade. With a collection probability of 65%$\pm$4% and a photon indistinguishability about 90.2%$\pm$0.3%, they obtained an entanglement fidelity if 88%$\pm$2%.

	Q-factor	F_P	Source brightness	Single-photon purity	Indistinguishability
Photonic crystal cavity [131]	43 ± 2	–	–	0.973 ± 0.007	0.894 ± 0.025
Open microcavity [53]	12600	$\approx$12	0.57 ± 0.02 (fibred)	0.979	0.925
Bulls-eye cavity [62]	$\approx$20	–	0.56 ± 0.02	0.991 ± 0.003	0.951 ± 0.005

Table 2.2: Figure of merit of the other confinement solutions. The reported brightnesses are the first lens brightnesses, except for the open cavity for which this is the fibred brightness.

Table 2.2 summarises the benchmarks of the three solutions. All of them are measured under resonant excitation and the emission from the open microcavity and the bulls-eye cavity is polarised. When it is not precised, the given brightness is the first lens brightness and the indistinguishabilities are not corrected by the purity.

In the following, we describe the technology used in Quandela, based on micropillar cavities. We describe the cavity modes and the deterministic assemby of the QD-cavity structures.

2.5 Deterministic coupling of a QD to a pillar cavity mode

2.5.1 Planar-cavity characteristics

The QDs are embedded in a cavity which can be described as a Fabry-Pérot interferometer composed of a medium with a refractive index n_{cav} and a length L_{cav} enclosed by two distributed Bragg reflectors (DBR) (figure 2.15a). The planar cavity is designed to enhance the emission at $\lambda \approx \lambda_{\text{QD}} \propto L_{\text{cav}}$. The DBRs are composed of layers of GaAs and of AlAs

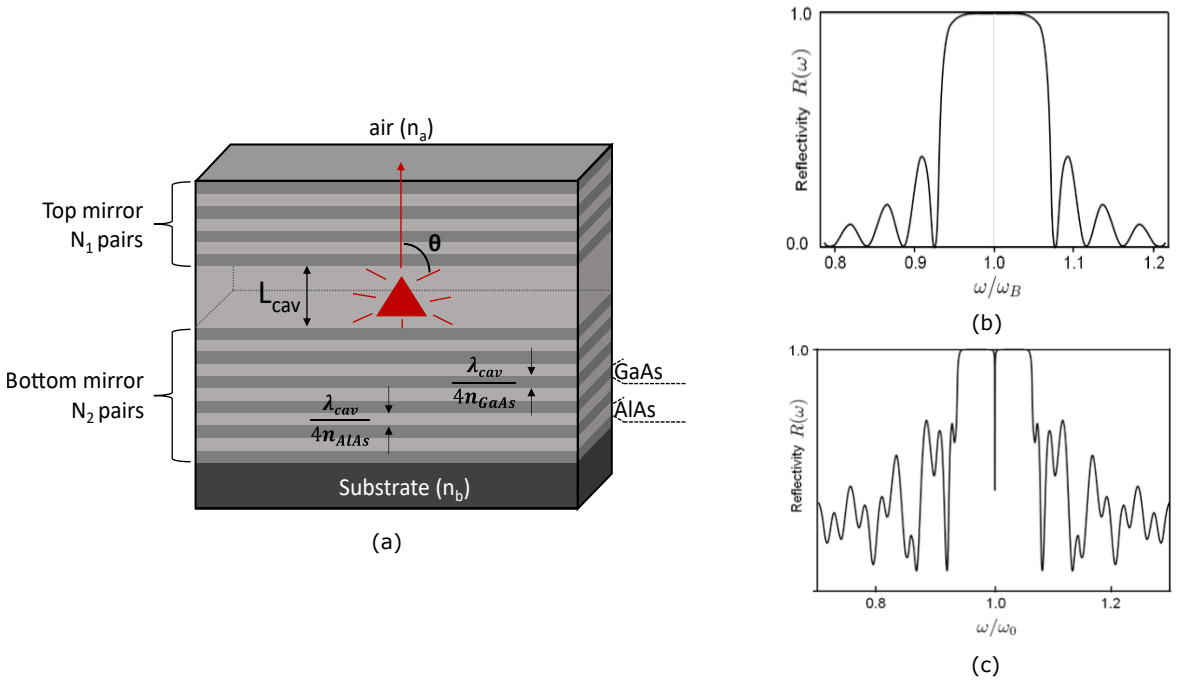

Figure 2.15: (a) Drawing of the planar cavity composed of two DBR separated by a distance L_{cav}. (b) and (c) are from the thesis of A. Dousse [147] (b) Theoretical plot of a 20-layers-pairs DBR reflectivity as a function of the normalized frequency. (c) Theoretical plot of the planar cavity reflectivity as a function of the normalized frequency.

whose optical thicknesses depend on the cavity resonant wavelength. Indeed, they are equal to its quarter:

$$L_{\text{GaAs}} n_{\text{GaAs}} = L_{\text{AlAs}} n_{\text{AlAs}} = \frac{\lambda_{\text{cav}}}{4}$$

The individual layer contributions add up constructively forming a high reflectivity stop band around the cavity wavelength, λ_{cav}. Light sent at a normal incidence within the reflectivity stop band is thus highly reflected. The reflectivity depends on the angle of incidence since the light "sees" a different optical thickness of the layer, proportional to $\frac{cos(\theta)}{\lambda_{\text{cav}}}$. Following the angle, the central wavelength is shifted by $\lambda_{\text{cav}} cos(\theta)$. The range of the high reflected wavelengths (R≈1) and the associated range of angles are expressed by [148]:

$$\Delta\omega = \frac{4\omega_{\text{cav}}}{\pi} \frac{n_{\text{GaAs}} - n_{\text{AlAs}}}{n_{\text{GaAs}} + n_{\text{AlAs}}} \tag{2.20}$$

$$cos\left(\frac{\Delta\theta}{2}\right) \approx 1 - \frac{1}{2}\frac{n_{\text{GaAs}} - n_{\text{AlAs}}}{n_{\text{GaAs}} + n_{\text{AlAs}}} \tag{2.21}$$

The maximal reflectivity, R_{DBR}, depends in particular on the number of layer pairs N [149] and can be written as:

$$R_{\text{DBR}} = \left(\frac{1 - \frac{n_b}{n_a}\left(\frac{n_{\text{GaAs}}}{n_{\text{AlAs}}}\right)^{2N}}{1 + \frac{n_b}{n_a}\left(\frac{n_{\text{GaAs}}}{n_{\text{AlAs}}}\right)^{2N}}\right)^2 \tag{2.22}$$

with, n_a and n_b respectively the refractive indexes of the medium on top and bottom of the DBR.

Hence, figure 2.15b, from the thesis of A. Dousse [147], presents the reflectivity as a function of the normalised frequencies for a 20 layer-pairs DBR. We can see the plateau of the high reflected wavelength (centred around the design wavelength) determined by the equation (2.22). On each side, the reflectivity oscillates and dampens.

The cavity, composed of two DBRs separated by a spacer of length L_{cav}, has a reflectivity spectrum like the one of figure 2.15c. The latter presents a reflectivity dip at the resonance wavelength of the cavity. The part which is spectrally matched with its reflectivity dip and is in the angle range set by the equation (2.21) is locally enhanced. This enhancement is due to successive constructive and destructive interferences of the reflected and transmitted part, respectively. The most enhanced signal remains the one emitted following the normal incidence.

If the number of layer of the top and bottom DBRs is set by the cavity reflectivity (equ. (2.22)), it also determines its quality factor as follows:

$$Q_0 = \frac{1}{2}\frac{1 - |r_1 r_2|}{|r_1 r_2|}\frac{c}{n_{\text{cav}} L_{\text{eff}}} \tag{2.23}$$

with $r_{1,2} = \sqrt{R_{1,2}}$ (for r_1, $n_a = n_{\text{air}}$, $n_b = n_{\text{cav}}$ and for r_2, $n_a = n_{\text{cav}}$, $n_b = n_{\text{substrate}}$), and L_{eff} the effective cavity thickness. It is defined as $L_{\text{eff}} = L_{\text{cav}} + L_D$, and allows to consider that the field penetrates the mirror to just a certain effective depth [150] defined as:

$$L_D \approx \frac{\lambda_{\text{cav}} n_{\text{AlAs}}}{4(n_{\text{GaAs}} - n_{\text{AlAs}})} \tag{2.24}$$

2.5.2 Pillar characteristics and emission in its fundamental mode

If the embedding in a planar-cavity enhances the QD spontaneous emission, it is only by a factor 1.2 [151]. Since $\Gamma_{CM} \propto F_{P,cav} \propto \frac{Q_0}{V_{\text{eff}}}$, to increase the extraction (linked to the Q-factor), and to accelerate the spontaneous emission (linked to the Purcell effect), we can play with the effective volume of the cavity. In other words, to enhance the emission in a well-defined mode of the cavity and increase its coherence, the optical field must be confined in the three directions [45, 152, 153].

Along the z-axis, the longitudinal confinement is achieved by the top and bottom DBRs. With the pillar shaped structure, the QD emission is now confined in the x- and y-axis thanks to the large refractive index of the GaAs (n_{GaAs} = 3.5) compared to vacuum's one. The confinement efficiency, in these two directions, depends on the pillar diameter. Considering a planar-cavity with a Q-factor Q_0, the spatial mode extends on an effective surface characterised by [151]:

$$S_{\text{eff}} = \frac{Q_0}{2}\left(\frac{\lambda}{n_{\text{GaAs}}}\right)^2 \tag{2.25}$$

As a result, the lateral confinement becomes effective in a pillar when $r_{\text{pillar}} < r_c \approx \sqrt{\frac{S_{\text{eff}}}{\pi}} \approx 9\ \mu$m (with $Q_0 \approx 7500$).

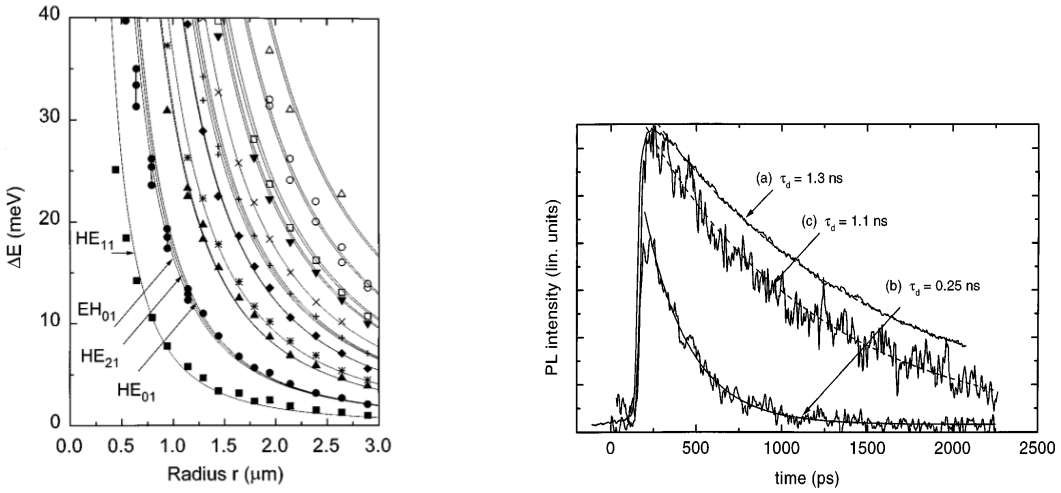

(a) (b)

Figure 2.16: (a) From reference [154], Plot of the influence of the pillar radius on the different confined modes energies (b) From reference [155] Trace (a): QD emission decay for a QD in a bulk. Traces (b) and (c): QD emission decay for a QD in a $3\mu m$-diameter pillar. For the curve b, QDs are in resonance with the pillar fundamental mode energy. Each measurement corresponds to standard photoluminescence experiment.

Figure 2.16a, from the work of Gérard et al. [154], presents the evolution of the energy of each confined mode as a function of the pillar radius. As plotted, modes confined in small pillars have higher energies than in larger ones. By carefully choosing the pillar radius, the transition energy of QD state located in its center can be matched with the fundamental mode energy within a certain range [154, 156].

In such a pillar, the spontaneous emission intensity from off-resonant modes is reduced while the emission from the resonant mode is enhanced [153]. Let us consider an emitter such as a QD, perfectly matched in energy with the one of the cavity optical mode. Let us furthermore assume that the QD transition dipole is aligned with the linear polarisation of the field in the cavity [157]. In this case, the lifetime of the QD spontaneous emission decreases [155, 158].

Figure 2.16b is from the pioneer work of Gérard et al. [155]. It shows the influence of the pillar on the QD state lifetime. This is a pulsed photoluminescence experiment on ensemble of QDs, embedded in a 3μm diameter isolated pillar. The lifetime of the spontaneous emission process is measured after the excitation at $t = t_0$. The trace (a) corresponds to the decay of an emission in bulk while traces (b) and (c) present the emission decay of QDs embedded in pillars. We can notice that if there is just a slight decay time drop between (a) and (c), while the trace (b) presents a significant reduction of it. For the latter, QDs were spectrally in resonance with the pillars fundamental mode. Hence, etching a pillar is not a sufficient condition to obtain a large emission enhancement. The spectral mode matching is also required.

As consequences, by reducing the spontaneous decay time into the cavity mode, the 3D-confinement of the optical field and the spectral mode matching lead to a larger spontaneous emission enhancement than in a 2D-planar cavity. This is controlled by the Purcell factor defined in the equation (2.19). From this factor, we can calculate the ratio of the photons preferentially emitted in the coupled mode of the pillar. This parameter is called β and it is expressed as:

$$\boxed{\beta = \frac{\Gamma_{\mathrm{CM}}}{\Gamma_{\mathrm{tot}}} = \frac{F_{\mathrm{p}}}{F_{\mathrm{p}} + 1}} \tag{2.26}$$

with, Γ_{CM}, the fraction of photons emitted into the cavity mode and Γ_{tot}, the fraction considering all the emitted photons. This formula assumes that the emission of the QD into other optical mode than the cavity is mostly unchanged as shown in Figure 2.16b traces (a) and (c).

To enhance the spontaneous emission in the cavity fundamental mode, and so to collect the maximum of photons, we want the highest F_{p}. For instance, with $F_{\mathrm{p}} = 5$, we get $\beta = 83\%$.

To do so and following the equation (2.19), we should increase the Purcell factor by reducing the pillar effective volume. This is supported by the work of Gazzano et al. [49] from which figure 2.17b is extracted. The red and black dashed lines represent respectively the evolution of the Purcell factor and of the pillar Q-factor as a function of the pillar diameter. The solid green line corresponds to the resulting extraction efficiency. As shown, a decrease of the pillar diameter leads to a higher Purcell factor. However, this reduction leads also to a decrease of the pillar Q-factor. Indeed, reducing the pillar radius should only impact the quality factor for diameter of the order of the diffraction limit. In practice $\mathrm{Q} \leqslant \mathrm{Q}_0$ is observed well above this limit. This is mostly due to etching issues. Indeed, the reactive ion process does not create smooth etched sidewalls and the imperfections cause diffusion and diffraction effects. Hence, the total extraction efficiency from the pillar top is reduced for small pillar (solid green line). The latter follows the equation:

$$\boxed{\eta = \frac{Q}{Q_0} = \frac{\kappa_{\mathrm{top}}}{\kappa_{\mathrm{top}} + \kappa_{\mathrm{bottom}} + \kappa_{\mathrm{loss}}}} \tag{2.27}$$

with Q (Q_0), the pillar (microcavity) quality factor, κ_{top} (κ_{bottom}), the escape rate for photons extracted from the top (bottom) DBR and κ_{loss}, the escape rate of photons lost through absorption and emission through the sidewalls.

κ_{bottom} is optimized with asymmetric DBRs so that $\kappa_{\mathrm{top}} \gg \kappa_{\mathrm{bottom}}$ can be reached. However, the pillar radius must be large enough to minimize κ_{loss}. With the current technology, we

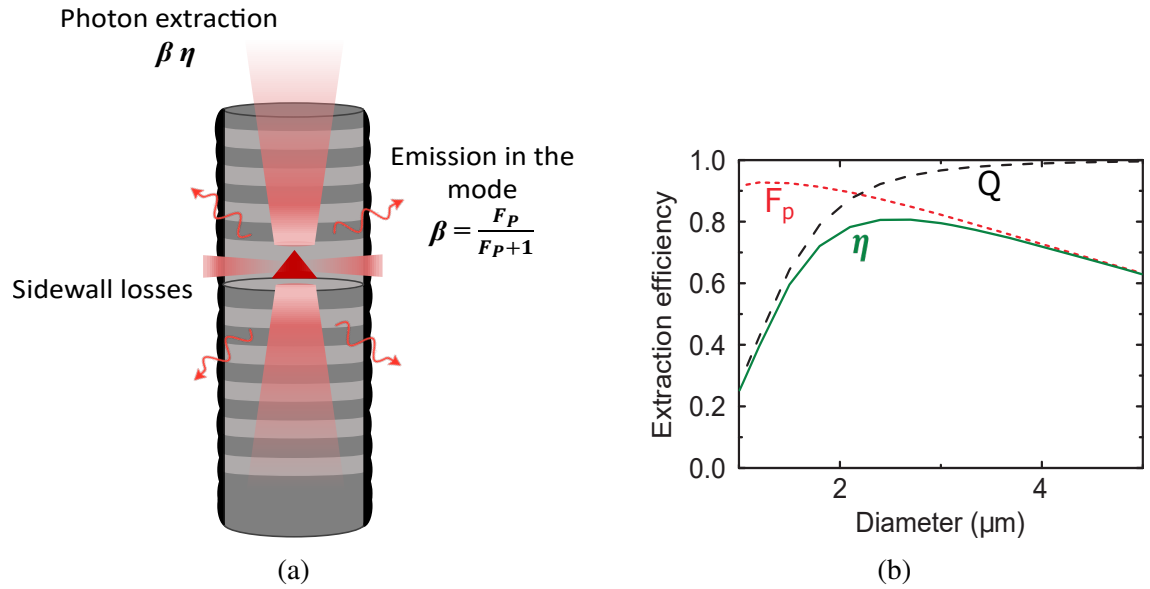

Figure 2.17: (a) Drawing of a pillar with the different parameters which affect the photons extraction. (b) From the reference [49]. Theoretical evolution of the extraction efficiency as a function of the pillar diameter (solid green line). Red dashed line: evolution of the Purcell factor. Black dashed line: evolution of the pillar Q-factor.

have a maximal output coupling of 84% under non-resonant excitation [49] and about 60-65% under resonant excitation [9].

2.5.3 Deterministic fabrication

2.5.3.1 Molecular beam epitaxy

The first step of the source manufacturing is made by molecular beam epitaxy (MBE) [159]. It is a standard fabrication technique of semiconductor hetero-structures. The process of the monocrystal growth is made by a successive deposition of layers with an atomic monolayer precision. To do so, a GaAs(100) wafer is placed in a high vacuum chamber. Then, Ga and As elements are heated and controllably deposed by successive opening and closing of shutters. The first distributed Bragg reflector (DBR) is deposited on the GaAs(100) wafer and it is composed of successive GaAs and AlAs layers. The number of layers is determined as a function of the expected cavity reflectivity. Once this is done, an InAs layer is grown.

Due to a lattice mismatch between the two components (the InAs has a lattice constant 7% higher than GaAs), mechanical stress enables a random creation of InGaAs clusters composed of few thousand atoms. These clusters are so-called QDs and they are embedded in the InAs layer called the "wetting layer". The self-assembled QDs are covered with a GaAs layer and then with the layers of the top DBR.

Figure 2.18 shows that like their positions on the wafer, the QDs sizes are random. Thus, the density is around 100 per μm^2 and the height is between 3 and 5nm for a width from 10 to

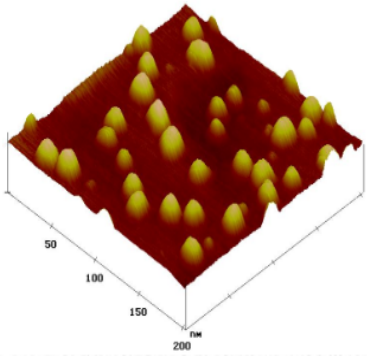

Figure 2.18: AFM picture of a part of the wafer. Each cluster is a QD.

20nm [160]. During this step of the fabrication, the QD takes its in-plane asymmetric shape leading to the exciton FSS (part 2.3.3). Depending on their sizes, the range of exciton emission wavelength is between 0.9 and 1.1μm at 10K.

2.5.3.2 Pillar manufacturing: in-situ lithography

To obtain the 3D-confinement of the optical mode, a pillar is etched from the planar cavity. The confinement along the z-direction is ensured by the DBRs. Since the QD position is random, the probability that the QD is located at the maximum of the optical field in the pillar center is very low. Yet, the QD-cavity assembling process remains random in many groups where pillar cavities are etched at a regular distance from each other. However, not only this leads to get pillars with either no QD or more than one QD, but the spectral matching is also probabilistic. Overall, to obtain a clean system where the pillar does not contains many dots, the fabrication yield is around 1/1000 to 1/10 000.

To fix these issues and get a deterministic process, we use the so-called "in-situ" lithography proposed by the group of Prof. P. Senellart at CNRS-C2N in 2008 [161]. This techniques enables to precisely measure the QDs positions (figure 2.19) and etch a pillar with the appropriate energy around them.

As discussed before, the planar cavity wavelength is already defined by the cavity length L_{cav} and the DBRs reflectivity. Pillars are defined with a typical range of diameter assuring a good out-coupling efficiency. This defines the fundamental mode energy range to which the QD will be put in resonance with. As a result, we need to work with a QD density that is small enough within this energy range. Spectrally far detuned QDs will not be a limitation. The as grown sample usually presents too many QDs in this spectral range. To control the QDs density around the cavity resonance, the wafer is annealed to shift the QD energy to higher energies [147]. Typically, the obtained density corresponds to around 4 QDs per $400\mu m^2$. Once this step is done, a layer of photoresist is deposited on the planar cavity and the wafer is put at 4K in a cryostat. The cartography of the QD positions is done via the measurement of their PL emission. To do so, the wafer is scanned at the nanometer scale in the x-,y-plane, and a continuous-wave laser, at 850nm, is sent. To be considered promising, a QD must be spatially isolated, so that there is only one optically active QD per pillar. Moreover, looking at the photo-luminescence spectrum, one of its state must be spectrally isolated and bright. Once a QD is selected, a continuous-wave laser, at 530nm, exposes the photoresist.

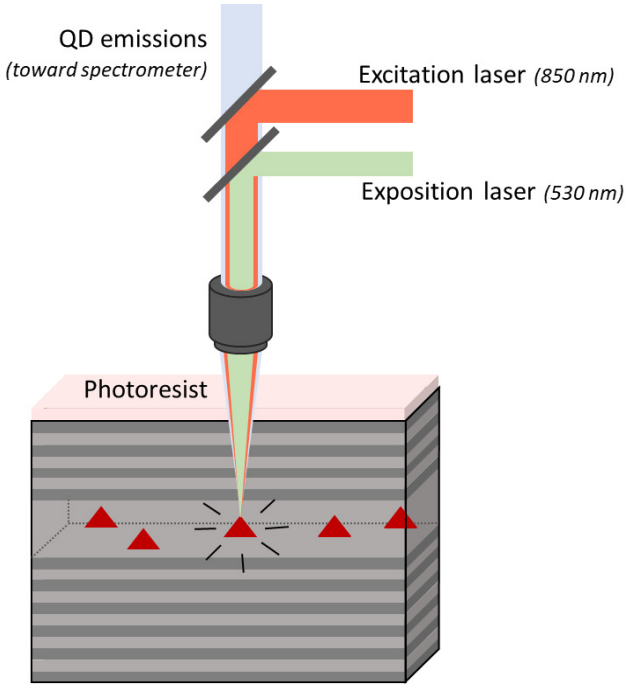

Figure 2.19: Schematic of the in-situ lithography. The self-assembled QDs embedded in the microcavity are excited by a non-resonant laser ($850nm$) and a laser at $530nm$ exposes the photoresits where pillars must be etched.

The latter polymerises as a disc in the resist centered on the QD position with a positioning accuracy below 50nm [161]. Thus, the QD is placed at the maximum of the electric field of the pillar fundamental mode, which has a Bessel spatial profile. In the first implementation of this technique in 2008, the disc diameter was determined by the laser beam diameter, itself carefully chosen so that the corresponding pillar mode eventually matches the energy of the QD selected state [162]. The photoresist exposition is done for several QDs before removing the wafer from the cryostat.

The wafer is then cut into several samples and the polymerised photoresist is removed. After a metallic deposition and a lift-off step, a reactive ion etching of the pillars around QDs is done. At the end of the process, a sample is composed of about thirty pillars, each of them embedding a single QD at its center, with the QD line within 0.3nm of the cavity resonance.

2.5.4 Fine spectral tuning techniques

We saw that the energy of the fundamental mode of the pillar is chosen to match the QD emission wavelength [155]. However, the errors in the fabrication process, such as the small error in the pillar size imprinted in the resist, or the non perfect verticality of the etching process, results in an non perfect QD-cavity resonance. This part will detail two solutions to finely tune the QD transition energy and put it in resonance with the pillar fundamental mode.

2.5.4.1 Thermal tuning

The first technique is based on increasing the temperature of the sample.

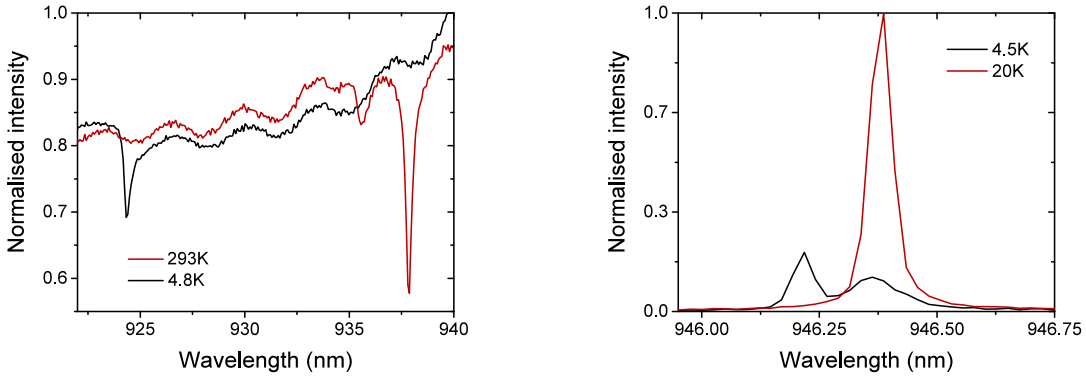

(a) (b)

Figure 2.20: (a) Reflectivity spectra at room temperature, 293K (red line) and at 4.5K (black line). The oscillations are due to the LED spectrum. (b) PL spectra at 4.5K (black line) and at 20K (red line). At 4.5K the QD state emits at a lower wavelength than the cavity mode one and it is in resonance at 20K.

Figure 2.20a presents the cavity reflectivity spectra before and after a cooling process. The solid red and black spectra correspond respectively to measurements done at 293K (room temperature) and at 4.5K. We can then notice that the cavity mode shifts by about fifteen nanometres towards lower wavelengths during the cooling process. This effect of temperature is then a intrinsic response of the sample, reflecting the change of refractive index with temperature. However, between 4.5K and 35K, the energy shift of the fundamental mode is mostly negligible. On the contrary, the QD states show a stronger dependence with the temperature, following the band-gap change. When heating the sample from 4K to 20-30K, the QD transitions shifts towards lower energies (so higher wavelengths) faster than the cavity mode. This is illustrated by the two spectra of figure 2.20b. The photoluminescence of a single photon source is plotted at two different temperatures. The solid black spectrum presents the QD state emission at 4.5K. Its emission wavelength is on the left of the broader cavity mode (off-resonance situation). When increasing the temperature to 20K, the QD line is put in resonance with the cavity and its emission is enhanced (solid red line).

However, rising the temperature leads to an increase of the emission via the phonon side-bands. It is thus not a good technique to get a bright source of indistinguishable photons.

2.5.4.2 Bias application and Stark effect

The second solution to change the QD states energy is based on the change of its electrostatic environment. In other words, we change the energy between the ground state and the different excited state by applying a bias [163]. Such technique also allows to control the charge state in a QD, and therefore to work with either neutral or charged exciton transitions [164]. To do so, two main evolutions from the first pillars generation have been realised:

the doping of the planar-cavity and the connection of the pillar to a larger structure to apply the voltage as explained below.

Only a few works have demonstrated an electrical control of a QD coupled to a cavity, showing how challenging such a fabrication is. The first coupling of a QD in a high-Q micro-cavity with electrical contacts has been showed by Strauf et al. in 2007 [165]. By defining trenches in the planar cavity, they used a controlled AlOx oxidation to confine the light in the cavity while the electrical contacts were around the cavity region and placed at few layers of the QD. The QD layer was then embedded by two n-doped gates.

Another technique consists in creating a gradient of doping concentration during the MBE process from the bottom layer of n^+-doped GaAs, and the n-doped layers of the bottom DBR, to the p-doped layers of the top DBR. The layer containing the QDs remains undoped. With such n-i-p doping structure, the energy bands are tilted in the absence of applied bias and the QD states energy are a little bit lower than their equivalent in a undoped cavity. Due to the pillar limited lateral size, placing the electrical contact is very challenging without losing on the extraction efficiency. Therefore, several approaches have been proposed. For instance, the groups of Prof. J.M. Gérard [166] and Prof. A. Forchel [167] planarised the sample with BCB to connect pillars from the top by gold contacts. The group of Prof. A. Forchel [168] also developed pillars contacted from the side by to diametral nano-wires. In our case, we exploit the techniques proposed in the work of Nowak et al. in 2014 [169] where the micropillars are connected to large un-etched surfaces with 1D arms in a cross shape (figure 2.21a). The electrical metallic contacts are then done on the large pads of typically 160μm$\times 160\mu$m. The electrical wires are bonded on these large surfaces with a Ti/Au Schottky contact.

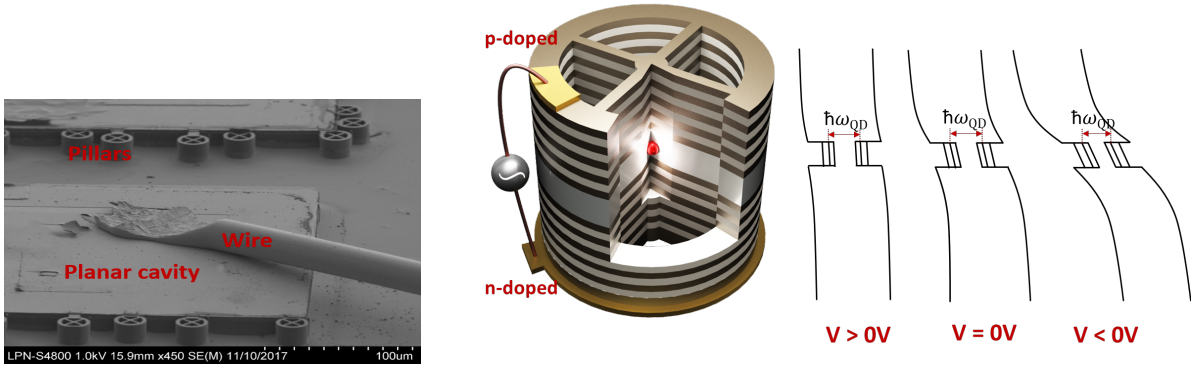

(a) (b)

Figure 2.21: (a) SEM picture of the current sample. The wire is bonded on the planar cavity and the pillar are tied to it with the cross shape structure. (b) Drawing of the voltage influence on the QD states energy levels. Because of the structure doping, the energy bands are already tilted. A positive voltage increases their energies while a negative voltage decreases them.

We work in a voltage range where the current remains close to zero. Indeed, the source is a diode [170] and when the current increases, the charges accumulation in the band gap alters QD states. Figure 2.21b summarises the effect of a bias application. To some extent, it is then possible to change the energy levels from their initial position. A negative voltage brings the conduction and the valence bands closer. As a consequence, the energy of the transition decreases, and the emission wavelength is higher than the one at 0V. On the contrary, a positive

bias makes them move apart. The energy of the transition increases and shifts the emission to a lower wavelength.

This solution is more robust and reliable than the temperature change. Most importantly, it should not affect the photon indistinguishability and we can both red shift and blue shift the QD wavelength. So, as long as the difference between the QD and cavity resonances is lower than typically 1nm, the detuning can be compensated with bias application. Beyond this upper bound, the QD charge state can change because of the tunneling of an electron or a hole.

2.6 Optical study of the sources

We now turn to the optical characterisation of the sources. We discuss their emission properties both under non-resonant and resonant excitation. We also discuss the differences of the resonant excitation scheme when studying either an exciton or a trion.

2.6.1 Benchmarks measurements

Our objective is to measure all the important figures of merit of a single photon source. From β and η parameters (defined in part 2.5.2), we can obtain the "first lens brightness" of a source. As defined in part 2.2.1, this represents the fraction of photons emitted in the fundamental mode of the pillar, extracted from its top and collected by a lens. Since pillars have numerical apertures lower than 0.4, we can consider a lens with a large enough numerical aperture typically around 0.6. Thus, the first lens brightness depends only on β, η, and on the occupation probability of the excited state, $p_e \leq 1$, whose value depends on the excitation scheme. Independently of the excitation scheme, the first lens brightness is then given by:

$$\boxed{\mathcal{B}_{FL} = \beta \times \eta \times p_e} \tag{2.28}$$

Experimentally, it is estimated from the collected photons rate corrected by the system transmission and the detector efficiencies.

Concerning the measurement of the emission purity, we use the method described in part 2.2.2. Figure 2.22a presents the plot of the second order correlation measurement under resonant fluorescence. The delay between subsequent peaks is linked to the laser repetition rate. The side peaks correspond to the second photon detected after a certain delay proportional to $\pm 12.3ns$, for a repetition rate of 81MHz. Therefore, the calculation considers the ratio between the area of the central peak over the areas of the lateral ones.

Finally, the mean wave-packet overlap is measured with a system based on a Mach-Zender interferometer (figure 2.22b). The emitted photons are diagonally polarised by a polariser (P) and sent on a polarising beam splitter (PBS). Thus, they have 50% chance to be transmitted or reflected. Depending on the taken path, the photon can take the arm whose length is set to create a delay according to time separating two consecutive photons. It is then

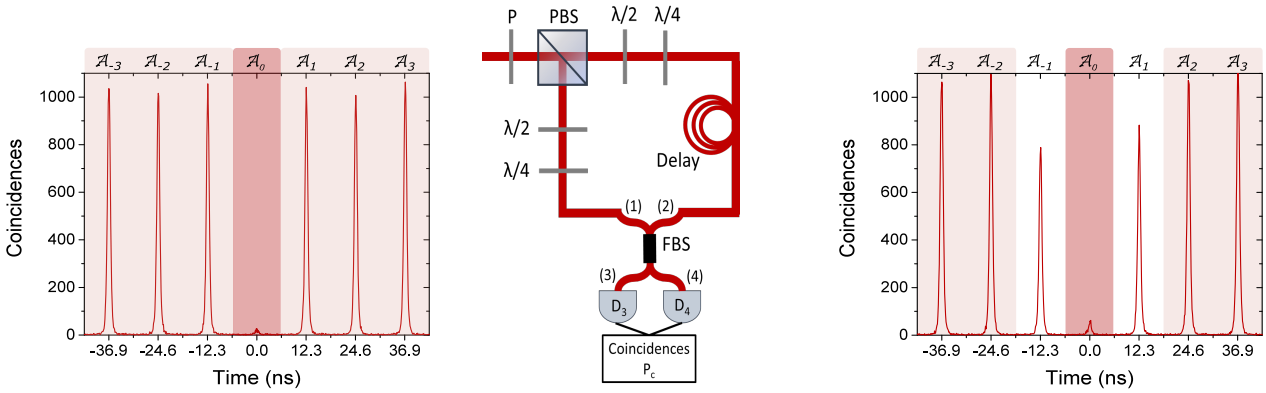

(a) (b) (c)

Figure 2.22: Time traces of (a) a second order correlation measurement and of (c) a mean wave-packet overlap under resonant fluorescence. (b) Schematic of the Mach-Zender interferometer used to measure the mean wave-packet overlap under resonant fluorescence. It is composed of a polariser (P), a polarising beam splitter (PBS), two half and quarter waveplates and a fibred 50:50 beam splitter (FBS).

proportional to the laser repetition rate and enables to send simultaneously two photons at the two inputs of a balanced 50:50 fibred beam splitter (FBS). In other words, two photons emitted from two consecutive laser pulses can reach the FBS at the same time. The measured time trace is plotted in figure 2.22c. For the calculation of the mean wave-packet overlap, the peaks $\mathcal{A}_{\pm 1}$ are excluded. Indeed, they represent the probability of the event: the "first photon" does not take the path with the delay and cannot interfere with another photon in the FBS.

The measured HOM visibility is then written as follows:

$$\boxed{V_{\mathrm{HOM}} = 1 - 2\left(\frac{\mathcal{A}_0}{\mathcal{A}_{\mathrm{k}}}\right)} \tag{2.29}$$

with $\mathcal{A}_{\mathrm{k}}$ ($k = \pm 2, \pm 3, ...$), the average area of the side peaks (usually three or four on each side), except peaks $\mathcal{A}_{\pm 1}$, and $\mathcal{A}_0$, the area of the peak into a window of $\pm 1ns$.

We should also consider that, adding to the intrinsic indistinguishability of the emission, given by $\mathcal{M}_{\mathrm{th}}$ (equ. 2.3), the non-null peak at zero delay can also be due to issues with the optical system. Indeed, coincidences on the two detectors can arise if the FBS is not perfect ($R \neq T$), or if the delay and the polarisation between the two arms are not well controlled. While the latter can be optimised carefully during the experiment, the imperfect FBS properties can be accounted for by using the following relation:

$$\boxed{\mathcal{M}_{\mathrm{exp}} = V_{\mathrm{HOM}}\left(\frac{R^2 + T^2}{2RT}\right)} \tag{2.30}$$

with R (resp. T) is the intensity reflectivity (transmission) coefficient of the beam splitter. When R = T = 0.5, the V_{HOM} visibility is simply the mean wave-packet overlap $\mathcal{M}_{\mathrm{exp}}$.

Once corrected from the setup imperfection, the value given by equation (2.30) represents the effective indistinguishability of the real, non-perfect, emission of single photon

sources. But, this value is affected by its non perfect single-photon purity. To push further the development of the sources, it is very important to be able to identify whether the limited $\mathcal{M}_{\text{exp}}$ arises either from non-zero $g^{(2)}(0)$ or from the limited intrinsic wavepacket overlap of the single photon part of the field. To access the mean wave-packet overlap of the single photon part, a recent study was conducted in the group of Prof. P. Senellart [171]. Prior to this work, the corrected mean wave-packet overlap was extracted using by $\mathcal{M}_{\text{corr}} = \mathcal{M}_{\text{exp}} - g^{(2)}(0)$ [172, 173], where $\mathcal{M}_{\text{exp}}$ includes the multi-photon component. The work of Ollivier et al. [171] proved that the impact of multi-photon events was underestimated, and that the effect of pure dephasing was milder than previously expected. Theoretically and experimentally, they proposed a correction equation written as follows:

$$\boxed{\mathcal{M}_{\text{corr}} = \frac{\mathcal{M}_{\text{exp}} + g^{(2)}(0)}{1 - g^{(2)}(0)}} \tag{2.31}$$

This correction factor can be applied to any single-photon source excited with fast pulses (about 10-15ps) and whose emission single-photon purity is above 90%.

Finally, in order to increase the indistinguishability of the collected photons, a Fabry-Pérot etalon is added in the collection. Its linewidth, about 15μeV [9], is chosen to match the QD emission and allows to further increase the phonon side-bands filtering.

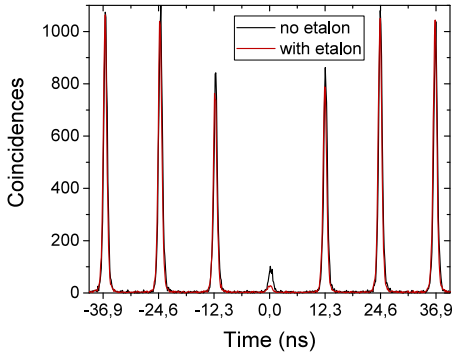

Figure 2.23: Time trace of mean photon wave-packet overlap measurements. In black (red) without (with) a Fabry-Pérot etalon in the collection path.

Figure 2.23 presents the measurement with and without an etalon. We can notice the small area of the peak at zero-delay evidencing a high indistinguishability of the ZPL emission. Without the etalon, the corrected mean photon wave-packet overlap is 86% while, with one, $\mathcal{M}_{\text{corr}}$ = 95%. However, the current filtering techniques leads to a significant reduction of the brightness. Thus, a trade-off must be found between these two benchmarks.

2.6.2 Non-resonant excitation or Photoluminescence

2.6.2.1 Excitation scheme

The photoluminescence of a single QD is measured by exciting it with a laser whose wavelength is set to higher energy from the QD transition. Here we discuss excitation schemes in the GaAs or in the wetting layer, corresponding to wavelength between 830nm and 850nm.

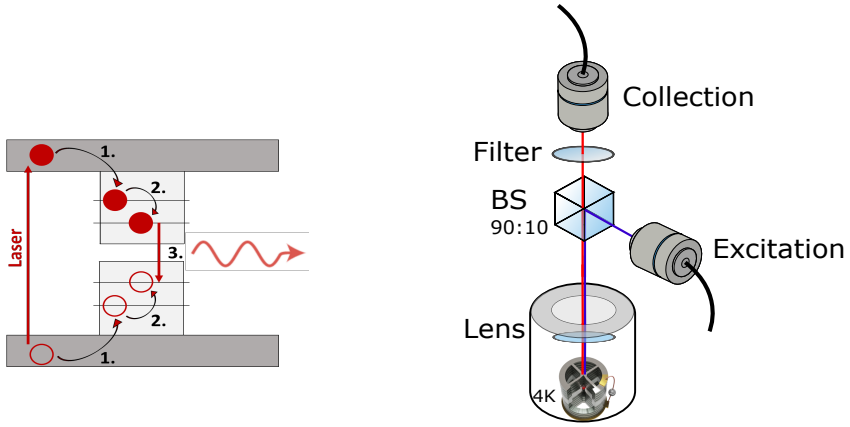

Figure 2.24: (a) Schematic of the PL emission. An electron-hole pair is created in the wetting layer or in the continuum of the GaAs bulk. (1. and 2.), the electron and the hole reach the s-shell states via relaxations and charge carrier captures. (3.) The QD state relaxation (here exciton) lead to a photon emission. (b) Schematic of the microscope for a non-resonant excitation.

The emission process is depicted in figure 2.24a. Having a much higher energy than the QD states, this laser is chosen to create electron-hole pairs in the continuum of the GaAs bulk or in the wetting layer. The emission takes place after rapid relaxations of electrons and holes from these energy levels to lower-energy ones. The latter are due to intraband relaxation, interaction with charge carriers and/or with phonons. Once the electron and the hole have reached the lowest excited state of the QD, the electron-hole pair recombines and a photon is emitted.

As shown by the schematic of figure 2.24b, a 90:10 BS enables both to send the excitation laser into the single photon source and collect most of the emitted photons. Since the reflected laser is also transmitted by the BS, a longpass or a bandpass filter is added to suppress it before the collection fibre.

2.6.2.2 Emission characteristics

An example of a photoluminescence spectrum is plotted in figure 2.25a. Due to a low spectrometer resolution (about 12 pixels for 1nm), the lines are broad and not well defined.

This excitation scheme leads to emission signal from multiple QD states (multiexcitons). We can also notice an emission line at the cavity frequency. This is due to a feed by the

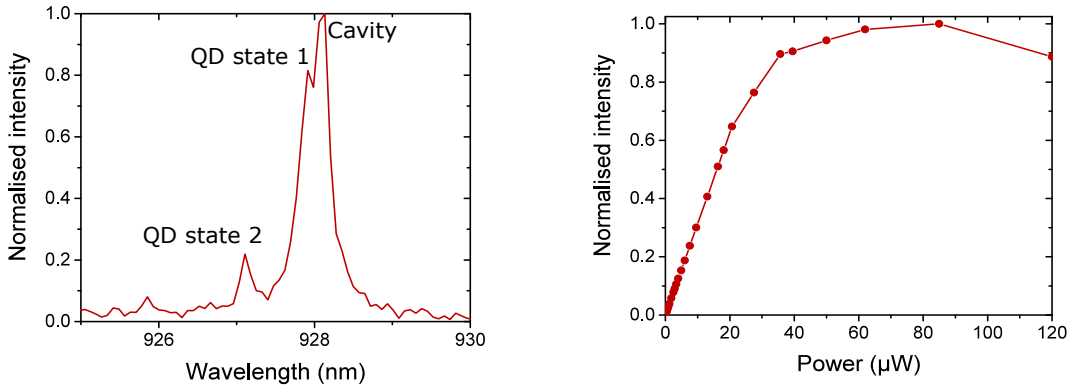

(a) (b)

Figure 2.25: (a) PL spectrum of a QD embedded in a pillar. (b) Saturation curve of an excitonic state in resonance with the pillar energy excited with a continuous-wave laser at 850nm.

multiple phonon-sidebands of the QD emission lines [174]. This "cavity" line is broader and does not saturate when the laser power increases. On the contrary, increasing the laser power leads to a saturation of the QD states emission. This approach enables to distinguish more precisely the cavity peak from the QD states. In this spectrum, we can distinguish two states. As explained later (part 2.6.3.4), the emission behavior of state 1, under resonant excitation, allows to assign it to a trion transition. However, we just worked with this state and we did not identify state 2.

Figure 2.25b represents the intensity from an exciton line of another source as a function of the laser power. In this case, a linear dependence is observed as a function of power before the saturation. If this dependence could also be assigned to a trion transition, the intensity drop leads to the conclusion that it is an exciton. Indeed, the large laser power leads to an average occupation of the QD by two-electron hole pairs, and the emission comes then preferentially from the biexciton transition.

Under this excitation scheme and with isolated pillars, it has been theoretically shown that it is not possible to obtain both a high brightness and a high photons indistinguishability [175]. Gazzano and coworkers indeed characterised our single photon sources under this excitation regime and, for a single-photon purity around 0.95, they obtained results close to theory with either a brightness of 0.79±0.08 and $\mathcal{M}$ = 0.55±0.05 or $\mathcal{B}_{\mathrm{FL}}$ = 0.53±0.05 and $\mathcal{M}$ = 0.9±0.10 [49]. This trade-off is due to the fact that under this excitation scheme the highest brightness is obtained by increasing the laser power. But high power non-resonant excitation leads to an increase of the number of the charge carriers in the wetting layer which are the origin of fluctuations of the QD electrostatic environment and dephasing. Moreover, the radiative cascade, leading to a multi-exciton recombination, leads to a time jitter before the last photon emission which also reduces the photon indistinguishability.

2.6.3 Resonant fluorescence

2.6.3.1 Excitation scheme

To get a better control of the emission characteristics and mainly to improve its indistinguishability, the sources are resonantly excited [49, 130, 176]. In the last few years, the resonant excitation of a single QD has been demonstrated and the resonance fluorescence of QDs was measured [177–179]. Under this excitation scheme, the laser and the QD state coupled to the cavity mode present the same energy. The excitation laser is a 3ps pulsed laser, but to spectrally match the cavity linewidth, its spectrum is shaped. As a consequence, its pulse duration is equivalent to a pulse duration of about 15ps. Since the emitted photons have the same wavelength, we can no longer place a spectral filter in the collection path to suppress the laser. Instead, a polarisation filtering can be used to suppress the laser and extract part of the single photon emission. The typical experimental optical system is presented in figure 2.26b, and is based on a cross-polarisation configuration.

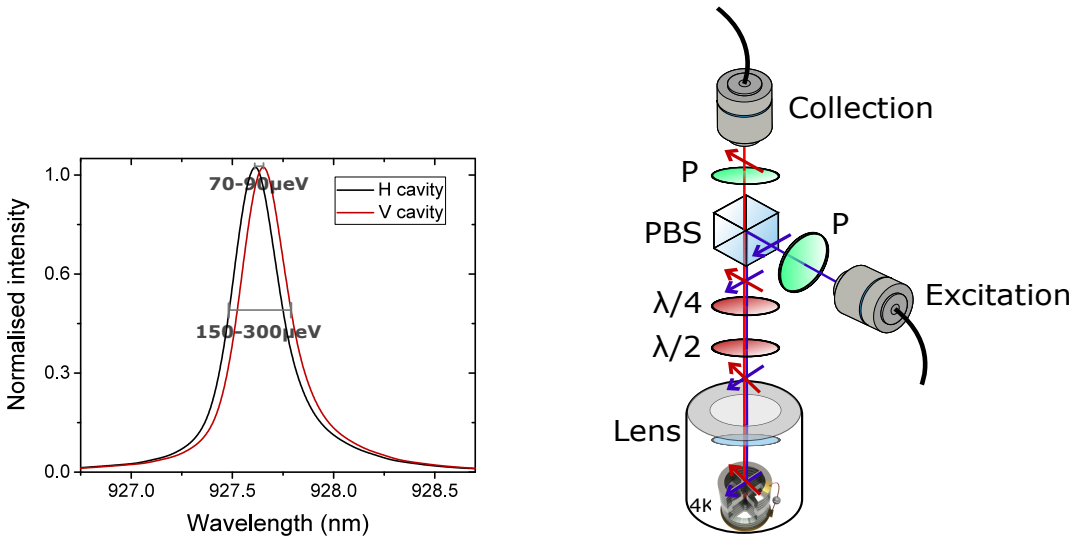

(a) (b)

Figure 2.26: (a) Plot of the cavity splitting. Due to the pillar birefringence modes $|H\rangle$ and $|V\rangle$, whose bandwidth is about 150-300μeV, have energies split by about 70-90μeV. (b) Schematic of the confocal microscope for resonant excitation regime.

As presented in figure 2.26a, the cavity fundamental mode presents two nearly-degenerate linearly-polarised modes whose energy splitting is typically 30-70μeV. This difference is smaller than the spectral linewidth of the cavity, which is around 150-300μeV. If the incident beam is linearly-polarised along one of this two axes, the reflected beam exhibits with the same polarisation. On the contrary, if it enters with any linear polarisation in between, the cavity birefringence creates different phase delays between the components projected onto H and V, resulting in an elliptical polarisation state. As a consequence, a part of the reflected laser is collected in cross-polarisation. This phenomenon is maximum for a diagonal input polarisation. We call "cavity rotated light" the part of the beam coupled to the cavity which sees its polarisation rotated in the Poincaré sphere. The latter is then collected even in a

cross-polarisation configuration.

As illustrated later on, this rotated light signal is very useful for alignment purposes. However, it should be strongly suppressed when operating the source under resonant excitation. As a result, the resonant excitation must be performed with a linear polarisation aligned along the H or V cavity axes.

The optical system, presented in figure 2.26b, is then based on a cross-polarisation configuration. Chapter 3 will more detail its development and characteristics. In brief, in the excitation path a polariser set the incident beam polarisation to fully reflect it by a polarising beam splitter (PBS). The two wave-plates ($\lambda/2$ and $\lambda/4$) before the cryostat enable to correct any ellipticity and match the incident polarisation to one of the cavity axes (H or V). In the collection path, the PBS and another polarisation filter (PBS or polariser) enable to collect only the photons emitted in the orthogonal polarisation.

Under this excitation scheme, we introduce the "polarised first lens brightness" ($\mathcal{B}_{\mathrm{PFL}}$). The latter is distinguished to the first lens brightness by the coefficient r_{pol} which traduces the fraction of photon emitted in the collection polarisation:

$$\boxed{\mathcal{B}_{\mathrm{PFL}} = \mathcal{B}_{\mathrm{FL}} \times r_{\mathrm{pol}}} \tag{2.32}$$

Considering this intrinsic limitation, the resonant excitation scheme works in a cavity only if the QD transition can emit single photon in a crossed polarisation with respect to the cavity axes. As discussed now, the r_{pol} coefficient depends on the QD charge state which emits the photons. Thus, based on the work of the Ollivier et al. [99], parts 2.6.3.3 and 2.6.3.4 will describe the way to distinguish the emission from an exciton to a trion's under resonant excitation, and how these different charge state lead to different sources performances.

2.6.3.2 Coherent control of a QD

Here, we first discuss the first coherent control measurements of a QD system [177,179] evidencing the Rabi oscillations under resonant excitation [180]. The laser is set at the energy of one of the QD states and the Rabi oscillations are measured by varying either the pulse duration, with a constant laser power, or the laser power, with a constant pulse duration. An attractive method to measure this coherent control is to use photo-current measurements, where the oscillations are observed in the current signal instead of in the emission. Figure 2.27b presents nice oscillations reported in 2010 by Ramsay and coworkers [181]. The observations using the direct resonant fluorescence signal were reported in 2007 [177–179] by using an orthogonal excitation and collection configuration: QDs were excited from the side and resonant fluorescence is collected perpendicularly to sample's surface.

The optical excitation of the QD transition, modelled as a two-level system composed of a ground state $|g\rangle$ and an excited state $|e\rangle$, corresponds to the creation of an electron-hole pair. Thus, the coherent drive can be seen as a unit-vector displacement on the Bloch sphere [182] (figure 2.27a). Considering an increasing pulse duration for a constant laser power, Rabi oscillations can be described as follows. By gradually increasing the pulse duration, the QD state is driven from $|g\rangle$ to $|e\rangle$ and the probability of reaching the excited state is maximum for a certain duration. The system is then in a position called $''\pi''$. Between 0 and $''\pi''$, the pulse duration is too short to drive the QD efficiently and at $''\pi''$ the laser has the correct duration

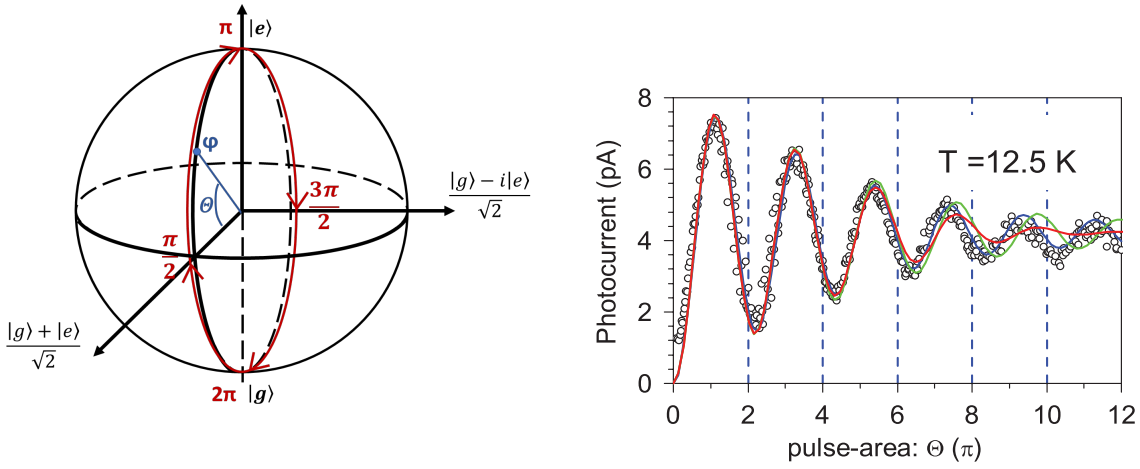

(a) (b)

Figure 2.27: (a) Drawing of a Bloch sphere and schematic of the Rabi oscillations phenomenon (b) Theoretical plot (red line) and experimental measurements (rounds) of a Rabi oscillations of an exciton, as function of the pulse area (from ref [181]). The final occupation of the exciton is measured using a photocurrent detection.

to do so. If the pulse duration keeps increasing, this probability decreases until reaching a minimum of emission at a position called "2π". Indeed, the system can go back to the ground state during the pulse. It is possible to increase again the pulse duration and in this case the probability increases before decreasing again. We then measure Rabi oscillations whose period is proportional to the dipole moment transition from $|g\rangle$ to $|e\rangle$ and to the electric field amplitude. We can write the Rabi frequency as [183]:

$$\Omega_R(t) = \frac{\mu A(t)}{\hbar} \tag{2.33}$$

with μ the dipole moment and A(t) the electric field envelope of the laser pulse, defined as $E(t) = \frac{1}{2}\,(A(t)\,e^{-i\omega_0 t} + A^*(t)\,e^{i\omega_0 t})$.

The same experiment can be realised by increasing the power of the excitation laser. The results and the phenomenon description are the same. In this case, the "π-position" corresponds to the required power to optimally excite the state.

The Rabi oscillations are usually plot as function of the pulse area (figure 2.27b). The latter is defined as the temporal integral over the Rabi frequency [184]:

$$\Theta = \int \Omega_R(t)dt \tag{2.34}$$

In figure 2.27b, we can also notice a damping of the oscillations. The latter is due to the finite lifetime of the two level system [185] as well as its interactions with the phonon bath [186]. As consequences, the probability of emitting a photon during longer pulses or under a higher power decreases following the decay of the excited state. The dephasing, due to phonon interactions, also induces a reduction of the occupation probability or a reduction

of the coherence. Hence, the oscillations damp until an equilibrium position, corresponding to populating equally the ground and the excited states for a two-level system.

Such observation is a good evidence that a QD, a semiconductor trap composed of thousands of atoms, can be considered as an artificial atom.

In the following, we present the detailed analysis of the coherent control in our QD sources, performed with the PhD work of Hélène Ollivier [99]. We discuss the coherent control of either excitons or trions in pillar cavities.

2.6.3.3 Resonant fluorescence of an exciton

Under resonant excitation, the exciton can be described as a three levels system: a ground state $|g\rangle$ and two excited states separated in energy by the FSS (figure 2.28a). The latter, labelled $|X\rangle$ and $|Y\rangle$, are the two intrinsic exciton eigenstates and are linearly-polarised dipoles.

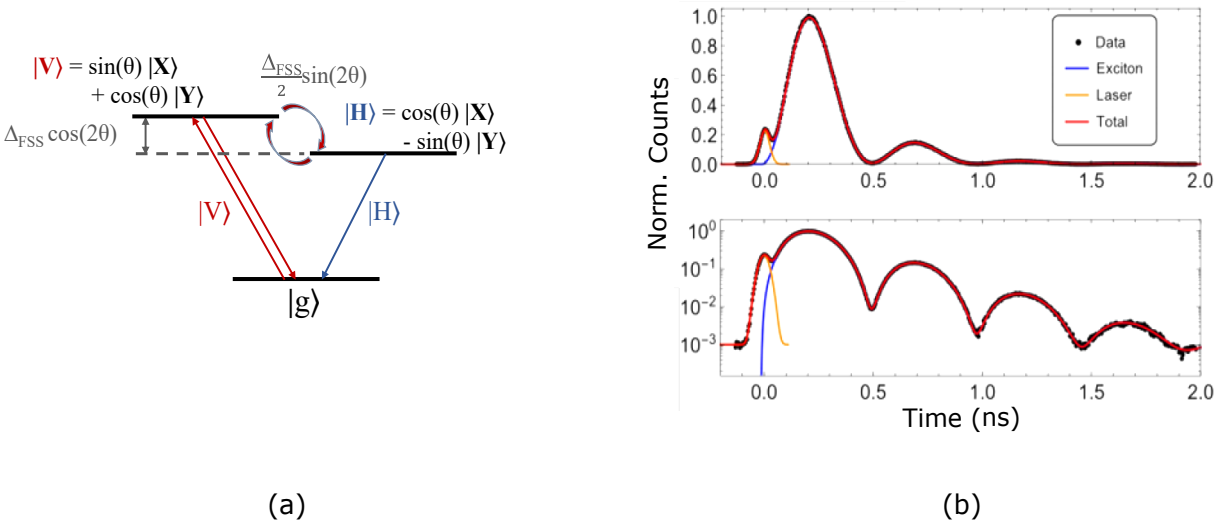

Figure 2.28: (a) Energy level structure of a neutrally charged quantum dot, with ground state $|g\rangle$ and two exciton eigenstates $|X\rangle$ and $|Y\rangle$, separated in energy by the fine structure splitting (FSS). The resonant excitation process results in an excitation along $|V\rangle$ and a photons collection along $|H\rangle$. The polarisation rotation is allowed by the FSS. (b) Lifetime of an exciton state (blue line) under resonant excitation. The orange line corresponds to the excitation laser With the log-scale, we can see the beating due to the FSS.

The angle θ between the axes of the cavity and of the QD is random. To avoid the signal coming from the rotated light arising from the pillar birefringence on the input laser beam and to only collect the emitted photons, the laser is linearly-polarised along one of the two cavity axes. In this condition, if the excitation is V-polarised, the collection is parallel to the H-polarisation. Due to a projection onto the exciton linear dipoles, both $|X\rangle$ and $|Y\rangle$ are excited, as long as the X and Y directions do not coincide with the H and V polarization

directions of the cavity. The link between these polarisation axes is written as follows:

$$\begin{cases} |V\rangle = cos(\theta)\,|Y\rangle + sin(\theta)\,|X\rangle \\ |H\rangle = -sin(\theta)\,|Y\rangle + cos(\theta)\,|X\rangle \end{cases} \tag{2.35}$$

So, let us consider the initial state $|\Psi(0)\rangle = |V\rangle$. The exciton state is driven at "π-pulse" and its time evolution follows:

$$|\Psi(t)\rangle = cos(\theta)e^{-\left(\frac{iE_Y}{\hbar}+\frac{1}{2\tau}\right)t}\,|Y\rangle + sin(\theta)e^{-\left(\frac{iE_X}{\hbar}+\frac{1}{2\tau}\right)t}\,|X\rangle \tag{2.36}$$

with $\Delta_{\text{FSS}} = E_Y - E_X$, and τ, the total Purcell-enhanced emission lifetime. Since we consider small cavity asymmetry, it is assumed to be the same for both exciton dipoles.

The probability so that a single-photons is emitted in the H-polarisation mode is then proportional to:

$$|\,\langle H|\Psi(t)\rangle\,|^2 = e^{\frac{-t}{\tau}} sin^2\left(\frac{\Delta_{\text{FSS}}}{2\hbar}t\right) sin^2(2\theta) \tag{2.37}$$

This equation shows that by exciting along the V-polarisation, a part of the single photons is emitted through the H-polarised mode after a delay inversely proportional to the FSS. Hence, the highest rate of photons emitted in the H-polarised mode is get when $\theta = \pi/4$ while it is null for $\Delta_{\text{FSS}} \to 0$ or if $\theta = 0$. As plotted in figure 2.28b, the exponential decay of the lifetime also shows oscillations due to the phase dependence of the frequency components $|X\rangle$ and $|Y\rangle$ at the rate $\Delta_{\text{FSS}}/2$. This behavior is a typical signature of the exciton emission. In this collection configuration, at least half of the photons are emitted in the same linear polarisation as the excitation laser and are not collected. Experimentally, considering the FSS, the angle between the QD dipoles and the cavity axes, and the relative emission and polarisation rotation rate, Olliviers and coworkers measured a polarised first lens brightness around 16% on half a dozen of exciton based sources [99], while $\mathcal{B}_{\text{FL}} \approx 62\%$.

Measuring the lifetime and observing these coherent oscillations with ultrafast detectors is one technique used to evidence whether the state under study is an exciton or a trion. Another method is to measure the polarisation dependence of the collected emission spectrum. The optical selection rule of an excitonic state leads to a change in the collection efficiency by changing the direction of the linear polarisation of the excitation laser. Figure 2.29a presents the polarisation directions of cavity axes (V and H), exciton axes (X and Y), and polarisation of the excitation and collection (resp. V_{exc} and H_{coll}). The half waveplate rotates the linear polarisation of the excitation laser so that we note ϕ the angle between the excitation/collection polarisation direction and the cavity axes. Figure 2.29b shows the signal collected for two excitation laser polarisation angles ϕ. When the polarisation of the excitation is parallel to one of the cavity axes ($\phi = 0$), the incident laser does not experience the cavity birefringence and only single photons from the QD are collected. For ϕ = 114° and all other angles ϕ, a spectrally broad signal (blue part) appears, corresponding to the light rotated by the cavity birefringence. Therefore, figure 2.29c represents the evolution of the intensity from both the cavity rotated light and the exciton as a function of this angle. As previously discussed, the cavity rotated light is maximised when the excitation and the collection have diagonal polarisations with respect to the cavity axes H and V. The QD exciton emission also show

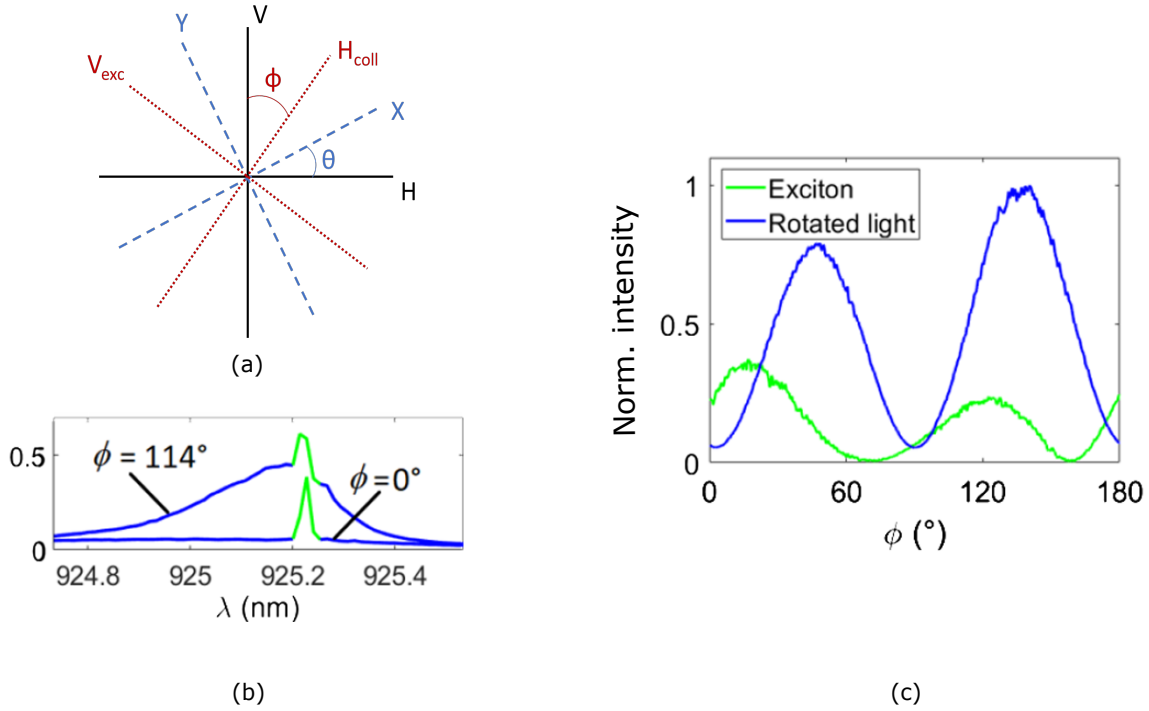

Figure 2.29: (a) Polarisation directions: cavity axes V and H, exciton axes X and Y, and polarisation of the excitation and collection, V_{exc} and H_{coll}, respectively. (b) Collected signal at two different angle ϕ of the half waveplate. It controls the direction of the excitation polarisation. At $\phi = 0°$, the excitation is parallel to one of the cavity axes and, only the single photons from the QD are collected (in green). At 114°, there is also the cavity rotated light (in blue). (c) Normalized intensity from the cavity rotated light (blue line) and from the exciton (green line) as a function of the angle of the half waveplate above the cryostat.

oscillations, corresponding to the angle between the laser polarisation and the exciton polarisation axes X and Y according to equation (2.37). These oscillations are the signature of an exciton.

2.6.3.4 Resonant fluorescence of a trion

We now consider the coherent control of a trion state corresponding to a charged exciton where an extra hole (positive trion) or electron (negative trion) is trapped before and during the excitation/emission process. Contrary to a neutral exciton, under linearly-polarised excitation and in the absence of in-plane magnetic field, the trion does not have polarised optical selection rules.

Considering a positive trion, the ground state is composed by two degenerates energy levels associated to spin holes $|\Uparrow_z\rangle$ and $|\Downarrow_z\rangle$. The optical selection rules can be written in the circular polarisation basis, but for the sake of simplicity, we write them in the H and V polarisation basis of the cavity modes, with (H, V, z) a direct orthonormal basis (figure 2.30a). In this condition we can write [187]:

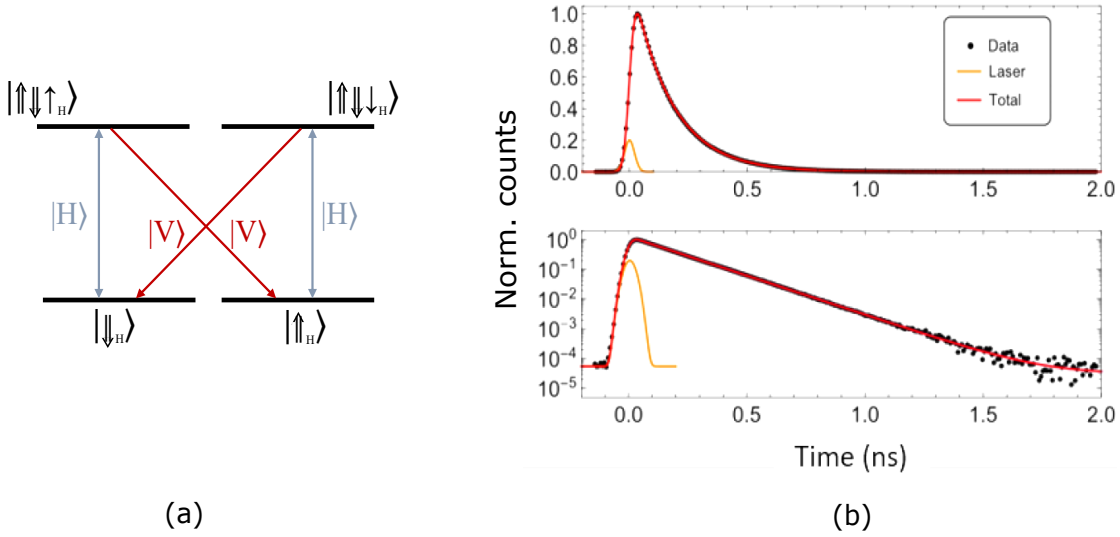

Figure 2.30: (a) Energy level structure of a positive charged quantum dot, with two ground states $|\Downarrow_H\rangle$ and $|\Uparrow_H\rangle$ and two exciton eigenstates $|\Uparrow\Downarrow\downarrow_H\rangle$ and $|\Uparrow\Downarrow\uparrow_H\rangle$. The resonant excitation process results in an excitation along $|H\rangle$ and a photons collection along $|V\rangle$. Since there is no polarization selection, almost 50% of the photons are emitted along the V-polarization (b) Lifetime of a positive trion state. With the log-scale, we can see the linear decrease of the emission probability over the time.

$$\begin{cases} |\Uparrow_H\rangle = \frac{1}{\sqrt{2}}(|\Uparrow_z\rangle + |\Downarrow_z\rangle) \\ |\Downarrow_H\rangle = \frac{1}{\sqrt{2}}(|\Uparrow_z\rangle - |\Downarrow_z\rangle) \end{cases}$$

The H-polarisation ties respectively the ground states $|\Uparrow_H\rangle$ and $|\Downarrow_H\rangle$ to the excited states $|\Uparrow\Downarrow\uparrow_H\rangle$ and $|\Uparrow\Downarrow\downarrow_H\rangle$, while the V-polarisation ties respectively the ground states $|\Uparrow_H\rangle$ and $|\Downarrow_H\rangle$ to the excited states $|\Uparrow\Downarrow\downarrow_H\rangle$ and $|\Uparrow\Downarrow\uparrow_H\rangle$. In this condition, if the laser is H-polarised, and if the spin state is in a statistical mixture of both spin up and spin down, both spin states are excited and a signal is always observed in the V-polarized collection. However, only half of the photons are emitted in the V-polarized collection so that the polarised first lens brightness is around the half of the first lens brightness. Another difference from the exciton is pointed out by the lifetime plot of figure 2.30b. Since the emission takes place in both polarization H and V, the emission is not delayed from the onset of the laser pulse (orange line) and the decay follows only the exponential decay without beatings.

As for the exciton, we look at the emission spectra collected in crossed polarisation for various excitation polarization angles ϕ. Figure 2.31a shows the collected spectra for two excitation half-waveplate angles. The QD emission is in magenta while the cavity rotated light is in blue. Figure 2.31b represents the evolution of these signals as a function of the half waveplate angle. As previously, the intensities are normalised by the cavity rotated light maximum. Due to the optical selection rules of the four trions transitions, the QD trion emission is independent of the polarisation angle of the excitation. The collected intensity remains constant while the cavity rotated light intensity oscillates as before.

These methods allow to identify the state in resonance with the cavity as a trion. But experimentally, in the sample structure under study, this state is usually obtained and stabilised

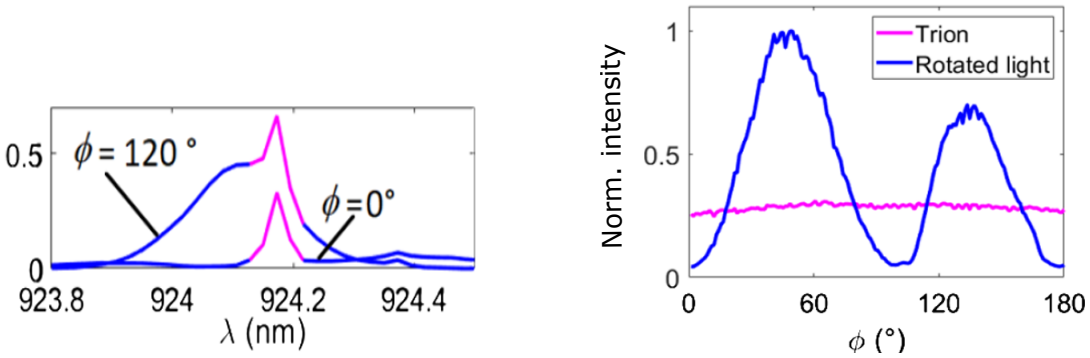

(a) (b)

Figure 2.31: (a) Collected signal at two different angles of the half waveplate. At 0°, only the single photons are collected (in magenta) while at 120°, there is also the cavity rotated light (in blue). (b) Normalized intensity from the cavity rotated light (blue line) and from the positive trion (magenta line) as a function of the angle of the half waveplate above the cryostat.

optically with the introduction of a hole in the QD.

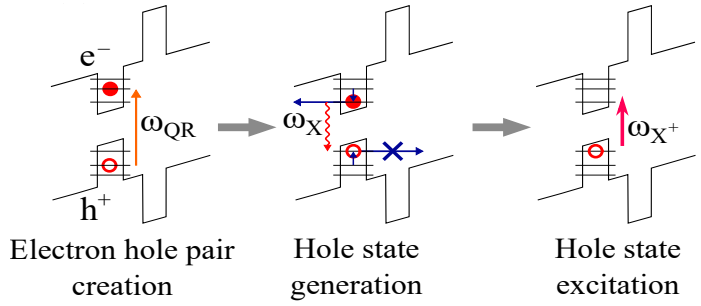

Figure 2.32: Schematic of the hole trap in the pillar structure and of the way to create and excite a positive trion state. The principle is proposed by Hilaire et al. in reference [188]

The method adopted here, and illustrated in figure 2.32, was described by Hilaire et al. [188]. It is based on a band design relying on an asymmetric tunnelling barrier. To obtain a positive trion, a non-resonant laser is used to create a first electron-hole. It is usually a continuous-wave laser with an energy close to the p-shell transition energy. After this excitation, the valence band barrier traps the hole while the absence of barrier for the conduction band lets the electron free to leave the QD. Adding to the fact that the lifetime of a trapped electron is shorter than a trapped hole, the electron escapes, while the hole stays trapped for few microseconds after the excitation, which leads to an efficient negative trion resonant excitation.

2.7 Conclusion

Quantum applications require "on-demand" bright sources of single and indistinguishable photons. If several techniques have been developed over the last twenty years to meet the theoretical expectations, self-assembled QDs embedded in 3D-cavities seem to be the most promising sources. The group of Prof. P. Senellart developed and optimised a source based on self-assembled GaAs/InGaAs QDs deterministically embedded in micro-pillars. This enabled to reach a first lens brightness about 65%, a purity and an indistinguishably respectively as large as 99.72%$\pm$0.12% and 99.56%$\pm$0.45% [9] . Nevertheless, once emitted the single-photons have to be distinguished from the excitation laser and collected into a single-mode fibre to be used. We then introduce a "polarised first lens brightness" ($\mathcal{B}_{\mathrm{PFL}}$) which corresponds to the fraction of photons emitted in the collection polarisation under resonant excitation. To quantify the collection efficiency, we also define as the "fibred brightness" ($\mathcal{B}_{\mathrm{F}}$), the fraction of the usable collected photons after considering the optical losses of the collection system η_{loss} and the coupling efficiency into the single-mode fibre η_{coupl}:

$$\boxed{\mathcal{B}_{\mathrm{F}} = \mathcal{B}_{\mathrm{FL}}(\times r_{\mathrm{pol}}) \times \eta_{\mathrm{system}} \times \eta_{\mathrm{coupl}}} \tag{2.38}$$

The "r_{pol}" coefficient is only used under resonant excitation and traduces the "polarised first lens brightness".

The objective of this thesis was to improve this benchmark without deteriorating the photons purity and indistinguishability. To do so, we worked on the optical system (chap. 3), we investigated another excitation regime (chap. 4) and finally we developed techniques to directly place the single-mode fibre above the micro-pillar so as to obtain a fiber-pigtailed single photon source ready to be inserted in standard cryostats (chap. 5).

Chapter 3

Efficient and stable single photons collection under resonant fluorescence excitation

"Ralliez-vous à mon panache blanc, vous le trouverez sur le chemin de la victoire"

attribuée à Henri IV

3.1 Introduction

The single photon sources based on semiconductor QDs discussed in this work have a high intrinsic brightness. Nevertheless, the optical system used to excite the system and collect the emitted single photons presents many sources of losses: optical components' absorption, coupling efficiency in a single mode optical fibre, instability, ... Thus, the final count rate measured in the collection fibre, i.e. "fibred brightness", is much lower than the "first lens brightness". However, many applications, such as quantum computing [7, 18, 189] or secure long-distance quantum communication [29], require a near-unity brightness. Moreover, since such experiments can require hours or even days of constant data acquisition, the device and optical system must guarantee, at the same time, efficiency and stability.

In this chapter, we will discuss the development of an optimised design of a stable confocal microscope for the resonant-excitation regime. Since under this excitation scheme, the excitation laser and the emitted signal have identical wavelength, a practical way to separate both in independent optical path is required. If the dark-field confocal method is well known in biomedical microscopy field [190, 191], it is already and usually used to carry out resonant fluorescence experiments based on QDs as single photons emitters. We can cite studies on interactions between single photons emitters and their environment [192] or in optical cavity [193]. Like in other work on self-assembled semiconductor QDs under resonance fluorescence [46, 194–196], we use a cross-polarisation configuration to ensure the filtering of the excitation laser and allow for high collection efficiency of the emitted single photons. A first version of such optical system was developed four years ago and is still used in the academic

group to study the physics of self-assembled QDs embedded in pillars [9, 99] and their applications [197, 198]. Due to the optical components and its design, the microscope presents losses, and limited collection efficiency and stability. The aim of this work was to develop a novel system with improved transmission and stability, and ease of use for non-expert users.

To increase the collection efficiency, we worked on the theory of the coupling efficiency. The first part will describe the theoretical study and the experimental results we obtained with fixed focus collimators. It will then broach the need of mode matching with the use of variable focus collimators.

To increase the laser rejection rate and therefore single-photon purity, we studied the different sources of depolarisation. The second part will present the changes in the system architecture to obtain an efficient dark-field confocal microscope.

Finally, the third part will describe in detail the new design which enables to reach a stability over days and obtain a more "user-friendly" system while in the fourth part, we will detail its application for single photon sources characterisation and use.

3.2 Coupling efficiency

Beam collimation and fibre coupling efficiencies are essential in the building of fibred optical systems. To do so, collimators are usually used. This optical component is theoretically a perfect solution to collimate a beam from a fibre and conversely to couple a beam into a fibre. In practice, certain parameters must be precisely controlled to approach the best performances. This study aims to model the influence, on the coupling efficiency, of the distance between two lenses and of the mode matching of optical modes. Once the theoretical model is established, part 3.2.2. will consider the coupling efficiency between two collimators facing each other, while part 3.2.3 will be about coupling efficiency and mode matching between a collimator and a pillar. The goal is, in any of the cases, to maximise the collection efficiency of emitted single photons.

3.2.1 Simulations

3.2.1.1 Calculation principle

The simulated optical system is described in figure 3.1. It is composed of two optical fibres placed at the focal point of two lenses separated by a variable distance, D.

The simulations describe the evolution of a beam coming out from a single-mode optical fibre or from a pillar. The aim is then to model the mode coupling between the latter, after its propagation, and the beam at the input of the fibre 2. To do so, beams are treated in the Gaussian beam approximation. Due to the difference between the refraction indices of the GaAs ($n \approx 3.5$) and the air, their diameters ($> 1.6\mu$m) or their high quality factor ($Q > 5000$), pillars can be considered as waveguides whose fundamental mode is Gaussian [199, 200]. Concerning the beam at the output of single-mode optical fibres, it is also possible to make

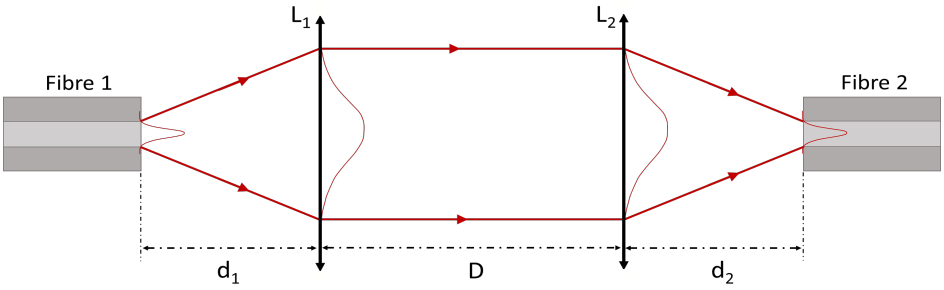

Figure 3.1: Schematic of the simulated optical system. It is composed of two fibres (1 and 2) separated from two lenses (L_1 and L_2) by respectively the distances $d_1 = f_1$ and $d_2 = f_2$. The two lenses are separated by the distance D.

the same approximation. The study of the electromagnetic field outside such fibres and their *normalised frequency* [201] validate it. This frequency, represented by "V", is a dimensionless parameter which characterises the number of modes in index-jumping fibres following the equation $M = \frac{V-2}{2}$. Since we work with single-mode fibres ($V \leqslant 2.405$) and pillars, the two simulations are established from theories of the propagation of Gaussian beams [202] and from Fourier optics [203] beyond the paraxial approximation [204].

The propagation, outlined in figure 3.1, can be mathematically summarised following the steps of figure 3.2. To simulate it, two models have been considered. The first one is based on an numerical model using Fourier transforms while the second one enables to calculate analytically each Gaussian profile during its propagation.

Both simulations start with an initial scalar Gaussian profile defined as follows:

$$G_0(x,y) = I \exp\left[-\frac{(x^2+y^2)}{{w_0}^2}\right] \tag{3.1}$$

In the case of a **fibre output**, we have,

$$w_0 = r_{FO}\left(0.65 + \frac{1.619}{V^{1.5}} + \frac{2.879}{V^6}\right) \text{ [205] and } V = \frac{\pi r_{FO} NA}{\lambda}$$

with w_0, Gaussian profile waist defined as the radius at $\frac{I_{max}}{e^2}$, V, the normalised frequency ($V \leqslant 2.4048$, for a single-mode fibre), λ, the working wavelength, r_{FO}, the core radius of the optical fibre and NA, the numerical aperture of the optical fibre.

Concerning the **output of a pillar**, the waist is estimated from the formalism of the reference [199] and used in the thesis [200]. The simulation method remains the same but before part 3.2.3, we will only consider the propagation of beams from single-mode fibres.

The propagation over a distance d is simulated by multiplying, in the Fourier space, the Gaussian profile to the transfer function of the vacuum:

$$H_d(\nu_x,\nu_y) = \exp\left[-ikd\right] \exp\left[i\pi\lambda d\left({\nu_x}^2 + {\nu_y}^2\right)\right]$$

$$\text{with } \begin{cases} k = \sqrt{{k_x}^2 + {k_y}^2 + {k_z}^2} = \frac{2\pi}{\lambda} \\ \nu_x = \frac{k_x}{2\pi},\ \nu_y = \frac{k_y}{2\pi} \end{cases}$$

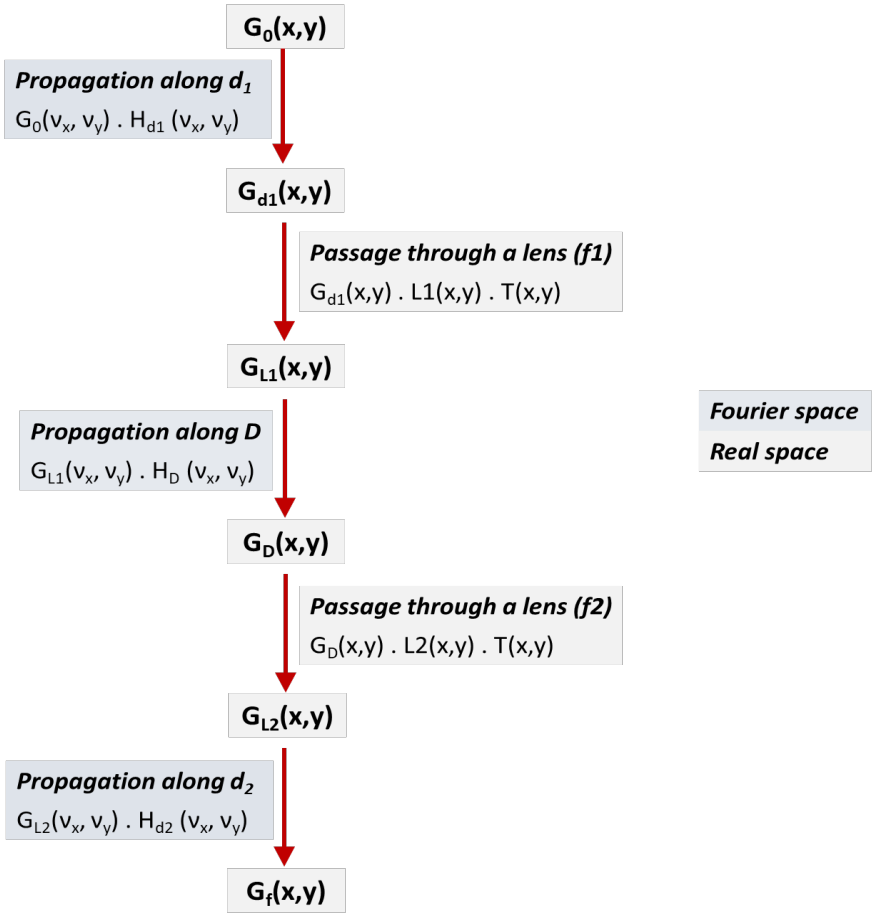

Figure 3.2: Mathematical translation of the figure 3.1 schematic. Each arrow corresponds to an action such as a propagation along a certain distance or the passage through a lens. The calculation in the Fourier space are written in the dark grey rectangle on the left while the rest corresponds to calculations and Gaussian profiles in the real space.

The passage through a lens is calculated in the real space. To model it, the Gaussian beam is multiplied by a phase term $L(x,y)$ representing the lens effect and a circular mask $T(x,y)$ corresponding to its finite diameter. These transfer functions are written as follows:

$$L(x,y) = \exp\left[\frac{i\pi}{\lambda f}(x^2+y^2)\right], \qquad T(x,y) = \begin{cases} 1, & \text{inside} \\ 0, & \text{otherwise.} \end{cases}$$

Considering the first simulation, it is implemented with a software in which each Gaussian mode is defined in two dimensions by a matrix. It will be called *"numerical model"* in the rest of this work. If this approach allows for a control of each propagation stage, numerical edge effects are introduced by the software at each Fourier transformation. Moreover, due to the 4° angle of divergence at the fibre output, there are scaling issues. The beam, which has an initial diameter of few micrometres, has a diameter of few millimetres after the propagation d_1. Fixing these issues is computationally demanding and requires hours of calculations. For this reason several simplifications were considered.

Supposing that all beams remain Gaussian during the propagation [204], it is also possible to calculate them analytically. In this second model, called *"analytical model"*, each propagation stage separating the two optical fibres, can be described by an analytical equation. For instance, equation (6.4) (in Appendix 1) enables to calculate the Gaussian 2D-profile after the lens 1 without the need of numerically propagate it. A complete list of the equations can be found in Appendix 1.

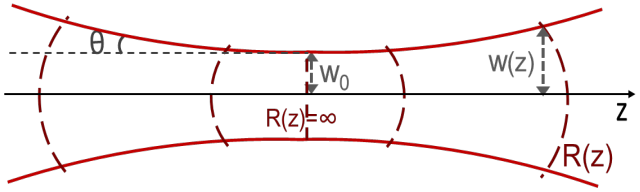

Figure 3.3: Schematic of a Gaussian beam propagation. We make the distinction between the beam radius where $R(0) = \infty$, w_0, and the radius evolution along "z", $w(z)$. Both correspond to the radius at $\frac{1}{e^2}$ of the maximum intensity. The Gaussian beam always diverges following a semi-angle θ.

In the following we will consider two kinds of waist: w_0 and $w(z)$. Both are defined as the beam radius at $\frac{1}{e^2}$ of the maximum intensity. We call w_0 the beam radius where the wavefront radius of curvature is R(0) = ∞. On the contrary, the evolution of the radius along "z" is described by $w(z)$ (figure 3.3). For these successive "z"-positions, the wavefront curvature radius has a finite value, creating the divergence of the Gaussian beam which is ruled by the semi-angle of divergence θ. The waist $w(z)$ can be directly obtained from each equations of the *"analytical model"* since Gaussian profiles can be written as follows:

$$G(x,y) = I \exp\left[-ikd\right] \exp\left[-\left(\frac{1}{w(z)^2} + \frac{ik}{2R(z)}\right)\right]$$

Thus, for each stage and for each equation of this model, the real part of the exponential corresponds to the waist (profile radius at $\frac{1}{e^2}$ of the maximum intensity) and the imaginary part to the curvature radius of the beam. Nevertheless, this model only considers infinite diameter lenses, not taking into account their real diameters and the diffraction effects that may result from it. Since in practice such effects need to be neglected, the next part will provide the condition on the beam diameter, with respect to the lens', so to overcome them.

To calculate the mode coupling, two equations can be used. The first one enables to estimate its evolution according to the chosen beam propagation's parameters. It corresponds to a scalar product between the incoming mode, G_i, and the target mode , G_t, considered as Gaussian [206]:

$$\boxed{C = \frac{\left|\iint (G_i\, G_t{}^*)\, dx\, dy\right|^2}{\left|\sqrt{\iint (G_i\, G_i{}^*)\, dx\, dy}\sqrt{\iint (G_t\, G_t{}^*)\, dx\, dy}\right|^2}} \tag{3.2}$$

For instance, in figure 3.1, the incoming beam is the one which propagates from the fibre 1, while the target mode is the one of fibre 2. Since it involves two Gaussian 2D-profiles, this equation can be used in both *numerical* and *analytical* simulations.

With the *analytical* model, it is also possible to directly calculate the maximum of coupling efficiency. To do so, we only consider the waists of the two Gaussian profiles (initial and target) at the position where $R_i = R_t = \infty$ (resp. w_{0i} and w_{0t}) [205, 207]:

$$C_{max} = \left(\frac{2 w_{0i} w_{0t}}{{w_{0i}}^2 + {w_{0t}}^2} \right)^2 \exp \left[- \frac{2u^2}{{w_{0i}}^2 + {w_{0t}}^2} \right] \tag{3.3}$$

with, w_{0i}, the waist of the beam (infinite radius of curvature) of the incoming beam after the desired propagation, w_{0t}, the waist of the target beam (infinite radius of curvature), and u, the lateral misalignment between the two waists.

3.2.1.2 Determination of the lens diameters

Choosing the proper lens diameters requires to use both models. For instance, let us consider the case presented in figure 3.4a. A Gaussian beam exits a fibre and propagates along a distance d_1 before passing through a thin lens (f_1), at λ = 930nm. The *analytical model* calculates the Gaussian 2D-profile after the infinite diameter lens with equation (6.4) (Annex 1), while the numerical model is used for diffraction through its diameter ($T(x, y)$). To estimate the diffraction issues, the coupling efficiency between the profile through an infinite diameter (*analytical model*) and the one through a finite-sized lens (combination of the two models) is calculated with *numerical* equation (3.2).

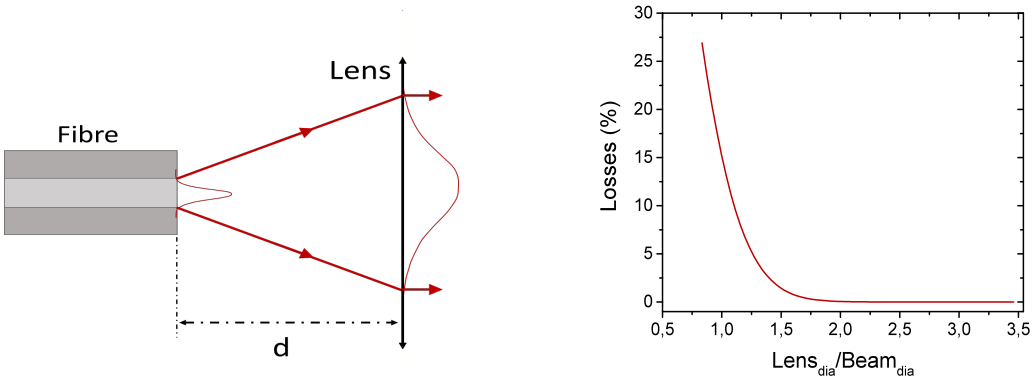

(a) (b)

Figure 3.4: (a) Schematic of the modeled propagation. (b) Losses, due to the lens finite diameter, as a function of the ratio between the lens diameter and the beam diameter.

Figure 3.4b shows the mode mismatch as a function of the ratio between the lens and the beam diameters. With this study, we can conclude that we can use the *analytical model* alone if the beam has a diameter at least two and a half times smaller than the lens. Diffractions due to lens aperture are then less than 1% and are considered as negligible.

3.2.2 Application with two collimators in front of each other

3.2.2.1 Theoretical model

When the output of an optical fibre is placed at the focal point of a lens, the Gaussian beam exits collimated. However, in practice, a collimated Gaussian beam is slightly divergent: the half angle of divergence follows $\theta \leqslant \frac{\lambda}{\pi w_0}$.

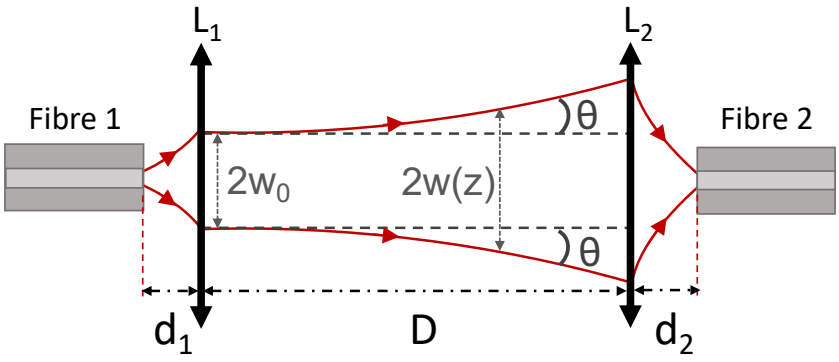

Figure 3.5: Schematic of a Gaussian beam propagation. It is composed of two fibres (1 and 2) separated from two lenses (L_1 and L_2) by respectively the distances d_1 and d_2. The two lenses are separated by the distance D. A "collimated" Gaussian beam always diverges following a semi-angle θ .

Even though we use two identical collimators and fibres ($d_1 = d_2 = f_1 = f_2$), by increasing the distance D, the second lens receives a larger beam with a higher curvature radius (figure 3.5).

Figure 3.6a presents the waist ($w(z)$) evolution after the second lens as a function of the distance D separating the two lenses (at 930nm). The lens focal plane is indicated by the "0"-graduation on the figure horizontal axis. We can notice that at this position ($d_2 = f_2 = 12mm$), waists $w(z)$ are always equal to $2.8\mu m$. But due to the increase of the distance D, the latter does not correspond to the position of $w(z) = w_0$ (where $R = \infty$). Since the incoming beam diameter and radius of curvature are larger when the distance D becomes longer, the beam converges after the lens focal point and so after the fibre 2 input. Following the *analytical* coupling equation (3.3), the coupling between the mode from fibre 1 and the one of the fibre 2 is maximum only when the mode matching is done both at their waist w_0 positions ($R = \infty$). Since, it is no longer the case with the distance D, the coupling efficiency is affected. Figure 3.6b presents the theoretical coupling efficiency (*numerical* equ. (3.2)) between two collimators separated by a variable distance D. Six curves are plotted for six different values of lens focal length. In each case, the collimators are the same and $f_1 = f_2 = d_1 = d_2$. We can notice that in all cases the coupling efficiency is degraded after a certain distance D due to the natural divergence of a collimated Gaussian beam. Nevertheless, the efficiency decreasing depends on the lens focal length. For lengths below 8mm, the beam, collimated by the first collimator, has a small diameter. Since the natural divergence angle is inversely proportional to the waist, the beam diverges rapidly. There is then a strong effect of the distance D as the coupling efficiency decreases fast: from D > 2.5m, it is lower than 80%. Considering longer focal lengths, the beam divergence is less pronounced, which allows for

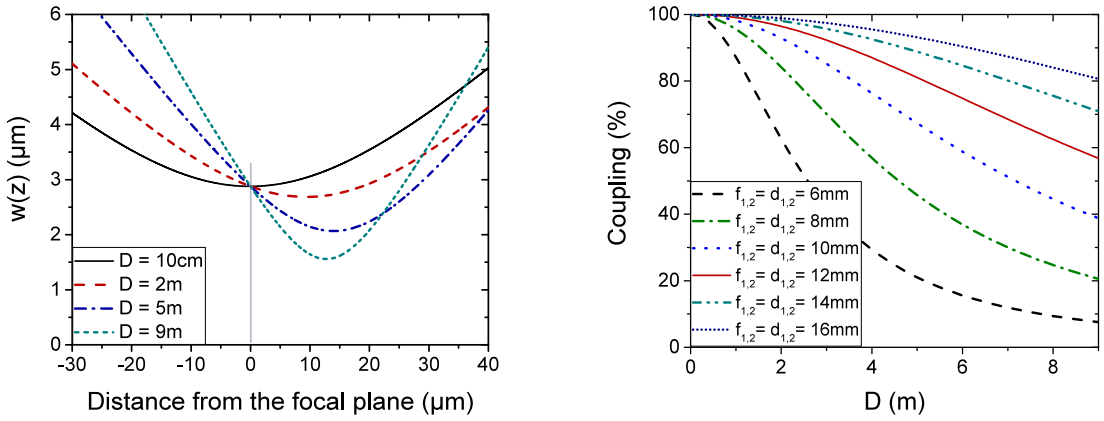

(a) (b)

Figure 3.6: (a) Waist $w(z)$ evolution as a function of the distance d_2 after the lens of the second collimator. Each line represents a different distance D separating the two collimators. The horizontal axis is calibrated from the lens focal plane position (indicated by the "0"-graduation). In this figure, the simulation considers $f_1 = f_2 = d_1 = d_2$ = 12mm, and $w_{0,\,\text{fibre1}} = w_{0,\,\text{fibre2}} = 2.8\mu m$. (b) Coupling efficiency as a function of the distance D separating the two collimators. Each lines corresponds to a different focal length of the lenses. For this figure, f_1 and f_2 are equal but have different values from 6mm to 16mm and $w_{0,\,\text{fibre1}} = w_{0,\,\text{fibre2}} = 2.8\mu m$.

higher tolerances on the distance D. In this case the coupling efficiency is then almost equal to 100% for D = [0 ; 1]m and lower than 80% for D = 4m in the worst case, f = 10mm.

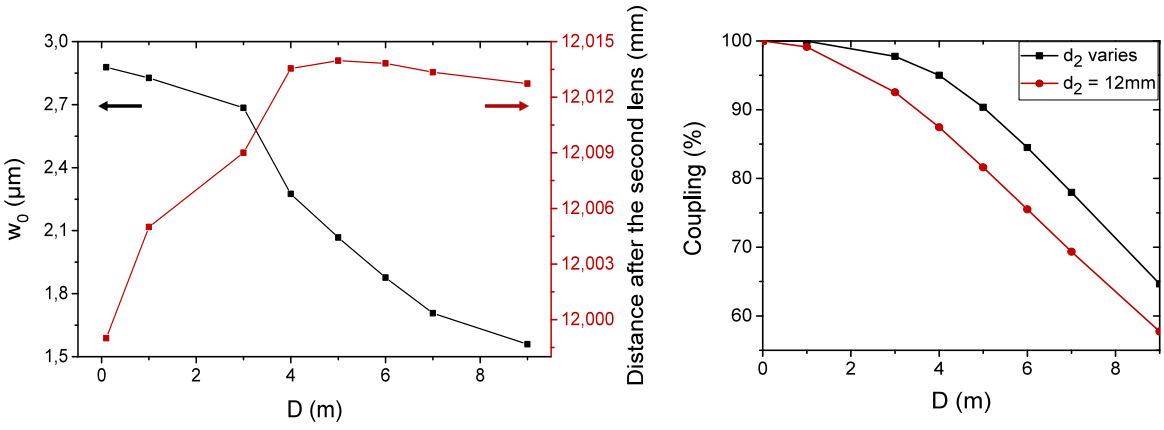

(a) (b)

Figure 3.7: (a) Waist w_0 size, after the lens of the second collimator, as a function of the distance D separating the two collimators (black line). The red line represents the distance between the second lens and the waist w_0 position. (b) Coupling efficiency as a function of the distance D separating the two collimators. For the red line (circles) $f_1 = f_2 = d_1$ = 12mm, this corresponds to the straight red line of figure 3.6b. To obtain the black line (squares), d_2 varies to match the "fibre output position" to the w_0 position (figure 3.7b, black line).

As shown in figure 3.7a, increasing the distance D also reduces the diameter of the beam waist, $w_{0\mathrm{i}}$. If the fibre 2 is placed at the position of the incoming beam waist, $w_{0\mathrm{i}}$, it receives a beam which does not match its own mode, $w_{0\mathrm{t}}$, affecting the coupling efficiency. In figure 3.7b, the system is built in a such way that, by varying the distance d_2, the fibre 2 input can be always placed at the incident beam waist, $w_{0\mathrm{i}}$. Since we know its position for each distance D (figure 3.7a), the coupling efficiency has been calculated via the *analytical* equation (3.3) by setting the distance d_2 so that the beam waist $w_{0\mathrm{i}}$ and the input of the fibre 2 are at the same position. Figure 3.7b presents the comparison between this coupling efficiency (black line-circles) and the one obtained for $d_2 = f_2 = 12mm$ (red line-squares), from figure 3.6a). Varying the distance d_2 then allows for a higher coupling. Nevertheless, due to a mismatch between the mode of the incident beam and the one of fibre 2, the coupling efficiency decreases quickly already after 3m.

We also must keep in mind that these results are upper bounds for each coupling efficiency because in practice, other parameters such as the precision of fibre position and aberrations, degrade the beam during its propagation. Since in our experimental setup we are bound to work with optical components having such parameters ($w_{0,\,\mathrm{fibre1}}$ = 2.8μm, f < 12mm), the entire optical system must be as compact as possible in order to maintain high coupling efficiencies.

3.2.2.2 Experimental validation

To validate the theoretical expectations and find adequate collimators for efficient optical systems, we studied different types of off-the-shelf collimators (by Thorlabs), whose available working wavelength is 980nm. In this part, we will present the results of the characterisation with two different types of fixed focus collimators:

- The first type is composed of an **aspheric lens** with a focal length of 12mm (Asph_{980}). The fibre is fixed so that its output is at the lens's focus point for a working wavelength of 980nm.
- The second collimator type is called **"fixed focus triplet collimator"** ("triplet" collimators). To optimise the correction of the spherical and cylindrical aberrations, it is composed of an optical system of three lenses. The fibre is screwed at its effective focus point. Some of them have a focal length of 6mm, they are aligned for the standard working wavelength of 980nm and they are studied at 980nm (T_{980} @980nm) and 930nm (T_{930} @930nm). The others have a focal length of 12mm, and a custom working wavelength: they are aligned and used at 930nm (T_{930} @930nm).

Since in the optimised optical system, the distance D between the collimators and the single photon source remain below 30cm, the coupling efficiency is evaluated in this distance range. The coupling is defined as the ratio between the power measured at the output of the fibre of the second collimator, $P_{\text{fibre output}}$, and the one measured in free-space just before the second collimator, $P_{\text{free-space}}$. The ratio is corrected by the system losses due to the collimator and the fibre adaptor of the power-meter (around 2%). We also consider the reflections at the fibre output (around 4%) in case of a non-coated PC-fibre. We can then write this "coupling" as:

$$C_{\text{exp}} = \frac{P_{\text{fibre output}}}{P_{\text{free-space}} \times Losses}$$

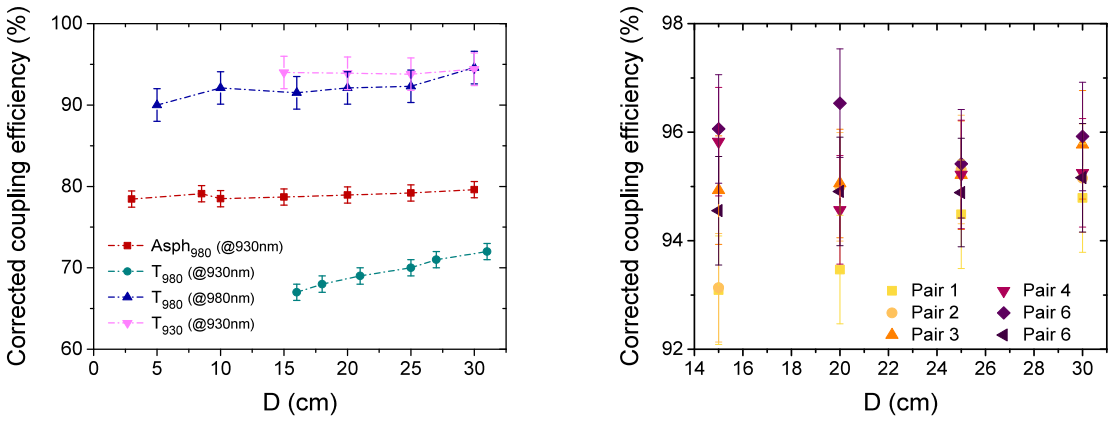

(a) (b)

Figure 3.8: Measured coupling efficiency (at 930nm or 980nm) as a function of the distance D separating two collimators. The values are corrected by the system losses evaluated around 6%. (a) Each curve corresponds to a different collimator type or a different working wavelength. The green line (squares) represents the coupling efficiency, at 930nm, between aspheric collimators aligned at 980nm. Referring to different triplet collimators aligned at 980nm, the red line (circles) corresponds to the coupling efficiency at 930nm while the blue line (up-triangles) at 980nm. Finally, the pink line (down-triangles) represents the coupling efficiency, at 930nm, between two custom triplet collimators aligned at 930nm. (b) Each point represents the coupling efficiency (only at 930nm) between pairs of four different triplet T_{930}.

Figure 3.8a presents the measured coupling efficiency of several pairs of "identical" collimators as a function of their separation. The green line (Asph_{980} (@930nm)) corresponds to two collimators composed of one aspheric lens, aligned at 980nm and coupled at 930nm. This difference in wavelength clearly affects the final performance, causing spherical aberrations and hence limiting the coupling efficiency to a value below 80%. Lines red (T_{980} (@930nm)), blue (T_{980} (@980nm)), and pink (T_{930} (@930nm)) have been obtained with "triplet" collimators, which were aligned and tested for two different wavelengths (980nm and 930nm). According to the data-sheet, these collimators reduce the spherical aberrations and increases the coupling efficiency. "Triplet" collimators, proposed by Thorlabs, and aligned at 980nm provide a coupling efficiency around 92% when tested at 980 nm (T_{980} (@980nm)). However, their use at 930nm limits the coupling efficiency well below 75% (T_{980} (@930nm)). A possible explanation for this strong difference can be due to the structure of the system: combining three lenses to optimise spherical aberrations makes the system more sensitive to chromaticity. Considering a system without space between the lenses, the effective focal length can be expressed as $1/f = 1/f_1 + 1/f_2 + 1/f_3$. Working at a different wavelength affects each lens, increasing the chromatic aberrations. Another explanation could be that for aspheric collimators, aspheric and chromatic aberrations compensate each other enabling better coupling efficiency at 930nm. In any case, working with custom triplet collimators aligned at 930nm enables us to obtain a coupling efficiency above 95% at 930nm (T_{930} (@930nm)). By combining four different custom triplet collimators (f=12cm), we could test six different combinations and measure the coupling efficiency by varying the distance D, at 930nm. As observed in figure 3.8b, we

could then obtain a coupling efficiency above 93% for all cases, showing the reproducibility of the approach.

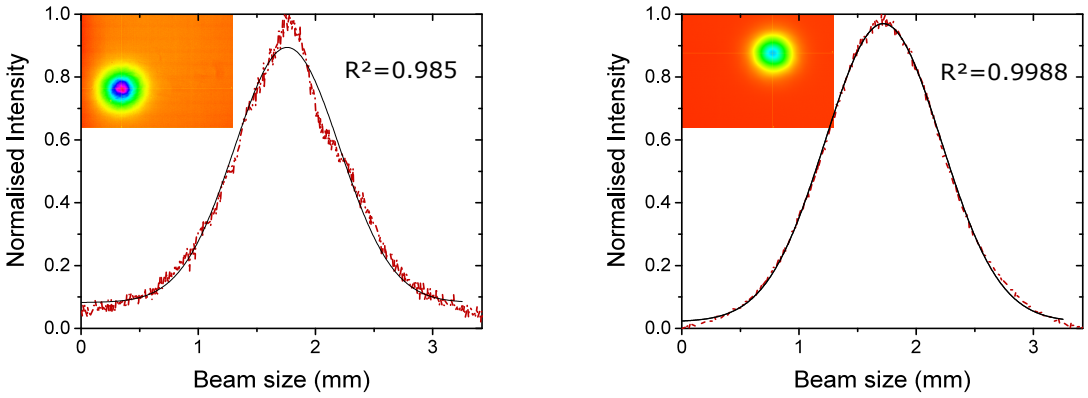

(a) (b)

Figure 3.9: (a) Gaussian profile from an aspheric collimator (f=12mm, aligned at 980nm). (b) Gaussian profile from a custom triplet collimator (f=12mm, aligned at 930nm).

The difference between the theoretical result of 100% and the experimental one can be explain by a non-perfect Gaussian beam at the collimator output ($M^2 > 1$) and a non-perfect beam collimation. Experimentally, we imaged the beam profiles from both aspheric and triplet collimators with a CMOS camera, whose 2D-profiles are presented in figure 3.9 insets. We notice that the beam from an aspheric collimator is less Gaussian ($R^2 = 0.985$) than the one from a "triplet collimator" ($R^2 = 0.9988$). Moreover, experimentally, by plugging and unplugging the fibre from an aspheric collimator, the beam waist of about 1mm, varies each time of about $\pm 4\mu$m, while the same process causes a variation of about $\pm 0.8\mu$m for a "triplet collimator". This size variation is due to a change in the distance between the fibre output and the lens. Following the results of figures 3.6a and 3.6b (f = 12mm), a difference of less than $20\mu m$ between the lens focal plane and the fibre output is enough to significantly decrease the coupling efficiency from 100% to 65%. So, the difference in coupling may also come from a variation in distance between the fibre output and the lens when we unplug and plug the fibre.

3.2.3 Optimisation of the coupling with the fundamental mode of a pillar

3.2.3.1 Replacement of the microscope objective

In the confocal microscope configuration, a lens is positioned just above the source device to both focus the collimated beam exiting a collimator and collimate the divergent emitted signal. Combining the fact that pillar sources have a numerical aperture (NA) around 0.35 with the need to avoid any diffraction issue, the optical component used to focus/collimate beams needs to have a numerical aperture of at least 0.65 (detailed in part 3.2.1.2).

Figure 3.10 presents the mode matching between the beam emitted by a connected pillar (black profiles) and the beam from the collection collimator (red profiles). Figure 3.10a refers to the collection through a microscope objective (Olympus LCPLN20XIR, NA = 0.4,

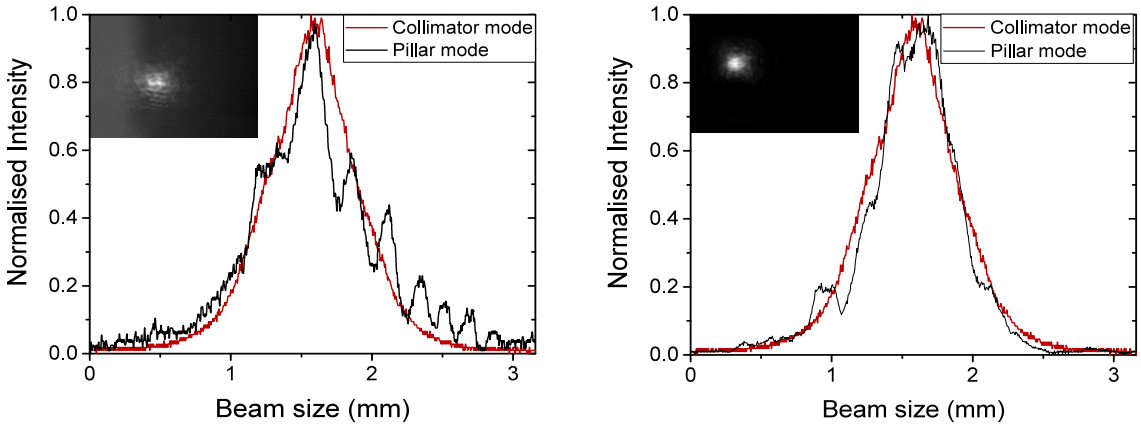

Figure 3.10: (a) Comparison between the Gaussian mode from a connected pillar after a microscope objective (NA = 0.4) (black profile) or (b) after an aspheric lens (NA = 0.65) (black profile), and the mode from a collimator with a zoom (red profiles).

WD = 8.18-8.93mm) while it is through an aspheric lens (Thorlabs C330TMD-B, NA = 0.68, f = 3.1mm) in figure 3.10b. Due to a low NA, the diffraction pattern seen in (a) leads to a reduction of the portion of collected light from the pillar and of the coupling efficiency in the collection collimator. Following the equation $Dia_{\text{syst}} = f_{\text{obj}} \times NA$ (with Dia_{syst} the diameter of the system), for a given Dia_{syst}, having a high numerical aperture leads to a decrease of the focal length of the optical system. Due to the need to optimise components transmission and the collection stability, we replaced a lossy microscope objective (T≈85%) by an aspheric lens, directly placed in the cryostat chamber and with >95% transmission. The latter, directly placed inside the cryostat chamber, allowed for an improved mode matching (figure 3.10b). Considering the 2D-profiles and the equation 3.2, we can approximate the microscope objective and aspheric lens coupling efficiencies to respectively 94% (figure 3.10a) and 98% (figure 3.10b). This remains an upper bound because we do not have access to the radius of curvature but the substitution improves the collection efficiency.

3.2.3.2 Mode size adaptation

We previously considered the coupling efficiency between two identical collimators. When working with a single photon source, we have to consider the coupling between the fundamental mode of a pillar and the mode of the collection fibre (figure 3.11a). So, beyond the collimator optimisation presented in the previous part, we need to consider a non-symmetric system whose high coupling efficiency is based on a high mode matching between them.

Considering the output of the pillar, the emitted beam is divergent in accordance with its numerical aperture. The latter depends on the pillar diameter. For instance, at 930nm, a pillar with a diameter of 2μm has a numerical aperture of 0.3 while for a diameter of 3μm, we have NA = 0.2 [199]. To ensure the best coupling efficiency, the beam from collimators must be focused on the pillar top and their diameters must match the beam size of the pillar mode. Since a change in the pillar diameter involves a change in the beam waist at its output, we need to adapt the beam size from the collimators to them. Considering our single photon

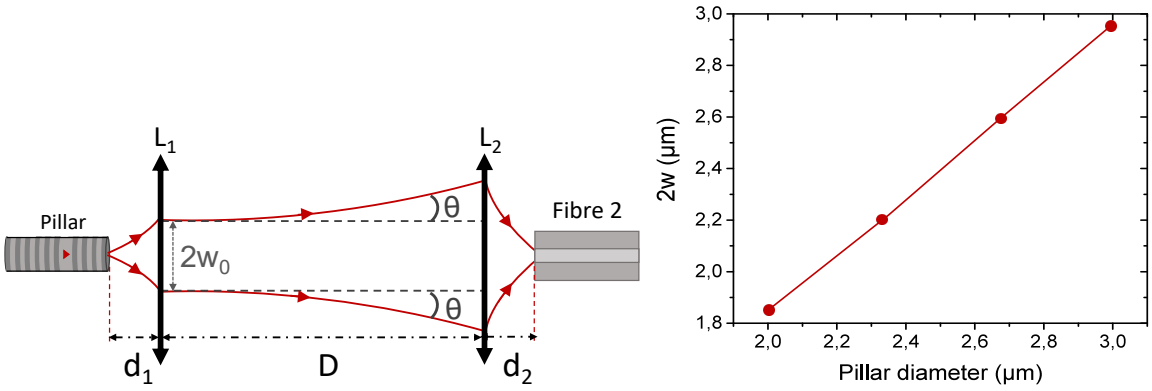

(a) (b)

Figure 3.11: (a) Schematic of the pillar coupling. The beam is collimated by the lens L_1 and coupling in the collection fibre via the lens L_2. (b) Theoretical prediction of the beam diameter at the output of a pillar as function of its diameter [199].

sources, figure 3.11b plots the theoretical prediction of the beam diameter at the pillar output ($2w_0$) as a function of its diameter [199]. Knowing this linear dependence enables to match the beam size of the collection to the one from the pillar.

In the previous optical system, both the collimator and the lens above the sample had fixed focal lengths. To ensure the mode matching, a telescope (namely a set of two lenses in an afocal configuration) is required. To obtain a beam diameter of few micrometres on the pillar, the ratio of the focal lengths of the telescope lenses are calculated as follows:

$$\frac{f_{t,1}}{f_{t,2}} = \frac{w_{0,\mathrm{FO}}}{w_{0,\mathrm{pillar}}} \frac{f_{\mathrm{obj}}}{f_{\mathrm{coll}}} \tag{3.4}$$

with $f_{t,1}$ (resp. $f_{t,2}$), the focal length of the telescope lens closer to the sample (closer to the collection collimator), f_{obj}, the focal length of the focusing optical component, f_{coll}, the collimator focal length, and $w_{0,\mathrm{FO}}$ (resp. $w_{0,\mathrm{pillar}}$), the waist at the fibre (pillar) output.

Since, the magnification is adapted to the pillar size, a good mode matching requires to find the right lenses pair for each different pillar size. For instance, considering f_{obj} = 15mm, f_{coll} = 11mm, $w_{0,\mathrm{FO}}$ = 2.8μm and $w_{0,\mathrm{pillar}}$ = 1.1μm, we get $f_{t,1} \approx 3\ f_{t,2}$.

This configuration is not optimal because is not always possible to find the correct lenses pair and also because of the need of constant realignment for each source. To make the optical system more compact and easier to use, we have combined the collimation process with the beam magnification requirement. Hence, we now use two collimators with a built-in zoom. Due to the ability of changing the effective focal length of the system, output beams can have diameters from 1mm (f_{coll} = 6mm) to 3mm (f_{coll} = 18mm). For each, the system is done in such way that the incident beam is always collimated. So, the excitation laser is well focused on the pillar and the "emitted" beam is also well coupled into the collection fibre.

In the case of our pillars, to set the right beam size from collimators, we measure the diameter of the cavity rotated light beam. As detailed in chapter 2 part 2.6.3.1, this beam corresponds to the light from the excitation laser which enters the pillar, gets a polarisation ellipticity and comes back out. Since it is not possible to image the single photon emission with a camera, we use the cavity rotated light to measure the size of the optical mode of the

pillar. Indeed, it possesses the same characteristics as the single-photon mode. To select this part of the light, a control on input and output polarisation is required and the incoming laser needs to be diagonally polarised with respect to the pillar axes.

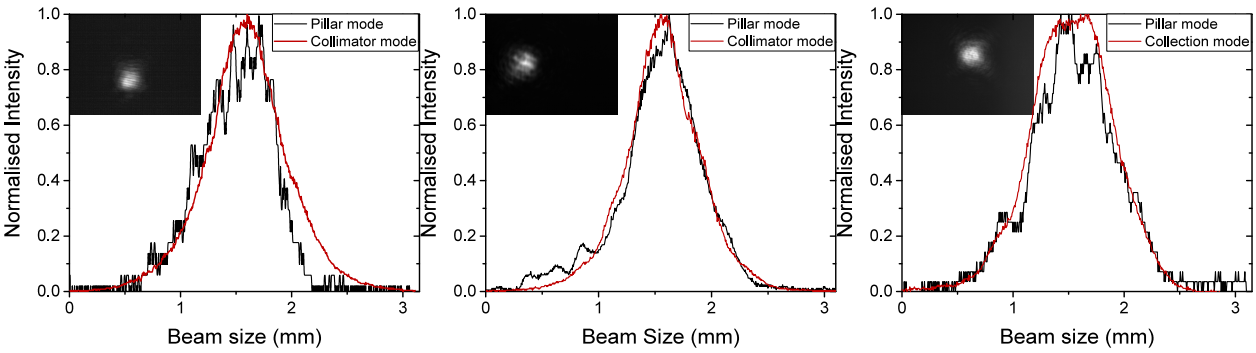

(a) (b) (c)

Figure 3.12: Adaptation of the collection collimator mode (red lines) to the cavity rotated light beam size (black lines). The focus lens is an aspheric lens with a focal length of 3.1mm and NA=0.65. (a) The cavity rotated light has a diameter of 1.4mm and the collimator mode is at 1.35mm (f_{coll} = 8mm in this case). The theoretical coupling efficiency is around 93%. (b) The cavity rotated light has a diameter of 1.2mm and the collimator mode is at 1.2mm as well (f_{coll} = 7mm in this case). The theoretical coupling efficiency is around 98.8%. (c) The cavity rotated light has a diameter of 1.45mm and the collimator mode is at 1.4mm as well ($f_{coll} \approx$ 8.5mm in this case). The theoretical coupling efficiency is around 96.4%.

This measurement is done with a camera placed in the collection path and a beam profiler software. Once done, we adjust the collimators rings to match the size keeping the beam collimated. Figure 3.12 shows the mode matching obtained with three different pillars from three different samples. The focusing lens in the cryostat is an aspheric lens with a focal length of 3.1mm and NA=0.65. For each pillar, the beam from the collimator has been adapted by changing its effective focal length. Using the equation 3.2, the expected coupling efficiency between the cavity rotated light and the beam profile from the collimator has been calculated. The results are respectively 93% (figure 3.12a), 98.8% (figure 3.12b) and 96.4% (figure 3.12c). Like previously, these indicate upper bounds, and the experimental coupling efficiency is about 70% $\pm$ 5%. This includes the components losses (about 9%) and all the coupling issues discussed in previous parts. Still, the measurement shows an improvement of about 27% compared to the previous case (55% $\pm$ 5%).

3.3 Polarisation selection and control

In resonant fluorescence experiment, fine control of polarisation is essential to collect efficiently only the single photons. To effectively filter the excitation laser, which has the same energy, we use the cross polarisation detection, whose efficiency is assessed by measuring the

extinction ratio. The latter is defined as the ratio between the maximum transmitted power in parallel-configuration and the minimum transmitted power in cross-configuration. As seen before, we choose to implement a confocal microscope based on a cross-polarisation arrangement to increase the coupling efficiency and amplify the laser rejection [208]. As discussed in following paragraphs, further optimisation of the focusing optical component [209] also permitted to increase laser extinction.

3.3.1 Polarisation selection

The central part of the polarisation selection in a cross-polarised confocal microscope is a polarising beam splitter (PBS). In our case it is set to reflect the horizontal polarisation and transmit the vertical one. So, the system is made in such way that the excitation laser beam is reflected by the PBS and the single photon signal, having orthogonal polarisation, passes through it. To do so, a first polariser P, placed in the excitation path, sets the linear polarisation to fully reflect the excitation laser. Between the PBS and the focus lens, a quarter-waveplate fixes any remained ellipticity of the incident beam and a half-waveplate sets the wanted axis of linear polarisation. In the reverse way, some reflected laser and the emitted photons both arrive on the PBS. The laser should be reflected while a certain ratio of the single photons is transmitted. Nevertheless, some reflected laser could also be transmitted through the PBS. To completely suppress it, increasing the extinction ratio, a second PBS is placed just after the first one as shown in figure 3.13a.

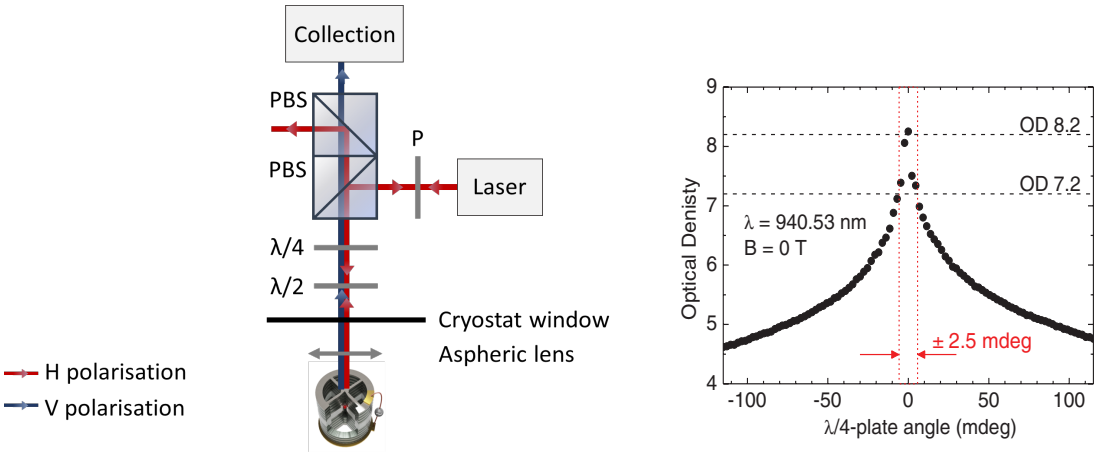

(a) (b)

Figure 3.13: (a) Schematic of the microscope configuration for resonant excitation. The collection (V-polarised) is crossed-polarised from the excitation linear polarisation. (b) From reference ref [196]. Order of magnitude of the laser extinction as a function of the quarter waveplate angle. The optical density (OD) is defined as OD = -log (1/T) with transmission T. To obtain a laser suppression above 10^8 (OD=8), the required precision is around ± 2.5 milli-degree.

Using similar configurations, Kuhlmann and coworkers previously demonstrated an extinction ratio of 10^8 [196] while Benalajla et al. recently reported an extinction of 10^{10} [208]

by using the confocal configuration. In our case, we obtain a ratio around 10^6, which we believe it is limited by the control of the two waveplates angles. Indeed, as presented in figure 3.13b, the extinction efficiency is very sensitive to the angle. The required precision is around ± 2.5 milli-degree and reaching it demands motorised mounts. However, the current extinction ratio is sufficient to filter the excitation laser. Due to the good mode matching between the beam of the excitation laser and the pillar diameter, the laser spot only covers a small surface, which can be consider as homogeneous. Moreover, due to the high cavity finesse and an optimal spectral agreement, a very little power (nW) is sent to the device to drive coherently the QD. Therefore, this strongly limits the amount of scattered laser from the sample and the photons collection remains efficient.

To obtain maximum polarisation selection, we also experimentally verified the efficiency of a PBS as a function of the angle of the incident laser beam. Indeed, the cross-polarisation selection is sensitive to the angle of the incident beam. We then investigated the tolerance of the PBS.

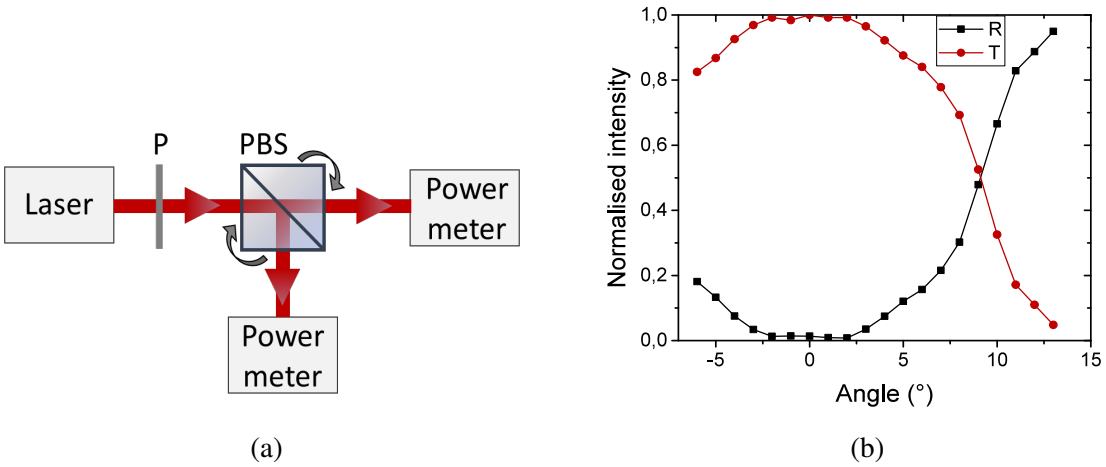

(a) (b)

Figure 3.14: (a) Schematic of the measurement system. A laser is linearly polarised by a polariser (P) to be fully transmitted by a polarising beam splitter (PBS). At beginning, the beam arrives orthogonal to the PBS ($\theta = 0°$). Then, we measure the power in transmission and in reflection for different angle of the PBS from the initial orthogonal position. (b) Power measured in transmission (red line with squares) and in reflection (black line with circles) after a PBS as a function of its angle.

Figure 3.14b plots the measured power transmitted and reflected by a PBS as a function of the angle of the incident laser beam. With a polariser, we set the polarisation in such way that the light is fully transmitted at $0°$ when the laser beam is orthogonal to the PBS. We can notice that the PBS has a tolerance range of incident angle of $\pm 2°$. Beyond it the laser is more and more reflected. Nevertheless, the alignment protocol ensures that the excitation laser and the emitted single photons remain within this angle range.

3.3.2 Depolarisation due to focusing optical components

In the previous section, we showed that a lens of relatively high NA is required for efficient single-photon collection. To do so, we replaced the microscope objective by an aspheric lens. If one of the reasons is to increase the collection efficiency (part 3.2.3.1), another one concern the polarisation control.

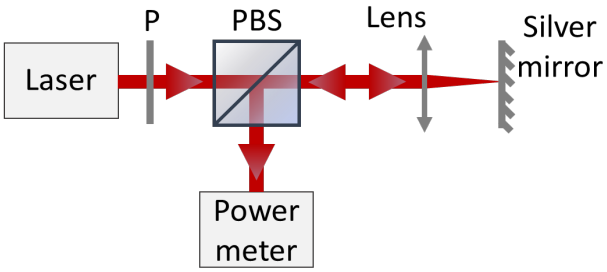

Figure 3.15: Schematic of the depolarisation measurement. A laser, linearly polarised by a polariser (P), passes through a polarising beam splitter (PBS) and is focused on a silver mirror by either a microscope objective or an aspheric lens. The depolarised part of the light is measured in reflection by a power meter.

Figure 3.15 depicts the experimental system used to quantify the depolarisation induced by either a microscope objective or an aspheric lens. The principle is the following: an incoming collimated laser beam is linearly polarised by a polariser and fully transmitted through a PBS. The beam is then focused on a silver mirror with either a microscope objective or an aspheric lens. Since the silver mirror keeps the orientation of the linear polarisation [208], the reflected beam should be fully transmitted back by the PBS. To estimate the induced-depolarisation, we measure the power reflected by the PBS. This experiment shows that the reflected power is four time higher with the microscope objective than with the aspheric lens. Since the objective also introduces around 15% of losses, this change enables to both increase the total system transmission and optimise laser extinction by reducing depolarisation.

We then choose to work with an aspheric lens, but we have to keep in mind that it also induce depolarisation [209]. This phenomenon, theoretically predicted [210] and experimentally verified [211] by Maeckler and Lehmann in 1952, appears when a laser beam is strongly focused on a dielectric reflective interface or a semiconductor surface such as our cavity sources.

Figures 3.16a and 3.16b present the theoretical shapes of an in-focus reflected beam after a lens with a large numerical aperture of 1.4. Figure 3.16a presents the part of the reflected beam with a polarisation parallel to the incident beam one while figure 3.16b corresponds to the part with an orthogonal polarisation. We can notice that the two spots are complementary, and their superimposition gives the entire incoming beam spot. Under a normal incidence and on a perfect reflecting surface the polarisation remains unchanged and the reflected beam should have the same shape as the incident one. The depolarisation is due to a dephasing between the part of the beam reflected on the semiconductor surface and the ones which enters to a certain depth before being reflected. If this effect is also present for normal incident beam, the focalisation emphasises it. Each angle, of the incident beam is reflected differently

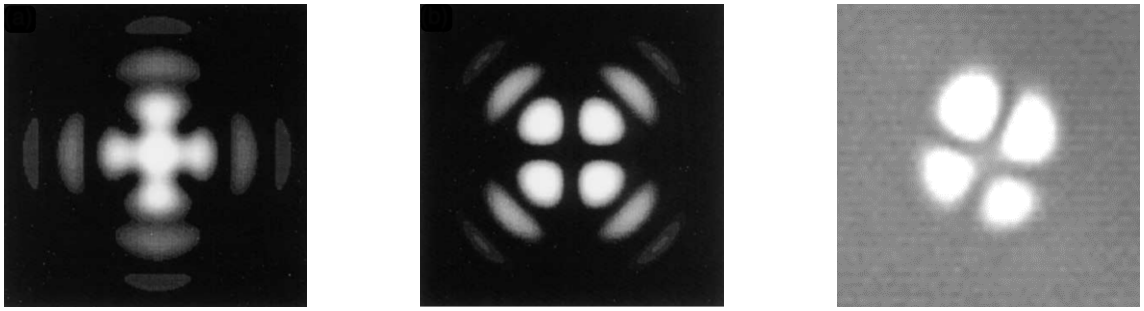

(a) (b) (c)

Figure 3.16: Theoretical clover-leaf patterns of the reflected beam with a polarisation (a) parallel (b) orthogonal to the incoming polarisation. In this model (from [209]), the lens has a NA of 1.4. (c) Experimental picture of the reflected beam with a polarisation orthogonal to the incoming beam. The beam, from the collection part, is pictured in the excitation part after being focused by an aspheric lens (f = 3.1cm, NA = 0.65) and reflected on the planar cavity.

in accordance with the associated Fresnel coefficients of the reflecting surface. Through the lens, the normal part of the incident beam which passes by its two orthogonal axes, H and V, is not depolarised. This explains the cross shape of the figure 3.16a. On the contrary, the part of the beam which passes through the rest of the lens is depolarised. This is from the portion of the beam which arrives with a non null angle and which interferes with the field reflected after the interface. Hence, the resulting effect is the clover-leaf pattern presented in figure 3.16b where each "petal" is π-dephased from the others. This phenomenon is also observed in our system even if the numerical aperture is lower (around 0.65) than in the model. To acquire the pattern of figure 3.16c, the laser, sent from the collection path, is linearly polarised to pass through the PBS. It is then focused on the planar cavity. The waveplates angles are set to let the reflected beam passing back through the PBS. By placing a camera in the excitation path, we can look at the part of the reflected beam which has been depolarised. Since the latter is reflected by the PBS, it has then a polarisation orthogonal to the incident one showing the clover-leaf shape predicted by the theory (figure 3.16b) [209]. The fact that the outer patterns are not present in the experimental picture is due to the numerical aperture of 0.65, much lower than the 1.4 of the theory. Since we work with a system based on the confocal microscope principle, this influence of the lens on the polarisation control is not an issue. The reason is that the collection fibre, acting as a modal filter, selects the central part of the beam. Indeed, due to the dephasing, the mode composed of the lobes will not be coupled into the mode TEM_{00} of the single-mode optical fibre.

The confocal arrangement enables thus to increase the laser rejection improving the cross-polarisation extinction ratio [208]. In this configuration, the collection efficiency is increased while the scattered light from laser is reduced. In addition, since the size of excitation beam focused on the pillar fits its diameter, less laser light is scattered back and depolarised. Therefore the "fibred" single-photon purity of the emitted light is closer to the intrinsic single photon source purity.

3.4 Confocal microscope performances

From the former optical system used by the academic group (figure 3.17a), two 30mm-cage optical systems have been developed and optimised for resonant excitation.

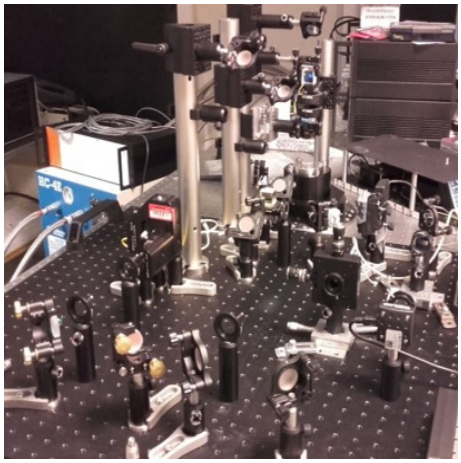

(a)

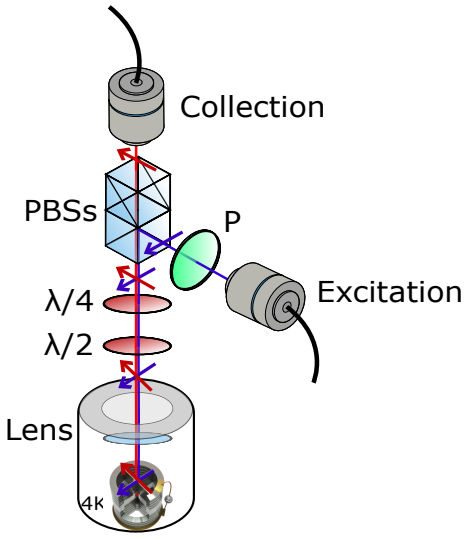

(b)

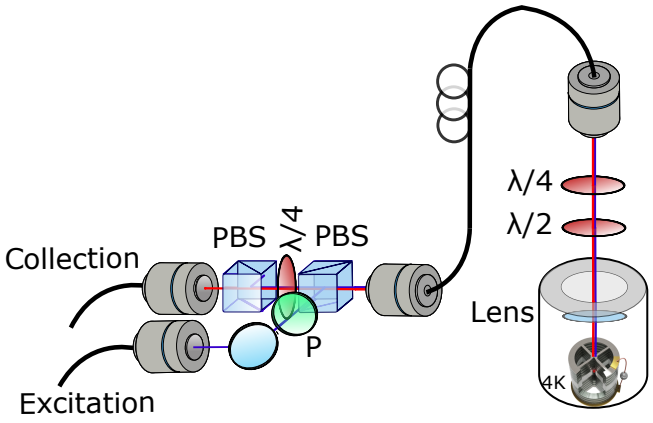

(c)

Figure 3.17: (a) Picture of the non-optimised system. Still used in the lab, it required to be more stable and efficient. Schematics of the confocal microscope optimised for resonant fluorescence. (b) Free-space confocal microscope (c) First fibred design of the microscope.

The first one consists in a complete free-space confocal microscope placed above the cryostat chamber (figure 3.17b). This was conceived to remove the instabilities of the previous system caused by optical components set on high posts (figure 3.17a). The collection collimator is then placed directly on the vertical direction above the cryostat chamber. Hence, from tens of mirrors usually required, we reduce the amount to only one in the current system, placed to align the excitation path.

Figure 3.18 presents the stability of the non-optimised optical setup presented in figure

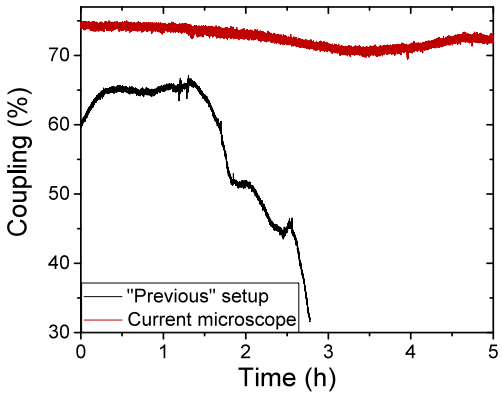

Figure 3.18: Coupling efficiency of the cavity rotated light as a function of the time. The black curve corresponds to the stability measurement with the "previous" setup, the one updated in this work. The red curve corresponds to the current and updated microscope.

3.17a (black line) and the one of the free-space confocal microscope of figure 3.17b (red line). We can notice that these changes, in the system components and their positioning, significantly increased the stability of the system.

Since our microscope is used to characterise the samples, collimators with zoom are required. Nevertheless, in the final applications just one pillar is selected. We could then simplify the system with variable focus collimators which are set to mode match the beam from the pillar in use. This has been done for the second version of the optical system. It consists in a combination of a free-space and a fibred excitation/collection scheme (figure 3.17c) with a variable focus collimator directly placed above the cryostat. The rest of the optical components fit in a rack size module and implement "triplet" collimators for an optimised coupling. This is an intermediate version towards a fibre-coupled source. But thanks to the imaging system, we can still characterise the samples with a more efficient optical system. To keep the polarisation selection, a quarter waveplate has been placed between the two PBSs to correct the remaining ellipticity. Secondly, to keep the polarisation inside the fibre, we use a fibre paddle. The cross-polarisation selection is then maintained by the control the fibre loops and their torsion [212, 213].

Finally, in both systems, to increase the collection efficiency, we use a fibre with a PC-coated connector on the collection collimator side(s) so to reduce reflection compared to APC-connectors.

Table 3.1 summarises the loss budget of these two optical system designs.

In both cases, the coupling efficiencies include the collimator losses. However, if for the version 1, the coupling efficiency only considers the coupling of cavity rotated light, for the second version, we also consider the coupling between the two "triplet" collimators positioned face-to-face. The optical system has then transmission which are respectively of about 52% (figure 3.17b) and 63% (figure 3.17c) more than the previous implemented version [99] (figure 3.17a).

	Version 1 (figure 3.17b)	Version 2 (figure 3.17c)
Waveplates	97%	95%
PBS	95%	95%
Coupling	70%±5%	76%±5%
Total	**64%±5%**	**68.5%±5%**

Table 3.1: Loss budget of the two versions of the optical system developed in this work.

We have then developed and optimised an optical system which is stable during days and fits in a rack size independent module. With the writing of an alignment protocol, the microscope becomes also usable by not experienced users.

3.5 Single photon source characterisation under resonant excitation

3.5.1 Microscope alignment and signal collection

Before working with a single photon source, the confocal microscope is aligned on a reflective metal surface on the sample. Used as a mirror, this enables to align the excitation to the collection. Then, the sample is moved to center the laser spot on the pillar (figure 3.19a).

During the alignment, a 3ps pulsed laser is used to optimise the coupling on the pillar via the cavity rotated light technique. Since the laser spectrum is broader than the cavity rotated light one, we can spectrally distinguish them. As plotted in figure 3.19b, the laser spectrum (red dashed line) is around twice as wide as the width of the cavity rotated light spectrum (blue dash-dot line). To only collect the cavity rotated light, the waveplates placed above the sample are rotated. The quarter waveplate fixes the polarisation ellipticity and the depolarisation of the reflected beam while the half waveplate sets the incident beam polarisation at 45° from the pillar axes. Since the collection polarisation is orthogonal to the excitation one, we then only collect the part of the light whose polarisation is rotated on the Poincaré sphere due to the pillar birefringence (blue dash-dot line in figure 3.19b).

(a)

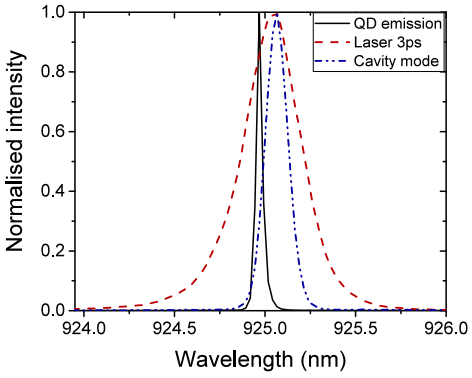

(b)

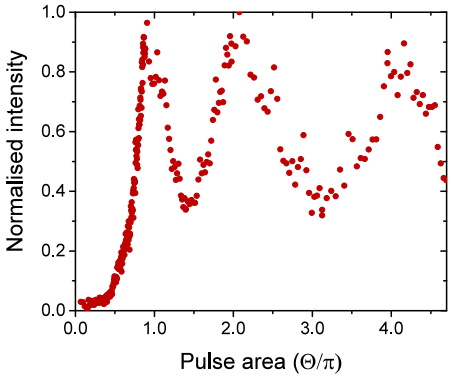

(c)

Figure 3.19: (a) Picture taken from the microscope imaging system. The spot of the excitation laser is on the studied pillar. (b) Analysed spectra during the alignment process. The excitation laser spectrum (a 3ps pulsed laser) is plotted by the red dashed line. The blue dash-dot line corresponds to the cavity rotated light spectrum while the black straight line represents the QD state emission. (c) Rabi oscillation measurement. The intensity is plotted as a function of the normalised laser power. It is corrected form the background by subtracting laser light, following a linear dependence, defined by the square root of the laser power. With a non-corrected intensities at 2π of 5644.5 (arb.u.) and at 4π of 6776 (arb.u.), the correction function slope is around $500 \times \sqrt{P_{\text{laser}}}$.

Once the cavity-rotated light is maximally coupled to the collecting fibre, we rotate the waveplates to optimise the laser filtering. By matching the excitation laser polarisation with one of the pillar axes, the incident and the reflected light have the same polarisation. Without polarisation rotation and since the excitation is along the axis $|H\rangle$ and the collection along $|V\rangle$, the collected signal should vanish. Nevertheless, considering an exciton whose polarised-axis does not correspond to the cavity's (figure 3.20), the excitation polarisation has a non-zero projection on both exciton axes, $|X\rangle$ and $|Y\rangle$. In a different way, a trion in a zero-magnetic field and excited with a linear polarisation emits unpolarised light. As a consequence, even in cross-polarisation, a part of the QD emission has a polarisation parallel to the collection one. If one of the electronic states is already in resonance with the fundamental pillar mode, it is not possible to completely vanish the collected signal by rotating the waveplates. The remaining spectrum corresponds to the QD emission (black straight line in figure 3.19b). On the contrary, if we can obtain a full signal extinction, this indicates the need of tuning the QD states in resonance with the cavity mode. To do so, either the sample temperature is raised or a bias is applied between the top and the bottom of the pillar (chap. 2 part 2.5.4). As seen in chapter 2, the emission is then enhanced and the emitted photons are partially collected in the polarisation orthogonal to the excitation one. The amount of single photons emitted in the collection polarisation is what defines the "polarised first lens brightness" and depends on the QD electronic state. The max-

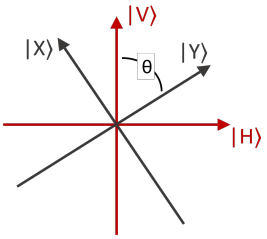

Figure 3.20: Drawing of the pillar and QD exciton state axes (resp. $|H\rangle$, $|V\rangle$ and $|X\rangle$, $|Y\rangle$)

imum brightness value for a trion QD state is almost the half of the emitted photons while for an exciton, we usually measure a maximum of $\mathcal{B}_{\text{PFL}} \approx 16\%$ [99].

To obtain the brightest emission and the best laser rejection, we need to calibrate the right amount of laser power to drive coherently the QD electronic state at its maximum occupation probability. To do so, we measure the Rabi oscillations by increasing the power of the excitation pulsed laser (figure 3.19c). With optimal excitation conditions, only few nano-watts are required to reach π and completely invert the QD population toward the excited state. As the laser power increases, the background signal linearly raises. The plotted oscillations are then corrected from the background by subtracting an intensity proportional to the laser power square root.

3.5.2 Single photon emission characterisation

In the following part we detail the characterisation study of four single photon sources, from four different samples. These sources are respectively based on one trion and three excitons. Since we perform resonant fluorescence, the detected signal is polarised. The polarised first lens brightness is calculated from the measured fibred brightness ($\mathcal{B}_{\text{F}}$) and by considering the confocal microscope transmission, the coupling efficiency of the cavity rotated light, the APDs detectors efficiency of about 30% and the laser repetition rate of 81MHz. Concerning the correction of the indistinguishability measurement, we use the equation (2.31) [171].

Sources A1 and D1 are from the same wafer. They have the same planar cavity parameters but they are differently annealed. Hence, we have Q=3000-4000, β=78%, and η=84%. Sources B1 and C1 are from another wafer. We have Q=10000-14000, β=88%, and η=70%. Extensive description of those cavity parameters can be found in chapter 2. Briefly, "β" is the amount of photons emitted in the fundamental mode of the pillar while "η" corresponds to the pillar extraction efficiency. So, assuming that at "π" the occupation probability of an excitonic state is 1, the first lens brightness is given by $\beta \times \eta$. Hence, the intrinsic source brightness of B1 and C1 sources is 61%, while it is 65.5% for A1 and D1. However, we must keep in mind that these are upper bounds; in accordance with the angle θ (chap. 2 part 2.6.3.3) and the FSS, the exciton occupation probability is usually lower than 1, as for a trion, for which it depends on the presence of either the extra hole or the extra electron (chap. 2 part 2.6.3.4).

Source	QD state	$\mathcal{B}_{\text{PFL}}$	$\mathcal{B}_{\text{F}}$	$\mathcal{P}$	$\mathcal{M}_{\text{corr}}$
A1 [99]	exciton	16%	6.4%	96.5%$\pm$1.5%	94%$\pm$2.6%
B1	trion	16.3%	11.1%	95%	89.8%
C1	exciton	15.9%	10.9%	93.4%	91.5%
D1	exciton	11.4%	7.8%	98.1%	91.8%

Table 3.2: Sources emission characteristics under resonant fluorescence. The source A1 is from reference [99]. Sources B1, C1 and D1 are from three different samples.

Table 3.2 summarises the emission characteristics of the studied sources: the polarised

first lens brightness ($\mathcal{B}_{\mathrm{PFL}}$), the fibred brightness ($\mathcal{B}_{\mathrm{F}}$), the single-photon purity ($\mathcal{P}$) and the corrected indistinguishability ($\mathcal{M}_{\mathrm{corr}}$). The details of the source A1 are extracted from the reference [99], in which the optical setup had an efficiency of about 40%. Considering the study of sources B1, C1, and D1, the microscope is the version 2 described in part 3.4 and has a transmission of 68.5%±5%. For each sources, tens of nanowatts allowed to reach the "π-pulse".

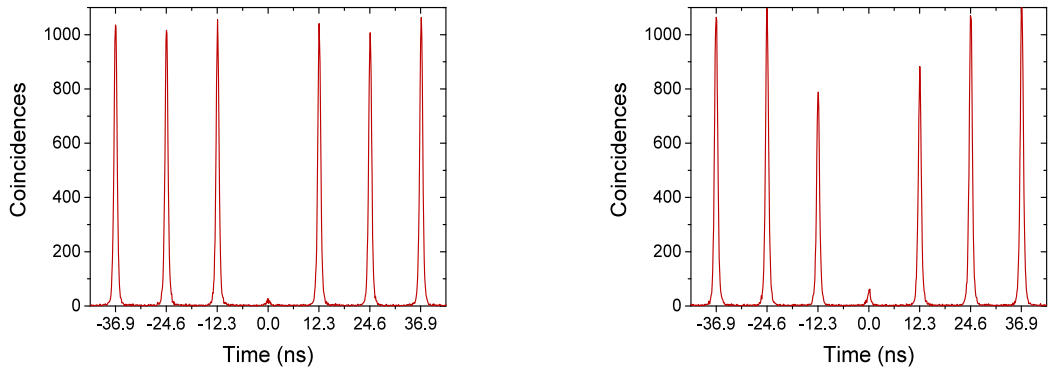

(a) (b)

Figure 3.21: - Sample D1 - (a) Second order correlation measurement, $g^{(2)}(0)$, and the single-photon purity is $\mathcal{P}$ = 1 - $g^{(2)}(0)$. (b) Mean wave-packet overlap measurement. The experimental setups and measurement protocols are described in chapter 2 parts 2.2.2 and 2.6.1

The second order correlation and the mean wave-packet overlap of source D1 are plotted in figure 3.21. Measured single-photon purity above 92% for all sources confirms that the collected light mostly contains single photons and not the reflected laser. The results show that with our optimised microscope system we could increase the collection efficiency, so that the fibred brightness, by about 40% from the system used in reference [99], while keeping the same emission characteristics.

3.6 Conclusion

Critical parameters have been studied to improve the coupling efficiency of single photon sources emission in a single-mode optical fibre. The current confocal microscope possesses a total efficiency of 68.5%±5% (version 2). As a intermediate step toward a complete fibred system, it combines a part which fits in a rack module with a part placed above the cryostat chamber. We achieve high fibred brightnesses with the same emission characteristics as in reference [99]. The system described in this chapter is fully optimised for resonance fluorescence experiments and stable during days. In chapter 4, we will detail the required

changes to the current version in order to implement a new excitation scheme: LA-phonon assisted excitation. In chapter 5, we will move toward a compact fully fibred setup optimised for both resonant fluorescence and LA-phonon assisted excitation schemes.

Chapter 4

Excitation using LA-phonon assisted excitation to obtain bright polarised single-photon sources

"C'est une révolte ? - Non sir, c'est une révolution"

attribuée à Louis XVI et au Duc de La Rochefoucauld-Liancourt

4.1 Introduction

In order to generate indistinguishable photons, it is crucial to perform a coherent population control of the QD. Previously, this was achieved using a resonant excitation, where the QD state is coherently driven from the ground state to the excited state. At "π-pulse", the inversion of the population is maximal. The system then relaxes to the ground state and emits single photons with high indistinguishability [9, 61]. However, the main limitation of this excitation scheme is the laser suppression. Since the resonant excitation laser is at the same frequency and in the same mode as the emitted photons, it can only be separated from the single photons using polarisation filtering. However, in our system this reduces the efficiency of the single photon collection, significantly limiting the maximum polarised brightness by at least a factor of two.

To increase it in resonant fluorescence, different strategies have been explored. The group of Prof. Warburton proposed a polarised cavity constituted of a fibred top distributed Bragg mirror [53] while the group of Prof. Chan-Yang Lu embedded a QD in an elliptical micropillar with a high cavity energy splitting [62]. In both cases, the laser is at the energy of one of these cavity modes and the QD is in resonance with the second. Hence, the single photons are emitted with a little shifted energy and in the orthogonal polarisation from the excitation laser. As consequences, in Tomm et al. [53], they enabled to reach a polarised fibred brightness of 50%, and in Wang et al. [62], they measured a polarised first lens brightness of 60%$\pm$2%. Alternatively, methods of efficient, off-resonant coherent single-photon emission have been studied [214], including off-resonant phonon-assisted excitation [215, 216], two-photon emission via biexciton radiative cascade [217], adiabatic rapid passage via a chirped

pulse [218, 219] or more recently coherent driving with dichromatic laser pulses [63]. Others groups also obtained promising results by preparing a biexciton radiative cascade via a off-resonant phonon-assisted excitation [10, 11, 215, 220].

In this chapter we will focus on the phonon-assisted excitation, which harnesses the interaction between the QD and the phonon bath. By using an excitation laser detuned from the ZPL by about 1meV, virtual energy levels corresponding to longitudinal acoustic (LA) phonons are excited [221]. Since the excitation laser is spectrally detuned in this scheme, it can be separated from the emitted single photons using spectral filters. Not using polarisation filtering will allow for the collection of all the emitted photons.

The first part of this chapter will describe in detail the process of the LA-phonon assisted excitation. The photon emission can be described as a three steps process: (i) the excitation of an upper virtual energy level, (ii) the phonon-induced relaxation between the two dressed states of the system and (iii) finally the photon emission by an adiabatic undressing of these two states.

In the second part, we will discuss the influence of laser parameters on the excitation efficiency. This part is based on several theoretical works. Each of them will be detailed to explain the choice of the optimal experimental parameters to get the most efficient excitation. Theoretical results obtained with our source parameters will then give a range of realistic values for experiments.

In the third part, we will present the theoretical emission characteristics, such as its coherence or the emission benchmarks.

Finally, the fourth part will be about the experimental results we got with our single photon sources. We will then demonstrate the ability of the LA-phonon assisted excitation to get a bright and linearly polarised emission of single and indistinguishable photons.

4.2 Theory of phonon-assisted excitation: a three-step process

The theory of QD LA-phonon assisted driving is based on the evolution of a two-level system. The QD is described as a ground state $|g\rangle$ and an excited state $|X\rangle$ driven by a coherent laser field. The associated Hamiltonian, in Schrödinger's picture and in the rotating wave approximation, is:

$$H_{\text{QD, Laser}} = \hbar\omega_{\text{X}} |X\rangle \langle X| - \left[\frac{\hbar\Omega(t)}{2} (|X\rangle \langle g|) + H.c.\right] \tag{4.1}$$

with ω_{X}, the QD resonance frequency, and $\Omega(t) \propto f(t)e^{-i\omega_{\text{L}}t}$, the Rabi frequency of the two-level system. ω_{L} is the laser frequency, and the field strength, f(t), is the real pulse envelope of the laser, related to its electric field. As seen in chapter 2 part 2.6.3.2, $\Omega(t)$ is linked to the pulse area following $\Theta = \int \Omega(t)dt$ [222].

The following sections will present the three steps of the process to get a controlled single photon emission.

4.2.1 Dressed states of the system

When the laser is off, the system is considered as a two-level system (figure 4.1 (i)). To take into account the detuning of the laser and represent the interaction, we expand the equations in a new basis called the "rotating frame". The two new states are $|g_R\rangle$ and $|X_R\rangle$. $|g_R\rangle$ corresponds to the ground state $|g\rangle$ detuned by an energy $\Delta = \hbar(\omega_L - \omega_X)$, from the state $|X_R\rangle$, which corresponds to the exciton state $|X\rangle$. For a positive detuning the "ground state", $|g_R\rangle$, has a higher energy than the excited state $|X_R\rangle$ (figure 4.1 (ii)). It is the reverse if the energy detuning is negative.

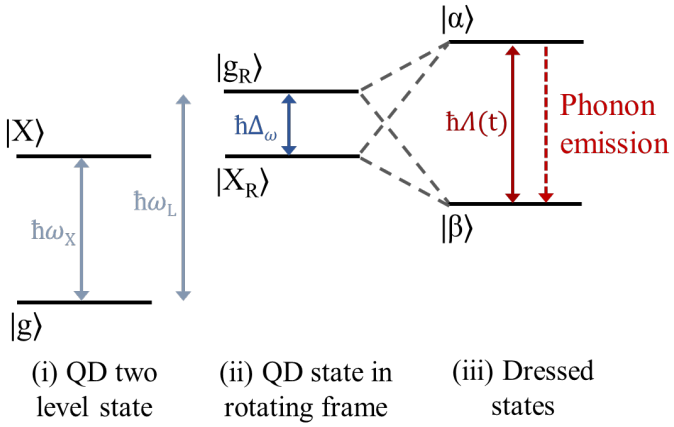

Figure 4.1: From [215]. Energy levels represented in (i) the lab frame, and (ii) the rotating frame. $|g_R\rangle$ includes the ground state $|g\rangle$ and the laser detuning ($\Delta_\omega = \omega_L - \omega_X$), while the $|X_R\rangle$ corresponds to the excited state $|X\rangle$. Once the laser is on, the states are optically dressed (iii) $|\alpha\rangle$, for the upper state, and $|\beta\rangle$, for the lower one, are a superposition of the $|g_R\rangle$, and $|X_R\rangle$.

When the laser is on, the states of the rotating frame are dressed [1] (figure 4.1 (iii)) [10]. Written as $|\alpha\rangle$, for the upper state, and $|\beta\rangle$, for the lower, they are a superposition of the ground state, $|g_R\rangle$, and the excited state, $|X_R\rangle$. In the rotating frame basis, the latter correspond to eigenstates of the light-matter Hamiltonian described in equation (4.1) and written in this basis. Considering an excitation laser with a field strength $f(t)$ and detuned by Δ from the QD state energy, we can write them as:

$$\begin{cases} |\alpha\rangle = cos(\theta_m(t))\,|g_R\rangle + sin(\theta_m(t))\,|X_R\rangle \\ |\beta\rangle = -sin(\theta_m(t))\,|g_R\rangle + cos(\theta_m(t))\,|X_R\rangle \end{cases} \tag{4.2}$$

[1] We use the term "dressed state" as in ref [10], when this would require quantifying the field. But, neglecting the vacuum Rabi splitting, we assume that under off-resonance the quantum and semi-classical models meet.

with $\theta_{\mathrm{m}}(t)$, the mixing angle defined by $tan(\theta_{\mathrm{m}}(t)) = \frac{\hbar f(t)}{\Delta+\hbar\Lambda(t)}$. These equations determine the phonon-relaxation and the evolution of the occupation probability of the states.

"$\Lambda(t)$" represents the effective Rabi frequency [222] and determines the energy splitting between the two dressed states:

$$\hbar\Lambda(t) = \sqrt{(\hbar f(t))^2 + \Delta^2} \tag{4.3}$$

The corresponding energies of the two dressed states are:

$$E_{\alpha/\beta}(t) = \frac{1}{2}\left(-\Delta \pm \hbar\Lambda(t)\right) \tag{4.4}$$

4.2.2 Exciton-phonon interaction

We now consider the exciton-phonon interactions. They can be modeled by a pure-dephasing Hamiltonian and the free phonon Hamiltonian:

$$H_{\mathrm{QD,phonon}} = \hbar\sum_q \omega_{\mathrm{q}} {b_{\mathrm{q}}}^{\dagger} b_{\mathrm{q}} + \hbar\sum_q \left(\gamma_{\mathrm{q}} {b_{\mathrm{q}}}^{\dagger} + {\gamma_{\mathrm{q}}}^{*} b_{\mathrm{q}}\right) |X\rangle \langle X| \tag{4.5}$$

with ${b_{\mathrm{q}}}^{\dagger}$ (b_{q}), the phonon creation (annihilation) operator in the mode q coupled to the dot by the coupling constant γ_{q}. The first term corresponds to the phonon bath while the second describes the exciton-phonon interaction.

The modulus of the exciton-phonon coupling is linked to the spectral density via $J(\omega) = \sum_q |\gamma_{\mathrm{q}}|^2 \delta(\omega - \omega_{\mathrm{q}})$ [223]. This quantity describes the efficiency of the coupling between the QD state and the phonon bath, and so the excitation efficiency.

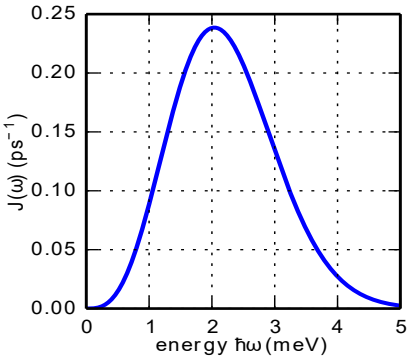

Figure 4.2: From [10]. Plot of the spectral density $J(\omega)$ of a GaAs-based QD as a function of an energy expressed as $\hbar\omega$ at T=1K.

Figure 4.2, from the work of Barth et al. [10], presents the spectral density of exciton-phonon coupling as a function of the phonon energy $\hbar\omega$ at T=1K. For phonon energies close to $\hbar\Lambda$, the phonon-assisted transitions between the dressed states ($|\alpha\rangle$ and $|\beta\rangle$) are allowed by the Hamiltonian (4.5), at a rate $\propto J(\omega)$. The exciton-phonon coupling is maximum for $\hbar\omega_{\mathrm{max}}$

= 2meV. Therefore, for an effective excitation, the goal is to get $\Lambda_{max} = \omega_{max}$. So, the control of the effective Rabi frequency is the key parameter to obtain an efficient LA-phonon assisted driving of the QD. Following equation (4.3), this is possible by setting the parameters $f(t)$ and Δ. The laser optimal detuning will then be less than 2meV. Concerning the temperature dependence of the spectral density while kT < 1meV, so that's T < 12K, we can assume that the exciton-LA phonon coupling remains unchanged.

Once the states are dressed, the exciton-phonon coupling leads to the phonon-assisted relaxation from the upper to the lower dressed state (figure 4.1 (iii)). The state $|\beta\rangle$ is then more and more populated and the evolution of $\theta_m(t)$ increase the occupation probability of $|X_R\rangle$. A positive energy detuning leads to the preparation of the exciton while a negative energy detuning prepares preferentially the ground state. In the following, we will only consider positive energy detunings.

4.2.3 Adiabatic undressing of the states and photons emission

When the laser is switched-off, the phonon-induced relaxation is deactivated, and the dressed states are then transformed back to the exciton bare states. Due to the increase of the $|\beta\rangle$ state population during the phonon-assisted relaxation, the state undressing boosts the $|X_R\rangle$ state occupation, hence the exciton occupation at the end of the pulse. This population transfer is ensured by an adiabatic state undressing. More detailed in the following, the laser switch-off must be then long enough to remain in the adiabatic regime, inducing an efficient process, but short enough not to allow for other relaxation processes. In this condition, for switch-off durations above few picoseconds, the undressing transforms the lower dressed state $|\beta\rangle$ to the exciton state $|X\rangle$ whose occupation probability is boosted to 1. Finally, the exciton state relaxes and a photon is emitted at the energy $\hbar\omega_X$ by an electron-hole pair recombination.

4.3 Optimisation of the excitation laser parameters

In this part, we discuss the parameters which influence the emission efficiency of the QD state. The excitation with both a continuous-wave and a pulsed laser will be broached. In each case, the key parameter in determining the efficiency is the effective Rabi energy (equ. (4.3)) which is reminded just below:

$$\hbar\Lambda(t) = \sqrt{(\hbar f(t))^2 + \Delta^2}$$

This parameter determines the energy separation between the two dressed states $|\alpha\rangle$ and $|\beta\rangle$. If this separation corresponds to an energy where there is a high spectral density of LA phonons (typically few meV), then the system can relax to the lower energy dressed state by emitting a phonon. The effective Rabi frequency determines then the process efficiency. To get the optimal conditions of the LA-phonon assisted excitation, the pulse strength, $f(t)$, the pulse duration, τ, and the laser detuning, Δ, must be carefully chosen.

4.3.1 Excitation via a continuous-wave laser and the influence of the field strength

With a continuous-wave laser, inverting a population is more complicated than just exciting the transition from the lower to the higher state. Indeed, due to a competition between the spontaneous and the stimulated emission processes, semi-classical physics pointed out that a simple two-level system cannot achieve steady-state population inversion [224]. The usual way to overcome this is to use a system with multiple levels. Nevertheless, another solution is to detune the laser energy and exploit the LA-phonon energy level [10, 215, 225].

Let us consider a continuous-wave laser detuned by Δ = 1meV. In this condition, we choose the laser field strength, f, which does not evolve after the laser switch-on. The stationary exciton occupation is then given by [11]:

$$C_X{}^{\infty} = \frac{1}{2}(1 + \frac{\Delta}{\hbar\Lambda}) \tag{4.6}$$

Following this equation, a low enough field strength should drive the system to a unity probability.

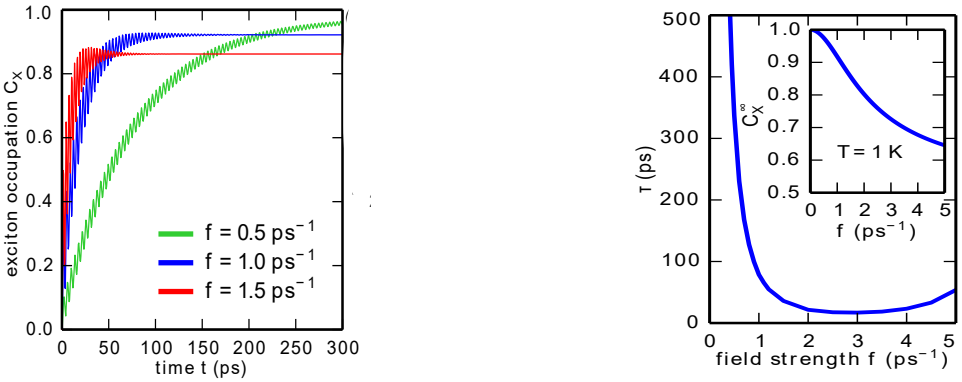

(a) (b)

Figure 4.3: (a) Evolution of the exciton occupation as a function of the time after the laser switch-on, at various field strengths f. (b) Evolution of the time required to reach 99% of the exciton occupation as a function the laser field strength f(t). *Inset* Evolution of the exciton occupation stationary state value, $C_X{}^{\infty}$ as a function of the the laser field strength f(t). From reference [10]. The calculations are made with a continuous wave laser detuned from the resonance by Δ = 1meV.

Figure 4.3 is from the work of Barth et al. [10]. It presents the theoretical influence of the laser field strength on the exciton occupation evolution (C_X) and on its stationary value ($C_X{}^{\infty}$). In figure 4.3a, three time evolutions of C_X, corresponding to three values of f, are plotted. We can first notice that this excitation regime really overcomes the exciton occupation issue. The latter reaches almost 1 for $f = 0.5\text{ps}^{-1}$ (green line), while as predicted by equation (4.6), C_X is lower with $f = 1\text{ps}^{-1}$ or $f = 1.5\text{ps}^{-1}$ (resp. blue and red lines). However, with $f = 0.5\text{ps}^{-1}$, even after 300ps the system has not yet reached its stationary occupation probability.

Figure 4.3b represents the required time to reach 99% of $C_X{}^{\infty}$ as a function of the laser field strength. The inset of figure 4.3b plots the value of $C_X{}^{\infty}$ as a function of the field strength, f. From the inset, we can notice that to reach an occupation probability above 90%, the field strength should be below 0.5ps^{-1}. However, following figure 4.3b, the required time is about 350ps for $f = 1\text{ps}^{-1}$ and becomes rapidly infinite below it. Hence, for low pulse strength, the time scale of the population inversion exceeds the radiative decay, and the photon can be emitted at any time. As a consequence, to achieve a high brightness, and following figure 4.3b, a trade-off can be found by setting $f > 2\text{ps}^{-1}$. If the exciton population is then limited to a stationary value below 0.8, this could be fixed with an adiabatic laser switch-off. In the following, the excitation laser will be then pulsed and its parameters will be discussed.

4.3.2 Excitation via a pulsed laser and influence of the pulse parameters

4.3.2.1 Role of the pulse temporal shape

When a pulsed laser is used, the first parameter to control is its temporal shape. Indeed, under LA-phonon assisted regime, the excitation efficiency is linked to both the laser switch-on and its switch-off.

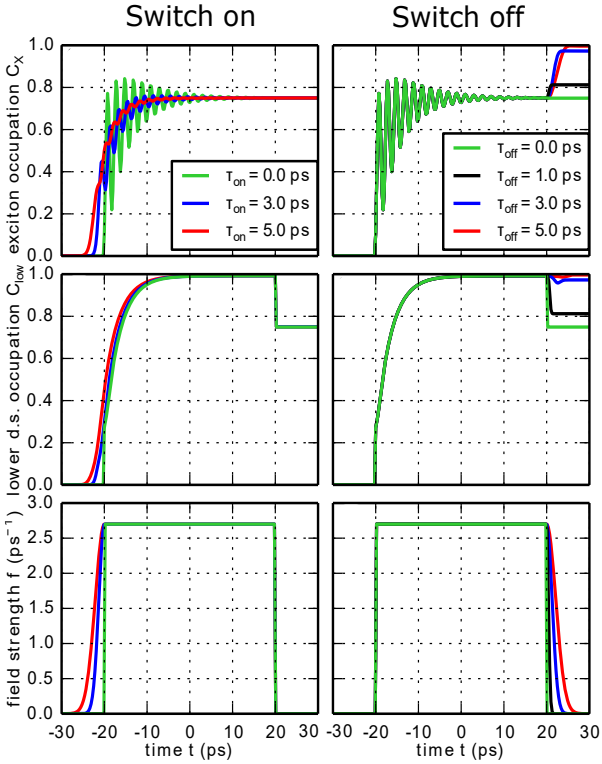

Figure 4.4: From the theoretical work of reference [10]. The **left panel** presents the influence of the laser switch-on on the lower dressed state and the exciton occupations (resp. C_{low} and C_X). Three switch-on duration are considered, 0ps, 3ps and 5ps. The **right panel** presents the influence of the laser switch-off on the same parameters. Four switch-off duration are considered, 0ps, 1ps, 3ps and 5ps. In both panels, C_{low} and C_X are plotted during the pulse length and for a pulse strength of 2.7ps^{-1} (about 15π).

Figure 4.4, also from Barth et al. [10], shows their influence on the exciton occupation preparation. The impact of the laser "switch-on" and "switch-off" are respectively represented in the left and the right panels. The bottom panel plots the laser field strength as a function of time. The middle and the top panels present respectively the evolution of the occupation of the lower dressed state $|\beta\rangle$ (C_{low}) and of the exciton occupation (C_X) for a given laser temporal shape. The laser temporal profile and its field strength are important to control the evolution of the dressed states energy splitting during the pulse (part 4.3.1). It must also be controlled to reach a high exciton state occupation efficiently and with a high fidelity.

Let us first consider the switch-on dynamics presented in the left column. As plotted, a sharp switch-on (green line) enables an occupation probability of 1 of the lower energy dressed state, but the exciton occupation oscillates before reaching the stationary state. We can make a parallel with a string hit suddenly and which oscillates before reaching its stable equilibrium position. On the contrary, with a Gaussian slope switch-on (red and blue lines) C_{low} remains at 1 and the exciton state also reaches an occupation just about 0.75. However, the increase is faster and follows a stable rise. This parameter is important to obtain a prepared state quickly and with a high fidelity.

On the right column, we can notice that both the state undressing and the exciton occupation C_X depend on the way the laser is switched off. Considering a square temporal envelop (green line), the abrupt switch-off undresses suddenly the dressed states. The lower state then loses a part of its occupation and the exciton occupation stays at the stationary value reached before the switch-off. On the contrary, if the temporal envelop follows a "Gaussian" slope (black, red and blue lines), the lower state keeps its occupation around 1. For switch-off durations above 3ps, the undressing process is slow enough to smoothly transform the lower dressed state $|\beta\rangle$ to the exciton state $|X\rangle$ whose occupation probability is boosted to 1. However, we have to be aware that in this paper [10], they consider the ideal case of a two level system without a cavity and no other relaxation processes, such as the radiative decay. But the latter must be considered when we want to emit single-photons. Experimentally, the QD is embedded in a cavity. Since it has non-negligible influences on both the needed exciton preparation time and its emission quality [214], we must deal with cavity losses and QD radiative decay. For instance, Ardelt et al. [225] measured a maximum exciton occupation of 0.72 ± 0.08. In this work, an individual self-assembled InGaAs QD embedded in a microcavity was driven by near-resonant 10ps laser (Δ = 0.69meV) whose pulse area was above 10π.

4.3.2.2 Role of the pulse strength

Controlling the laser temporal shape is a first step to obtain an efficient excitation but this is not a sufficient condition. As with a continuous-wave laser, the pulse strength must be considered.

Figure 4.5 shows the time evolution of respectively the dressed states energy splitting, the lower dressed state $|\beta\rangle$ occupation (C_{low}) and the exciton occupation (C_X) as a function of the laser field strength (bottom graph). The latter is a 20ps pulsed laser, detuned by Δ = 1meV, with a Gaussian shape to ensure the adiabatic switch-on and -off. According to these theoretical results, if the laser is not strong enough the states occupation remain limited. The green line is the result of a 10π pulse ($f(t)_{max} = 1.5 ps^{-1}$). This corresponds to the pulse area defined as $\int f(t)\, e^{-i\omega_L t}\, dt$. As $f(t)$ varies during the pulse duration, the energy splitting

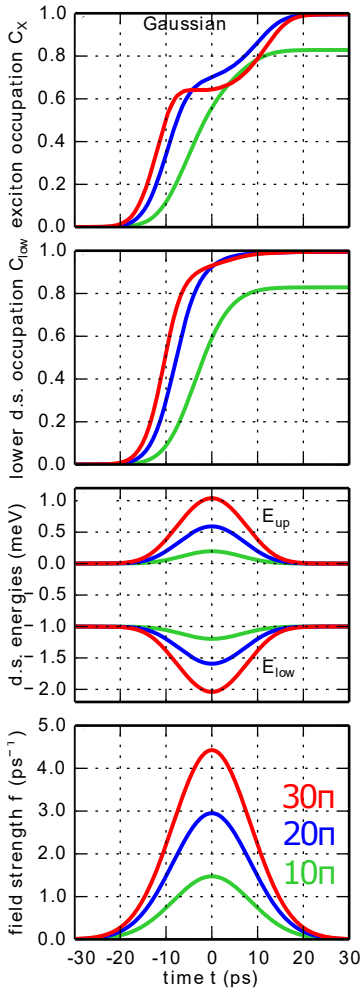

Figure 4.5: From reference [10]. Influence of a Gaussian time-shape pulse strength on the energy slitting between the two dressed states (equ. 4.4), the lower dressed state occupation (C_{low}) and the exciton occupation (C_X). The pulse areas are 10π (green), 20π (blue) and 30π (red), and the 20ps pulsed laser is detuned by Δ = 1meV.

between the two dressed states follows it. However, the highest energy splitting is around 1.4meV. This is below the required 2meV to obtain an optimal exciton-phonon coupling. Thus, both the lower dressed state and the exciton occupations stay around 0.8. On the contrary, when the pulse area is above 20π ($f(t)_{\max} = 3\text{ps}^{-1}$) (blue and red lines), it reaches 1. The occupation evolution also points out that the process is not efficient during the entire pulse duration. The increase of the C_X coefficient is not steady. Indeed, the energy splitting of the dressed states is above 2meV around the maximum of the Gaussian shape, decreasing the exciton-phonon coupling during few picoseconds. For 30π ($f(t)_{\max} = 4.5\text{ps}^{-1}$), this is not yet an issue and $C_X = 1$, but for a stronger pulse, the efficiency is then impacted and C_X does not reach 1. So, to drive efficiently the quantum dot, the pulse area should be at least about 15π and not larger than 30π.

4.3.2.3 Role of the pulse duration

Since, the population transfer takes place after the LA-phonon relaxation, so at the end of the pulse, the pulse duration has also an influence on the preparation of the exciton occupation.

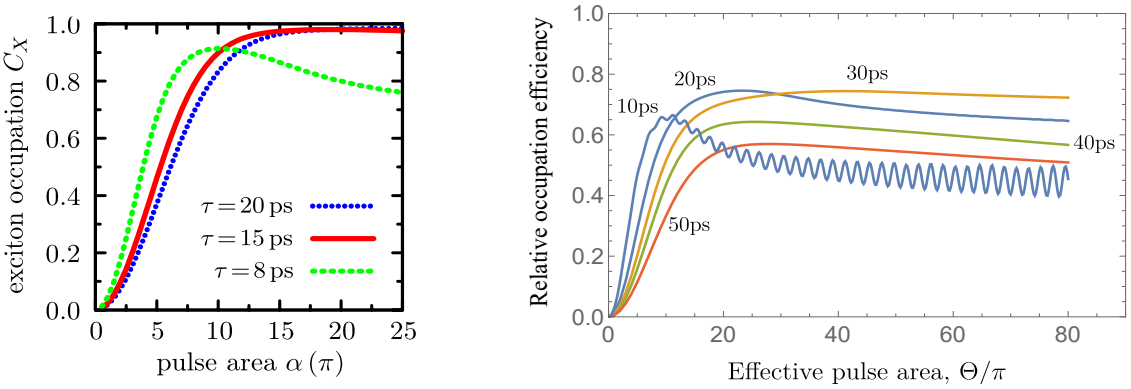

Figure 4.6: Theoretical exciton occupation as a function of the laser pulse area at various pulse duration. (a) From reference [11]. The laser has a Gaussian time-shape and its detuning is Δ = 1meV. (b) From the theoretical model used in reference [226] applied to our sources parameters ($\hbar\gamma$ = 0.66μeV, $\hbar\kappa$ = 20.6μeV, $\hbar g$ = 6.6μeV). The laser has a Gaussian time-shape and its detuning is Δ_λ = -0.3nm (Δ = 0.43meV).

Figure 4.6a (from Glässl et al. [11]) shows the theoretical exciton occupation C_X as a function of the pulse area at various pulse durations. A GaAs QD is driven by a Gaussian laser shape, detuned by Δ = 1meV from the exciton line. For a pulse length lower than 10ps, the inversion of the phonon-assisted preparation is not efficient and C_X stays below 0.9. Moreover, the process seems to be more sensitive to the increasing of pulse area and it becomes even more inefficient for pulse areas larger than 12π. On the contrary, pulse durations above 10ps enable to reach the maximum of almost 1, setting this duration as a lower bound to get an efficient excitation. Nevertheless, if it is important to reach a high exciton occupation, the photons must also be emitted with a near-unity probability. This parameter depends on the QD lifetime, and in this work, they model a GaAs QD without a cavity. So, to fulfill these two requirements, we need to consider a QD embedded at least in a 2D cavity.

Figure 4.6b presents the theoretical influence of the pulse duration on the relative exciton occupation, as a function of the pulse area. Here, we consider the typical parameters of our experiments (an InGaAs QD embedded in a pillar) with a laser detuning of Δ_λ = -0.3nm (Δ = 0.43meV). The relative occupation is calculated from the mean photon number of the cavity multiplied by the cavity decay rate. Considering small $g^2(0)$ value, this approximates the probability of having a photon emitted via the cavity mode. This model, described by Gustin and Hughes [226], considers a QD and a cavity lifetime equal respectively to 1ns and to 32ps at 8K, and $\hbar g$ = 6.6μeV. The Purcell factor is about 12.8. For a pulse duration about 10ps, the exciton occupation only reaches 0.65 and oscillates when the pulse area increases. As shown previously, this short pulse does not fully allow for an equilibrium to be reached during the

excitation pulse. From this figure, we can also set the 30ps as an upper bound. Indeed, above it, the exciton occupation remains below 0.6. Eventually, we can notice that with our QDs embedded in pillars, the maximum occupation is not 1 but 0.8. This theoretical limitation will be experimentally validated in part 4.5.2.1. Hence, this excitation scheme is less efficient than resonant excitation. But, in any case, we will see that it enables a higher single photon collection.

To summarise the above discussion, the pulse duration must be between 15ps and 30ps for an efficient source driving.

4.3.2.4 Role of the laser detuning parameter

In previous parts, only positive energy detunings have been considered. This choice can be explained and experimentally validated.

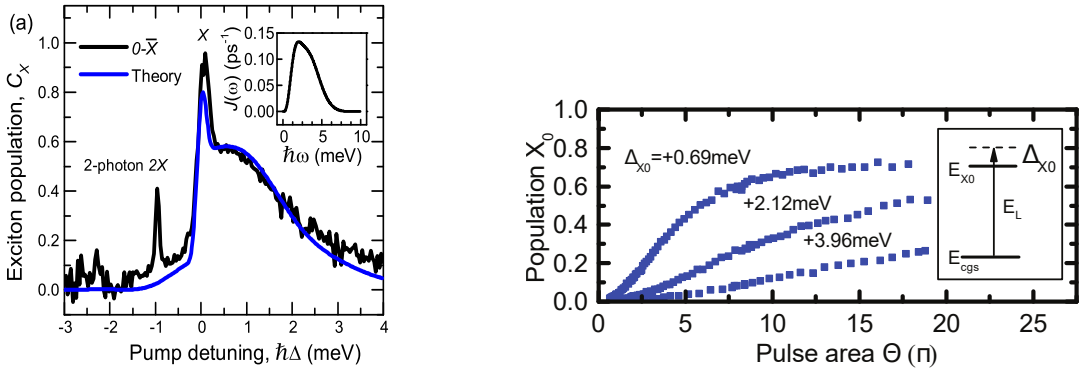

(a) (b)

Figure 4.7: (a) From reference [215]. Exciton population as a function of the laser detuning from the resonance. The experimental measurements are plotted with the black line and fit with the theory plotted in blue. For both, the 15ps pulsed laser is detuned by = 0.83meV and has a pulse area of 7.24π. The source is a InGaAs/GaAs QD embedded in an n-i-Schottky diode structure. (b) From reference [225]. Measured exciton population as a function of the laser pulse area for three positive detunings. The pulse duration is about 10ps and the QD is embedded in a 260nm thick GaAs layer acting as a weak microcavity. A bottom DBR enables to extract the emitted photon preferentially from the top.

Figure 4.7a, from Quilter et al. [215], presents the fit between the experimental and the theoretical evolutions of the exciton population as a function of the laser detuning (resp. black and blue lines). The resonant excitation corresponds to $\hbar\Delta$ = 0meV. The InGaAs/GaAs QD, located in an n-i-Schottky diode structure, is driven by a laser with a pulse duration of 16.8ps and a pulse area of 7.24π. During a pump and probe experiment, the electron-hole pair recombinations are indirectly detected via the measurement of the induced photocurrent. As predicted (blue line), negative energy detuning does not allow a preparation of the excited state. The dynamics due to LA-phonon interactions has a large temperature dependence [223], and at 4K it is easier to emit a phonon than absorb one. Hence, the exciton state is not populated during the excitation process. This can be also formally evidenced with the help of

equation (4.2). The latter expresses the dressed states as a superposition of the exciton states in the rotating frame. Following the relation of $|\beta\rangle$, a negative energy detuning leads to an increase of the coefficient associated to $|g_R\rangle$ and a decrease of the $|X_R\rangle$ coefficient. Hence, the system remains in the ground state, $|g\rangle$ and no electron-hole pair is created. If the energy detuning is positive, the QD states in the rotating frame are inverted (figure 4.1) and the excited state $|X_R\rangle$ is preferentially prepared. Since it is linked to the exciton excited state $|X\rangle$, the latter is indirectly populated. As seen before, the exciton population is less than the equivalent under resonant excitation, and it decreases when the detuning increases. The phonon spectral density, plotted in the inset, gives an explanation of this occupation behavior. For fixed pulse duration and strength, increasing the detuning enlarges the distance between the two dressed state energies. When it goes above 2meV, it reduces the coupling between the QD and the phonon bath. The preparation process is then less efficient. Following the experimental line, the highest excitation occupation is 0.67 ± 0.06 for a 15ps laser detuned by 0.83meV and with a pulse area of 7.24π [215]. The main limitation of the exciton occupation in this work is the laser power, but, with this indirect measurement, this sample allowed to prove an occupation probability higher than 50%.

Figure 4.7b, from Ardelt et al. [225], shows the measured exciton occupation as a function of the laser pulse area for three positive laser energy detunings. In this case, the measurement is based on the single-photon detection. The InGaAs QD is embedded in a 260nm thick GaAs layer acting as a low-Q microcavity, whose DBRs asymmetry enables to extract the emitted photon preferentially from the top. The laser is shaped by a 4f line to obtain a pulse duration of about 10ps. In these conditions, they measured a maximum population of $72\%\pm8\%$ for a detuning of Δ = 0.69meV. As seen previously, this exciton occupation is reached for a pulse area larger than 10π, and, if the detuning is above 1.5meV, the excitation is less efficient, limiting the source brightness.

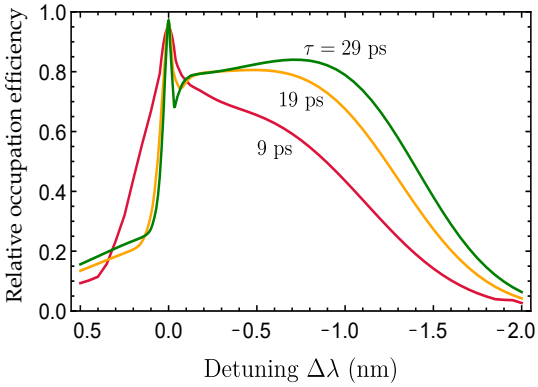

Figure 4.8: Theoretical exciton population as a function of the detuning at various pulse durations. The probability of occupation is normalised with the one under resonant excitation. The model parameters are: QD and the cavity lifetime equal respectively to 1ns and to 32ps at 8K, QD-cavity coupling is 6.58μeV, and so the Purcell factor is 12.8.

Figure 4.8 presents the simulated exciton occupation, normalised with the maximal occupation under resonant excitation, as a function of the laser detuning at various pulse durations. The theory, based on the work of Gustin and Hughes [226], is used to predict the results we can obtain with our sources. We then consider an InGaAs/GaAs QD embedded

in a micropillar whose parameters are detailed in the figure caption. The excitation power is optimised to maximise the exciton occupation for a fixed Gaussian pulse. Not only is the exciton occupation higher with longer pulses but the detuning range becomes larger. The setting of this parameter is then less critical but the maximum efficiency remains about 85%. It should be possible to increase it by using longer pulse duration and stronger pulse strength. For instance, with a pulse of 60ps at 60π and for a detuning of Δ_λ = -1nm (Δ = 1.43meV), the maximum occupation efficiency should be about 0.9. However, in this regime, we expect that both the $g^{(2)}(0)$ and indistinguishability will be poorer. Hence, we will not consider these large values for the following experiments.

To summarise this section on the optimisation of the excitation parameters, with QDs in micropillars, the best LA-phonon assisted driving is obtained with a Gaussian laser time-shape. The pulse area and duration must be above respectively 10π and τ = 19ps. Only positive energy detunings are relevant and they must be between Δ = 0.21meV($\approx$-0.15nm) and Δ = 1.15meV($\approx$-0.8nm).

4.4 Theoretical prediction of the emission characteristics

In this part, we will discuss the coherence of the LA-phonon assisted excitation, as well as the purity and the indistinguishability of the emitted photons. These figures of merit characterise the quality of the emission and enable a right comparison with the resonant excitation regime. This part is also based on theoretical works. They give an idea of the expected experimental results we could obtain with our sources.

4.4.1 A controlled inversion population to emit indistinguishable photons

Under resonant fluorescent experiment, the system is coherently driven from the ground state, $|g\rangle$, to the excited state, $|X\rangle$. This can be illustrated using the Bloch sphere picture. The state is then represented by a unitary vector travelling on the sphere from $|g\rangle$ to $|X\rangle$ and inversely, creating the so-called Rabi oscillations. On the contrary, a LA-phonon assisted driving involves decoherence [221, 223]. The length of the vector reduces along the trajectory and can even vanish before reaching the upper pole $|X\rangle$.

Figure 4.9 shows (a) the vector trajectory in the Bloch sphere and (b) its length evolution during a LA-phonon assisted driving. The theoretical results are obtained after the excitation of the two-level system by a detuned 20ps Gaussian pulse (Δ = 1meV) with various pulse areas. Due to the phonon-assisted relaxation process, decoherences lead to a fast decrease of the vector length. The time needed to reach the minimum depends on the pulse area. For a pulse duration of 20ps, a larger pulse area induces a faster relaxation process. The Bloch vector length drops faster. Nevertheless, we can notice that the minimum has a finite

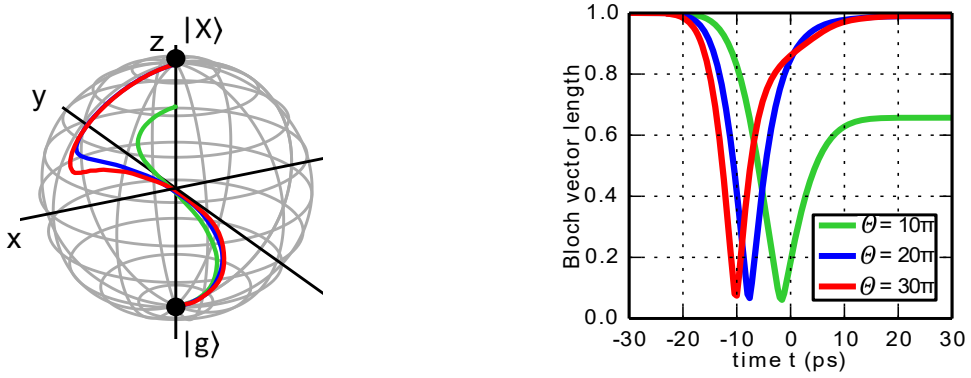

(a) (b)

Figure 4.9: From reference [10]. (a) Drawing of the system trajectory in the Bloch sphere between the ground state, $|g\rangle$, and the excited state, $|X\rangle$. (b) Time evolution of the Bloch vector length under three different pulse areas. The 20ps pulsed laser detuning is $\Delta = 1meV$.

value. The Gaussian pulse, which is not perfectly adiabatic, generates coherence between the dressed states. This drives the state slightly off the (time-dependent) axis defined by the states $|\alpha\rangle$ and $|\beta\rangle$, so that it starts to precess about this axis. In the same time, the phonon-assisted relaxation takes place along this axis, but the trajectory does not go through the center of the sphere because of the initial off-axis. At the end of the pulse, the state which is now close to $|\beta\rangle$ evolves smoothly toward $|X\rangle$ thanks to the adiabaticity of the Gaussian pulse. Above 20π, the vector length re-approaches 1 when it reaches the excited state, $|X\rangle$. This reflects the almost complete occupation of the lower dressed state and its transfer to the bare exciton state. As seen previously, a weaker pulse ($\Theta = 10\pi$) does not allow a complete relaxation and the vector stays inside the sphere with a length around 0.65. These theoretical observations reveal the possibility to induce a controlled population inversion. Even though the LA-phonon assisted excitation is incoherent during the phonon-relaxation process, the adiabatic switch-off of the laser leads to a coherent evolution to the excited state at the end of the pulse.

In this regime, Gustin and Hughes [226] did simulations to quantify the expected indistinguishability of the emitted photons. Since the excitation scheme involves phonon-assisted relaxation, which is source of decoherence, this raises the question of the emitted photons indistinguishability. Theoretically, they considered a QD embedded in a cavity, whose parameters are $\hbar g = 20\mu$eV and $\hbar\kappa = 50\mu$eV. With a QD lifetime of 660ps without cavity coupling, the Purcell factor is $4g^2/\kappa\gamma = 32$. The pulse duration is 20ps and the laser is detuned by 1meV. Due to the effective coherent population transfer to the excited state [10], they predicted an indistinguishability of 98%. This excitation regime seems not to deteriorate this emission property which remains similar to the one measured in resonant fluorescence [9,61].

4.4.2 Prediction of the single-photon purity

Concerning the expected emission purity, Cosacchi et al. [227] demonstrated that this excitation regime should allow to reach higher purity than under resonant excitation. This is explained by exploiting the three-steps process principle of the LA-phonon assisted scheme.

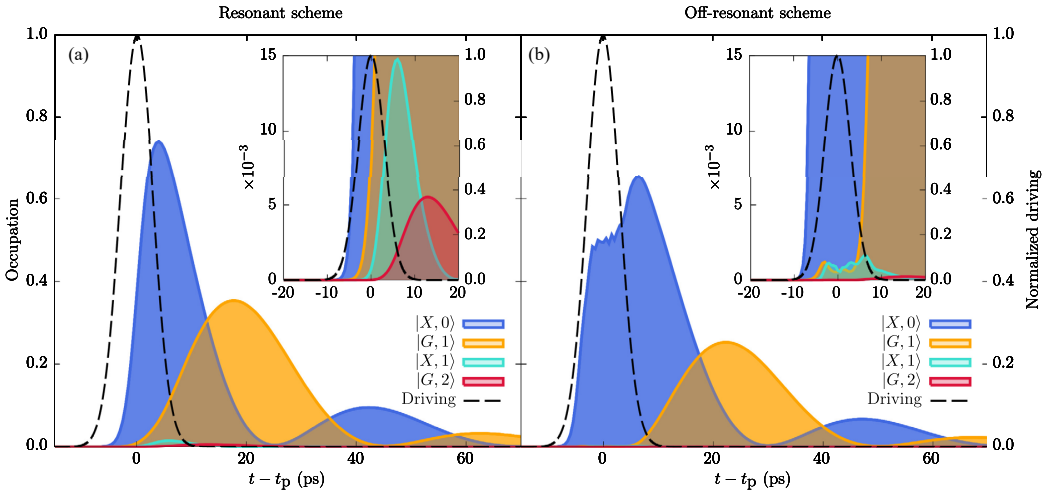

Figure 4.10: From reference [227]. Comparison of the time-dependence occupations (a) under resonant excitation, at "π" and (b) under LA-phonon assisted excitation. The 7ps laser pulse is plotted by the black dashed lines. The first excitation/emission process corresponds to the states $|X,0\rangle$ (blue) and $|G,1\rangle$ (yellow) while the QD re-excitation is represented by the states $|X,1\rangle$ (green) and $|G,2\rangle$ (red). The two insets are scale enlargements between $\pm$20ps.

Figure 4.10, from Cosacchi et al. [227], shows the comparison of the different excitation steps time dependence, between the resonant and the LA-phonon assisted schemes. They considered a GaAs QD embedded in a cavity and excited with a 7ps pulsed laser. The cavity parameters are $\hbar g = 25\mu$eV and $\hbar\kappa = 50\mu$eV, while QD lifetime is 33ps. Hence, the Purcell factor is 2.5. The occupation of the successive QD states are plotted as a function of the delay after the laser pulse (black dashed line). In blue, this is the occupation evolution of the state $|X,0\rangle$, where the number (0,1 or 2) refers to the photon number in the Fock state basis. It corresponds to the QD excitation before any photon emission in the cavity. In yellow, the electron-hole pair recombines and a photon is emitted ($|G,1\rangle$). The two last states correspond to the re-excitation process. In green, the QD state is excited after the first photon emission ($|X,1\rangle$) while $|G,2\rangle$ represents the relaxed state after the second photon emission. Let us now consider the LA-phonon assisted excitation (figure 4.10b), even though the occupation of the state $|X,0\rangle$ increases straight after the begining of the laser pulse, it reaches quickly a plateau during which the phonon-assisted relaxation occurs. Then, as previously discussed with the population transfer from $|\beta\rangle$ to $|X\rangle$, it keeps building up at the end of the laser pulse, which causes a delay of the photon emission ($|G,1\rangle$). This delay significantly reduces the probability of re-excitation. A comparison with the plots of figure 4.10a enables the authors to conclude that the expected single-photon purity of the emission could then be higher than under resonant excitation.

However, we cannot directly apply their conclusions to our experimental work. It seems

they considered parameters to obtain a clear increase of the emission purity under a strong coupling regime. Indeed, under resonant fluorescence, the highest purity is 90.7%, which is lower than the experimental state of the art of about 99% [9, 61]. Moreover, the laser pulse duration is about 7ps, and it seems they intentionally reduced the source brightness by setting the energy detuning a little above or below 1meV. We can then notice that decreasing the first lens brightness by about 18% enables them to increase the purity by about 7%. So, even if they estimated a maximum purity under LA-phonon assisted regime at 98.8%, this is only in this particular case and at the cost of the brightness. However, this work pointed out the ability of the LA-phonon assisted excitation scheme to improve the purity of a source in some unfavourable conditions. In our case, we always opt for the highest brightness. Hence, the excitation laser parameters are optimised with a pulse area above 10π, a detuning by about 1meV and a pulse duration above 19ps. Moreover, with a Purcell factor about five times higher, the spontaneous emission of our sources is then more enhanced. The higher Purcell factor and the longer pulse duration might allow QD re-excitations although the three-step process of excitation should avoid it. As a consequence, the gain in single-photon purity might be more limited than in the work of Cosacchi et al.

In any case, the LA-phonon assisted excitation is theoretically a promising way to invert the population of a two-level system and have a coherent transfer to the QD excited state at the end of the pulse. We can then have an emission of single and indistinguishable photons with a high brightness. Next parts will focus on the experimental results we obtained with our source, using the excitation parameters as previously discussed.

4.5 Characterisation of the source under LA-phonon assisted excitation

4.5.1 Adaptation of the optical setup

In chapter 3, the described confocal microscope was optimised for resonant fluorescence experiments. This excitation scheme required a polarisation selection to filter the laser. This was ensured by a PBS. Since under LA-phonon assisted excitation the laser is spectrally filtered, the optical system design is then different.

The first design is directly based on the free(space microscope optimised for resonant fluorescence experiments. As shown in figure 4.11a, the PBS is replaced by a 90:10 BS. It ensures a high single-photon collection but only 10% of the laser power is sent to the source. In part 4.3.2.2, we concluded that this excitation scheme requires, at least, a pulse strength around 10π. With our system, due to the high coupling efficiency of the excitation beam and the laser repetition rate of 81MHz, the power corresponding to the "π-pulse" is about few nanowatts. It is then easily possible to reach pulse strengths above 10π. The other change is about the insertion of three or four high transmission bandpass filters in the collection path. The latter have a bandwidth of 0.8nm. To filter the laser, detuned by about 0.6nm from the

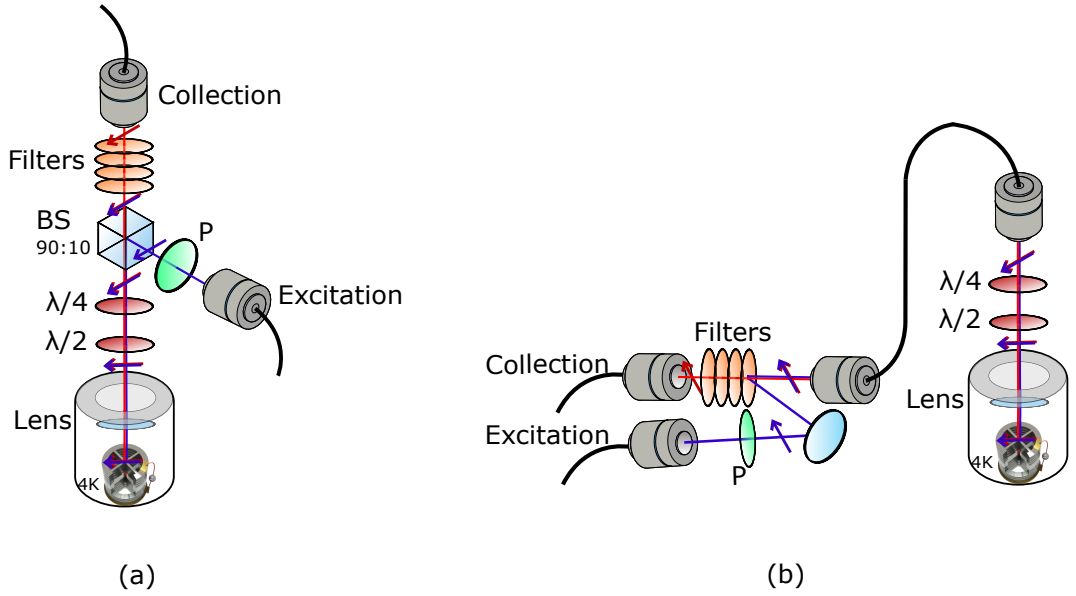

Figure 4.11: Schematics of the confocal microscope optimised for LA-phonon assisted excitation. (a) Free-space microscope based on the RF design (b) First fibred design of the microscope.

ZPL, without reducing the collection of the single photons, they are tilted in relation to each other. Although the polarisation is no longer used to filter the laser, the excitation polarisation must be still controlled to allow for a precise excitation of one of the QD linear dipole, and a polarised emission. A polariser, a quarter and a half wave-plates are then used to set the linear polarisation in accordance with the QD polarised-axis. The quarter waveplate allows the correction of any ellipticity to have a pure linear-polarisation. Since, the pillar mode matching and the high transmission are still required, the rest of the optical system remains the same.

	Version 1 (figure 4.11a)	Version 2 (figure 4.11b)
Waveplates	97%	97%
90:10 BS	80%	–
Bandpass filters	80%±2%	80%±2%
Coupling	70%±5%	76%±5%
Total	**44%±5%**	**59%±5%**

Table 4.1: Loss budget of the two versions of the optical system.

Table 4.1 summarises the loss budget of the two optical system versions. Due to the tilted bandpass filters and the fact that in practice, the BS has a transmission of 80%, the free-space system has an efficiency around 43%±5%. Since the transmission is still less than the one for resonant excitation, some changes have been made to fix the source of losses, leading to the fibred setup presented in figure 4.11b. Removing the 90:10 BS and using a less

lossy collimator enable to reach a transmission of 59%±5%. For this system, the coupling efficiency takes into account both the collimator/collimator coupling efficiency and the cavity rotated light coupling into the collimator placed above the cryostat. Other changes, such as bandpass filter with higher transmission or less lossy fibre to fibre connectors, should increase the microscope transmission by at least 10%

Thanks to the spectral filtering of the excitation laser, this microscope has been proven to work in "parallel-polarisation" configuration. Under this excitation regime, the polarisation ellipticity of the reflected laser, due to the pillar birefringence, is no longer an issue. Both the excitation and the collection can be set along the same polarisation axis, for instance, along one of an exciton linear dipole ($|X\rangle$ or $|Y\rangle$). To do so, the polariser placed in the excitation path, and the waveplates above the cryostat chamber allow to set and rotate the laser linear-polarisation to match it with one of the QD dipoles. To find the proper angle, we temporarily add a polariser in the collection path to collect only the orthogonal polarisation.

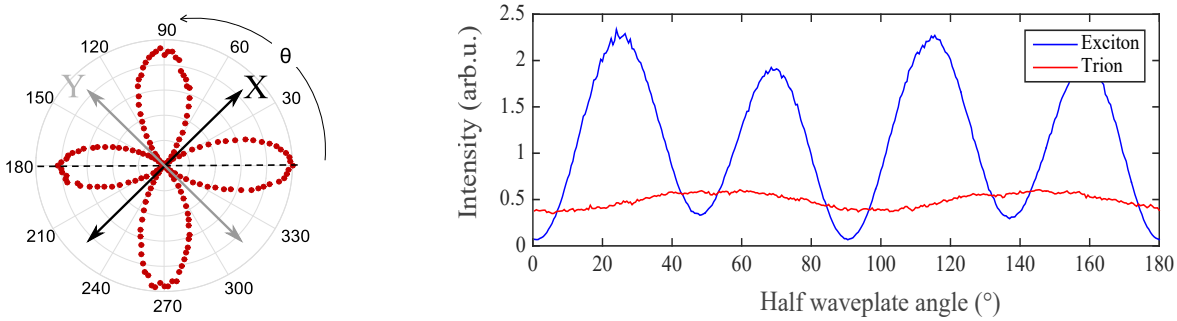

(a) (b)

Figure 4.12: (a) Plot of the collection intensity as a function of the angle of the linear polarisation of the excitation laser. Due to the cross-polarisation configuration, exciting along one of the dipole vanishes the collection. (b) Collected signal from either an exciton (blue line) or a trion (red line) as a function of the half waveplate angle. The system is in cross-polarisation configuration.

Figure 4.12a plots the collected signal intensity from an exciton as a function of the half waveplate angle. The two dipole axes $|X\rangle$ or $|Y\rangle$ are represented by arrows. On this figure, we can notice that the signal vanishes when the excitation has a linear polarisation along one of the QD dipoles, $|X\rangle$ or $|Y\rangle$. Indeed, due to the cross-polarisation collection, once the excitation polarisation set along X or Y, almost no signal is emitted by the other dipole (more detailed in next part). For any linear polarisation in between, a part of the emitted photons are collected in the orthogonal polarisation from the excitation's. We then measure the signal oscillations presented by the blue line of figure 4.12b. On the contrary, since a trion emits unpolarised light under linearly polarised excitation, rotating the half-waveplate should not drastically affect the collected signal intensity (red line).

When we measure oscillations, we set the half waveplate angle to collect a minimum of signal from an exciton, while with a trion its angle is not an important parameter. Then, we remove the collection polariser. In this condition, the QD is optimally excited and all the emitted photons are collected.

Finally, in order to control the laser pulse duration, different solutions have been considered such as the use of a "homemade" monochomator based on the 4f principle.

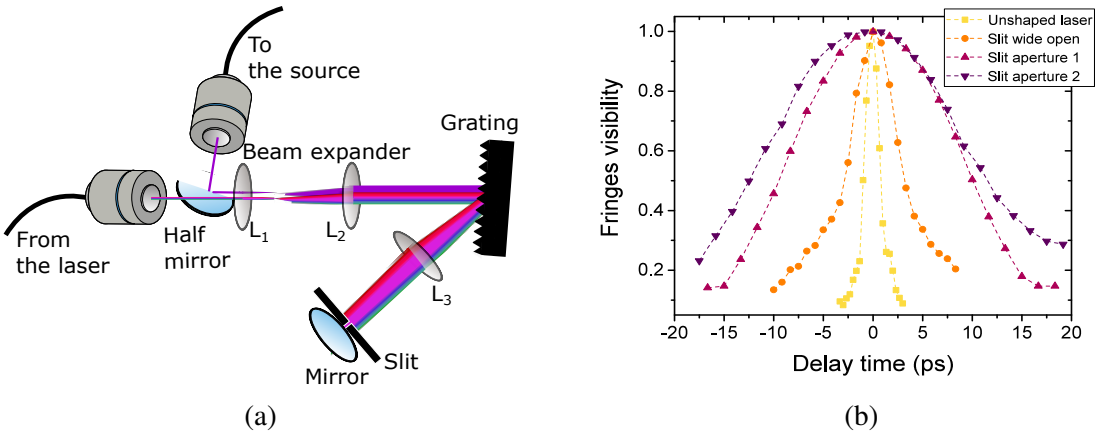

(a) (b)

Figure 4.13: (a) Schematics of the homemade monochromator based on the 4f principle. The focal length of the lenses are f_1 = 3.5cm (for L_1), f_2 = 15cm (for L_2) and f_3 = 40cm (for L_3) (b) Pulse duration of the unshaped laser (yellow rounds), and of the shaped laser for three different slit apertures. Closing the slit makes the pulse longer.

As depicted in figure 4.13a, the 4f-line pulse shaper is composed of a beam-expander, to illuminate the grating with a 2cm diameter spot, a grating, and a lens, to focus each wavelength in the Fourier plane where a slit and a mirror are positioned. In usual 4f optical setup, all the components are doubled to generate a spectrally uniform collimated beam. To make it more compact, we place a mirror right after the slit with a small angle with respect to the orthogonal position. It then reflects the selected wavelength which comes back with a slight angle. This allows to spatially separate the shaped beam from the incident beam. A "D-shaped" mirror is then placed on the reverse way to send the shaped laser beam to the source. Thanks to a precise control of the split lateral position and of its aperture, we can respectively spatially select the central wavelength of the shaped laser and change its pulse duration (figure 4.13b). By filtering specific frequency components in the Fourier plane, closing the slit allows to increase the laser pulse duration. To make the system even more compact and increase its transmission, we also studied fibred Bragg grating. This system looks like a fibred beam splitter whose central part is manufactured as a grating. The shaped laser is then transmitted and goes out from one output while the rest of the spectrum is reflected and send in the second output of the filter. The central wavelength can be slightly tuned by applying a stress on the grating or by changing the temperature. But, with this solution the pulse duration is fixed.

4.5.2 Measured emission from a QD under LA-phonon assisted excitation

4.5.2.1 Comparison with the resonant excitation

To validate the LA-phonon-assisted excitation scheme as a way to get a bright source of single and indistinguishable photons, the performances have been measured. According to the theory, the occupation probability of the exciton is expected to be lower than under resonant excitation. Experimentally, we estimated it from the intensities obtained at "π" (resonant excitation) and at maximum fluorescence intensity (LA-phonon assisted excitation).

To compare the resonant and the LA-phonon assisted regimes, the measurements have been performed in the cross-polarisation configuration. We worked with an InGaAs QD embedded in a pillar and excited by a 16ps pulsed laser. Since the theory only considers a two-level system, a charged exciton in zero magnetic field has been used. Indeed, in the cross-polarisation configuration, a trion can be considered as a two-level system while, due to the FSS, an exciton is a three-level system.

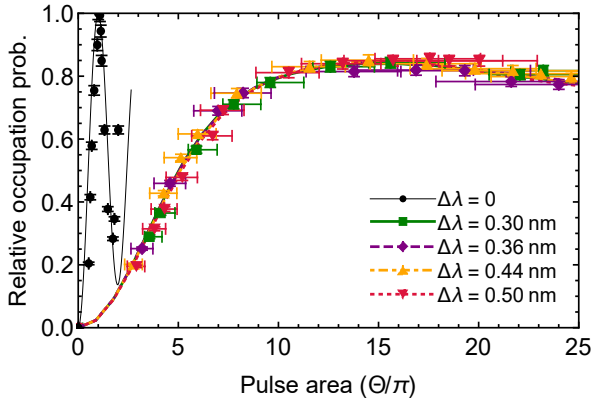

Figure 4.14: Measured relative state occupation probabilities under resonant and LA-phonon assisted schemes at 7K. We considered a charged exciton excited in cross-polarisation configuration by a 16ps pulsed laser. Four laser detunings have been used under LA-phonon assisted excitation. The error bars are within the size of the plotted points. The emission intensity is normalized to the maximum achieved under resonant excitation to allow comparison of the relative occupation probability between the two schemes. The solid lines give the theoretical prediction based on the model in reference [226]. The considered cavity parameters are $\hbar\kappa$ = 20.6μeV, $\hbar$g = 6.58μeV and $\hbar\gamma$ = 0.658μeV, so F_p = 12.8.

Figure 4.14 presents the relative occupation probability as a function of the laser pulse area at various laser detunings. The pulse area is proportional to the square root of the intracavity power. We estimate it by correcting the power measured above the cryostat chamber by the cavity transmission. The latter depends on the pillar quality factor and plays a filtration role on the excitation laser depending on the detuning. As a consequence, increasing the laser detuning from resonance leads to an increase of the required laser power to reach maximum fluorescence intensity. The experimental results are plotted with squares, whose size includes the error bar. The solid lines show the theoretical prediction from [226] using the experimental parameters of our system. They reproduce qualitatively well the experimental data. The

considered cavity has a lifetime of 32ps, a QD-coupling rate of $\hbar g = 6.58\mu$eV and the QD lifetime is about 1ns ($\hbar\gamma = 0.658\mu$eV) without the cavity coupling. Hence, the Purcell factor is 12.8. The Rabi oscillations measurements (black squares and lines), in resonant excitation, are used as reference to convert the fluorescence intensity into relative occupation of the excited state. For the considered range of detuning the LA-phonon assisted excitation is predicted to stay highly efficient. This is confirmed by our experimental results which show almost no change of the occupation probability as a function of the detuning. Remarkably, we obtained a reduction of the maximum occupation probability as compared to resonant excitation of only $15\%\pm1\%$. This demonstrates that the off-resonant phonon-assisted excitation scheme is very efficient, in agreement with the various theoretical works described above.

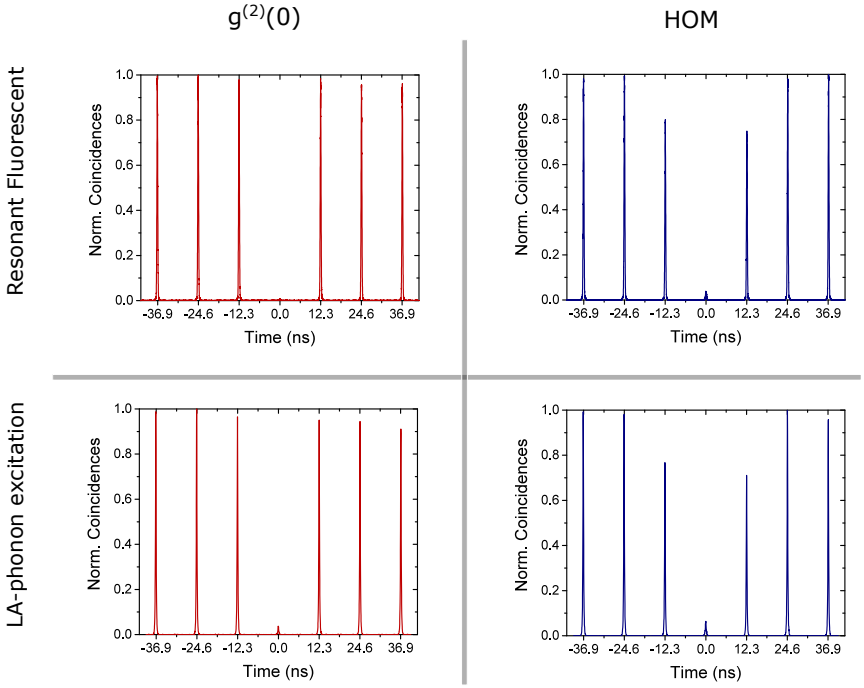

Figure 4.15: Plots of the second order correlation (red traces) and the mean wave packet overlap (blue traces) measurements under resonant and LA-phonon assisted excitations. The measured system is an exciton excited in cross- (RF) and parallel-polarisation (LA-phonon) configuration with a 16 ps laser. Under LA-phonon assisted excitation, the laser detuning is Δ_λ = -0.6nm.

The purity and indistinguishability of the emitted photons for the two schemes have been compared. Since for these measurements we considered an exciton, under LA-phonon excitation they have been performed in the parallel-polarisation configuration. Figure 4.15 presents the $g^2(0)$ (in red) and the HOM visibility (in blue) traces under both excitation regimes. Between the resonant and the LA-phonon assisted excitations, the purity is respectively 0.989 ± 0.001 and 0.943 ± 0.001 while the corrected indistinguishably [171] is 0.915 ± 0.001 and 0.920 ± 0.005. As expected, the LA-phonon assisted excitation does not affect the photon indistinguishability. However, the $g^2(0)$ under LA-phonon assisted excitation is significantly higher than under resonant excitation. We do not fully understand the reason of this increase. It may be due to imperfect suppression of the laser, or due to re-excitation processes when

using long pulse durations. As seen previously, opting for the highest brightness may limit the photons purity from an exciton which is now considered as a two-level system.

4.5.2.2 Linear polarisation purity from a linear dipole

Since the laser is spectrally filtered, the cross-polarisation configuration is no longer required. As seen in the two previous chapters, the pillar, and the QD have polarised axes. Under resonant excitation, the laser polarisation is set to one of the pillar axis, $|H\rangle$ or $|V\rangle$. In this condition, the laser light remains linearly polarised along this axis and only the single photons emitted in the orthogonal polarisation are collected.

Under LA-phonon assisted excitation, it is possible to align the laser polarisation along one of the dipole axis, $|X\rangle$ or $|Y\rangle$. As seen in chapter 2 part 2.6.3, according to the considered QD state, the selection in polarisation is different. An exciton presents two linearly-polarised dipoles separated in energy by the fine structure splitting, while there is no strict selection rules in linear polarisation basis for a trion. Some quantum applications require bright sources of polarised single photons [54]. So, to fulfil it with a trion, which emits unpolarised light (under linearly polarised excitation), we must add a linear polariser and then we lose half of the photons. However, the parallel-polarisation configuration enables us to set the linear polarisation of the laser along one of the exciton dipoles ($|X\rangle$ or $|Y\rangle$) (part 4.5.1). As a consequence, the selected exciton dipole becomes a genuine two-level system. Since only one dipole is excited, the emitted light must have a high degree of linear polarisation, which is a key component in optical quantum technologies.

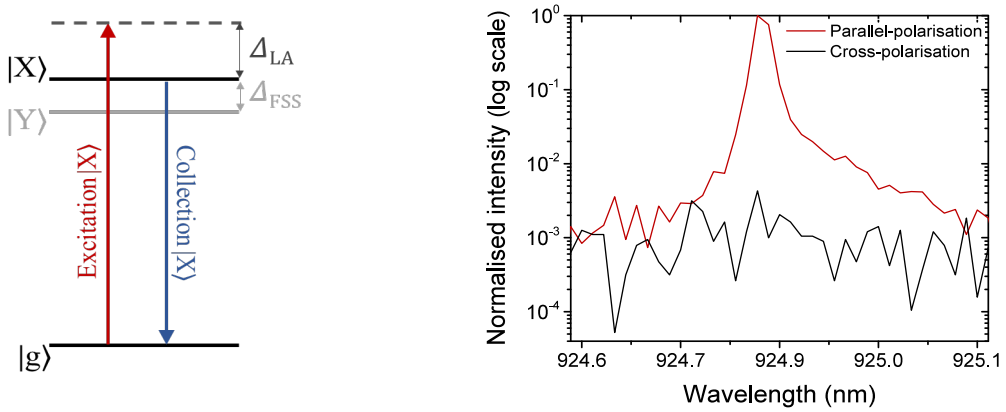

(a) (b)

Figure 4.16: (a) Schematic of the exciton excitation scheme in parallel-polarisation configuration. The excitation laser, polarised along X, is detuned by Δ_{LA} from the resonance. After the phonon emission, the exciton dipole $|X\rangle$ emits a photon along the X polarisation. (b) In red (black), the signal is measured when the excitation laser is aligned on one of the two exciton dipole axis, and the collection polarisation is aligned parallel (orthogonal) to this direction.

To measure the linear polarisation purity of the emission, a half-waveplate followed by a polariser is placed in the collection path. When the linear polarisation of the excitation is

aligned with one of the dipole axes, for instance $|X\rangle$, the emission has the same polarisation. The collection polariser is aligned along this linear polarisation. The half-waveplate is used to rotate the direction of the analysed polarisation. In figure 4.16b, the red solid line corresponds to the situation when the exciting laser has a linear polarisation along the dipole $|X\rangle$, and when the collection is parallel. Then, by rotating the half-waveplate, we set a cross-polarisation configuration. Since the laser excites precisely the dipole $|X\rangle$ and there is no exciton spin flip during the exciton lifetime, no signal is emitted along the orthogonal polarisation corresponding to the dipole $|Y\rangle$. In collection, the "almost-flat" black signal is then measured. The degree of linear polarisation is calculated following $D = \frac{I_{//} - I_{\perp}}{I_{//} + I_{\perp}}$. From the measurement of three sources, we obtain an average of D = 98.2%$\pm$0.4%. This method enables to work in parallel-polarisation configuration and then have the bright sources of highly polarised single photons required for quantum applications [54].

4.5.2.3 Benchmarks of a linear dipole emitter

To completely fulfil the quantum application requirements, this linear dipole must emit single and indistinguishable photons wit a high efficiency. In part 4.5.2.1, we made a comparison between the resonant and LA-phonon assisted scheme in cross-polarisation. The goal now is to fully characterise our source in parallel-polarisation configuration. Figure 4.17 presents the first lens brightness (a), the second order correlation (b) and the corrected mean wavepacket overlap (c) [171] measurements as a function of the laser pulse duration at various laser detunings. The polarisation of the excitation laser is aligned with one of the two exciton dipoles and the power is adjusted to maximise the emission.

As discussed above, the occupation probability when using LA-phonon assisted excitation is around 15% less than under resonant excitation. However, due to parallel collection and the spectral suppression of the excitation laser, all of the photons can be collected. Hence, we no longer consider the polarised first lens brightness which is the main collection limitation in resonance fluorescence experiments. According to figure 4.17a, a short detuning (Δ_λ = -0.4nm) and a long pulse duration ($\tau \approx$ 22ps) enable to get a first lens brightness above 50%$\pm$1%. Even though it is still limited by the extraction efficiency of the connected pillars cavities, with a confocal microscope transmission around 59%$\pm$5% (version 2), we are then able to get a fibred brightness of 30%$\pm$5%. This is about a factor of three higher than that we could achieve in resonant excitation, evidencing the potential of LA-phonon assisted excitation as a route towards bright single-photon sources.

Figure 4.17b considers the influence of the same parameters on the mean wavepacket overlap measurement. As predicted by Gustin et al. [226], it is above 90%. The plotted values are corrected by the second order correlation of the emission following the model of reference [171]. After this correction, the photon indistinguishability does not seem affected by neither the pulse duration nor the laser detuning.

Finally, figures 4.17c and 4.17d report the second order correlation measurement. Figure 4.17c plots the influence of the detuning and the pulse duration while figure 4.17d plots it as a function of the measured first lens brightness. We can then notice that optimising the first lens brightness deteriorates the single-photon purity. As discussed previously, even if a small detuning seems to allow for higher purity, a trade-off needs to be found between first lens brightness and emission purity. Concerning the limitation of the purity around 96%, even for

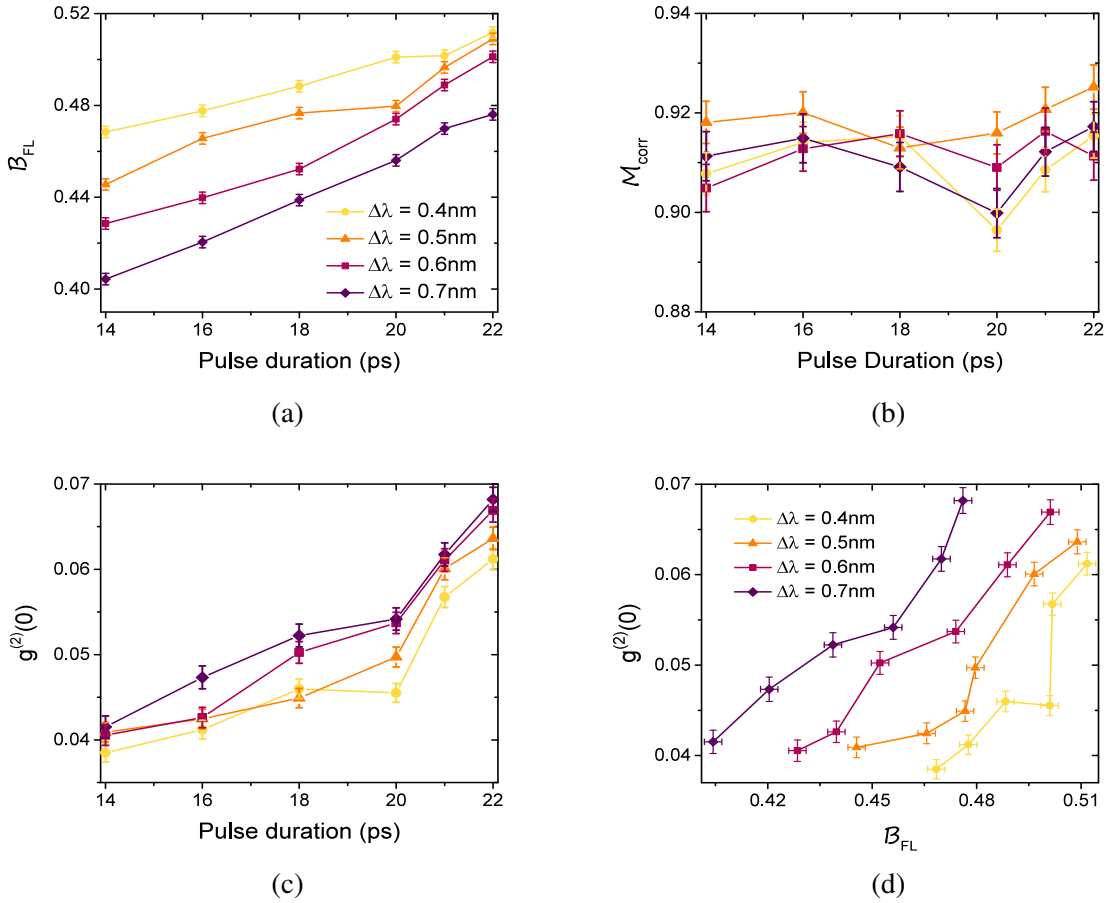

Figure 4.17: Plots of (a) the first lens brightness ($\mathcal{B}_{\mathrm{FL}}$), (b) the corrected mean wavepacket overlap ($\mathcal{M}_{\mathrm{corr}}$) and (c) the second order correlation ($g^{(2)}(0)$) as a function of the pulse duration at various laser detunings for the resonance. The emission is from one of the two exciton dipole and is collected in parallel-polarisation configuration. The mean wavepacket overlap is corrected by the $g^2(0)$ values with the equation from reference [171]. (d) Plot of the purity as a function of the first lens brightness ($\mathcal{B}_{\mathrm{FL}}$).

shorter pulse durations, this is mainly due to a non-optimised laser filtering. Indeed, adding a Fabry-Prérot ethalon in the collection path enables us to reach purity above 98% for 19ps laser pulses.

In conclusion, our results show that we have significantly increased the fibred brightness of our sources, while maintaining high their other qualities for quantum applications.

4.5.3 Experimental results from several sources and limitations

Given the right range of values for the laser parameters, multiple sources have been characterised and used with the fibred optical system presented in part 4.5.1 (version 2). In

order to work in parallel-polarisation configuration and have linearly-polarised emitted photons, only excitons are considered. We then detail the emission characteristics from sources A2, B2, C1 and D2 (table 4.2). The emission indistinguishabilities are corrected following reference [171].

Sources A2 and B2, and sources C1 and D2 are respectively from the same wafer. They have the same planar cavity parameters but they are differently annealed. Considering A2 and B2, the wafer parameters are Q=3000-4000, β = 78% and η = 84%. For C1 and D2, they are Q=10000-14000, β = 88% and η = 70%.

Source	First lens brightness	Fibred brightness	Purity	Corr. indistinguishability
A2	49%	28.9%	95.5%	91.5%
B2	13.8%	8%	–	–
C1	28.5%	16.8%	94.7%	95%
D2	19.1%	11.3%	96.8%	–

Table 4.2: Emission characteristics of different sources under LA-phonon assisted excitation.

.

The source A2 is the one presented in part 4.5.2.3. To get a purity above 95.5% and a corrected indistinguishability above 90%, the laser detuning is -0.4nm and the pulse duration is 18ps. The associated first lens brightness is then 49%. To calculate its fibred brightness ($\mathcal{B}_{\mathrm{F,\,LA}}$), we consider the transmission of the fibred optical system, T_{setup} = 59%$\pm$5%.

Considering sources B2, C1 and D2, they are excited by 19ps pulsed laser whose the detuning is about Δ_λ = -0.5nm. The source C1 is the same as the one presented under resonant excitation (chap 3, part 3.5.3.2). Since, source D2 was not annealed, the bias of -1V enables us to stabilise the QD state and the temperature is set at 15K to put it in resonance with the pillar energy. The fibred brightnesses ($\mathcal{B}_{\mathrm{F,\,LA}}$) are calculated from the measured photon count rates corrected by the APDs efficiencies. The first lens brightness ($\mathcal{B}_{\mathrm{FL,\,LA}}$) is then estimated with the microscope transmission, T_{setup} = 59%$\pm$5%.

We can notice that, excluding source A2, the exciton occupation probabilities did not actually reach 85% of the occupation under resonant fluorescence, being limited to about 60%. For the moment there is no clear explanation of this effect. But as a consequence, the fibred brightness remains intrinsically limited by a less efficient excitation regime. In any case, except for source B2, the first lens brightnesses ($\mathcal{B}_{\mathrm{FL,\,LA}}$) are higher than the polarised first lens brightnesses ($\mathcal{B}_{\mathrm{PFL,\,RF}}$) from excitons under resonant excitation (chap 3, part 3.5.2). This still leads in the end to higher fibred brightnesses ($\mathcal{B}_{\mathrm{F,\,LA}}$).

Considering source B2, the low brightness is due to the excitation of two close QD transitions. Since, the laser energy does no longer correspond to one of the QD state energy, two of them can be excited. As plotted in the inset of figure 4.18a, there is a sort of competition and the emission is from two QD transitions. Figure 4.18a presents the occupation probability of the QD state as a function of the pulse area. The probability is normalised with the maximum intensity obtained under resonant excitation. Even though the laser detuning is small (Δ_λ =

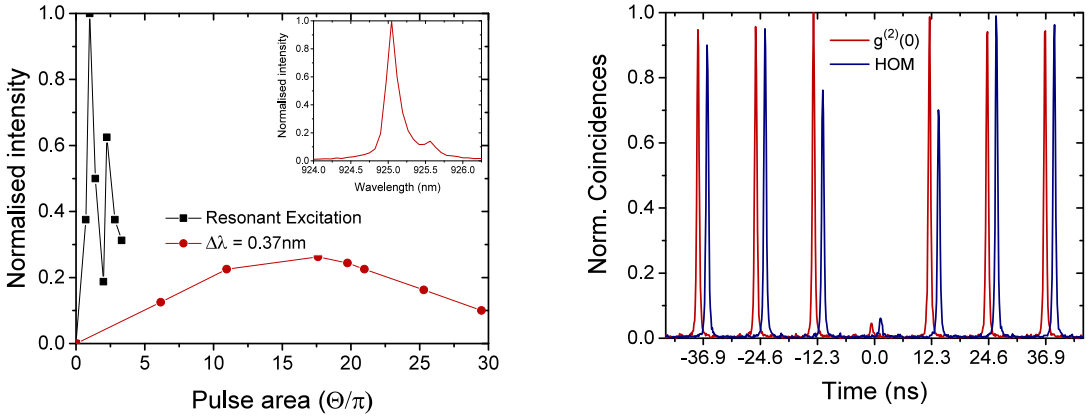

(a) (b)

Figure 4.18: (a) - Sample B2 - Comparison of the state occupation probabilities under resonant and LA-phonon assisted schemes. The measured relative emission intensity for an exciton collected in cross-polarisation are plotted as a function of the 22ps laser pulse area. The error bars are within the size of the plotted points. **Inset** QD emission under LA-phonon assisted excitation, and in parallel-polarisation configuration. The laser is detuned by Δ_λ = -0.5nm. Two states are in resonance with the cavity. (b) - Sample C1 - Plots of the second order correlation (red trace) and mean wave-packet overlap (blue trace) measurements. The HOM visibility line is 2ns offset for clarity. It is from an exciton emission collected in parallel-polarisation configuration with a 19ps laser (Δ_λ = -0.6nm).

-0.37nm), the state occupation probability under LA-phonon assisted excitation is about 25% of the occupation at "π". The excitation is not efficient. Finally, since the emitted photons are from two states, the indistinguishability is below 80%.

Figure 4.18b presents the emission purity (red trace) and indistinguishability (blue trace) of the source C1. Considering sources A2 and C1, the corrected emission indistinguishability is above 90%, as predicted by the theoretical paper [226]. Nevertheless, as discussed above, the purity of each source stays below 96%.

4.6 Conclusion

The LA-phonon assisted excitation is a three-step process which has been well theoretically described from 2010 to 2019, showing successively the possibility to efficiently excite the QD, to improve the single-photon purity and to reach high indistinguishability. Our work, implementing this excitation scheme for a QD in a cavity, and exploiting the exciton transitions is the first one to demonstrate the interest of this approach for efficient single-photon sources. This excitation scheme is all the more efficient when the laser parameters are carefully chosen. For our sources a pulse duration above 19ps, a pulse area above 10π and a detuning between

-0.15nm to -0.8nm from the resonance enables us to reach an occupation probability around 85% of the occupation under resonant fluorescence. Thanks to a continuous optimisation of the optical system and the parallel-polarisation configuration, the fibred brightness reaches values from 11% to 29% in accordance with the source first lens brightness. Concerning the photon indistinguishability, it follows the theoretical expectation and is above 90%. Nevertheless, the photon purity remains below 96%. Finally, the parallel-polarisation configuration enables us to collect all the photons emitted with a high linear polarisation purity. This excitation regime is very promising, and allows to overcome the brightness limitation imposed by the resonant excitation while guaranteeing a high photon purity and indistinguishability.

Chapter 5

A fibre-coupled source: collection of the emission in a single mode fibre

"De l'audace, encore de l'audace, toujours de l'audace !"

attribuée à Danton

5.1 Introduction

Up to this point, the source devices were controlled with a free-space confocal microscope. After working on the optical system optimisation (chap. 3) and on another excitation scheme (chap. 4), this chapter will broach the study of fibre-coupled sources. The aim is now to overcome the need of a large, complex and expensive low-vibration cryogenic system and nano-positioners in order to provide a "plug-and-play" single photon source. This chapter will describe the way to implement a single-mode fibre above a pillar source to directly collect single photons. An optical system is then used to filter the remaining excitation laser either with cross-polarisation or with spectral filters. This module fits in standard racks [228, 229], and permits to significantly increase single-photons collection.

Many attempts to precisely fix a fibre above a single photon source have been undertaken. Due to the high precision positioning requirement and the need, in most cases, to cool the source at 4K, this technique remains challenging. The group of H. Sasakura [230] proposed a source/fibre coupling with two collimating lenses but the system required an active positioning at low temperature. Other groups obtained very promising results of direct coupling between the source and the single-mode fibre: G. Shambat et al. [231] and D. Cadeddu et al. [124] proposed respectively photonic crystal cavities or nano-trumpets attached to fibre tips. Recently, H. Snijders et al. [207] succeeded in embedding a source between two single-mode fibres. They measured a fibred brightness of $5\% \pm 2\%$ with a cavity-mode-to-fibre coupling of 85%, showing the ability to get a bright source of single and indistinguishable photons.

In this chapter, we report the results of fibre-coupling self-assembled InGaAs/GaAs QDs deterministically embedded in pillars in different types of cryostats.

The first part will set the different optical components used in this study. We will also detail the validation of the *analytical* model used to estimate the coupling efficiency between a fibre and a pillar.

In the second part, we will discuss how to optimise the coupling configuration. This part will detail the results obtained with either so-called "lensed fibres" or standard fibres.

Finally, the third and fourth parts will present the experimental results measured with fibre-coupled sources. The third part will consider a fibre set above the source in a low-vibrations cryostat while the fourth will present the performances in a standard cryostat. In both cases, emissions and coupling results will be detailed and compared with the free-space performances.

5.2 Description of the studied components and experimental validation of the theoretical model

In chapter 3, we measured coupling efficiency in between two collimators in front of each other. However, measuring the coupling efficiency between the single photons at the pillar output and a single-mode fibre is more challenging. Indeed, this is the ratio between the pillar emission and the output of the single-mode fibre placed at few microns above it, when both are in a cryostat at 4K.

First, the components used for both the theoretical and the experimental studies are described. In the second part, we detail the validation of the theoretical coupling efficiencies by considering standard fibres coupled at room temperature.

5.2.1 Theoretical and experimental studies

In order to estimate pillar to fibre coupling, pillar diameters must be considered. Experimental measurements estimate them between 2μm and 3.4μm, permitting to calculate the emitted beam sizes at the output of the pillar following the work of A. Yariv [199] and of Nowak et al. [169]. Table 5.1 summarises the data for the four pillar sizes which will be considered in this chapter.

The numerical apertures are estimated by propagating the beam and fitting its divergence angle, while the Rayleigh distances are calculated following $z_r = \frac{\pi {w_0}^2}{\lambda}$.

In this chapter, two kinds of single-mode fibres will be considered. The first is a standard fibre used in laboratories, optimised to work at 930nm and with a core diameter of 4.4μm; it will be called SM(4.4μm). The second is a fibre with a high numerical aperture (NA) and will be called SM(hNA). To achieve this large numerical aperture whilst working in the range of near infrared wavelengths, the core and the cladding of such fibres must have wide different refractive indexes [232]. Different techniques have been developed such as chalcogenide glass cores (AsSe) and a GeAsSe cladding glass [233] or claddings with high air-filling fraction

Connected pillar diameter	Emitted beam diameter ($\frac{I_{max}}{e^2}$)	Pillar numerical aperture	Rayleigh distance
2μm	1.85μm	0.37	2.9μm
2.3μm	2.22μm	0.3	4.16μm
2.8μm	2.59μm	0.25	5.66μm
3.4μm	2.96μm	0.2	7.4μm

Table 5.1: Emitted beam diameters at $\frac{I_{max}}{e^2}$ and the numerical apertures of the four pillars which will be considered in the theoretical predictions of this chapter.

[232, 234]. The fibre studied in this chapter has been chosen for its NA of 0.35 and its core diameter of 1.8μm. As shown in figure 5.1, contrary to SM(4.4μm) fibre, with this NA and an output beam diameter equal to 2.16μm, the beam propagation is similar to the one from a pillar. This can be interesting to perform coupling without a lens. In this case, the system must be as symmetrical as possible.

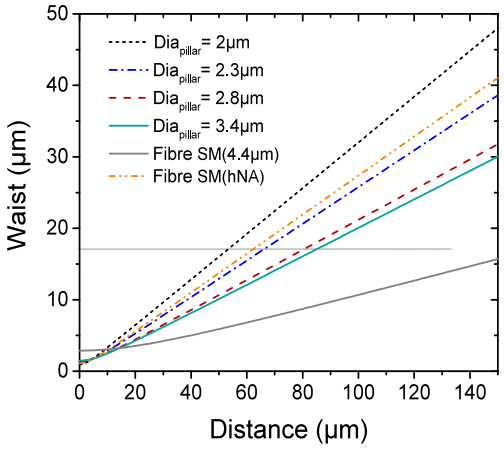

Figure 5.1: Beam waist as function of the propagation distance from pillars of different diameters or fibres.

In this study, we will consider coupling efficiencies between fibres and pillars. Nevertheless, to validate these experimentally, as shown in figure 5.1, pillars will be emulated by a high-NA fibre with a 1.8μm core. To make the distinction between a fibre with a high numerical aperture used to fibre a pillar and the same fibre used to emulate a pillar, the fibre will be respectively called SM(hNA) and SM(emulated).

Considering either single-mode fibres or pillars, all studies have been carried out in the Gaussian approximation [199, 201].

5.2.2 Validation of the analytical model used to estimate the coupling efficiency

To validate the theoretical predictions given by the *analytical* model (detailed in chap. 3), the coupling efficiencies between fibres with different core diameters have been measured; SM(4.4μm) and SM(hNA) fibres are considered. The system theoretically simulated and experimentally used is drawn in figure 5.2a.

Experimentally, two fibres are placed in front of each other: one is set on a fixed support while the other on a translation stage. The coupling efficiency is defined using:

$$C_{\text{exp}} = \frac{P_{\text{out}}}{P_{\text{in}} \times T_{\text{fibre}}}$$

with P_{in}, the power at the output of the "Source" fibre, and P_{out}, the one at the output of the "Collection" fibre. The latter is corrected by the "Collection" fibre transmission, T_{fibre}. Since, this depends on the fibre type and its connectors (PC or APC), the value is measured at the beginning of each experimental study. For instance, the SM(hNA) fibre is always spliced to a SM(4.4μm) fibre and the transmission measured to be in between 57% and 95% in accordance with the splice quality.

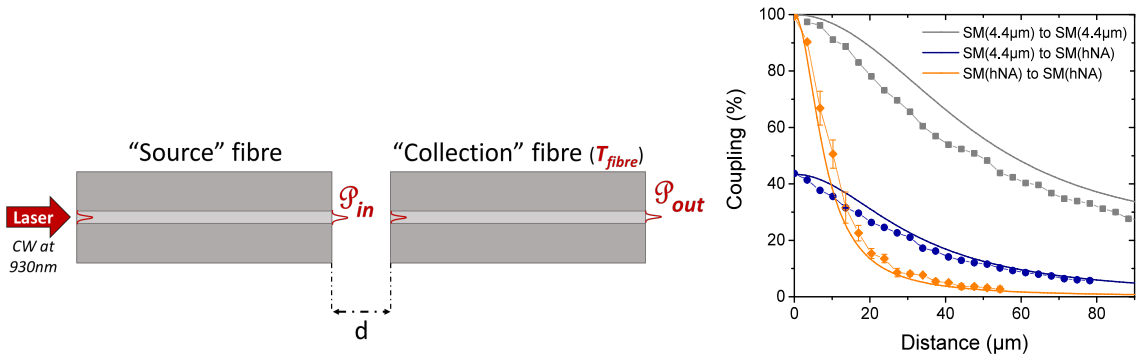

(a) (b)

Figure 5.2: (a) Schematic of the system. Two fibres are place in front of each other; the laser, used for the study, is a continuous-wave diode at 930nm. (b) Coupling efficiency between (grey lines -squares-) two SM(4.4μm), (blue lines -circles-) a SM(4.4μm) and a SM(hNA), and (orange lines -diamonds-) two SM(hNA), as a function of the distance. The theoretical results are plotted in solid lines while the experimental measurements are in dashed lines with symbols. When not visible, the error bars are within the size of the symbols size.

Figure 5.2b presents the theoretical (solid lines) and experimental results (symbols) of the coupling efficiency as a function of the distance between the two fibres. Each step, of about 3μm, is measured with the micro-metric screw of the translation stage. Due to the large beam divergence at the "Source" fibre output, the highest coupling efficiency is always obtained when the fibres are in contact. Considering two identical fibres, the coupling efficiency can theoretically reach 100% while the mode size mismatch limits it to about 43% for a SM(4.4μm) in front of a SM(hNA).

5.3 Comparison of different optical coupling systems

In this part, we discuss the coupling efficiency between either lensed or standard single-mode fibres, and pillars with various diameters.

5.3.1 Coupling efficiency with lensed fibres

A lensed fibre is a standard single-mode fibre, SM(4.4μm) in our case, with one of the output modified to focus the output beam. Over the past 50 years, several processes have been developed depending on the needs. We can cite the creation of either a fibre-ended micro-lens by photolithography [235], or by photopolymerisation [236], or the addition of a graded-index (GRIN) lens [237].

In this work, three types of lensed fibres are studied: one attached to an aspheric lens, one with a GRIN lens, and one whose output is modeled in conic shape.

5.3.1.1 General theoretical considerations

To model the effect of a "lensed output" on the beam free-space propagation, the *analytical* model of chapter 3 is used. This also enables us to study the influence of such output on the coupling efficiency with a pillar.

From a fibre with a core diameter of 4.4μm, to obtain a focused spot with a diameter about the pillar size, the magnification of the focusing element should be around 0.5. In the Gaussian approximation, the latter is linked to the lens focal length, f, the Rayleigh distance from the fibre, $z_{r,\,\text{fibre}}$, and the distance, d, between the fibre and the lens. The magnification can then be written as follows [238]:

$$\frac{w_{0,\,\text{pillar}}}{w_{0,\,\text{fibre}}} = \frac{1}{\sqrt{\left(1-\frac{d}{f}\right)^2+\left(\frac{z_{r,\,\text{fibre}}}{f}\right)^2}} \tag{5.1}$$

With a waist of 2.76μm and a working wavelength of 930nm, the Rayleigh distance is 25μm. So, due to the divergence of the beam, to obtain the required magnification, we must have d$\neq$0 and d > f (same for the distance D). Indeed, this equation is presented by a simple image using a thin lens, but it allows to explain that a space between the lens and either the fibre output or the pillar is required.

The modeled system is depicted in figure 5.3. It is composed of a SM(4.4μm) fibre placed at a distance d from a lens. The divergent beam from the fibre is then focused on a pillar. The distance between the lens and the pillar, also called working distance, is labelled D. The reverse direction can also be simulated.

As seen in chapter 3 part 3.2.1.2, the beam size must be taken into account. To avoid losses due to finite aperture, beams must have diameters at least two and a half times smaller than the lens diameter. For instance, as shown in figure 5.1, to fulfill the size condition with a lens clear aperture of 85μm, the beam diameter must satisfy $2w(z) < 34\mu$m, with z = (d, D). As a result, the maximum propagation distance D is between 53μm to 85μm with pillar

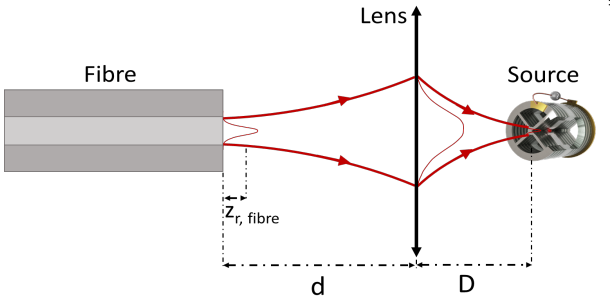

Figure 5.3: Schematic of the system used for theoretical estimations

diameters respectively between 2μm and 3.4μm. Due to a lower divergence, the maximum distance d from the SM(4.4μm) fibre is about 150μm.

To optimise the parameters of an ideal "lensed" fibre, and calculate the required magnification (equ. (5.1)), we consider the beam waists of both the fibre and the pillar. From figure 5.1 and the lens aperture, we can also deduce both the upper bound of the distance separating the fibre output to the lens, and the distance between the pillar and the lens, from which it is then possible to estimate its focal length. To do so, the calculations consider a fixed distance d whose value is chosen according to the lens aperture. We then estimate the coupling efficiency between this "lensed" fibre and a pillar for variable distance D and focal length. In figure 5.4, the calculations consider a lens clear aperture of 85μm, and d = 120μm. Each coupling efficiency estimation is theoretically calculated with equation (3.2).

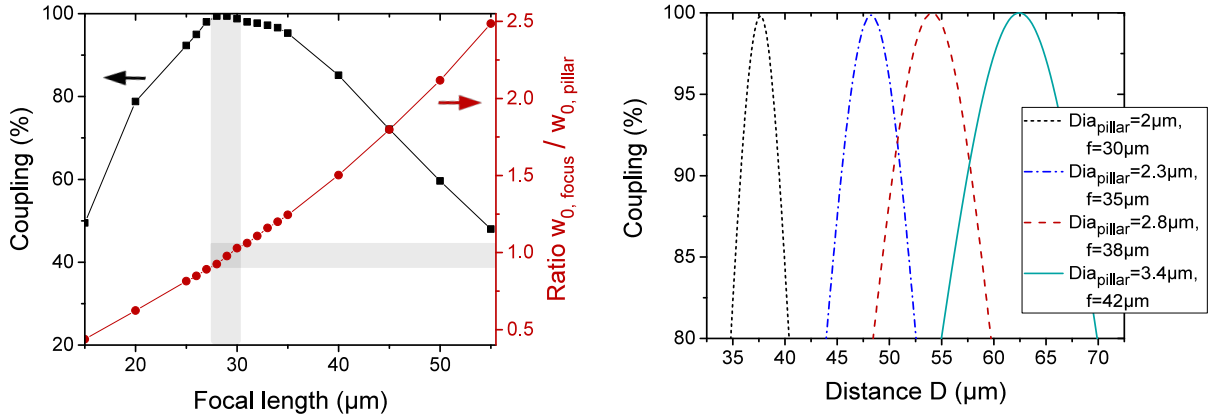

(a) (b)

Figure 5.4: Theoretical results. The SM(4.4μm) is separated from the lens by d = 118μm. (a) Coupling efficiency (black squares) and normalised waist size (red circles) as a function of the focal length. The coupling is calculated with a 2μm pillar diameter. For each focal length, the distance between the lensed fibre and the pillar is set to maximise the coupling. The normalised waist is the ratio between the waist from the lensed fibre, after the propagation, and the beam diameter at the pillar top. For both, curvature radius are infinite. (b) Coupling efficiency as a function of the distance between the lensed fibre and different pillar sizes. The lens focal length is optimised for each pillar diameters.

The black line (squares) of figure 5.4a presents the theoretical coupling efficiency between the focus spot from the lensed fibre and a 2μm pillar diameter as a function of the lensed fibre focal length. The distance between the two is set to optimise the coupling efficiency whilst satisfying the beam size condition. The red line (circles) represents the ratio of the focused spot waist and the beam waist of the pillar. Since both correspond to the position where the radius of curvature is infinite, the coupling efficiency is close to 100% when the ratio is about 1. When the spot is smaller or larger than the pillar mode, the mode mismatch quickly limits the maximum coupling efficiency. In any case, the coupling efficiency is above 90% on a focal lengths range of about 10μm. This calculation, which can be done for each pillar size, allows to find the custom focal length and the working distance D adapted to optimised the coupling efficiency.

Figure 5.4b presents the coupling evolution as a function of the distance between the pillar and the lens. The calculations have been done for four different pillar sizes and their respective optimised focal lengths. As plotted, we can find a distance range of few microns in which the coupling efficiency is above 95%, whatever the pillar size. We can also notice that the larger the pillar diameter is, the broader this range is. As plotted, the range is only 2.4μm for a pillar diameter of 2μm while it reaches 6.7μm for a diameter of 3.4μm. It is due to a lower beam divergence when the pillar is larger. Even though the fibre positioning is challenging, 100% coupling efficiency seems to be achievable, whatever the pillar size, as long as a customised lensed fibre is used.

In practice, this method would require a customised fibre per pillar. However, as shown in figure 5.4a, a ratio between 0.75 and 1.25 between the two waists allows coupling efficiencies above 90%. Thus, a trade-off can be found by using only one fibre for all pillars, while keeping a high coupling efficiency.

Pillar diameter	Coupling
2μm	80%
2.3μm	91%
2.8μm	98%
3.4μm	99.9%

Table 5.2: Theoretical maximum coupling efficiency between pillars of different diameters and a lensed fibre designed for a spot size of 3μm.

Considering a lensed fibre which gives a 3μm focused spot, table 5.2 summarises the expected coupling efficiencies with several pillars. These coupling maxima are calculated with equation (3.3). Since most of the pillars have diameters between 2.3μm and 2.8μm, the lensed fibres studied in the following parts have been chosen to satisfy this focused spot diameter. Accordingly, the choice of the distances d and D, like the focal length f, will depend on the lensed fibre we will consider.

5.3.1.2 Experimental results using lensed fibres

The first type of lensed fibre is not strictly speaking a lensed fibre as it consists in an aspheric lens (f=2.76mm) set to a certain distance from a SM(4.4μm) fibre (figure 5.5) to obtain the right focus spot diameter.

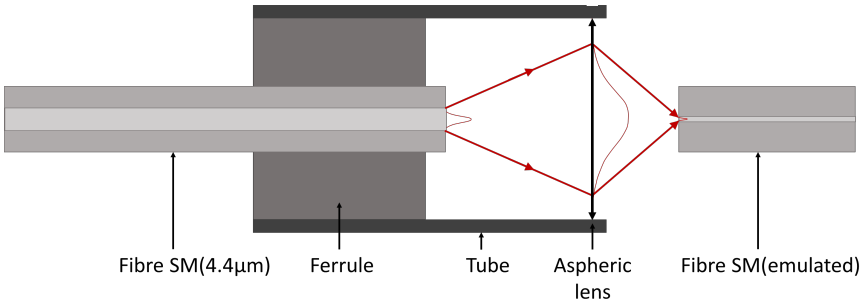

Figure 5.5: Schematic of the lensed fibre (type 1). A SM(4.4μm) fibre is placed in a ferrule and a tube which holds an aspheric lens. The position of the lens is determined according to the size of beam at the fibre output, the focal spot diameter and the lens focal length. The coupling efficiency is theoretically estimated and measured with a SM(emulated) fibre.

To measure the diameter of the beam at the focal point, a camera is placed in front of the fibre. Using a translation stage, five beam profiles are measured at five different positions. The focus spot diameter is then deduced by the extrapolation of the beam convergence and the divergence, with a beam propagation simulator. We obtained, $2w_{0,\,\mathrm{spot}} = 2.6\mu$m.

Experimentally, pillars are emulated by a SM(emulated) fibre. The working distance D is measured while the distance d is deduced from the other parameters. To compare with the theoretical estimation, the data used in the simulation are summarised in table 5.3.

$\mathrm{dia}_{\mathrm{mode}}$ SM(4.4μm)	$\mathrm{dia}_{\mathrm{mode}}$ focused spot	$\mathrm{dia}_{\mathrm{mode}}$ SM(emulated)	Distance SM(4.4μm)/Lens	Distance Lens/SM(emulated)
5.76μm	2.6μm	2.16μm	8.83mm	4mm

Table 5.3: Data used in the *analytical* calculation of the coupling efficiency between the considered lensed fibre and a SM(emulated) fibre. The mode diameter of the focus spot and the image working distance are measured and the object working distance is deduced from the latter data.

The experimental setup consists in a lensed fibre, fixed, and the SM(emulated) fibre placed in front of it, and translated. This is the same configuration as in figure 5.2a, where "source" fibre is represented by the SM(emulated) fibre and the "collection" fibre by the "lensed" fibre. In the same way, the experimental coupling efficiency is defined as the ratio between P_{out} and P_{in}, but without considering the lensed fibre transmission.

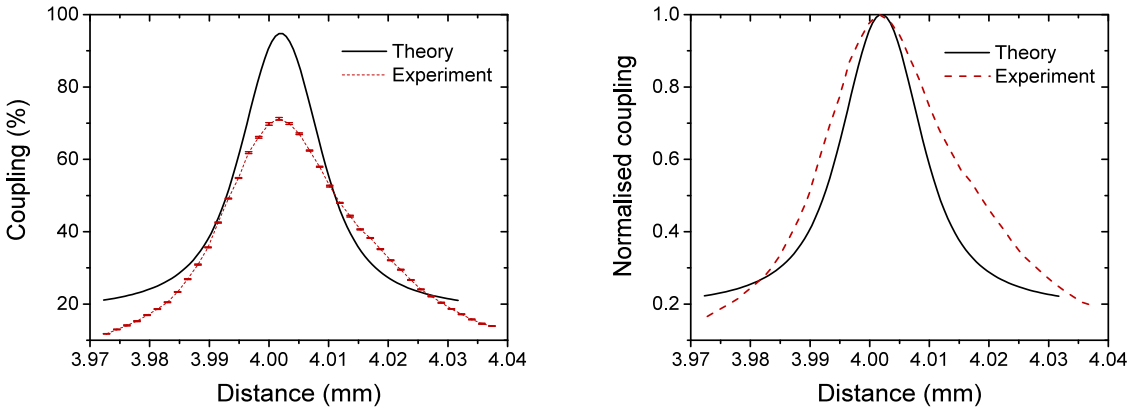

(a) (b)

Figure 5.6: Comparison between the theoretical (black lines) and the experimental (red dashed lines) coupling efficiencies between a SM(emulated) fibre and the lensed fibre. (a) Coupling as percentage ratio from the input power. (b) Normalised coupling

Figure 5.6a presents theoretical (black lines) and experimental (red points) results of the coupling efficiency for a beam from the SM(emulated) coupled into the lensed fibre. The first observation is about the theoretical maximum coupling. Due to a size mismatch between the focused spot diameter and the mode of the SM(emulated), the coupling is theoretically limited to about 94%. A clear point emerging from the plot is the reduced experimental maximum coupling efficiency by about 25%. Nevertheless, from the normalised curves presented in figure 5.6b, we can notice that the experimental values follow the theoretical evolution along the distance separating the two fibres. We did not find the cause(s) for these additional losses, but one of them is probably due to the lensed fibre itself. Due to a working distance of 4mm, the beam from the SM(emulated) has a a diameter about 2.8mm when it reaches the aspheric lens, which has a clear aperture of 4.16mm. In this condition, the beam size does not satisfy the diameter requirements and the diffraction effect cannot be neglected. Theoretically, the losses due to diffraction through the aspheric lens are at least 2%, while experimentally we measured 5% of losses between the lensed fibre connector and the lens output. Moreover, an aspheric lens is usually optimised to focus a collimated beam: there can then be "natural" aberrations due to the beam divergences. Despite the other origins of losses were not determined, due to the measured experimental coupling efficiency about 70%, this lensed fibre approach cannot be considered acceptable for implementation.

The second type of lensed fibre consists in a single-mode fibre, SM(4.4μm) in our case, attached to a silica spacer and a graded-index (GRIN) fibre (figure 5.7). This principle has been already proposed in the work of G. Nemova and R. Kashyap [237] and the group of S.A. Boppart reported a numerical analysis of the beam propagation inside and after the fibre [239].

The characterisation is done for two lensed fibres, labelled A and B, keeping the required focused spot diameter of 3μm.

The waist size of the focused spot is measured using the "knife edge" technique [240, 241]. The diameters of the focused spots are 4.6μm for the fibre A and 3μm for fibre B.

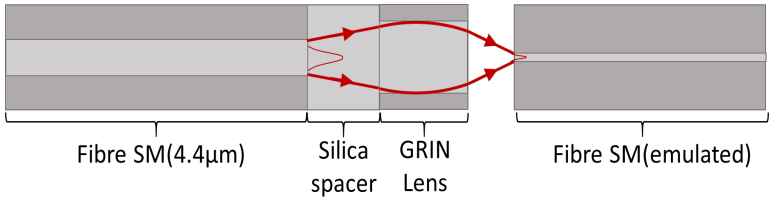

Figure 5.7: Schematic of the second type of lensed fibre. A SM(4.4μm) fibre is extended by a silica spacer and a GRIN lens. Their lengths are determined according to the size of the focal spot and its distance from the GRIN lens output. In our case, the silica spacer and the GRIN lens have a thickness about respectively 500μm$\pm$10μm and 400μm$\pm$10μm. The SM(4.4μm) fibre has a core of 4.4μm and the GRIN lens has a core of 85μm.

According to equation (3.3), the maximum coupling efficiency between fibre A and a typical pillar should be limited to values in between 48% and 83% depending on its diameter. Experimentally, we measured the coupling efficiency between these lensed fibres and a pillar emulated by a SM(emulated) fibre.

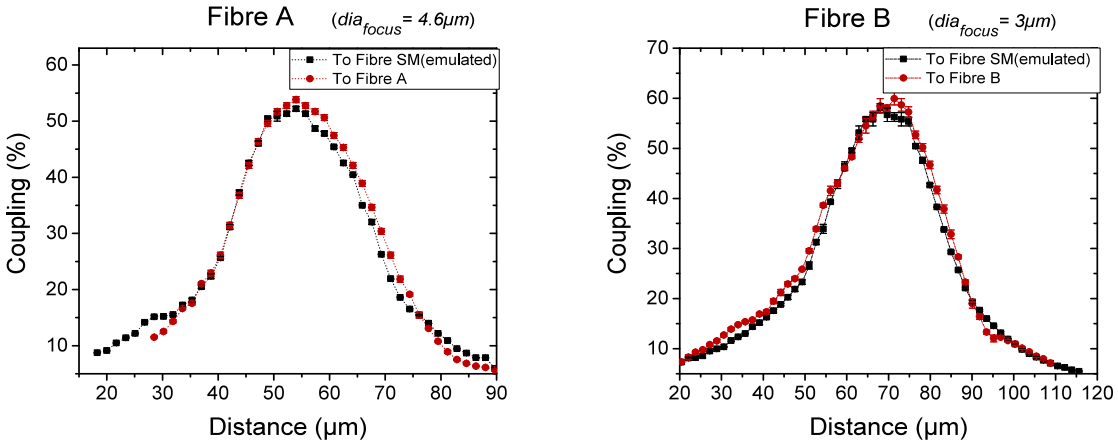

(a) (b)

Figure 5.8: Experimental coupling efficiencies as a function of the distance between a SM(emulated) fibre and the lensed fibres (a) A and (b) B. **Black lines**: From the lensed fibre A (or B) to the SM(emulated) fibre. For this coupling, the power at the output of the SM(emulated) fibre is corrected by the fibre transmission. **Red lines**: From the SM(emulated) fibre to the lensed fibre A (or B).

The results with the fibre A are plotted in figure 5.8a while figure 5.8b corresponds to the fibre B. Both figures present the coupling evolution as a function of the distance between the two fibres (lensed fibre and SM(emulated)). The black lines (squares) correspond to the coupling efficiencies for a laser beam exiting the lensed fibre and coupled into the SM(emulated) fibre. This is the ratio between the power measured in free-space after the lensed fibre, P_{in}, and the power measured after the SM(emulated) fibre corrected by its losses, $P_{\text{out, corr}} = P_{\text{out}}/T_{\text{SM(emulated)}}$. The SM(emulated) fibre transmission has been estimated by the measured ratio of the output and input powers. Mostly because of the splice quality be-

tween the high NA core and the standard one, the transmission was about 57%.

The red lines (circles) represent the reverse direction, where the beam goes from the SM(emulated) fibre to the lensed fibre. In this direction we want to estimate the real ratio of collected photons. So, P_{out}, at the output of the lensed fibre is not corrected by the transmission factor.

Due to the principle of reversibility of light, all the experimental curves follow the same evolution as a function of the distance, independently of the direction of propagation. We can also notice that in each case, coupling reaches the same maximum value despite the fact that black lines, compared to the red ones, are corrected by the SM(emulated) fibre transmission (about 57%). The reason for this is not obvious and several reasons can be suggested.

Considering fibre A, due to size mismatch with a SM(emulated) fibre (focus spot diameter of 4.6μm) the coupling efficiency is limited to 60% . If we only consider the black line of figure 5.8a, this is the main reason of the experimental value limitation. However, this does not explain the large coupling limitation with the fibre B in both directions. Indeed, its focused spot diameter is 3μm, and the theoretical maximum of coupling with a SM(emulated) fibre is then 90%; the reason is structural. To obtain such spot diameters, the silica spacer has a thickness of 500μm$\pm$10μm and the GRIN lens has a clear aperture of 85μm. However, after propagating inside the spacer, the beam exiting the SM(4.4μm) fibre has a diameter around 105μm, and being larger than the GRIN lens diameter, it gets truncated. This is confirmed by the 20%$\pm$5% of losses from these lensed fibres. Hence, even though it was not verified, this also probably deteriorates the Gaussian profile arriving on the SM(emulated) fibre. This profile mismatch could explain the difference between the theory and the experiment (black squares of figure 5.8b). This spacer thickness issue leads also to high losses inside the fibre.

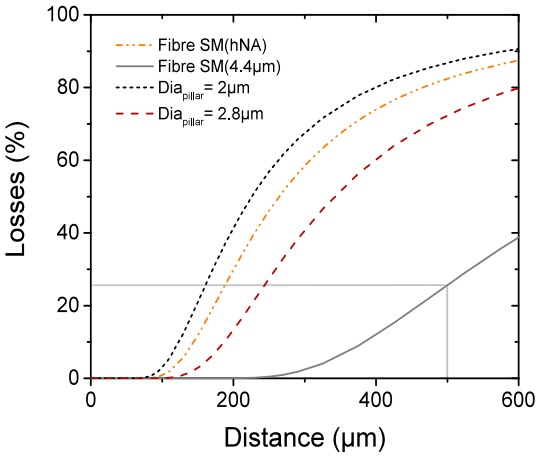

Figure 5.9: Losses due to an aperture diameter of 85μm as a function of the propagation distance after either fibres or pillars.

Figure 5.9 represents the theoretical losses due to the GRIN lens finite diameter, as a function of the distance from the fibre or pillar output. We can notice that for a beam exiting a SM(4.4μm) fibre, the losses due to the truncation are around 25%. This is consistent with the measurement of the lensed fibre transmission about 80%$\pm$5%.

In the reverse direction (red circles), the beam from the SM(emulated) fibre propagates over the working distance about 55μm for fibre A and 70μm for fibre B. As shown by figure

5.9, the GRIN lens does not truncate them. The decrease in the maximum of coupling is only due to a size mismatch. Indeed, considering a silica spacer with a thickness of 500μm, a working distance of 70μm and a focal length of 60μm, the spot at the SM(4.4μm) input has a diameter of 17.6μm, which is about three times larger than the SM(4.4μm) mode. In this condition, the theoretical coupling efficiency, estimated with the equation (3.3), should be limited to about 35%, a value which is even below the experimental results. Since the two simulations used in this work consider thin lenses, this approximation cannot be applied for GRIN of 400μm length [239]. In any case, considering the measured performances, this lensed fibre approach also does not present a reliable solution to fibre a pillar.

Finally, we also characterised a SM(4.4μm) fibre whose output is manufactured in conic shape to allow for beam focusing (figure 5.10). Nevertheless, the experimental transmission of such structure was around 60% and the coupling efficiency with a SM(emulated) did not exceed 30%. The latter was mainly due to a focus beam diameter of 6μm, measured with the "knife edge" technique. Considering these values and the fact that the equation (3.3) even predicts a coupling efficiency of 40% this solution was not chosen either.

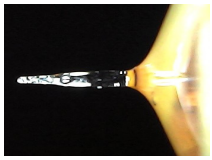

Figure 5.10: Third type of lensed fibre.

Following the experimental results obtained with the different kinds of lensed fibres, having a focused spot with a diameter of about 3μm leads to large losses and the collection efficiencies do not exceed 70%. Hence, these solutions are not implemented and the coupling efficiency with standard fibres has been further investigated.

5.3.2 Coupling efficiency between a standard single-mode fibre and a pillar

We consider now a standard single-mode fibre placed above pillars without the use of any lens (figure 5.11a). As previously, to estimate the coupling efficiency between the fibre and the pillar, we used equation (3.2) and calculate the mode matching. We also estimated the coupling efficiency between the pillar and the fibre.

Figure 5.11b (solid lines) and 5.11c (all lines) present the coupling evolution, depending on the distance between respectively a SM(4.4μm) or a SM(hNA) fibre, and pillars with various diameters. Figure 5.11b also shows the coupling evolution for a beam, from a SM(4.4μm), coupled into a pillar (dashed lines). For both figures, maximum coupling is always found at d = 0μm. Following equation (3.3), optimal mode matching and so, the best coupling efficiency, is reached when both curvature radius are at the same position. Since beams from fibres and pillars are divergent, this condition is only fulfilled when the fibre is in contact with the pillar. However, depending on the fibre and the Rayleigh length, there can be a tolerance. In fact the coupling decrease is less sharp with a SM(4.4μm) fibre (z_r = 25μm), than with a SM(hNA) (z_r = 4μm). Nevertheless, even being at few microns from the contact point it is not a sufficient condition to obtain 100% coupling since, accordingly to the same equation, a mode matching is also required.

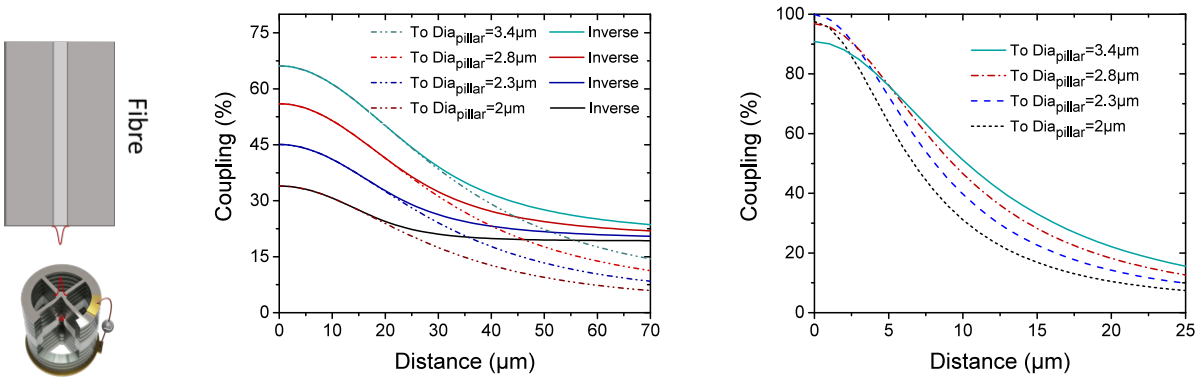

(a) (b) (c)

Figure 5.11: (a) Schematic of the studied system. The fibre is directly placed on the top of the pillar. (b) and (c) Theoretical coupling efficiencies as a function of the distance between pillar and fibre outputs. Various pillar diameters as considers. (b) With a SM(4.4μm) fibre. The calculations have been done from both sides: from the pillar to the fibre and vice versa. (c) With a SM(hNA) fibre. The calculations have been done from the fibre to the pillar. The results from the reverse direction overlap.

Considering a SM(4.4μm) fibre (figure 5.11b), the maximum possible coupling with a pillar diameter of at least 3.4μm is only 66%. Since pillars with such size are rare, in practice the upper bound of the coupling efficiency should be around 50%. Considering that most of the pillars have diameters about 2.5μm, this calculation points also out the influence of the propagation direction on the coupling efficiency. From the fibre to the pillar, coupling drops below 10% while, in the reverse direction, it stays around 20%. Since the core diameter of the SM(4.4μm) is about two times larger than the pillar's, the fibre has then a larger tolerance on the beam diameter exiting the pillar. On the contrary, the increasing beam size from the fibre is less and less coupled into the pillar. In any case, losing at least half of the emitting photons directly from the pillar output cannot be considered as a reliable solution.

On the contrary, with a SM(hNA) it is possible to obtain couplings higher than 90% independently of the size of the pillar (figure 5.11c). Same results are obtained with a beam from the fibre and coupled into the pillar because here the system is almost symmetric. Nevertheless, due to small Rayleigh distances, coupling is more sensitive to the distance between them. After ten micrometers, the coupling drops to 50% due to larger beam divergence from either a SM(hNA) or a pillar, compared to the SM(4.4μm) fibre. The radius of curvature, like the beam size, increase faster in both directions.

Despite this sensitivity to distance, with a precise positioning of the SM(hNA) above the pillar, this approach seems definitely the most appropriate to collect efficiently the emitted single photons. From this starting point, several technical approaches have been developed to implement experimentally this configuration, as detailed in next section.

5.4 Fibre coupling of a single photon source in a low vibration cryostat

This part describes the insertion of a SM(hNA) fibre in a low vibration cryostat containing a bright single photon source, fixed on a 3-axes nano-positioners.

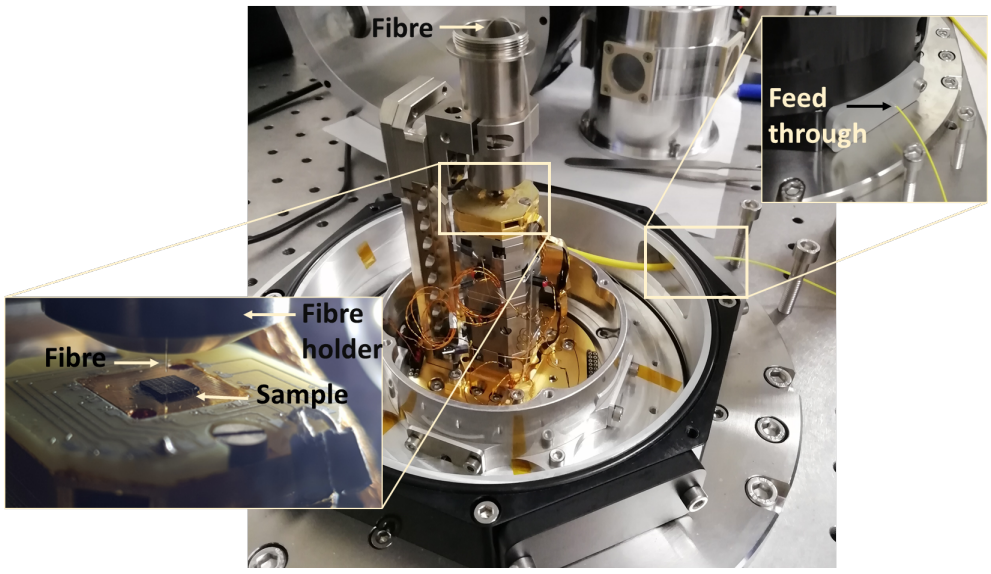

Figure 5.12: Pictures of the experimental configuration, inside the low-vibration cryostat chamber (central picture). The picture on the left is a zoom on the sample holder, where the fibre is hold by a dedicated mount, while the right picture shows the fibre through the feed-through hole.

For this experiment, the fibre is hold by a dedicated metal support which is itself mounted in place of the former aspheric lens set above the source device inside the cryostat chamber. The other fibre output is spliced to a standard fibre which links the source to the optical system via a feed-through hole, made by a specialised company. Figure 5.12 is a combination of pictures presenting the experimental conditions just described. Depending on the excitation regime, the optical system is either the one described in chapter 3 (figure 3.17c) or the one of chapter 4 (figure 4.11b). In each case, the collimator and the wave plates placed above the cryostat chamber are removed. This configuration is used as an intermediate step before directly attaching the fibre to the pillar.

5.4.1 Fibre positioning above the sample

In the presented experimental setup, the 3-axis nano-positioners are used to centre, with high precision, the source device with respect to the SM(hNA) fibre core at 4 Kelvin. This also enables us to control the distance between the two and optimise the collection efficiency. Since in this configuration there is no space for an imaging system, we use the reflectivity spectrum from the pillar to determine where the fibre is located with respect to the source.

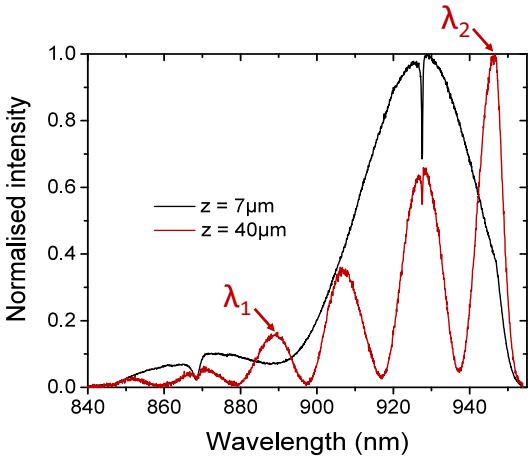

Figure 5.13: Reflectivity spectra for two different fibre heights from the pillar top. The actual distances (7μm for the black line and 40 μm for the red) are determined from the Fabry-Pérot oscillation spacing.

By illuminating the source device with a LED, a part of the light spectrum enters into the pillar and is not reflected. Thus, we get a broad spectrum with a dip corresponding to the resonance of the cavity. Since the fibre output and the pillar top are parallel, the spectrum is also modulated by a Fabry-Pérot effect in accordance with the distance between the two. Figure 5.13 presents two reflectivity spectra obtained for two fibre heights. The distance is estimated according to this equation:

$$\Delta(nm) = \frac{\lambda_1 \times \lambda_2}{2|\lambda_1 - \lambda_2|} \tag{5.2}$$

with λ_1, the wavelength of the rightmost peak, and λ_2, the wavelength of a peak to its left. Usually, λ_2 is measured as far as possible from λ_1.

Following the theoretical results presented in part 5.3.2, the highest coupling efficiency with a SM(hNA) is reached when the fibre is in contact with the pillar. However, in practice, this is challenging because touching the pillar might damage it or change both the pillar resonance and the QD emission energies [109]. Thus, we use the Fabry-Pérot interferences to bring the source as close as possible without touching the fibre. When physical contact is reached, the reflectivity dip blue-shifts due the applied stress and the sample is moved back of one step. Once the optimal height is reached with the Fabry-Pérot interferences, the pillar is properly centred by increasing the dip contrast.

5.4.2 Collection efficiency and emission benchmarks

Once the fibre is placed above the pillar, we compare its performances with respect to the free-space excitation/collection scheme. Specifically, here we use the source B1 of chapter 3 used under LA-phonon assisted excitation regime: a trion studied in parallel-configuration. The free-space confocal microscope of reference is the version 1 described in chapter 3. The fibred system used here is based on the version 2, also presented in chapter 3, except that the

collimator and the two waveplates above the cryostat are removed. The measured fibred system transmission is then $T_{\text{setup,fibred}} = 72\% \pm 2\%$, without considering the fibre/pillar coupling efficiency. The latter is deduced comparing the first lens brightness obtained in free-space ($\mathcal{B}_{\text{FL, freespace}}$) and the fibred brightness from the fibre-coupled pillar ($\mathcal{B}_{\text{F, fibred}}$). The former, of about $20.5\% \pm 2\%$, is estimated by correcting the measured fibred brightness with the free-space system, by its total transmission. From the fibred brightness of the fibre-coupled source, estimated at $12.8\% \pm 2\%$, the coupling efficiency between the pillar and the SM(hNA) fibre is then calculated as follows:

$$C_{\text{pillar / fibre}} = \frac{\mathcal{B}_{\text{F, fibred}}}{\mathcal{B}_{\text{FL, freespace}} \times T_{\text{setup, fibred}}} \tag{5.3}$$

Following equation (5.3), we then have $\boxed{C_{\text{pillar / fibre}} = 87\% \pm 2\%}$. Even though this value is below the theoretical prediction, it presents an increase of at least 15% with respect to the free-space coupling of the cavity rotated light; its improvement is in progress. Table 5.5 summarises the emission characteristics of the source B1 excited either in free-space or with a fibre set above the pillar.

	Free-space collection	fibre-coupled source
$\mathcal{B}_{\text{FL}}$	$20.5\% \pm 2\%$	$20.5\% \pm 2\%$
T_{setup}	$60\% \pm 5\%$	$72\% \pm 2\%$
Coupling	$70\% \pm 2\%$	$87\% \pm 2\%$
$\mathcal{B}_{\mathbf{F}}$	$\mathbf{8.6\% \pm 5\%}$	$\mathbf{12.8\% \pm 2\%}$

Table 5.4: Comparison of the sources collection efficiencies under LA-phonon assisted excitation (parallel-configuration).

The optimisation of the optical system transmission combined with the improvement of the coupling efficiency enable to increase the fibred brightness by about 49%.

5.5 Pigtailing of the fibre for a standard cryostat

In the perspective of a "plug and play" bright and efficient single photon source, the fibre-coupled device must be placed in a cost-efficient cryostat which is not isolated from vibrations. Hence, since the source is no longer set on positioners, we will describe the fibre positioning and fixing above the pillar at room temperature. The first results measured under both non-resonant and LA-phonon assisted regime will be also detailed.

5.5.1 Fixation of the fibre at room temperature

Contrary to the previous situation, the fibre is aligned above the pillar at room temperature, and must stay fixed during the cooling process. To do so, several approaches have been considered such as gluing it with the pillar (figure 5.14b) or holding it above with either a silica or a metallic mount (resp. figures 5.14d and 5.14c). The most challenging steps of the process are (i) to centre precisely the fibre while controlling the distance with the pillar and (ii) keep the fibre precisely above the pillar during the cooling.

Considering the first point (i), the technique is the same as the one used for the fibre inside the cryostat chamber: at room temperature, the sample is set on precise translation stage and the light from the LED is sent on it. The alignment with the selected pillar is then done following the Fabry-Pérot interferences (equ. (5.2)) and the reflectivity dip contrast. At the end of this process, the fibre is centred and about 5μm above the pillar. After this, the full structure is placed in the cryostat chamber and the fibre is spliced to the one of the feed through hole which links the source to the optical system module (figure 5.14a).

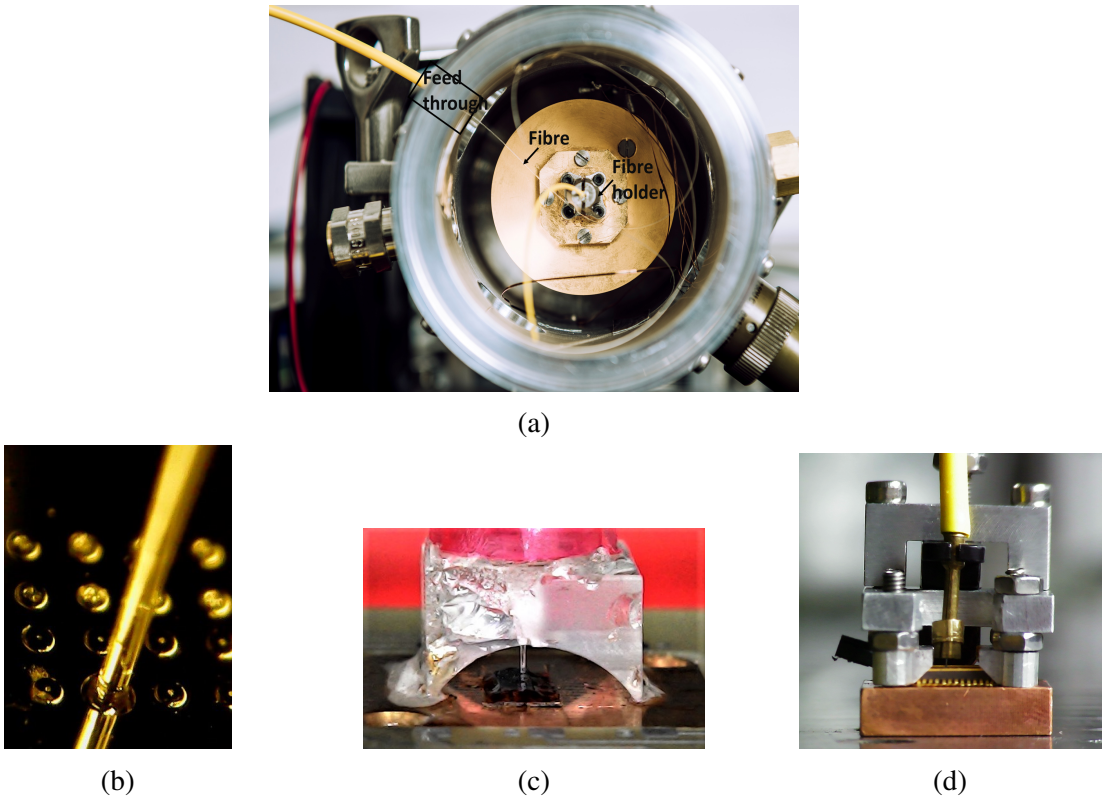

(a) (b) (c) (d)

Figure 5.14: (a) Picture of the fibre-coupled source inside a small and low-cost cryostat chamber. The fibre, set above the pillar and hold by a fibre holder, is spliced to the fibre making the link to the optical system via the feed through hole. Pictures of a single-mode fibre (b) glued on a pillar or hold above a pillar by either (c) a silica support or (d) a metallic support.

Figure 5.14b is a picture of a fibre glued on a pillar. With this technique the fibre stays above the pillar during the cooling, but since the glue has a large retraction coefficient, it applies non-negligible strains, emphasised by the fibre in contact, at 4K. Moreover, this strain

effect is both not reproducible and not controllable, which is problematic for the single-photon emission.

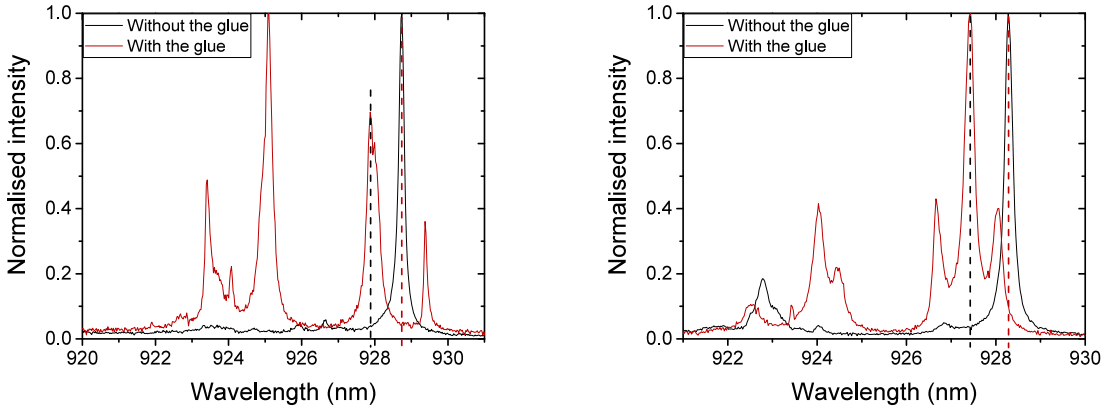

(a) (b)

Figure 5.15: Photoluminescence spectra of two pillars, (a) and (b). The black (red) lines correspond to the sources spectra without (with) the glue. The dashed lines correspond to the fundamental mode energy which is shifted by about 0.8nm due to the glue-induced strain.

Figures 5.15a and 5.15b present the photoluminescence spectra from two different pillars placed at 4K without or with a droplet of glue (resp. the black and the red lines). For these measurements, we only consider the influence of the strain due to the glue contraction. But even without the effect of the fibre, we can clearly notice a blue shift by about 0.8nm of the cavity energies due to a reduction of the pillar effective volume [154]. The drop of glue has also a large effect on the QD states energies. If it is not possible to estimate the shift, we can observe that the initial energy matching obtained during the in-situ lithography is lost. Given the shifts differences, either any QD states can be put in resonance or if we could tune one, it would not be the one selected during the in-situ lithography. Moreover, the glue addition requires to send more power on the source, creating an unstable charge environment around the QD. As a consequence, the source is no longer efficient. Finally, since the stress is not quantifiable, it is not possible to anticipate the shift during the fabrication process. If in the work of P. Stepanov et al. [242], the strain is controlled by the thickness of SiO_2, in our case, the glue leads to undesirable and harmful effects for the source emission.

As a result, the fibre has to be hold by a mount above the selected pillar and its height must be set as described previously. Figure 5.14c and 5.14d show respectively the fibre hold by a silica and a metallic support. The glue fixes the latter on the sample holder once the fibre is aligned. Contrary to the metallic one, the silica support has the same dilatation parameters as the fibre's. This leads to less displacement of the fibre due to several contraction effects. Other mounts are also under study and this solution of fibre holder is still under development. Indeed, the drift of the fibre in relation with the pillar, and vice versa, during the cooling remains the main issue.

Figure 5.16 represents the three typical situations we can get during the cooling process of the fibre-coupled source. The plot of figure 5.16a presents the evolution of the reflectivity

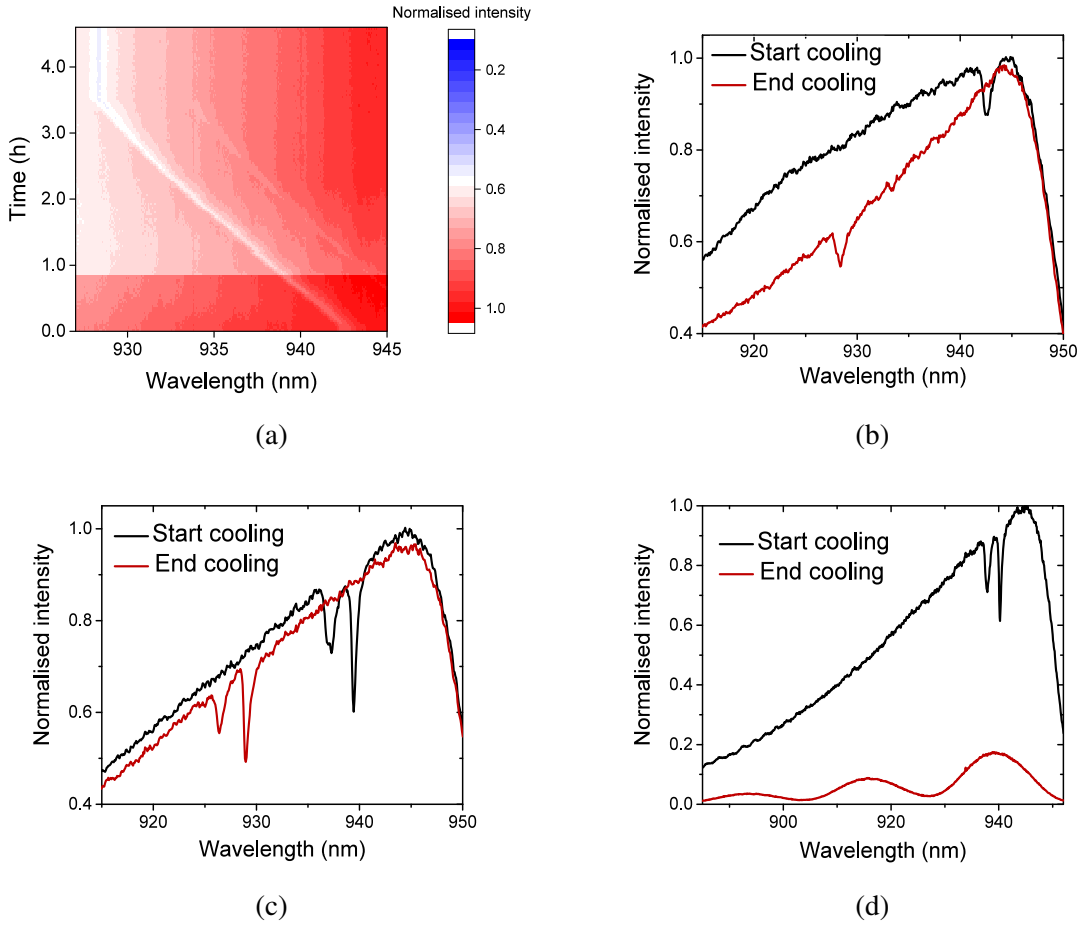

Figure 5.16: (a) Reflectivity spectra during a cooling process. This evolution corresponds to the case when the fibre remains centre during all the process and is still perfectly above the pillar at 4K. (b), (c) and (d) First (at room temperature -black lines-) and last (at 4K -red lines-) spectra of the measurements. (b) First and the last spectra of the evolution presented in (a). (c) Case when the fibre is not perfectly aligned at room temperature and remains in this position during the cooling. At 4K, the second mode of the pillar is also collected, reducing the collection efficiency of the single photons emitted in the pillar fundamental mode. (d) Case when the fibre moves out of the pillar top during the cooling process. The pillar reflectivity dip vanishes and disappears. The red line of the insert corresponds to the Fabry-Perot interferences between the fibre and the wafer.

spectra during a cooling cycle while figure 5.16b plots only the first (at room temperature -black line-) and the last (at 4K -red line-) spectrum of this process. The spectra succession over the cooling process allows to clearly follow the blue shift of the pillar fundamental mode due to the temperature drop. Figure 5.16c and 5.16d present also the first spectrum (black lines) and the last (red lines) but for two other cases. In figures 5.16a and 5.16b, the fibre stays perfectly aligned to the pillar all along the cooling. In figure 5.16c, we can notice that the second mode of the pillar is collected even at room temperature. This could appear when the pillar diameter is too large. Experimentally, we notice that the second mode is always collected for pillar diameters above 3μm. Nevertheless, in the presented case, the pillar size

was 2.5μm, and the second mode collection was most likely due to a lateral misalignment of the fibre core with respect to the pillar. During the cooling process, the fibre remains at this position and the second mode is still collected at 4K. As a consequence, the single photons collection efficiency is reduced. Finally, figure 5.16d corresponds to the case where the fibre moves out of the pillar, and the red line corresponds to the Fabry-Perot interferences between the fibre and the wafer. This is an extreme case, as usually the fibre remains above the pillar arms or above the ring. In any case, due to this complete misalignment, no signal from the pillar is collected, and the complete alignment process needs to be done again.

The alignment and pigtiling processes are still under development as we have some issue to keep the fibre perfectly aligned and at the right distance with respect to the pillar centre. Generally, the fibre is found to be a little misaligned (figure 5.16c) or drifted during the cooling process. Still, the results we obtained and which are presented in next part are very promising. In fact, this same technique was used in the work of Ortiz et al. [243] where phonons in micro-pillar cavity are studied at room temperature. Removing the constraint to work at 4K proved the reliability and the stability of such fibre alignment.

5.5.2 Results and comparison with a free-space system

Once the fibre was fixed and the structure (fibre and source) cooled down at 4K, the source emission has been compared to the one obtained in free-space. Specifically, we studied the photoluminescence of the source E.

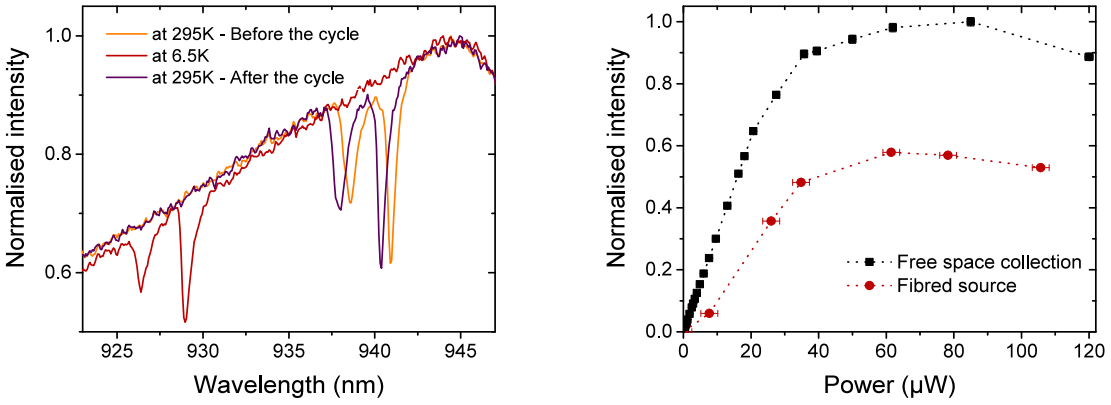

(a) (b)

Figure 5.17: (a) Reflectivity spectra of the source E before the cooling process, at room temperature (orange line), 6.5K (red line), and after the warming process of the source, at room temperature (purple line). For each spectra, the pillar fundamental mode is represented by the dip at long wavelength energy. The presence of the second mode at shorter wavelength points out an alignment issue. (b) Photoluminescence saturation curves from the source E. The source is excited by a continuous-wave laser at 850nm, for free-space or fibred collection as indicated. See text for details.

Figure 5.17a presents the reflectivity spectra of the fibre-coupled source before the cool-

ing process (orange line), at 6.5K (red line) and after the warming up of the source (purple line). Even though the pillar is small enough, we can notice that on each spectra, the second mode of the pillar is collected. At room temperature, like at 4K, its presence can be attributed to a misalignment of the core fibre with respect to the pillar. Since the second mode is still present at 4K, we deduce that no lateral displacement occurred during the cooling process. Nevertheless, the need of temperature tuning to align the QD transition in resonance with the cavity could make us conclude that the fibre got closer during it, applying a strain which blue-shifts the QD transitions. This assumption is also supported by the observed blue-shift of the cavity modes after the warming up, shown by the difference in energy between the orange and the purple lines of figure 5.17a. Here, the fibre is still applying a stress even at room temperature. In any case, a shift lower than 0.5nm allowed to put one of the QD transition in resonance with the cavity mode by raising the temperature up to 37K. It is at this temperature that the measurements of the source photoluminescence as a function of the laser power have been done.

The saturation curves are plotted in figure 5.17b: the black squares and the red circles correspond to the measurements from respectively the free-space system and the fibre-coupled source. For most of the points, the error bars are within the symbol's size. In free-space, the power is directly measured before the cryostat window. On the contrary, for the fibre-coupled source, the plotted power corresponds to the measured power at the input of the optical system corrected by its transmission, of about 30.5%$\pm$5%. Concerning the intensities in free-space, they are corrected by the optical system transmission, which is estimated around 44%$\pm$2% (including the cavity rotated light coupling), while the signal intensities from the fibre-coupled source are just corrected by the optical system transmission. Hence, from the system transmissions and the measured single photons rates, the coupling efficiency with the pillar can be determined by the method described in part 5.4.2 and the equation (5.3). We deduce a coupling efficiency of $\boxed{C_{\text{pillar / fibre}} = 60\%\pm5\%}$.

This value of coupling efficiency is a very promising result: from the previous study we proved the ability to reach a coupling above 85% with optimal alignment, which could be reached with better fibre fixation and stability during the cooling process. Concerning the optical system, the last version has a transmission of about 70%.

Finally, another fibre-coupled source F, from the same wafer as sources D2 (chap. 4) and E, has been studied under LA-phonon assisted excitation. Since the study in free-space was not performed, only results with the fibre-coupled pillar are presented. Once again, the applied bias is used to stabilise the QD states and the temperature required for these measurements is 33.8K because of strain induced by the fibre, likely touching the pillar, as previously discussed. Despite this, it has been possible to collect single photons.

Figure 5.18a presents the saturation curve of the fibre-coupled source emission measured on APDs detectors with an efficiency of 30%. The power is corrected by the system transmission, estimated to about 57.5%$\pm$2%. Considering the repetition rate of the excitation pulse laser of 81MHz, the extracted fibred brightness is around $\boxed{\mathcal{B}_{\text{F}} = 2\%\pm0.1\%}$. Even though the value is lower than the results obtained with the fibred-source B1 (part 5.4.2), in this case we use a test sample whose the first lens brightness was not optimised. Moreover, the optical system presents a lower transmission and the source alignment could not be optimised

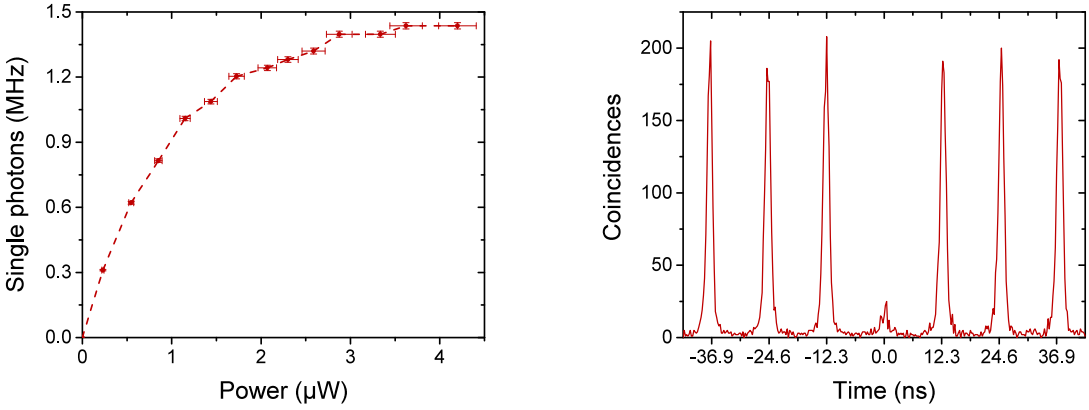

(a) (b)

Figure 5.18: Sample F. (a) Measurement of the emission saturation under LA-phonon assisted excitation. The 21ps pulsed laser (80MHz) is blue-detuned by 0.6nm from the QD emission wavelength (at 928nm). (b) Plot of the auto-correlation measurement ($g^{(2)}(0)$) under LA-phonon assisted excitation.

once at 4K. Nevertheless, this result is close to the published state-of-the-art of about 5% for a similar system [207]. Single-photon purity measurements were performed, obtaining a value around 90% (figure 5.18b), but considering the relative temperature of 33.8K, the emission indistinguishability is strongly reduced. Despite the source cannot be considered as a perfect single photon source, these are first promising results.

The best way to align and maintain the fibre above the pillar is still under study and the optical system transparency is still improving. Studies on the fibre drifts during the cooling process are also in progress; other sources will be then fibred soon.

5.6 Conclusion

The *analytical* model described in chapter 3 has been successfully used to estimate the coupling efficiency between different types of fibres and pillars with various diameters. Both standard and lensed single-mode fibres were considered. Supported by experimental measurements, this study allowed to conclude that fibres of high NA are the most promising due to a high similarity with pillars emission properties, guaranteeing coupling efficiency above 90%, whatever the pillar diameters.

The first experiment has been carried out with a fibre set above the pillar in a low-vibration cryostat. The source device, put on a sample holder, could be perfectly centred with respect to the fibre core at 4K. The coupling efficiency was then estimated around 87%$\pm$2%,

providing an intermediate step and a proof of concept towards a bright fibre-coupled source of single and indistinguishable photons. Considering fibre-coupled sources with fixed fibre, the development is still in progress. Even though there are still some technical issues during the cooling process, the first experiments are promising. It has been then possible to obtain coupling efficiency around 60%±5%.

Efforts have also been put into the development of new designs for the optical systems: the optimisation of the collection efficiency is still in progress but the transmission has overcome 70%. Moreover, the latter, like the cryostat, currently have designs which fit into racks of respectively 3U and 7U sizes

The following table summarises the expected fibred brightness with a source excited under the LA-phonon assisted regime with a first lens brightness of about 50% (chap. 4). The free-space system considered here is the version 2 described in chapter 3 part 3.4.

	Free-space	Fibre-coupled source	
		In low-vibrations cryostat	In small volume cryostat
$\mathcal{B}_{\text{FL}}$	50%±1%	50%±1%	50%±1%
T_{setup}	77%±2%	72%±2%	72%±2%
Coupling	76%±5%	87%±2%	60%±5%
$\mathcal{B}_{\mathbf{F}}$	**29%±5%**	**31.4%±2%**	**21.6%±5%**

Table 5.5: Comparison of the fibred brightness as a function of the excitation/collection system. The source is excited under LA-phonon assisted excitation regime and is supposed to have a first lens brightness of 50%.

This study presents the potential of the fibred system to reach and overcome the fibred brightness obtained in free-space. It also showed that we can build a compact, stable, and "plug and play" product which fits in rack size modules without deteriorating the sources performances.

Chapter 6

Conclusion

The main objective of this thesis was to explore different technical solutions to obtain practical and efficient solid-state sources of single and indistinguishable photons. Ideally, such sources have a first lens brightness of 1 and the optical system required to use them has a perfect transmission. Nevertheless, in real experimental conditions, the fibred brightness remains a limited fraction of the first lens brightness, which is itself limited in accordance with the excitation scheme. Eventually, the optical system needed to be optimised to become more efficient, stable, and user-friendly.

The first aim of this thesis was then to develop an efficient compact and stable optical system based on the confocal microscope principle. The first version has been built for a free-space excitation and photon collection under resonant fluorescence. This work raised two main challenges: reaching an efficient coupling of the single-photon beam into a single-mode fibre, while keeping a high laser rejection. Concerning the coupling efficiency, it required a careful study of spatial mode matching. To do so, simulations have been implemented (in the Gaussian beam approximation) to predict the theoretical limitations due to the distance between the source and the collection collimator or due to a mode mismatch. We also studied and compared different types of collimators to reach high collection of the emitted single photons. The polarisation selection is imposed by the excitation scheme. Since under resonant excitation it is necessary to reject efficiently the laser in the collection mode, the optical system is based on a cross-polarisation configuration. To reach a high extinction ratio, we identified different causes of depolarisation and found the right configuration to suppress it efficiently. Due to this configuration and a high mode matching between the laser beam and the pillar, an extinction ratio of about 10^6 was achieved, ensuring high emission purity of the collected photons. The current system has been developed in three different versions. In the first and the second versions, the objective placed above the cryostat has been replaced by an aspheric lens set inside the cryostat chamber. Concerning the first one, it is a fully free-space system, and its total transmission (including the cavity rotated light coupling efficiency) amounts to $64\% \pm 5\%$. The second version (an intermediate step to the third one), relies on a collimator directly placed above the cryostat and linked to a compact optical system with a single-mode fibre. It provides a collection efficiency of about $68.5\% \pm 5\%$. Finally, the last system relies on a single-mode fibre directly set above the source. Without considering the coupling efficiency between the source and the fibre, this fibred optical system has a transmission of $81.5\% \pm 5\%$. After these successive improvements, the confocal microscope gained in coupling efficiency,

and now can fit in a standard rack module. Still, the resonant excitation scheme imposed a significant brightness limitation, because under this configuration at least the half the photons are emitted in the same polarisation as the laser, they are thus rejected.

To overcome this brightness limitation, we investigated another excitation scheme based on the interaction between the QD transitions and the longitudinal acoustic (LA) phonon bath. It was recently theoretically proposed that phonons can be used to efficiently excite the QD in a near-resonant excitation scheme while preserving high single-photon purity and indistinguishability. The laser is then slightly detuned toward higher energy (about 1meV), and by carefully setting its pulse duration and area, we can have an efficient and indirect excitation of the QD exciton via LA-phonon emissions. This near-resonant excitation also allows us to spectrally filter the laser and then collect all the emitted photons. Experimentally, we reported a relative reduction in the exciton occupation probability as compared to resonant excitation with a pi-pulse of only 15%$\pm$1%. The first lens brightness was then shown to reach 51%$\pm$1%, which is an improvement of a factor three with respect to the resonant excitation regime. Concerning the emission purity and indistinguishability, even though this excitation scheme involves an interaction with the phonon bath, the theory predicted high benchmarks. We indeed reported a purity of 93.9%$\pm$0.1% and an indistinguishability of 91.5%$\pm$0.3%, without any phonon sideband filtering. The indistinguishability is then at a same level as for the resonant excitation scheme with the same devices. However, the single photon purity is slightly degraded, probably due to imperfect laser filtering and re-excitation when making use of longer excitation pulses. Another important result is the high degree of the emission linear-polarisation. This property is a major result to consider our source as a true building block for quantum applications. By exciting only one of the two excitonic linear dipoles, we demonstrated a polarisation purity of 99.4%$\pm$0.7%; so that a polarisation selection is no longer necessary on the collection path to generate indistinguishable photons. Finally, concerning the optical system, the main change is the parallel-polarisation configuration. The polarising beam splitter has been replaced by a 90:10 beam splitter and band pass filters have been added to suppress the laser. With a transmission of 59%$\pm$5% (version 2 optimised for LA-phonon assisted excitation and considering $\mathcal{B}_{\mathrm{FL}}$ = 50%), we can expect fibred brightness as high as 29%$\pm$5%. Note however that this brightness is currently limited by the extraction efficiency of the connected pillar cavities as well as the setup efficiency. As discussed earlier, improvements are expected on the setup transmission side. Moreover, a thorough study is under way at C2N, in collaboration with Quandela, to reduce the losses due to the cavity arms and the residual absorption in the mirror layers.

Finally, beyond increasing the optical system efficiency and changing the excitation scheme, we worked toward a fibre-integrated system to remove the need for a large and expensive system based on a low-vibration cryostat and including nano-positioners. In order to provide a "plug-and-play" single photon source, we worked on a method to set and fix a single-mode fibre above a pillar to directly collect the single photons. The coupling efficiency between different types of fibres and pillars with various diameters has been theoretically estimated and experimentally validated. This study enabled to select a single-mode fibre which should allow a coupling efficiency above 90%, whatever the pillar diameters. The first experiment was carried out with a fibre set above the pillar, and both placed in a low-vibration cryostat chamber. The source, put on a sample holder, could be perfectly centred with respect

to the fibre core at 4K. The coupling efficiency was then estimated to be about 87%±2%. This intermediate step towards a fixed fibre above a pillar was a proof of concept of the ability to get a bright fibred source of single and indistinguishable photons. Considering fibre-coupled sources with fixed fibres, the development is still in progress, but the first experiments are already very promising. So far, it has been possible to get a coupling efficiency about 60%±5%. For now, despite the need for an additional optical system to suppress the laser either with the polarisation or with spectral filters (version 3), a significant increase of the overall source efficiency is expected with this configuration. Hence, we estimate that with this direct fiber-integration combined and the LA-phonon assisted regime, it should be possible to reach a fibred brightness of 31.4%±5% (version 3 optimised for LA-phonon assisted excitation and considering $\mathcal{B}_{\mathrm{FL}}$= 50%).

As a result, we have developed and optimised a compact, stable, and "plug and play" product which fits in rack modules (figure 6.1), and whose fibred brightness is at least as high as the one from the optimised free-space excitation/collection scheme (version 2) under LA-phonon assisted excitation.

(a) (b)

Figure 6.1: (a) Prometheus, the new product of Quandela including (b) the fibred source in a small cryostat, the optical system, the laser and all the electrical components required to drive the system. With a size of about 1m80×90cm, it is composed of a computer (placed in the top module), four 3U rack modules and one 7U rack module placed in the bottom for the cryostat. The latter requires a compressor, which is not on the picture

Perspectives: Towards sources emitting in the telecom wavelength ranges

The sources investigated in this thesis, which emits photons of typical 930nm wavelength, have already been used for Boson sampling applications [16, 18], and are currently commercialised by Quandela to research groups developing quantum computation and simulation protocols. Nevertheless, to develop quantum networks and remote quantum computing, the photons must be able to propagate over long distances, in silica fibers, with limited absorption and wave packet dispersion. Hence, the emission wavelength must be either in the telecom O-band (1.3μm) or in the telecom C-band (1.5μm) to be compatible with the current infrastructures [244]. To achieve this requirement, two solutions can be considered: frequency conversion of the emitted photons or the emission directly in the suitable frequency domain.

Concerning the first solution, several group have proposed to convert the frequency of photons emitted by either QDs, NV-centers in diamonds [245–248] or SPDC sources [249], via non-linear crystals and down-conversion process. Since the conversion towards the telecom C-band involved large noise counts due to spontaneous scattering processes from the strong classical pump [247], the first experiments converted photons into the O-band range [245, 246, 250]. To overcome the spectral filtering issue, several filters (fiber Bragg grating or bandpass/longpass filters) were placed after the down-conversion components to only collect the converted single photons. In 2012, Pelc et al. [251] demonstrated a quantum frequency conversion, towards 1560nm, of single photons emitted at 910nm by InAs/GaAs QDs embedded in planar-cavity. To do so, they used a periodically poled lithium niobate (PPLN) waveguides and a pulsed pump laser at 2.2μm. The latter enabled to temporally and spectrally shape the single photons wavepacket. These then allowed for two-photon interferences [252] and entanglement generations [253–255]. Even though converting the wavelength does not impact the single-photon indistinguishability [256], their purity is degraded due to the residual pump laser, and remains below 90% [247, 256]. Moreover, due to low coupling efficiencies of the single photons into the waveguide, a non-perfect conversion process and a large post-conversion filtering, the total conversion efficiency remains limited to about 30% [256]. However, such conversion efficiency combined with the most efficient sources at 930 nm would still provide a strong improvement compared to SPDC sources operating at telecom wavelength.

Finally, concerning the second solution, several groups developed growth methods to obtain high quality quantum dots emitting in one of the telecom bands. The first approach consists in either increasing the InAs/GaAs QDs size or reducing the strain between them and the surrounding barrier material [257–260]. The single photons emitted by such sources have wavelength in the telecom O-band. Alternatively, InAs/InP QDs seem to be promising emitters of single and indistinguishable photons in the C-band [261–263]. The current main issue is the insertion of these quantum dots in efficient photonic structure to obtain an efficient collection of the photons [263–265]. In this perspective, Quandela has launched a new project with the objective to fabricate a new generation of sources emitting single photons directly at telecom wavelengths. It will be built on the recent progresses on the growth side, combining them with the tools of in-situ lithography for efficient photon collection.

Appendix

Analytical model: Gaussian equations for each propagation steps

The following describes each equation of the analytical model. The propagation follows the steps of the schematic of figure 3.2.

1. As established in reference [201], the spatial profile at the output of the first single-mode fibre can be approximated as a Gaussian profile and expressed as follows:

$$G_0(x,y) = I \exp\left[-\frac{(x^2+y^2)}{{w_0}^2}\right] \tag{6.1}$$

To note: For this step and all the others, the waist w_0 is defined as the radius at $\frac{1}{e^2}$ of the maximum intensity.

2. Propagation along a distance d_1. To collimate the divergent beam, this distance is equal to the lens focal length, f_1. The equation (6.1) is written in the Fourier domain and by multiplying it with the vacuum transfer function. Then the result is written back in the reel space.

$$G_{\mathrm{d1}}(\nu_\mathrm{x},\nu_\mathrm{y}) = I\pi{w_0}^2 \exp\left[-ikd_1\right] \exp\left[-\pi(\pi{w_0}^2 - i\lambda d_1)\left({\nu_\mathrm{x}}^2+{\nu_\mathrm{y}}^2\right)\right] \tag{6.2}$$

$$G_{\mathrm{d1}}(x,y) = \frac{I\pi{w_0}^2}{\pi{w_0}^2 - i\lambda d_1} \exp\left[-ikd_1\right] \exp\left[-\frac{\pi}{\pi{w_0}^2 - i\lambda d_1}(x^2+y^2)\right] \tag{6.3}$$

3. Passage through an infinite diameter lens. This equation was obtained by multiplying, in the real space, the equation (6.3) with the phase term of a thin lens, with a focal length of f_1.

$$G_{l1}(x,y) = \frac{I\pi {w_0}^2}{\pi {w_0}^2 - i\lambda d_1} \exp\left[-ikd_1\right] \exp\left[-\pi\left(\frac{1}{\pi {w_0}^2 - i\lambda d_1} - \frac{i}{\lambda f_1}\right)(x^2+y^2)\right] \tag{6.4}$$

4. Propagation along a distance D separating the two lenses:

$$G_D(x,y) = I_D \exp\left[-ik(d_1+D)\right] \exp\left[-e_D(x^2+y^2)\right] \tag{6.5}$$

with,

$I_D = \frac{I\pi {w_0}^2 f_1}{\pi {w_0}^2(f_1-D) - i\lambda[(D(f_1-d_1)+f_1 d_1]}$

$e_D = \frac{\pi}{\lambda}\frac{\lambda(f_1-d_1) - i\pi {w_0}^2}{\pi {w_0}^2(f_1-D) - i\lambda[(D(f_1-d_1)+f_1 d_1]}$

This equation was obtained in the same way as for the step 2 equation.

5. Passage through a thin lens with an infinite diameter and a focal length, f_2:

$$G_{l2}(x,y) = I_{l2} \exp\left[-ik(d_1+D)\right] \exp\left[-e_{l2}(x^2+y^2)\right] \tag{6.6}$$

with,

$I_{l2} = \frac{I\pi {w_0}^2 f_1}{\pi {w_0}^2(f_1-D) - i\lambda[(D(f_1-d_1)+f_1 d_1]}$

$e_{l2} = \frac{\pi}{\lambda}\left(\frac{\lambda(f_1-d_1) - i\pi {w_0}^2}{\pi {w_0}^2(f_1-D) - i\lambda[(D(f_1-d_1)+f_1 d_1]} - \frac{i}{f_2}\right)$

This equation was obtained in the same way as for the step 3 equation.

6. Propagation along a distance d_2. To focalise the beam, this distance is equal to the lens focal length, f_2. This equation gives the final profile of this model.

$$G_{d2}(x,y) = G_f(x,y) = I_{d2} \exp\left[-ik(d_1+D+d_2)\right] \exp\left[-e_{d2}(x^2+y^2)\right] \tag{6.7}$$

with,

$I_{d2} = \frac{I\pi {w_0}^2 f_1 f_2}{\pi {w_0}^2[f_2(f_1-D)-d_2(f_1+f_2-D)] - i\lambda[f_2 D(f_1-d_1)+f_1 f_2 d_1+d_2(f_2-D)(f_1-d_1)-f_1 d_1 d_2]}$

$e_{d2} = \frac{\pi}{\lambda}\frac{\lambda[(f_1-d_1)(f_2-D)-f_1 d_1] - i\pi {w_0}^2(f_1+f_2-D)}{\pi {w_0}^2[f_2(f_1-D)-d_2(f_1+f_2-D)] - i\lambda[f_2 D(f_1-d_1)+f_1 f_2 d_1+d_2(f_2-D)(f_1-d_1)-f_1 d_1 d_2]}$

This equation was obtained in the same way as for the step 2 equation.

This equation is for the general case but usually the system is symmetric and $f_1 = f_2 = d_1 = d_2$.

Bibliography

[1] I.M. Georgescu, S. Ashhab, and F. Nori. Quantum simulation. Rev. Mod. Phys., 86:153–185, Mar 2014.

[2] C.L. Degen, F. Reinhard, and P. Cappellaro. Quantum sensing. Rev. Mod. Phys., 89:035002, Jul 2017.

[3] H. Kimble. The quantum internet. Nature, 453:1023–1030, 2008.

[4] E. Diamanti, B. Lo, HK.and Qi, and Z. Yuan. Practical challenges in quantum key distribution. npj Quantum Inf, 2:16025, 2016.

[5] D.P. DiVincenzo. The physical implementation of quantum computation. Fortschritte der Physik, 48(9-11):771–783.

[6] M.A. Nielsen and I. Chuang. Quantum computation and quantum information. American Journal of Physics, 70(5):558–559, 2002.

[7] J. Wang, F. Sciarrino, A. Laing, and M.G. Thompson. Integrated photonic quantum technologies. Nat. Photonics, 14:273–284, 2020.

[8] I. Aharonovich, D. Englund, and M. Toth. Solid-state single-photon emitters. Nature Photon., 10:631–641, 2016.

[9] N. Somaschi, V. Giesz, L. De Santis, J. C. Loredo, M. P. Almeida, G. Hornecker, S. L. Portalupi, T. Grange, C. Antón, J. Demory, C. Gómez, I. Sagnes, N. D. Lanzillotti-Kimura, A. Lemaítre, A. Auffeves, A. G. White, L. Lanco, and P. Senellart. Near-optimal single-photon sources in the solid state. Nature Photonics, 10:340–345, 5 2016.

[10] A. M. Barth, S. Lüker, A. Vagov, D. E. Reiter, T. Kuhn, and V. M. Axt. Fast and selective phonon-assisted state preparation of a quantum dot by adiabatic undressing. Physical Review B, 94:045306, 2016.

[11] M. Glässl, A. M. Barth, and V. M. Axt. Proposed robust and high-fidelity preparation of excitons and biexcitons in semiconductor quantum dots making active use of phonons. Physical Review Letters, 110:1–5, 2013.

[12] Arya-K. Babbush R. et al. Arute, F. Quantum supremacy using a programmable superconducting processor. Nature, page 505–510, 2019.

[13] E. Knill, R. Laflamme, and G.J. Milburn. A scheme for efficient quantum computation with linear optics. Nature, 409:46–52, 2001.

[14] N. Gisin and R. Thew. Quantum communication. Nature Photon., 1:165–171, 2007.

[15] M. Varnava, D.E. Browne, and T. Rudolph. How good must single photon sources and detectors be for efficient linear optical quantum computation? Phys. Rev. Lett., 100:060502, Feb 2008.

[16] J. C. Loredo, M. A. Broome, P. Hilaire, O. Gazzano, I. Sagnes, A. Lemaitre, M. P. Almeida, P. Senellart, and A. G. White. Boson sampling with single-photon fock states from a bright solid-state source. Physical Review Letters, 118, 3 2017.

[17] H. Wang, Y. He, Y.H. Li, Z.E Su, B. Li, H.L Huang, X. Ding, M.C. Chen, C. Liu, J. Qin, J.P. Li, Y.M. He, C. Schneider, M. Kamp, C.Z. Peng, S. Höfling, C.Y. Lu, and J.-W. Pan. High-efficiency multiphoton boson sampling. Nature Photonics, 11:361–365, 6 2017.

[18] H. Wang, J. Qin, X. Ding, M.-C. Chen, S. Chen, X. You, Y.-M. He, X. Jiang, L. You, Z. Wang, C. Schneider, J.J. Renema, S. Höfling, C.-Y. Lu, and J.-W. Pan. Boson sampling with 20 input photons and a 60-mode interferometer in a 10^{14}-dimensional hilbert space. Phys. Rev. Lett., 123:250503, Dec 2019.

[19] H.-S. Zhong, H. Wang, Y.-H. Deng, M.-C. Chen, L.-C. Peng, Y.-H. Luo, J. Qin, D. Wu, X. Ding, Y. Hu, P. Hu, X.-Y. Yang, W.-J. Zhang, H. Li, Y. Li, X. Jiang, L. Gan, G. Yang, L. You, Z. Wang, L. Li, N.-L. Liu, C.-Y. Lu, and J.-W. Pan. Quantum computational advantage using photons. Science, 2020.

[20] A. Aspuru-Guzik and P. Walther. Photonic quantum simulators. Nature Physics, 8:285–291, 2012.

[21] H.R. Grimsley, S.E. Economou, E. Barnes, and N.J. Mayhall. An adaptive variational algorithm for exact molecular simulations on a quantum computer. Nature Communications, 2019.

[22] F. Schlawin. Entangled photon spectroscopy. Journal of Physics B: Atomic, Molecular and Optical Physics, 50(20):203001, oct 2017.

[23] B. Dayan. Theory of two-photon interactions with broadband down-converted light and entangled photons. Phys. Rev. A, 76:043813, Oct 2007.

[24] H.-B. Fei, B.M. Jost, S. Popescu, B.E. A. Saleh, and M.C. Teich. Entanglement-induced two-photon transparency. Phys. Rev. Lett., 78:1679–1682, Mar 1997.

[25] L.A. Howard, G.G. Gillett, M.E. Pearce, R.A. Abrahao, T.J. Weinhold, P. Kok, and A.G. White. Optimal imaging of remote bodies using quantum detectors. Phys. Rev. Lett., 123:143604, Sep 2019.

[26] G. Brida, M. Genovese, and I. Ruo Berchera. Experimental realization of sub-shot-noise quantum imaging. Nature Photonics, 4:227–230, 4 2010.

[27] E. Toninelli, M.P. Edgar, P.-A. Moreau, G.M. Gibson, G.D Hammond, and M.J. Padgett. Sub-shot-noise shadow sensing with quantum correlations. Optics Express, 25:21826, 9 2017.

[28] X.L. Chu, S. Götzinger, and V. Sandoghdar. A single molecule as a high-fidelity photon gun for producing intensity-squeezed light. Nature Photonics, 11:58–62, 1 2017.

[29] K. Takemoto, Y. Nambu, T. Miyazawa, Y. Sakuma, T. Yamamoto, S. Yorozu, and Y. Arakawa. Quantum key distribution over 120km using ultrahigh purity single-photon source and superconducting single-photon detectors. Sci Rep, 5(14383).

[30] T. Zhong, H. Zhou, R.D. Horansky, C. Lee, V.B. Verma, A.E. Lita, A. Restelli, J.C. Bienfang, R.P. Mirin, and et al. Gerrits, T. Photon-efficient quantum key distribution using time–energy entanglement with high-dimensional encoding. New Journal of Physics, 17(2):022002, 2015.

[31] Z. Zhang, C. Chen, Q. Zhuang, F.N.C Wong, and J.H. Shapiro. Experimental quantum key distribution at 1.3 gigabit-per-second secret-key rate over a 10 dB loss channel. Quantum Science and Technology, 3(2):025007, apr 2018.

[32] C. Crocker, M. Lichtman, K. Sosnova, A. Carter, S. Scarano, and C. Monroe. High purity single photons entangled with an atomic qubit. Opt. Express, 27(20):28143–28149, Sep 2019.

[33] M. Caleffi, A.S. Cacciapuoti, and G. Bianchi. Quantum internet: from communication to distributed computing! 5 2018.

[34] M. Varnava, D.E. Browne, and T. Rudolph. Loss tolerance in one-way quantum computation via counterfactual error correction. Phys. Rev. Lett., 97:120501, Sep 2006.

[35] N.H. Lindner and T. Rudolph. Proposal for pulsed on-demand sources of photonic cluster state strings. Phys. Rev. Lett., 103:113602, Sep 2009.

[36] D. Buterakos, E. Barnes, and S.E. Economou. Deterministic generation of all-photonic quantum repeaters from solid-state emitters. Phys. Rev. X, 7:041023, Oct 2017.

[37] R. Raussendorf, J. Harrington, and K. Goyal. A fault-tolerant one-way quantum computer. Annals of Physics, 321:2242–2270, 2006.

[38] A. Montanaro. Quantum algorithms: an overview. npj Quantum Inf, 2:15023, 2016.

[39] P.C. Maurer, G. Kucsko, C. Latta, L. Jiang, N.Y. Yao, S.D. Bennett, F. Pastawski, D. Hunger, N. Chisholm, M. Markham, D.J. Twitchen, J.I. Cirac, and M.D. Lukin. Room-temperature quantum bit memory exceeding one second. Science, 336(6086):1283–1286, 2012.

[40] K.T. Kaczmarek, P.M. Ledingham, B. Brecht, S.E. Thomas, G.S. Thekkadath, O. Lazo-Arjona, J.H.D. Munns, E. Poem, A. Feizpour, D.J. Saunders, J. Nunn, and I.A. Walmsley. High-speed noise-free optical quantum memory. Phys. Rev. A, 97:042316, Apr 2018.

[41] H.G. Barros, A. Stute, T.E. Northup, C. Russo, P.O. Schmidt, and R. Blatt. Deterministic single-photon source from a single ion. New Journal of Physics, 11(10):103004, oct 2009.

[42] J. McKeever, A. Boca, A.D. Boozer, R. Miller, J.R. Buck, A. Kuzmich, and H.J. Kimble. Deterministic generation of single photons from one atom trapped in a cavity. Science, 303(5666):1992–1994, 2004.

[43] L.M. Duan, M. Lukin, J. Cirac, and P. Zoller. Long-distance quantum communication with atomic ensembles and linear optics. Nature, 414(6862):413–418, 2001.

[44] A. Beveratos, R. Brouri, T. Gacoin, A. Villing, J.-P. Poizat, and P. Grangier. Single photon quantum cryptography. Phys. Rev. Lett., 89:187901, Oct 2002.

[45] P. Michler, A. Kiraz, C. Becher, W. V. Schoenfeld, P. M. Petroff, Lidong Zhang, E. Hu, and A. Imamoglu. A quantum dot single-photon turnstile device. Science, 290(5500):2282–2285, 2000.

[46] W.B. Gao, P. Fallahi, E. Togan, J. Miguel-Sanchez, and A. Imamoglu. Observation of entanglement between a quantum dot spin and a single photon. Nature, 491(7424):426—430, November 2012.

[47] W. Gao, A. Imamoglu, H. Bernien, and R. Ranson. Ultrafast all-optical switching by single photons. Nature Photon, 9:363–373, 2015.

[48] J. Claudon, J. Bleuse, N.S. Malik, M. Bazin, P. Jaffrennou, N. Gregersen, C. Sauvan, P. Lalanne, and J.-M. Gérard. A highly efficient single-photon source based on a quantum dot in a photonic nanowire. Nature Photon, 4:174–177, 2010.

[49] O. Gazzano, S. Michaelis De Vasconcellos, C. Arnold, A. Nowak, E. Galopin, I. Sagnes, L. Lanco, A. Lemaître, and P. Senellart. Bright solid-state sources of indistinguishable single photons. Nature Communications, 4, 2013.

[50] M. Collins, C. Xiong, I. Rey, T.D. Vo, J. He, S. Shahnia, C. Reardon, T.F. Krauss, M.J. Steel, Clark A.S., and B.J. Eggleton. Integrated spatial multiplexing of heralded single-photon sources. Nat Commun, 4:2582, 2013.

[51] M. Munsch, N.S. Malik, E. Dupuy, A. Delga, J. Bleuse, J.M. Gérard, J. Claudon, N. Griegersen, and J. Mørk. Dielectric GaAs antenna ensuring an efficient broadband coupling between an InAs quantum dot and a gaussian optical beam. Phys. Rev. Lett., 110:177402, Apr 2013.

[52] D. Wang, H. Kelkar, D. Martin-Cano, D. Rattenbacher, A. Shkarin, T. Utikal, S. Götzinger, and V. Sandoghdar. Turning a molecule into a coherent two-level quantum system. Nat. Phys., 15:483–489, 2019.

[53] N. Tomm, A. Javadi, N.O. Antoniadis, D. Najer, M.C. Löbl, A.R. Korsch, R. Schott, S.R. Valentin, A.D. Wieck, A. Ludwig, and R.J Warburton. A bright and fast source of coherent single photons. Nat. Nanotech., 2021.

[54] P. Senellart, G. Solomon, and A. White. High-performance semiconductor quantum-dot single-photon sources. Nature Nanotech., page 1026–1039, 2017.

[55] S. Ramelow, A. Mech, M. Giustina, S. Gröblacher, W. Wieczorek, J. Beyer, A. Lita, B. Calkins, T. Gerrits, S-.W. Nam, A. Zeilinger, and R. Ursin. Highly efficient heralding of entangled single photons. Opt. Express, 21(6):6707–6717, Mar 2013.

[56] M-.M. Weston, H-.M. Chrzanowski, S. Wollmann, A. Boston, J. Ho, L-.K. Shalm, V-.B. Verma, M-.S. Allman, S-.W. Nam, R-.B. Patel, S. Slussarenko, and G-.J. Pryde. Efficient and pure femtosecond-pulse-length source of polarization-entangled photons. Opt. Express, 24(10):10869–10879, May 2016.

[57] F. Kaneda, K. Garay-Palmett, A-.B. U'Ren, and P-.G. Kwiat. Heralded single-photon source utilizing highly nondegenerate, spectrally factorable spontaneous parametric downconversion. Opt. Express, 24(10):10733–10747, May 2016.

[58] Q.A. Turchette, C.S. Wood, B.E. King, C.J. Myatt, D. Leibfried, W.M. Itano, C. Monroe, and D.J. Wineland. Deterministic entanglement of two trapped ions. Physical Review Letters, 81(17):3631, 1998.

[59] F. Ripka, H. Kübler, R. Löw, and T. Pfau. A room-temperature single-photon source based on strongly interacting rydberg atoms. Science, 362(6413):446–449, 2018.

[60] A. Lohrmann, B.C. Johnson, J.C. McCallum, and S. Castelletto. A review on single photon sources in silicon carbide. Reports on Progress in Physics, 80(3):034502, jan 2017.

[61] X. Ding, Y. He, Z.-C. Duan, N. Gregersen, M.-C. Chen, S. Unsleber, S. Maier, C. Schneider, M. Kamp, S. Höfling, C.-Y. Lu, and J.-W. Pan. On-demand single photons with high extraction efficiency and near-unity indistinguishability from a resonantly driven quantum dot in a micropillar. Phys. Rev. Lett., 116(020401), Jan 2016.

[62] H. Wang, Y. He, and T. Chung. Towards optimal single-photon sources from polarized microcavities. Nature Photonics, 13:770–775, 2019.

[63] Y.M. He, H. Wang, C. Wang, M.C. Chen, X. Ding, J. Qin, Z.C. Duan, S. Chen, J.P. Li, R.Z. Liu, C. Schneider, M. Atatüre, S. Höfling, C.Y. Lu, and J.W. Pan. Coherently driving a single quantum two-level system with dichromatic laser pulses. Nature Physics, 15:941–946, 2019.

[64] M. Pelton, C. Santori, J. Vuc̆ković, B. Zhang, G. S. Solomon, J. Plant, and Y. Yamamoto. Efficient source of single photons: A single quantum dot in a micropost microcavity. Phys. Rev. Lett., 89:233602, Nov 2002.

[65] R. Hanbury Brown and R. Q. Twiss. Correlation between photons in two coherent beams of light. Nature, 177:27–29, 1956.

[66] H.J. Kimble, M. Dagenais, and L. Mandel. Photon antibunching in resonance fluorescence. Phys. Rev. Lett., 39:691–695, Sep 1977.

[67] P. Grangier, G. Roger, and A. Aspect. Experimental evidence for a photon anticorrelation effect on a beam splitter: A new light on single-photon interferences. Europhysics Letters (EPL), 1(4):173–179, feb 1986.

[68] R.J. Glauber. The quantum theory of optical coherence. Phys. Rev., 130:2529–2539, Jun 1963.

[69] C.K. Hong, Z.Y. Ou, and L. Mandel. Measurement of subpicosecond time intervals between two photons by interference. Phys. Rev. Lett., 59:2044–2046, Nov 1987.

[70] C. Cohen-Tahnoudji, B. Diu, and F. Laloe. Quantum Mechanics. 1977.

[71] C. Santori, D. Fattal, J. Vu ˇckovi , G.S. Solomon, and Y. Yamamoto. Indistinguishable photons from a single-photon device. Nature, 419:594–597, Oct 2002.

[72] L. Besombes, K. Kheng, L. Marsal, and H. Mariette. Acoustic phonon broadening mechanism in single quantum dot emission. Phys. Rev. B, 63:155307, Mar 2001.

[73] D. Gammon, E. S. Snow, B. V. Shanabrook, D. S. Katzer, and D. Park. Homogeneous linewidths in the optical spectrum of a single gallium arsenide quantum dot. Science, 273(5271):87–90, 1996.

[74] X.-Q. Li and Y. Arakawa. Optical linewidths in an individual quantum dot. Phys. Rev. B, 60:1915–1920, Jul 1999.

[75] M. Bayer, G. Ortner, O. Stern, A. Kuther, A.A. Gorbunov, A. Forchel, P. Hawrylak, S. Fafard, K. Hinzer, T.L. Reinecke, S.N. Walck, J.P. Reithmaier, F. Klopf, and F. Schäfer. Fine structure of neutral and charged excitons in self-assembled in(ga)as/(al)GaAs quantum dots. Phys. Rev. B, 65(195315), May 2002.

[76] C. Kammerer, C. Voisin, G. Cassabois, C. Delalande, P. Roussignol, F. Klopf, J.P. Reithmaier, A. Forchel, and J.M. Gerard. Line narrowing in single semiconductor quantum dots: Toward the control of environment effects. Physical Review B: Condensed Matter and Materials Physics, 66:041306, 2002.

[77] K. Konthasinghe, J. Walker, M. Peiris, C. K. Shih, Y. Yu, M. F. Li, J. F. He, L. J. Wang, H. Q. Ni, Z. C. Niu, and A. Muller. Coherent versus incoherent light scattering from a quantum dot. Phys. Rev. B, 85:235315, Jun 2012.

[78] A. Kuhlmann, J. Houel, and A. Ludwig. Charge noise and spin noise in a semiconductor quantum device. Nature Phys, 9:570–575, 2013.

[79] C. Arnold, J. Demory, V. Loo, A. Lemaître, I. Sagnes, M. Glazov, O. Krebs, P. Voisin, P. Senellart, and L. Lanco. Macroscopic rotation of photon polarization induced by a single spin. Nat Commun., 6:6236, 2015.

[80] F. Graffitti, P. Barrow, M. Proietti, D. Kundys, and A. Fedrizzi. Independent high-purity photons created in domain-engineered crystals. Optica, 5(5):514–517, May 2018.

[81] T.B. Pittman, B.C. Jacobs, and J.D. Franson. Single photons on pseudodemand from stored parametric down-conversion. Phys. Rev. A, 66:042303, Oct 2002.

[82] F. Kaneda and P. G. Kwiat. High-efficiency single-photon generation via large-scale active time multiplexing. Science Advances, 5(10), 2019.

[83] T.M. Babinec, B.J.M. Hausmann, M. Khan, Y. Zhang, Maze J.R., P.R. Hemmer, and M. Lončar. A diamond nanowire single-photon source. Nat. Nanotechnol., 5:195, 2010.

[84] E. Neu, D. Steinmetz, J. Riedrich-Möller, S. Gsell, M. Fischer, M. Schreck, and C. Becher. Single photon emission from silicon-vacancy colour centres in chemical vapour deposition nano-diamonds on iridium. New Journal of Physics, 13(2):025012, feb 2011.

[85] L. Marseglia, K. Saha, A. Ajoy, T. Schröder, D. Englund, F. Jelezko, R. Walsworth, J. L. Pacheco, D. L. Perry, E. S. Bielejec, and P. Cappellaro. Bright nanowire single photon source based on siv centers in diamond. Opt. Express, 26(1):80–89, Jan 2018.

[86] L.-W. Wang, J. Kim, and A. Zunger. Electronic structures of [110]-faceted self-assembled pyramidal InAs/GaAs quantum dots. Phys. Rev. B, 59:5678–5687, Feb 1999.

[87] A. J. Williamson, L. W. Wang, and A. Zunger. Theoretical interpretation of the experimental electronic structure of lens-shaped self-assembled InAs/GaAs quantum dots. Phys. Rev. B, 62:12963–12977, Nov 2000.

[88] G. Bastard. Superlattice band structure in the envelope-function approximation. Phys. Rev. B, 24:5693–5697, Nov 1981.

[89] J.-Y. Marzin, J.-M. Gérard, A. Izraël, D. Barrier, and G. Bastard. Photoluminescence of single InAs quantum dots obtained by self-organized growth on GaAs. Phys. Rev. Lett., 73:716–719, Aug 1994.

[90] J.-Y. Marzin and G. Bastard. Calculation of the energy levels in InAsGaAs quantum dots. Solid State Communications, 92(5):437 – 442, 1994.

[91] Y. Toda, O. Moriwaki, M. Nishioka, and Y. Arakawa. Efficient carrier relaxation mechanism in InGaAs/GaAs self-assembled quantum dots based on the existence of continuum states. Phys. Rev. Lett., 82:4114–4117, May 1999.

[92] G. Medeiros-Ribeiro, F.-G. Pikus, P.-M. Petroff, and A.-L. Efros. Single-electron charging and coulomb interaction in InAs self-assembled quantum dot arrays. Phys. Rev. B, 55:1568–1573, jan 1997.

[93] U. Banin, Y. Cao, D. Katz, and O. Millo. Identification of atomic-like electronic states in indium arsenide nanocrystal quantum dots. Nature, 400(6744):542–544, aug 1999.

[94] D. Bimberg, M. Grundmann, and N.N. Ledentsov. Quantum dot Heterostructures. John Wiley Sons, 1999.

[95] J. Suffczyński, T. Kazimierczuk, M. Goryca, B. Piecha, A. Trajnerowicz, K. Kowalik, P. Kossack, A. Golnik, K.-P. Korona, M. Nawrocki, J.-A. Gaj, and G. Karczewsk. Excitation mechanisms of individual cd te zn te quantum dots studiedby photon correlation spectroscopy. Phys. Rev. B, 74:085319, aug 2006.

[96] C. Santori, M. Pelton, G. Solomon, Y. Dale, and Y. Yamamoto. Triggered single photons from a quantum dot. Phys. Rev. Lett., 86:1502–1505, Feb 2001.

[97] E. Moreau, I. Robert, J. M. Gérard, I. Abram, L. Manin, and V. Thierry-Mieg. Single-mode solid-state single photon source based on isolated quantum dots in pillar microcavities. Applied Physics Letters, 79:2865–2867, 2001.

[98] D. N. Krizhanovskii, A. Ebbens, A. I. Tartakovskii, F. Pulizzi, T. Wright, M. S. Skolnick, and M. Hopkinson. Individual neutral and charged $in_xga_{1-x}As-GaAs$ quantum dots with strong in-plane optical anisotropy. Phys. Rev. B, 72:161312, Oct 2005.

[99] H. Ollivier, I. Maillette de Buy Wenniger, S. Thomas, S.C. Wein, A. Harouri, G. Coppola, P. Hilaire, C. Millet, A. Lemaître, I. Sagnes, O. Krebs, L. Lanco, J. C. Loredo, C. Antón, N. Somaschi, and P. Senellart. Reproducibility of high-performance quantum dot single-photon sources. ACS Photonics, 7(4):1050–1059, 2020.

[100] A. Franceschetti and A. Zunger. Direct pseudopotential calculation of exciton coulomb and exchange energies in semiconductor quantum dots. Phys. Rev. Lett., 78:915–918, Feb 1997.

[101] E. Blackwood, M. J. Snelling, R. T. Harley, S. R. Andrews, and C. T. B. Foxon. Exchange interaction of excitons in GaAs heterostructures. Phys. Rev. B, 50:14246–14254, Nov 1994.

[102] T. Takagahara. Theory of exciton doublet structures and polarization relaxation in single quantum dots. Phys. Rev. B, 62:16840–16855, Dec 2000.

[103] R. Warburton. Single spins in self-assembled quantum dots. Nature Mater., 12:483–493, 2013.

[104] P. Michler. Single quantum dots: Fundamentals, applications, and new concepts, volume 90 of Topics in Applied Physics. Springer Berlin Heidelberg, 2003.

[105] P. Lodahl, S. Mahmoodian, and S. Stobbe. Interfacing single photons and single quantum dots with photonic nanostructures. Rev. Mod. Phys., 87:347–400, May 2015.

[106] R. Seguin, A. Schliwa, S. Rodt, K. Pötschke, U. W. Pohl, and D. Bimberg. Size-dependent fine-structure splitting in self-organized $InAs/GaAs$ quantum dots. Phys. Rev. Lett., 95:257402, Dec 2005.

[107] D.-J.-P. Ellis, R.-M. Stevenson, R.-J. Young, A.-J. Shields, P. Atkinson, and D.-A. Ritchie. Control of fine-structure splitting of individual InAs quantum dots by rapid thermal annealing. Applied Physics Letters, 90(1):011907, jan 2007.

[108] A. Tartakovskii, M. Makhonin, I. Sellers, J. Cahill, A. Andreev, D. Whittaker, J.-P. Wells, A. Fox, D. Mowbray, M. Skolnick, K. Groom, M. Steer, H. Liu, and M. Hopkinson. Effect of thermal annealing and strain engineering on the fine structure of quantum dot excitons. Phys. Rev. B, 70:1–4, 2004.

[109] R. Trotta, J.-S. Wildmann, E. Zallo, O.-G. Schmidt, and A. Rastelli. Highly entangled photons from hybrid piezoelectric-semiconductor quantum dot devices. Nano. Lett., 14(6):3439, jun 2014.

[110] B.-D. Gerardot, S. Seidl, P.-A. Dalgarno, R.-J. Warburton, D. Granados, J.-M. Garcia, K. Kowalik, O. Krebs, K. Karrai, A. Badolato, and P.-M. Petroff. Manipulating exciton fine structure in quantum dots with a lateral electric field. Applied Physics Letters, 90(4):041101, 2007.

[111] A. Muller, W. Fang, J. Lawall, and G.-S. Solomon. Creating polarization-entangled photon pairs from a semiconductor quantum dot using the optical stark effect. Phys. Rev. Lett., 103(21):217402, nov 2009.

[112] K. Kowalik, O. Krebs, A. Golnik, J. Suffczyński, P. Wojnar, J. Kossut, J. A. Gaj, and P. Voisin. Manipulating the exciton fine structure of singlecdtezntequantum dots by an in-plane magnetic field. Physical Review B, 75(19), may 2007.

[113] O. Benson, C. Santori, M. Pelton, and Y. Yamamoto. Regulated and entangled photons from a single quantum dot. Phys. Rev. Lett., 84:2513–2516, Mar 2000.

[114] E.T. Jaynes and F. W. Cummings. Comparison of quantum and semiclassical radiation theories with application to the beam maser. Proceedings of the IEEE, 51(1):89–109, 1963.

[115] E. M. Purcell, H. C. Torrey, and R. V. Pound. Resonance absorption by nuclear magnetic moments in a solid. Physical review, 69(1-2):37, 1946.

[116] T. Grange, N. Somaschi, C. Antón, L. De Santis, G. Coppola, V. Giesz, A. Lemaître, I. Sagnes, A. Auffèves, and P. Senellart. Reducing phonon-induced decoherence in solid-state single-photon sources with cavity quantum electrodynamics. Physical Review Letters, 118, 6 2017.

[117] J. Iles-Smith, D. McCutcheon, Nazir A., and J. Mørk. Phonon scattering inhibits simultaneous near-unity efficiency and indistinguishability in semiconductor single-photon sources. Nature Photon., 11:521–526, 2017.

[118] D. Valente, J. Suffczyński, T. Jakubczyk, A. Dousse, A. Lemaître, I. Sagnes, L. Lanco, P. Voisin, A. Auffèves, and P. Senellart. Frequency cavity pulling induced by a single semiconductor quantum dot. Phys. Rev. B, 89:041302, jan 2014.

[119] T. Lund-Hansen, S. Stobbe, B. Julsgaard, H. Thyrrestrup, T. Sünner, M. Kamp, A. Forchel, and P. Lodahl. Experimental realization of highly efficient broadband coupling of single quantum dots to a photonic crystal waveguide. Phys. Rev. Lett., 101:113903, sep 2008.

[120] M. Versteegh, M. Reimer, and K. Jöns. Observation of strongly entangled photon pairs from a nanowire quantum dot. Nature Communications, 5(5298), 2014.

[121] G. Bulgarini, M.E. Reimer, M. Bouwes Bavinck, K.D. Jöns, D. Dalacu, P.J. Poole, E.P. A. M. Bakkers, and V. Zwiller. Nanowire waveguides launching single photons in a gaussian mode for ideal fiber coupling. Nano Letters, 14(7):4102–4106, 2014. PMID: 24926884.

[122] R. Uppu, Freja T. Pedersen, Ying Wang, Cecilie T. Olesen, Camille Papon, Xiaoyan Zhou, Leonardo Midolo, Sven Scholz, Andreas D. Wieck, A. Ludwig, and P. Lodahl. Scalable integrated single-photon source. Science Advances, 6(50), 2020.

[123] P. Stepanov, A. Delga, N. Gregersen, E. Peinke, M. Munsch, J. Teissier, J. Mørk, M. Richard, J. Bleuse, J-.M. Gérard, and J. Claudon. Highly directive and gaussian far-field emission from "giant" photonic trumpets. Applied Physics Letters, 107(14):141106, 2015.

[124] D. Cadeddu, J. Teissier, F.R. Braakman, N. Gregersen, P. Stepanov, J-.M. Gérard, J. Claudon, R.J. Warburton, M. Poggio, and M. Munsch. A fiber-coupled quantum-dot on a photonic tip. Applied Physics Letters, 108(1):011112, 2016.

[125] I.E. Zadeh, A.W. Elshaari, K.D. Jöns, A. Fognini, D. Dalacu, P.J. Poole, M.E. Reimer, and V. Zwiller. Deterministic integration of single photon sources in silicon based photonic circuits. Nano Letters, 16(4):2289–2294, 2016. PMID: 26954298.

[126] L. Leandro, J. Hastrup, R. Reznik, G. Cirlin, and N. Akopian. Resonant excitation of nanowire quantum dots. npj Quantum Inf, 6(93), 2020.

[127] L. Monniello, A. Reigue, R. Hostein, A. Lemaitre, A. Martinez, R. Grousson, and V. Voliotis. Indistinguishable single photons generated by a quantum dot under resonant excitation observable without postselection. Phys. Rev. B, 90:041303, Jul 2014.

[128] R. Uppu, H.T. Eriksen, H. Thyrrestrup, A.D. Uğurlu, Y. Wang, S. Scholz, A.D. Wieck, A. Ludwig, M.C. Löbl, R.J. Warburton, P. Lodahl, and L. Midolo. On-chip deterministic operation of quantum dots in dual-mode waveguides for a plug-and-play single-photon source. Nat Commun., 11:3782, 2020.

[129] D. Englund, D. Fattal, E. Waks, G. Solomon, B. Zhang, T. Nakaoka, Y. Arakawa, Y. Yamamoto, and J. Vučković. Controlling the spontaneous emission rate of single quantum dots in a two-dimensional photonic crystal. Phys. Rev. Lett., 95:013904, Jul 2005.

[130] S. Laurent, S. Varoutsis, L. Le Gratiet, A. Lemaître, I. Sagnes, F. Raineri, A. Levenson, I. Robert-Philip, and I. Abram. Indistinguishable single photons from a single-quantum dot in a two-dimensional photonic crystal cavity. Applied Physics Letters, 87(16):163107, 2005.

[131] F. Liu, A.J. Brash, and J. O'Hara. High purcell factor generation of indistinguishable on-chip single photons. Nature Nanotechnologies, 13:835–840, 2018.

[132] P. Lodahl, A. Floris van Driel, I.S. Nikolaev, A. Irman, K. Overgaag, D. Vanmaekelbergh, and W.L. Vos. Controlling the dynamics of spontaneous emission from quantum dots by photonic crystals. Nature, 430:654–657, 2004.

[133] S. Noda, M. Fujita, and T. Asano. Spontaneous-emission control by photonic crystals and nanocavities. Nature Photon., 1:449–458, 2007.

[134] K. H. Madsen, S. Ates, J. Liu, A. Javadi, S. M. Albrecht, I. Yeo, S. Stobbe, and P. Lodahl. Efficient out-coupling of high-purity single photons from a coherent quantum dot in a photonic-crystal cavity. Phys. Rev. B, 90:155303, Oct 2014.

[135] Y. Akahane, T. Asano, B.-S. Song, and S. Noda. Fine-tuned high-q photonic-crystal nanocavity. Opt. Express, 13(4):1202–1214, Feb 2005.

[136] A. Faraon, E. Waks, D. Englund, I. Fushman, and J. Vučković. Efficient photonic crystal cavity-waveguide couplers. Applied Physics Letters, 90(7):073102, 2007.

[137] A. Faraon, A. Majumdar, D. Englund, E. Kim, M. Bajcsy, and J. Vučković. Integrated quantum optical networks based on quantum dots and photonic crystals. New Journal of Physics, 13(5):055025, may 2011.

[138] C. Bentham, I.E. Itskevich, R.J. Coles, B. Royall, E. Clarke, J. O'Hara, N. Prtljaga, A.M. Fox, M.S. Skolnick, and L.R. Wilson. On-chip electrically controlled routing of photons from a single quantum dot. Applied Physics Letters, 106(22):221101, 2015.

[139] A. Muller, E.B. Flagg, M. Metcalfe, J. Lawall, and G.S. Solomon. Coupling an epitaxial quantum dot to a fiber-based external-mirror microcavity. Applied Physics Letters, 95(17):173101, 2009.

[140] R.J. Barbour, P.A. Dalgarno, A. Curran, K.M. Nowak, H.J. Baker, D.R. Hall, N.G. Stoltz, P.M. Petroff, and R.J. Warburton. A tunable microcavity. Journal of Applied Physics, 110(5):053107, 2011.

[141] G. Cui, J.M. Hannigan, R. Loeckenhoff, F.M. Matinaga, M.G. Raymer, S. Bhongale, M. Holland, S. Mosor, S. Chatterjee, H.M. Gibbs, and G. Khitrova. A hemispherical, high-solid-angle optical micro-cavity for cavity-qed studies. Optics express, 14(6):2289–2299, 2006.

[142] M. Davanço, M.T. Rakher, D. Schuh, A. Badolato, and K. Srinivasan. A circular dielectric grating for vertical extraction of single quantum dot emission. Applied Physics Letters, 99(4):041102, 2011.

[143] L. Sapienza, M. Davanço, A. Badolato, and K. Srinivasan. Nanoscale optical positioning of single quantum dots for bright and pure single-photon emission. Nat Commun, 6:7833, 2015.

[144] L. Sapienza, J. Liu, J.D. Song, S. Fält, W. Wegscheider, A. Badolato, and K. Srinivasan. Combined atomic force microscopy and photoluminescence imaging to select single InAs/GaAs quantum dots for quantum photonic devices. Sci. Rep., 7:6205, 2017.

[145] H. Wang, H. Hu, T.-H. Chung, J. Qin, X. Yang, J.-P. Li, R.-Z. Liu, H.-S. Zhong, Y.-M. He, X. Ding, Y.-H. Deng, Q. Dai, Y.-H. Huo, S. Höfling, C.-Y. Lu, and J.-W. Pan. On-demand semiconductor source of entangled photons which simultaneously has high fidelity, efficiency, and indistinguishability. Phys. Rev. Lett., 122:113602, Mar 2019.

[146] J. Liu, R. Su, Y. Wei, and et al. Yao, B. A solid-state source of strongly entangled photon pairs with high brightness and indistinguishability.s. Nat. Nanotechnol., (14):586–593, 2019.

[147] A. Dousse. Deterministic cavity-quantum dot coupling and fabrication of an ultrabright source of entangled photon pairs. PhD thesis, 2010.

[148] Batop Optoelectronics. Bragg mirror. https://www.batop.de/information/r$_B ragg.html$.

[149] L.R. Brovelli and U.Keller. Simple analytical expression for the reflectivity and the penetration depth of a bragg mirror between arbitrary media. Optics Communications, 116:343–350, May 1995.

[150] D. I. Babic and S. W. Corzine. Analytic expressions for the reflection delay, penetration depth, and absorptance of quarter-wave dielectric mirrors. IEEE Journal of Quantum Electronics, 28(2):514–524, 1992.

[151] C. C. Lin, D. G. Deppe, and C. Lei. Role of waveguide light emission in planar microcavities. IEEE Journal of Quantum Electronics, 30(10):2304–2313, 1994.

[152] G. Björk, S. Machida, Y. Yamamoto, and K. Igeta. Modification of spontaneous emission rate in planar dielectric microcavity structures. Phys. Rev. A, 44:669–681, Jul 1991.

[153] G. S. Solomon, M. Pelton, and Y. Yamamoto. Single-mode spontaneous emission from a single quantum dot in a three-dimensional microcavity. Physical Review Letters, 86:3903–3906, 2001.

[154] J.-M. Gérard, D. Barrier, J.-Y. Marzin, R. Kuszelewicz, L. Manin, E. Costard, V. Thierry-Mieg, and T. Rivera. Quantum boxes as active probes for photonic microstructures: The pillar microcavity case. Applied Physics Letters, 69(4):449–451, 1996.

[155] J.-M. Gérard, B. Sermage, B. Gayral, B. Legrand, E. Costard, and V. Thierry-Mieg. Enhanced spontaneous emission by quantum boxes in a monolithic optical microcavity. Phys. Rev. Lett., 81:1110–1113, Aug 1998.

[156] J. P. Reithmaier, M. Röhner, H. Zull, F. Schäfer, A. Forchel, P. A. Knipp, and T. L. Reinecke. Size dependence of confined optical modes in photonic quantum dots. Phys. Rev. Lett., 78:378–381, Jan 1997.

[157] J.-M. Gerard and B. Gayral. Strong purcell effect for InAs quantum boxes in three-dimensional solid-state microcavities. J. Lightwave Technol., 17(11):2089, Nov 1999.

[158] L. A. Graham, D. L. Huffaker, Q. Deng, and D. G. Deppe. Controlled spontaneous lifetime in microcavity confined ingaalas/GaAs quantum dots. Applied Physics Letters, 72(14):1670–1672, 1998.

[159] L. Goldstein, F. Glas, J. Y. Marzin, M. N. Charasse, and G. Le Roux. Growth by molecular beam epitaxy and characterization of InAs/GaAs strained-layer superlattices. Applied Physics Letters, 47:1099–1101, 1985.

[160] P. B. Joyce, T. J. Krzyzewski, G. R. Bell, T. S. Jones, S. Malik, D. Childs, and R. Murray. Effect of growth rate on the size, composition, and optical properties of InAs/GaAs quantum dots grown by molecular-beam epitaxy. Physical Review B - Condensed Matter and Materials Physics, 62:10891–10895, 2000.

[161] A. Dousse, L. Lanco, J. Suffczyński, E. Semenova, A. Miard, A. Lemaître, I. Sagnes, C. Roblin, J. Bloch, and P. Senellart. Controlled light-matter coupling for a single quantum dot embedded in a pillar microcavity using far-field optical lithography. Physical Review Letters, 101:30–33, 2008.

[162] G. Björk, H. Heitmann, and Y. Yamamoto. Spontaneous-emission coupling factor and mode characteristics of planar dielectric microcavity lasers. Phys. Rev. A, 47:4451–4463, May 1993.

[163] K. Kowalik, O. Krebs, A. Lemaître, S. Laurent, P. Senellart, P. Voisin, and J. A. Gaj. Influence of an in-plane electric field on exciton fine structure in InAs-GaAs self-assembled quantum dots. Applied Physics Letters, 86, 2005.

[164] M. Bayer, O. Stern, P. Hawrylak, S. Fafard, and A. Forchel. Hidden symmetries in the energy levels of excitonic 'artificial atoms'. Nature, 405:923–926, 2000.

[165] S. Strauf, N. Stoltz, M.T. Rakher, L.A. Coldren, P.M. Petroff, and D. Bouwmeester. High-frequency single-photon source with polarization control. Nature Photon., 1:704–708, 2007.

[166] C. Böckler, S. Reitzenstein, C. Kistner, R. Debusmann, A. Löffler, T. Kida, S. Höfling, A. Forchel, L. Grenouillet, J. Claudon, and J.M. Gérard. Electrically driven high-q quantum dot-micropillar cavities. Applied Physics Letters, 92(9):091107, 2008.

[167] T. Heindel, C. Schneider, M. Lermer, S. Höfling, S. Reitzenstein, and A. Forchel. Highly efficient electrically triggered quantum dot micropillar single photon source. Journal of Physics Conference Series, 245:012005, 09 2010.

[168] J. Beetz, C. Kistner, M. Lermer, C. Schneider, S. Reitzenstein, S. Höfling, M. Kamp, and A. Forchel. In-plane manipulation of quantum dots in high quality laterally contacted micropillar cavities. Applied Physics Letters, 98, 05 2011.

[169] A.K. Nowak, Portalupi S.L., V. Giesz, O. Gazzano, C. Dal Savio, P.F. Braun, K. Karrai, C. Arnold, L. Lanco, I. Sagnes, A. Lemaître, and P. Senellart. Deterministic and electrically tunable bright single-photon source. Nature Communications, 5:1–7, 2014.

[170] A. Zrenner, E. Beham, S. Stufler, F. Findeis, M. Bichler, and G. Abstreiter. Coherent properties of a two-level system based on a quantum-dot photodiode. Nature, 418:612–614, 2002.

[171] H. Ollivier, S. E. Thomas, S. C. Wein, I. Maillette de Buy Wenniger, Coste, J. C. Loredo, N. Somaschi, A. Harouri, A. Lemaitre, I. Sagnes, L. Lanco, C. Simon, C. Anton, O. Krebs, and P. Senellart. Hong-ou-mandel interference with imperfect single photon sources. arXiv(2005.01743), 2020.

[172] A.B. U'Ren, C. Silberhorn, J.L. Ball, K. Banaszek, and I.A. Walmsley. Characterization of the nonclassical nature of conditionally prepared single photons. Phys. Rev. A, 72:021802, Aug 2005.

[173] R. Trivedi, K.A. Fischer, J. Vučković, and K. Müller. Generation of non-classical light using semiconductor quantum dots. Advanced Quantum Technologies, 3(1):1900007.

[174] S.L. Portalupi, G. Hornecker, V. Giesz, T. Grange, A. Lemaître, J. Demory, I. Sagnes, N.D. Lanzillotti-Kimura, L. Lanco, A. Auffèves, and P. Senellart. Bright phonon-tuned single-photon source. Nano Letters, 15(10):6290–6294, 2015.

[175] A. Kiraz, M. Atatüre, and A. Imamoğlu. Quantum-dot single-photon sources: Prospects for applications in linear optics quantum-information processing. Phys. Rev. A, 69:032305, Mar 2004.

[176] S. Ates, S. M. Ulrich, S. Reitzenstein, A. Löffler, A. Forchel, and P. Michler. Post-selected indistinguishable photons from the resonance fluorescence of a single quantum dot in a microcavity. Physical Review Letters, 103:1–4, 2009.

[177] A. Muller, E. B. Flagg, P. Bianucci, X. Y. Wang, D. G. Deppe, W. Ma, J. Zhang, G. J. Salamo, M. Xiao, and C. K. Shih. Resonance fluorescence from a coherently driven semiconductor quantum dot in a cavity. Phys. Rev. Lett., 99:187402, Nov 2007.

[178] K. Kuroda, T. Kuroda, K. Watanabe, T. Mano, K. Sakoda, G. Kido, and N. Koguchi. Final-state readout of exciton qubits by observing resonantly excited photoluminescence in quantum dots. Applied Physics Letters, 90(5):051909, 2007.

[179] R. Melet, V. Voliotis, A. Enderlin, D. Roditchev, X. L. Wang, T. Guillet, and R. Grousson. Resonant excitonic emission of a single quantum dot in the rabi regime. Phys. Rev. B, 78:073301, Aug 2008.

[180] T. H. Stievater, Xiaoqin Li, D. G. Steel, D. Gammon, D. S. Katzer, D. Park, C. Piermarocchi, and L. J. Sham. Rabi oscillations of excitons in single quantum dots. Physical Review Letters, 87:5–8, 2001.

[181] A. J. Ramsay, T. M. Godden, S. J. Boyle, E. M. Gauger, A. Nazir, B. W. Lovett, A. M. Fox, and M. S. Skolnick. Phonon-induced rabi-frequency renormalization of optically driven single InGaAs/GaAs quantum dots. Physical Review Letters, 105:1–4, 2010.

[182] T. Faust, J. Rieger, M. Seitner, Kotthaus, and E.M. J.P. Weig. Coherent control of a classical nanomechanical two-level system. Nature Phys., 9:485–488, July 2013.

[183] I. I. Rabi. Space quantization in a gyrating magnetic field. Phys. Rev., 51:652–654, Apr 1937.

[184] H. Giessen, A. Knorr, S. Haas, S. W. Koch, S. Linden, J. Kuhl, M. Hetterich, M. Grün, and C. Klingshirn. Self-induced transmission on a free exciton resonance in a semiconductor. Phys. Rev. Lett., 81:4260–4263, Nov 1998.

[185] H. Kamada, H. Gotoh, J. Temmyo, T. Takagahara, and H. Ando. Exciton rabi oscillation in a single quantum dot. Phys. Rev. Lett., 87:246401, Nov 2001.

[186] A.J. Ramsay, A.V. Gopal, E.M. Gauger, A. Nazir, B.W. Lovett, A.M. Fox, and M.S. Skolnick. Damping of exciton rabi rotations by acoustic phonons in optically excited InGaAs/GaAs quantum dots. Phys. Rev. Lett., 104:017402, Jan 2010.

[187] O. Krebs, P. Maletinsky, T. Amand, B. Urbaszek, A. Lemaître, P. Voisin, X. Marie, and A. Imamoglu. Anomalous hanle effect due to optically created transverse overhauser field in single InAs/GaAs quantum dots. Phys. Rev. Lett., 104:056603, Feb 2010.

[188] P. Hilaire, C. Millet, J.C. Loredo, C. Antón, A. Harouri, A. Lemaître, I. Sagnes, N. Somaschi, O. Krebs, P. Senellart, and L. Lanco. Deterministic assembly of a charged-quantum-dot–micropillar cavity device. Phys. Rev. B, 102:195402, Nov 2020.

[189] S. Slussarenko and G.J. Pryde. Photonic quantum information processing: A concise review. Applied Physics Reviews, 6(4):041303, 2019.

[190] R. M. Macnab. Examination of bacterial flagellation by dark-field microscopy. Journal of Clinical Microbiology, 4(3):258–265, 1976.

[191] L. Li, Tian, Xi Wu, Feng Liu, and Na Li. Analytical methods based on the light-scattering of plasmonic nanoparticles at the single particle level with dark-field microscopy imaging. Analyst, 142(2):248–256, 2017.

[192] H. S. Nguyen, G. Sallen, C. Voisin, Ph. Roussignol, C. Diederichs, and G. Cassabois. Ultra-coherent single photon source. Applied Physics Letters, 99(26):261904, 2011.

[193] D. Najer, I. Söllner, P. Sekatski, V. Dolique, M.C. Löbl, D. Riedel, R. Schott, S. Starosielec, S.R. Valentin, A.D. Wieck, N/ Sangouard, A. Ludwig, and R.J. Warburton. A gated quantum dot strongly coupled to an optical microcavity. Nature, (575):622–627, 2019.

[194] A. Vamivakas, C. Lu, C. Matthiesen, Y. Zhao, Fält S., A. Badolato, and M. Atatüre. Observation of spin-dependent quantum jumps via quantum dot resonance fluorescence. Nature, (467):297–300, 2010.

[195] S. T. Y ılmaz, P. Fallahi, and A. Imamoğlu. Quantum-dot-spin single-photon interface. Phys. Rev. Lett., 105:033601, Jul 2010.

[196] A.V. Kuhlmann, J. Houel, D. Brunner, A. Ludwig, D. Reuter, A.D. Wieck, and R.J. Warburton. A dark-field microscope for background-free detection of resonance fluorescence from single semiconductor quantum dots operating in a set-and-forget mode. Review of Scientific Instruments, 84, 7 2013.

[197] L. De Santis, C. Antón, B. Reznychenko, N. Somaschi, G. Coppola, J. Senellart, C. Gómez, A. Lemaître, I. Sagnes, A.G. White, L. Lanco, A. Auffèves, and P. Senellart. A solid-state single-photon filter. Nature Nanotechnology, 12:663–667, 7 2017.

[198] J. C. Loredo, C. Antón, B. Reznychenko, P. Hilaire, A. Harouri, C. Millet, H. Ollivier, N. Somaschi, L. De Santis, A. Lemaître, I. Sagnes, L. Lanco, A. Auffèves, O. Krebs, and P. Senellart. Generation of non-classical light in a photon-number superposition. Nature Photonics, 13:803–808, 11 2019.

[199] A. Yariv. Optical electronics in modern communications. Oxford university press, 1997.

[200] B. Gayral. Controlling spontaneous emission dynamics in semiconductor microcavities: An experimental approach. Annales de Physique, 26:39–43, 2001.

[201] D. Marcuse. Gaussian approximation of the fundamental modes of graded-index fibres. J. Opt. Soc. Am., 68:103–109, 1978.

[202] N. Delen and B. Hooker. Free-space beam propagation between arbitrarily oriented planes based on full diffraction theory: a fast Fourier transform approach. 1998.

[203] J.W. Goodman. Introduction of Fourier optics, volume Seconde Edition. 1996.

[204] G.P. Agrawal and D.N. Pattanayak. Gaussian beam propagation beyond the paraxial approximation. J.Opt.Soc.Am, 69:575–578, 1978.

[205] D. Marcuse. Loss Analysis of Single-Mode Fiber Splices. The Bell System Technical Journal, 56(5), 1977.

[206] R.E. Wagner and W.J. Tomlinson. Coupling efficiency of optics in single-mode fiber components. Applied Optics, 21:2671–2688, 1982.

[207] H. Snijders, J. A. Frey, J. Norman, V. P. Post, A. C. Gossard, J. E. Bowers, M. P. Van Exter, W. Löffler, and D. Bouwmeester. Fiber-coupled cavity-qed source of identical single photons. Physical Review Applied, 9, 3 2018.

[208] M. Benelajla, E. Kammann, B. Urbaszek, and K. Karrai. The physical origins of extreme cross-polarization extinction in confocal microscopy, 2020.

[209] L. Novotny, R.D. Grober, and K. Karrai. Reflected image of a strongly focused spot. Optics Letters, 26, 2001.

[210] H. Maeckler and G. Lehmann. Ann. Phys., 10:153, 1952.

[211] G. Lehmann and H. Maeckler. Ann. Phys., 10, 1952.

[212] R. Ulrich and A. Simon. Polarization optics of twisted single-mode fibers. Appl. Opt., 18(13):2241–2251, Jul 1979.

[213] R. Ulrich, S. C. Rashleigh, and W. Eickhoff. Bending-induced birefringence in single-mode fibers. Opt. Lett., 5(6):273–275, Jun 1980.

[214] D.E. Reiter, T. Kuhn, M. Glässl, and V.M. Axt. The role of phonons for exciton and biexciton generation in an optically driven quantum dot. Journal of Physics: Condensed Matter, 26(42):423203, oct 2014.

[215] J. H. Quilter, A. J. Brash, F. Liu, M. Glässl, A. M. Barth, V. M. Axt, A. J. Ramsay, M. S. Skolnick, and A. M. Fox. Phonon-assisted population inversion of a single InGaAs/GaAs quantum dot by pulsed laser excitation. Physical Review Letters, 114:1–5, 2015.

[216] M. Reindl, J.H. Weber, D. Huber, C. Schimpf, S.F. Covre Da Silva, S.L. Portalupi, R. Trotta, P. Michler, and A. Rastelli. Highly indistinguishable single photons from incoherently excited quantum dots. Physical Review B, 100:155420, 2019.

[217] L. Hanschke, K.A. Fischer, S. Appel, D. Lukin, J. Wierzbowski, S. Sun, R. Trivedi, J. Vučković, J.J. Finley, and K. Müller. Quantum dot single-photon sources with ultra-low multi-photon probability. npj Quantum Inf, 4, 2018.

[218] C. M. Simon, T. Belhadj, B. Chatel, T. Amand, P. Renucci, A. Lemaitre, O. Krebs, P. A. Dalgarno, R. J. Warburton, X. Marie, and B. Urbaszek. Robust quantum dot exciton generation via adiabatic passage with frequency-swept optical pulses. Physical Review Letters, 106:1–4, 2011.

[219] S. Lüker, K. Gawarecki, D.E. Reiter, A. Grodecka-Grad, V.M. Axt, P. Machnikowski, and T. Kuhn. Influence of acoustic phonons on the optical control of quantum dots driven by adiabatic rapid passage. Physical Review B, 85(12):121302, 2012.

[220] S. Bounouar, M. Müller, A. M. Barth, M. Glässl, V. M. Axt, and P. Michler. Phonon-assisted robust and deterministic two-photon biexciton preparation in a quantum dot. Phys. Rev. B, 91:161302, Apr 2015.

[221] A. J. Ramsay, A. V. Gopal, E. M. Gauger, A. Nazir, B. W. Lovett, A. M. Fox, and M. S. Skolnick. Damping of exciton rabi rotations by acoustic phonons in optically excited InGaAs/GaAs quantum dots. Physical Review Letters, 104:1–5, 2010.

[222] L. Allen and J.H. Eberly. Optical resonance and two-level atoms., volume 28. 1987.

[223] B. Krummheuer, V. M. Axt, and T. Kuhn. Theory of pure dephasing and the resulting absorption line shape in semiconductor quantum dots. Physical Review B - Condensed Matter and Materials Physics, 65:1–12, 2002.

[224] S. Hughes and H.J. Carmichael. Crystal vibrations invert quantum dot exciton. Physics, 8:29, 2015.

[225] P.-L. Ardelt, L. Hanschke, K.A. Fischer, K. Müller, A. Kleinkauf, M. Koller, A. Bechtold, T. Simmet, J. Wierzbowski, H. Riedl, G. Abstreiter, and J.J. Finley. Dissipative preparation of the exciton and biexciton in self-assembled quantum dots on picosecond time scales. Phys. Rev. B, 90:241404, Dec 2014.

[226] C. Gustin and S. Hughes. Efficient pulse-excitation techniques for single photon sources from quantum dots in optical cavities. Advanced Quantum Technologies, 1900073:1900073, 2019.

[227] M. Cosacchi, F. Ungar, M. Cygorek, A. Vagov, and V. M. Axt. Emission-frequency separated high quality single-photon sources enabled by phonons. Physical Review Letters, 123:17403, 2019.

[228] A. Schlehahn, S. Fischbach, R. Schmidt, A. Kaganskiy, A. Strittmatter, S. Rodt, T. Heindel, and S. Reitzenstein. A stand-alone fiber-coupled single-photon source. Sci. Rep., 8:1340, 2018.

[229] K. Żołnacz, A. Musiał, N. Srocka, J. Große, M.J. Schlösinger, P.I. Schneider, O. Kravets, M. Mikulicz, J. Olszewski, K. Poturaj, G. Wójcik, P. Mergo, K. Dybka, M. Dyrkacz, M. Dłubek, S. Rodt, S. Burger, L. Zschiedrich, G. Sęk, S. Reitzenstein, and W. Urbańczyk. Method for direct coupling of a semiconductor quantum dot to an optical fiber for single-photon source applications. Optics Express, 27:26772, 2019.

[230] H. Kumano, T. Harada, I. Suemune, H. Nakajima, T. Kuroda, T. Mano, K. Sakoda, S. Odashima, and H. Sasakura. Stable and efficient collection of single photons emitted from a semiconductor quantum dot into a single-mode optical fiber. Applied Physics Express, 9(3):032801, 2016.

[231] G. Shambat, J. Provine, K. Rivoire, T. Sarmiento, J. Harris, and J. Vučković. Optical fiber tips functionalized with semiconductor photonic crystal cavities. Applied Physics Letters, 99(19):191102, 2011.

[232] W.J. Wadsworth, R.M. Percival, G. Bouwmans, J. C Knight, T.A. Birks, T.D. Hedley, and P.St J. Russell. Very high numerical aperture fibers. IEEE Photonics Technology Letters, 16(3):843–845, 2004.

[233] H.G Dantanarayana, N. Abdel-Moneim, Z. Tang, L. Sojka, S. Sujecki, D. Furniss, A.B. Seddon, I. Kubat, O. Bang, and T.M. Benson. Refractive index dispersion of chalcogenide glasses for ultra-high numerical-aperture fiber for mid-infrared supercontinuum generation. Opt. Mater. Express, 4(7):1444–1455, Jul 2014.

[234] R.P. Espindola, R.S. Windeler, A.A. Abramov, B.J. Eggleton, T.A. Strasser, and D.J. DiGiovanni. External refractive index insensitive air-clad long period fibre grating. Electronics Letters, 35(4):327–328, 1999.

[235] L.G. Cohen and M.V. Schneider. Microlenses for coupling junction lasers to optical fibers. Applied Optics, 13:89–94, 1974.

[236] R. Bachelot, A. Fares, R. Fikri, D. Barchiesi, G. Lerondel, and P. Royer. Coupling semiconductor lasers into single-mode optical fibers by use of tips grown by photopolymerization. Opt. Lett., 29(17):1971–1973, 2004.

[237] G. Nemova and R. Kashyap. Highly efficient lens couplers for laser-diodes based on long period grating in special graded-index fiber. Optics Communications, 261:249–257, 5 2006.

[238] S.A Self. Focusing of spherical gaussian beams. Appl. Opt., 22(5):658–661, Mar 1983.

[239] W. Jung, W. Benalcazar, A. Ahmad, U. Sharma, H. Tu, and S. A. Boppart. Numerical analysis of gradient index lens–based optical coherence tomography imaging probes. Journal of Biomedical Optics, 15(6):066027, 2010.

[240] John M. Khosrofian and Bruce A. Garetz. Measurement of a gaussian laser beam diameter through the direct inversion of knife-edge data. Applied Optics, 22:3406, 1983.

[241] Y. Suzaki and A. Tachibana. Measurement of the m sized radius of gaussian laser beam using the scanning knife-edge. Applied Optics, 14:2809, 1975.

[242] P. Stepanov, M. Elzo-Aizarna, J. Bleuse, N.S. Malik, Y. Curé, E. Gautier, V. Favre-Nicolin, J.-M. Gérard, and J. Claudon. Large and uniform optical emission shifts in quantum dots strained along their growth axis. Nano Letters, 16(5):3215–3220, 2016.

[243] O. Ortiz, F. Pastier, A. Rodriguez, Priya, A. Lemaitre, C. Gomez-Carbonell, I. Sagnes, A. Harouri, P. Senellart, V. Giesz, M. Esmann, and N. D. Lanzillotti-Kimura. Fiber-integrated microcavities for efficient generation of coherent acoustic phonons. Applied Physics Letters, 117(18):183102, 2020.

[244] H. Takesue, S. Nam, Q. Zhang, R.H Hadfield, T. Honjo, K. Tamaki, and Y. Yamamoto. Quantum key distribution over a 40-db channel loss using superconducting single-photon detectors. Nature Photon, (1):343–348, 2007.

[245] H. Takesue. Single-photon frequency down-conversion experiment. Phys. Rev. A, 82:013833, Jul 2010.

[246] N. Curtz, R. Thew, C. Simon, N. Gisin, and H. Zbinden. Coherent frequency-down-conversion interface for quantum repeaters. Opt. Express, 18(21):22099–22104, Oct 2010.

[247] J.S. Pelc, C. Langrock, Q. Zhang, and M.M. Fejer. Influence of domain disorder on parametric noise in quasi-phase-matched quantum frequency converters. Opt. Lett., 35(16):2804–2806, Aug 2010.

[248] S. Zaske, A. Lenhard, and C. Becher. Efficient frequency downconversion at the single photon level from the red spectral range to the telecommunications c-band. Opt. Express, 19(13):12825–12836, Jun 2011.

[249] R. Ikuta, Y. Kusaka, T. Kitano, H. Kato, T. Yamamoto, M. Koashi, and N. Imoto. Wide-band quantum interface for visible-to-telecommunication wavelength conversion. Nat Commun, (2):537, 2011.

[250] A. Radnaev, Y. Dudin, R. Zhao, H.H. Jen, S.D. Jenkins, A. Kuzmich, and T.A.B. Kennedy. A quantum memory with telecom-wavelength conversion. Nature Phys, (6):894–899, 2010.

[251] J.S Pelc, L. Yu, K. De Greve, P.L. McMahon, C.M. Natarajan, V. Esfandyarpour, S. Maier, C. Schneider, M. Kamp, S. Höfling, R.H. Hadfield, A. Forchel, Y. Yamamoto, and M.M. Fejer. Downconversion quantum interface for a single quantum dot spin and 1550-nm single-photon channel. Opt. Express, 20(25):27510–27519, Dec 2012.

[252] R. Patel, A. Bennett, I. Farrer, C.A. Nicoll, D.A. Ritchie, and A.J. Shields. Two-photon interference of the emission from electrically tunable remote quantum dots. Nature Photon, (4):632–635, 2010.

[253] K. De Greve, L. Yu, P. McMahon, J.S. Pelc, C.M. Natarajan, N.Y. Kim, E. Abe, S. Maier, C. Schneider, M. Kamp, S. Höfling, R.H. Hadfield, A. Forchel, M.M. Fejer, and Y. Yamamoto. Quantum-dot spin–photon entanglement via frequency downconversion to telecom wavelength. Nature, (491):421–425, 2012.

[254] L. Yu, C. Natarajan, T. Horikiri, C. Langrock, J.S. Pelc, M.G. Tanner, E. Abe, S. Maier, C. Schneider, S. Höfling, M. Kamp, R.H. Hadfield, M.M. Fejer, and Y. Yamamoto. Two-photon interference at telecom wavelengths for time-bin-encoded single photons from quantum-dot spin qubits. Nature Commu, (6):8955, 2015.

[255] V. Krutyanskiy, M. Meraner, J. Schupp, V. Krcmarsky, H. Hainzer, and P.B. Lanyon. Light-matter entanglement over 50km of optical fibre. npj Quantum Inf, (5):72, 2019.

[256] B. Kambs, J. Kettler, M. Bock, J.N. Becker, C. Arend, A. Lenhard, S.L. Portalupi, M. Jetter, P. Michler, and C. Becher. Low-noise quantum frequency down-conversion of indistinguishable photons. Opt. Express, 24(19):22250–22260, Sep 2016.

[257] V. M. Ustinov, N. A. Maleev, A. E. Zhukov, A. R. Kovsh, A. Yu. Egorov, A. V. Lunev, B. V. Volovik, I. L. Krestnikov, Yu. G. Musikhin, N. A. Bert, P. S. Kop'ev, Zh. I. Alferov, N. N. Ledentsov, and D. Bimberg. InAs/InGaAs quantum dot structures on GaAs substrates emitting at 1.3 m. Applied Physics Letters, 74(19):2815–2817, 1999.

[258] A. Hospodkova, E. Hulicius, J. Oswald, J. Pangrác, T. Mates, K. Kuldová, K. Melichar, and T. Šimeček. Properties of movpe InAs/GaAs quantum dots overgrown by InGaAs. Journal of crystal growth, 298:582–585, 2007.

[259] E. Goldmann, M. Paul, F.F. Krause, K. Müller, J. Kettler, T. Mehrtens, A. Rosenauer, M. Jetter, P. Michler, and F. Jahnke. Structural and emission properties of InGaAs/GaAs quantum dots emitting at 1.3 μm. Applied Physics Letters, 105(15):152102, 2014.

[260] L. Dusanowski, P. Holewa, A. Maryński, A. Musiał, T. Heuser, N. Srocka, D. Quandt, A. Strittmatter, S. Rodt, J. Misiewicz, S. Reitzenstein, and G. Sęk. Triggered high-purity telecom-wavelength single-photon generation from p-shell-driven InGaAs/GaAs quantum dot. Opt. Express, 25(25):31122–31129, Dec 2017.

[261] C. Carmesin, F. Olbrich, T. Mehrtens, M. Florian, S. Michael, S. Schreier, C. Nawrath, M. Paul, J. Höschele, B. Gerken, J. Kettler, S. L. Portalupi, M. Jetter, P. Michler, A. Rosenauer, and F. Jahnke. Structural and optical properties of InAs/(In)GaAs/GaAs quantum dots with single-photon emission in the telecom c-band up to 77 k. Phys. Rev. B, 98:125407, 2018.

[262] A. Musiał, P. Holewa, P. Wyborski, M. Syperek, A. Kors, J.P. Reithmaier, G. Sęk, and M. Benyoucef. High-purity triggered single-photon emission from symmetric single InAs/inp quantum dots around the telecom c-band window. Advanced Quantum Technologies, 3(2):1900082, 2020.

[263] S.L. Portalupi, M. Jetter, and P. Michler. InAs quantum dots grown on metamorphic buffers as non-classical light sources at telecom c-band: a review. Semiconductor Science and Technology, 34(5):053001, apr 2019.

[264] N. Srocka, A. Musiał, P.-I. Schneider, P. Mrowiński, P. Holewa, S. Burger, D. Quandt, A. Strittmatter, S. Rodt, S. Reitzenstein, and G. Sęk. Enhanced photon-extraction efficiency from InGaAs/GaAs quantum dots in deterministic photonic structures at 1.3 m fabricated by in-situ electron-beam lithography. AIP Advances, 8(8):085205, 2018.

[265] N. Srocka, P. Mrowiński, J. Große, M. von Helversen, T. Heindel, S. Rodt, and S. Reitzenstein. Deterministically fabricated quantum dot single-photon source emitting indistinguishable photons in the telecom o-band. Applied Physics Letters, 116(23):231104, 2020.

"Quoique vous fassiez, faites-le avec passion.
Vivez avec passion"

attribuée à Chirstian Dior

université PARIS-SACLAY | ÉCOLE DOCTORALE Ondes et matière (EDOM)

Titre: Vers des sources semi-conductrices de photons uniques et indiscernables, efficaces et faciles à utiliser, pour des applications quantiques

Mots clés: Boîtes quantiques, microscope, excitation assistée par des phonons acoustiques longitudinaux, sources fibrées

Résumé: L'amélioration constante des performances des sources semi-conductrices de photons uniques en ont fait des composants essentiels pour les applications quantiques nécessitant un flux élevé de photons uniques et indiscernables. Dans ce travail, nous utilisons des boîtes quantiques (BQ) couplées à des micro-piliers optiques ayant déjà prouvées leur capacité à atteindre ces exigences. Dans ce contexte, nous développons différentes techniques pour obtenir une source efficace, tout en améliorant la facilité d'utilisation pour les utilisateurs non experts.

Nous détaillons donc le développement et l'optimisation d'un microscope confocal stable et compact pour collecter efficacement les photons uniques dans une fibre monomode pendant plusieurs jours. Ce dernier s'adapte à la fois à différents types de collection (espace libre ou fibré) ainsi qu'à différentes techniques d'excitation de la BQ: excitation sous fluorescence résonante, ou assistée par l'émission de phonons acoustiques longitudinaux (AL). Cette seconde manière d'exciter se base sur les interactions entre les transitions de la BQ et les phonons acoustiques longitudinaux grâce à un laser légèrement désaccordé en énergie. Ainsi, ce dernier est filtré spectralement, et tous les photons uniques émis sont collectés. Nous démontrons alors une brillance multipliée par trois, ainsi qu'une émission, linéairement polarisée, de photons uniques et indiscernables. Enfin, afin de fournir une source de photons uniques "plug-and-play", nous détaillons le développement d'un système complétement fibré afin de s'affranchir de positionneurs et d'un cryostat à faibles vibrations, volumineux et chers. Ainsi, nous proposons une méthode pour placer et fixer une fibre monomode au-dessus d'un pilier. Ce travail est toujours en cours, mais les premiers résultats montrent le potentiel de cette technique.

Title: Practical and efficient solid-state sources of single and indistinguishable photons for quantum applications

Keywords: Quantum dots, microscope, LA-phonon assisted excitation, fibred sources

Abstract: The constant improvement in performance of solid-state single-photon sources have established them as a prime candidate for quantum optics applications, whose require high flux of indistinguishable and pure single photons. Here, we use individual self-assembled quantum dots (QD) coupled to optical pillar cavities which proved their abilities to fulfil these requirements. In this framework, we investigate different development techniques to get a practical and efficient source, while also improving the ease-of-use for non-expert users.

The first result is the development and optimisation of a compact and stable confocal microscope to efficiently collect the emitted single photons into a single-mode fibre over days, while making it easy to use. The latter is adapted for both the collection (free-space or fibred) and the excitation schemes of a QD: the resonant fluorescence or the longitudinal-acoustics (LA) phonon assisted excitation. This second excitation regime is based on the interactions between QDs transitions and the phonon bath thanks to a slight energy detuning of the excitation laser. Thus, the laser can be spectrally filtered, and then all the emitted photons are collected. We then report a first lens brightness multiplied by a factor of three, and an emission of single and indistinguishable photons with a high linear-polarisation purity. Finally, to provide a "plug-and-play" single-photon source, we detail the development of a fully fibred system to overcome the need of a large and expensive system based on a low-vibration cryostat and positioners. We then report method to set and fix a single-mode fibre above a pillar. This work is still in progress, but the first results already show the potential of this technique.